The Jahn Teller and Surface Interactions in C_{60} Nano Systems

Haifa S. Alqannas, M.Sc.

Thesis submitted to The University of Nottingham
for the degree of Doctor of Philosophy
July 2014

To you Mum

Contents

Abstract

Scanning Tunnelling Microscopy (STM) is the fastest possible method of imaging the molecular orbitals of the C_{60} anions with resolution at the single atom level. For the particular anions of fullerene C_{60}, the splitting of the molecular orbitals due to the internal Jahn-Teller effects (JT) add further difficulties in understanding the published experimental images. In the current work, the effect of JT interaction on STM recorded images is studied. For higher charged states, the Coulomb interaction affects the distribution of electrons around the ion, and then as a consequence, the STM current. The external interaction between the molecule and the surface substrate is equally important. Symmetry analysis using group theory and Hückel molecular orbital (HMO) theory are applied in order to describe the influence of the surface interactions on JT minima associated with D_{3d}, D_{5d}, D_{2h}, and C_{2h} symmetries. It represents some fullerene anions, which are adsorbed to the surface with different orientations, such as pentagon, hexagon, and double-bond prone toward the surface. Several ions with higher charges are investigated, such as C_{60}^{2-}, C_{60}^{3-}, and C_{60}^{4-}. In case of high symmetry orientations, the JT minima of the ions on a surface are split into subgroups with equal energies, depending on the type of orientation. The interpretation of the experimental observations is always possible for any orientation from the JT minima distribution and the contribution to the images from different components of the degenerate molecular orbitals.

Acknowledgements

It was a gift to do research under supervision of Dr. Janette Dunn. It is the time to express my great gratitude to her for the friendly continual support, and for sharing her knowledge and skills. Thanks so much for giving me the opportunity to exploit each single available chance to build up my research experience.

A special thanks to Dr.Ian Hands for his encouragement and technical support during my first year.

It is beyond words to express my thanks to my wonderful mother Aish Almaktoom for her unlimited support and my husband and my lovely children: Abdulmohsen, Ritaj, Mosaad and my sweet younger sister Afra, who have in one way or other significantly contributed to the completion of this work.

In addition to those considerable people, it was my good luck to meet Andrew Lakin in our research group and I would like to thank him for the continual discussions and support, and who made our research area more challenging and enjoyable.

My last appreciation to Dr.Fatma Bahabri and Dr.Wedad Alharbi for helping me in every way to follow this opportunity to study in UK.

Chapter 1

Introduction

The Jahn Teller Effect (JT) is one of the most important interactions observed in many fields of physics and chemistry, attracting the attention of both theoretical and experimental workers. Concerns about the degenerate electronic states in linear molecular systems led Jahn and Teller, in 1936, to discover the effect, which carries their names. Jahn and Teller formulated a theorem for a non linear molecular system, where for a degenerate electronic state, coupling to molecular vibrations will reduce the symmetry and lower the system energy [1]. Their theory was based on the stability of the degenerate electronic states with respect to the distortions of the molecular structure. As a consequence, the geometry of a molecule, such as CO_2, is distorted due to the existence of the JT effect.

The JT effect is concerned with the fundamental problem of how to describe quantum systems in condensed matter physics and chemistry, in which electronic and vibrational degrees of freedom (phonons) are coupled. This coupling is more important in the case of degenerate electronic states linked to a molecular configuration. As a result, some symmetry reduction interaction will occur, whereby the molecular deformation can remove the degeneracies of the states. Reduced symmetry will usually bring about a breaking of the degeneracy, and so JT interactions will reduce the energy of the system. Use of the term, electron-phonon, implies that there are both heavy and light particles to be considered. In general, the theory is useful and applicable to any molecular problems with more than two electrons. In the case of strong interactions between electronic and vibrational motion, the symmetry will be distorted permanently due to the static JT effect. However, this effect will be considered as dynamic, in the case of weak interaction. It is not difficult to understand this behaviour in motion due to the high symmetry in the molecular orbitals. In other words, the molecule has multiple chances to reduce the total system energy. In fact, equivalent configurations have the same energy as each other. The system $H \otimes h$ was the first example where

the symmetry of the ground state is changed [2][3]. A good step in starting a study of any JT system is to investigate the adiabatic potential energy surface (APES). In general, when the coupling is strong, the nuclear motion is assumed to be confined to the lowest APES (LAPES). The LAPES can be obtained by solving the Schrödinger equation for a molecule, involving the JT coupling between the vibronic modes and the electrons within the electronic basis. Analysing the LAPES is necessary to study the nature of the system, and to determine the associated energies and wave functions.
Several years later, Öpik and Pryce in [4] provided a way to define the minimum wells of the APES in a simple system, such as $E \otimes e$.

Subsequently, the detection of fullerenes in 1985 by Kroto and co-workers, in ref.[5], opened up a new area in carbon research, particularly because of their unusual properties and the wide range of potential applications. Some of these properties are due to the rarely high molecular symmetry in nature, which results in high electronic and vibrational degeneracies, as exemplified by the JT effect. This perfect high symmetry structure, as in fig. 1.1, is discussed in detail in forthcoming chapters.

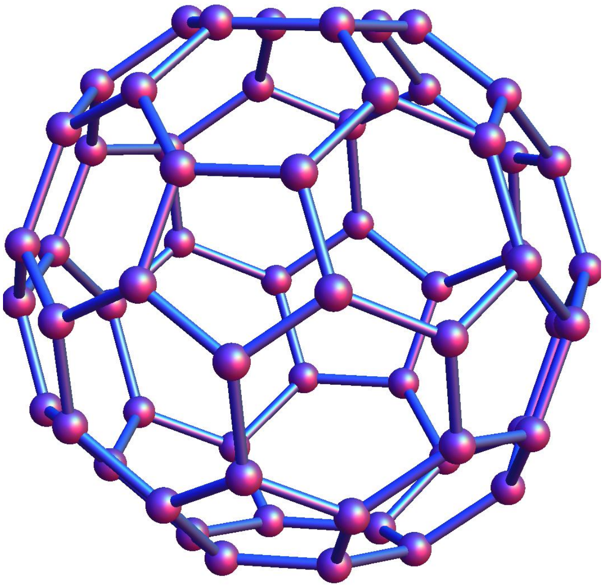

Figure 1.1: The structure of C_{60} fullerene

In general, fullerene C_{60} is active, but becomes stable above room temperature. It can also be purified, and may be produced using the carbon arc method, or its variations [6]. There are numerous and widespread potential applications for fullerenes, and related carbon nanotubes, including nanoelectronics, photovoltaics, chemical sensors or catalysts and medical applications, such as drug delivery. Exploitation of the orientational properties of C_{60} could form the basis for the design of new functionaliased catalysts or ordered thin films. The fullerene molecule C_{60} is the essential basic unit of organic conductors, where a wide range of carbon nano applications are based on fullerenes, including single-molecule transistors and nanotubes. In the solid state, the unsaturated molecular orbitals with generous vibrational and electronic states, such as fullerene ions, are usually prepared to build electronic bonds. More specifically, the C_{60} molecular form is almost spherical, and has sufficient empty states for other ions or electrons. Studies of these anions have also gained wide technological importance due to their particular properties, arising from the JT effect, such as C_{60}^{3-} ions in materials of the form A_3C_{60} (A = alkali metal), which can be superconducting up to relatively high temperatures [7],[8] and through NMR studies in ref. [9], whereas C_{60}^{4-} ions in materials of the form A_4C_{60} are insulating [10],[11],[12]. For example, the σ bonds within the molecules in many organic solids are greater than the π bonds to preserve the molecular features. Studying the molecular orbital structures is a very important step, in order to gain an overall understanding of molecular behavior.

Scanning Tunnelling Microscopy (STM) is a method of imaging a surface with a resolution as high as single atoms. Modern STM is now of sufficiently high resolution to be able to distinguish structural features of such molecules via observations of the so-called Local Density of States (LDOS) near the Fermi level. STM can be used in two important scanning modes, namely constant height and constant current. The STM technique is able to respond to molecules adsorbed onto the surface, where by using either modes, this response produces an image of the molecule itself.
However, it can be a challenge to interpret these images, as the molecules can be distorted by the JT effect and by interactions with the surface. For example, ref. [13] shows evidence that the JT effect can distort the fullerene C_{60} into D_{3d} symmetry. Doped C_{60} molecules are known to exhibit strong JT interactions. Therefore, studies of JT effects in these molecules are the first step in order to have sufficient overview of the behaviour of C_{60} and other fullerene molecules.

The main topic proposed for this work, in the first part, is to simulate theoretical STM images of the molecular orbitals for C_{60}^{2-} anions, subject to static and dynamic JT distortions in linear [14],[15] and quadratic coupling [16], adsorbed onto surfaces at various geometries as single molecules and doubly-charged ion starting from a Hückel molecular orbital (HMO) approach. Hückel theory is faster and simpler than the Density Functional Theory (DFT) usually used as in References [17],[18],[19],[20]. However, perfect agreement between the results for the neutral molecule is obtained by using both methods. This study will be extended to cover other higher charged ions, such as C_{60}^{4-} and C_{60}^{3-} of doped fullerenes adsorbed onto surfaces in various geometries.

In the case of doubly-charged ion, C_{60}^{2-} will be distorted to D_{3d} or D_{5d} symmetry by the JT effect. The surface interactions reduce the symmetry further. In fact, even at low temperatures [21], it must be taken into consideration that tunnelling between the wells is expected to occur on a shorter timescale than the millisecond timescale of the STM procedure [22]. In case of this dynamic JT effect, the system can be predicted to jump between wells and spend almost negligible time at intermediate distortions. Therefore, the STM images are a combination of images from individual minimum wells. This dynamic JT effect allows tunnelling between wells, whereas the system would be locked in one well, in the static JT effect.

The effect of the substrate is one of the main factors complicating the C_{60}^{n-} STM images with JT effect present. Our focus is on the STM images produced from the lowest unoccupied molecular orbital (LUMO) of the doubly-charged ion C_{60}^{2-} adsorbed onto a substrate, while considering both the surface and JT interactions.

The most interesting point is: how will the JT effect be influenced by the existence of a surface interaction in the C_{60}^{n-} molecules, and the other complications of the JT effect, which need to be considered. Indeed, constructions of multi-electron states that are written in terms of single electron states, which build up the LUMO will be provided. The kind of signatures that the surface interaction may produce will be investigated. We will also investigate how the JT effect with surface interactions reduce the energy of the system.

In order to model the JT effect, with other external interactions, such as with a surface, this work will assume that the anions are adsorbed onto a substrate. Then, the STM probes the states of C_{60}^{n-} ions in different orientations. The process will start with an overview of how the JT effect will be treated, and then the surface interaction will be taken into account. This will conclude by combining the two interactions to find out the effect of the possible orientations on the surface on which the C_{60} is adsorbed. Then, this formalism will be used to provide STM images of some fullerene ions of interest absorbed on a substrate with different orientations, such as pentagon, hexagon, or double bond facing the surface.

The theoretical simulations of STM images on surfaces, which form the major part of this work, will be followed by the calculation of the quantum mechanical width of special lines arising from transitions between energy levels of the fullerene molecule C_{60}. In fact, the calculations of JT effects in the fullerene anion C_{60}^{-}, which have been investigated in an earlier work [23], will be extended, by providing a fundamental model of experimental data reported in the literature. In particular, values for the electron-phonon coupling constants are determined from studies of the photoemission radiation of C_{60}^{-}, and the lowering of the total energy for C_{60}^{n-} occurring from electron-phonon coupling. On doping the fullerene ion, the additional electron moves to occupy the T_{1u} orbital. These effects have been investigated in detail, when second order coupling constants are considered in the system. This ion was investigated in an earlier work [23], the APES takes the form of a three-dimensional trough with an equal energy surface upon which the system is allowed to move between wells in the trough. However, including quadratic couplings in the problem causes the equal energy points on the trough to be warped to form minima. These minima are found to be either pentagonal (D_{5d}) or trigonal (D_{3d}), depending on the magnitudes of the JT effect parameters. In this stage, the focus will be on trigonal minima D_{3d} in a $T \otimes h$ system, because experiments indicate that the D_{3d} trigonal minima is the most likely ground state. The problem will be dealt with by applying a unitary shift transformation method and energy minimisation procedure presented originally by Bates, Dunn and Sigmund in 1987 [24] in order to locate the position of the wells. The advantage of this method is that the nuclear states become very simple to use in further calculations. The method involves locating potential energy wells, and obtaining vibronic states in terms of phonon operators. The results obtained using this method agree with those previously obtained in an earlier work [23]. The work leading to this result is presented in a later chapter, but with the added advantage of using numerical and analytical techniques to investigate the width of transition lines in spectra of JT active species.

The general work will go through several stages; these will start with an initial overview on the JT effect followed by basic background regarding the C_{60} molecule. These will then be linked, in order to understand the JT interaction in C_{60} ions. This will be presented in chapter 2. Detailed knowledge of the structures and the different forms of symmetries, such as mirror planes, inversion, and rotations will be needed. Also, the vibrational modes of the C_{60} molecule are clearly important for advancing the overall understanding of these fascinating systems. In addition, this chapter will give a basic theoretical background and some calculation methods, such as including the technique developed by Bates, Dunn and Sigmund in [24], in order to study the strong coupling in the $T \otimes (e+t_2)$ JT system, by applying unitary shift transformation. This method which has been applied in a simple system, and has been extended to other complicated cases, such as $T_{1u} \otimes h$ in [23], will be used to investigate JT interaction with Hamiltonian systems of interest. Then due to this transformation, new locations of nuclear displacement will be expected. This approximation method makes the nuclear states simpler, while keeping the same accurate results. In fact, many steps will be useful for determining these positions (APES), and the associated energy states using the Öpik and Pryce method in ref.[4]. Their method is very useful for locating the minimum wells in the LAPES and the associated states. However, some related group theory, and the symmetry of the icosahedral system will be needed.

Introduction to the STM process will be provided in order to simulate STM images for C_{60} molecules. This technique can probe the molecule on a substrate at atomic resolution to produce STM images of the molecular orbitals. Chapter 2 will end by simulating some STM images of C_{60} molecules, as have been published in ref.[25].

Reproducing simulated images of the singly charged ion C_{60}^{-}, which have been used successfully in describing images observed experimentally (as previously obtained in References [26],[22]) will be included in chapter 3. The surface Hamiltonian will be reproduced for different orientations of the possible symmetry operations. An approximation method will be investigated in order to show how useful it is in obtaining results faster than the proper method usually used.

In chapter 4, the work will investigate the surface interaction in a more complicated system, such as the doubly-charged C_{60}^{2-} and C_{60}^{4-} ions. The corresponding JT problems are attributed to $p^2 \otimes h$ and $p^4 \otimes h$, which have been extended from single electron state problem as in ref. [22]. It is necessary to know that, A_g will couple to H_g states due to the JT effect. Therefore, it will be necessary to start by constructing the electronic basis of the ion, including spin-orbital interaction, then formulating the Hamiltonian, which describes the interaction with the substrate. The total Hamiltonian will include some interactions, such as the interactions between the two electrons, the interaction between the molecule and the surface, the JT interactions between the electrons and the vibrations of the fullerene cage. Due to the electron added, a modified theory for two electron states will be applied, as well as the alternative direct integration method, which can generate the wave function of the ions, in terms of single electron states. Some results for several orientations of the molecules will be shown for chosen values of surface parameters, which in some way will lead to a good match with the images published in 2005 in ref.[18] of a C_{60}^{4-} ion. Some experiments reveal the possibility of observing the JT effect in the atomic resolution.

Chapter 5 will then look at the triply charged ion, C_{60}^{3-}, which is attributed to $p^3 \otimes h$ in the same way as in chapter 4. However, different symmetries will be taken into account, such as D_{2h} and C_{2h} opoint group. In this ion, T_{1u} will couple to H_u states by the JT effect. This is of particular interest, as materials including this ion could be superconductors. These are also far from trivial calculations, because of the additional electron. In addition, it is worth assessing from a theoretical view, whether it is possible to find out if the published image in [18] is due to JT distortion to D_{2h} symmetry.

Then, chapter 6 will be focused on how to use these results of C_{60}^{4-} and C_{60}^{3-} ions to match the theoretical results with the experimental images in ref.[18].

In chapter 7, the form of the Hamiltonian, which describes the JT interaction in $T_{1u} \otimes h$ system will be used, and the corresponding energies $\langle \mathrm{E} \rangle$ will be obtained for the system using the electronic basis obtained from the matrix published in [23]. Then, further investigations are described. The matrix elements of the Hamiltonian squared will be derived to evaluate the corresponding energy squared $\langle \mathrm{E}^2 \rangle$ for the same system. The widths of transition lines (Γ) between energy levels in D_{3d} minima will be investigated by applying the uncertainty principle to the energy; assuming that the energy has a Gaussian distribution. Finding the relation between the widths of transition lines Γ, and the expectation energies of the system, ΔE, which is a function of the linear coupling constants and quadratic coupling constants, will be needed in order to compare these constant parameters with the experimental results in ref. [27]. These approximation values will provide useful information about the expected values of the JT parameters, which can be used in future work.

This work will end with chapter 8, which summarises the key results and discusses the points they raise. Moreover, suggestions for future work are presented.

Chapter 2

Basic background

2.1 Introduction

Solving the Schrödinger equation to find the wave functions of any atomic system is required to determine the eigenvalues and eigenvectors of the molecule. However, as the number of atoms increases, the analytical solutions become more complicated. As a result, some basic assumptions are needed to simplify the system Hamiltonian, and increase accuracy. Most of the assumptions required to model the molecule are presented in subsequent sections of this background chapter.

Any discussion about fullerene C_{60} ions should include important interactions, such as JT effect, as a main part of the Hamiltonian system. This complicated Hamiltonian needs to be resolved, in estimating the minimum of the system APES then, the eigenvalues and eigenvectors [4]. Indeed, group theory plays an important role in representing the orbitals of the molecules in a simple way, using the irreducible representation.

Applying the Deng and Yang method to reduce the order of the Hückel Hamiltonian to ten 6×6 sub-Hamiltonians in ref.[28] is the first step in simulating images of C_{60} molecules using a scanning tunnelling microscope in different modes. Starting with the neutral molecule, which is Highest Occupied Molecular Orbital HOMO, simplified HMO theory is applied, as it is not a JT problem. In order to model C_{60} on a surface, it is important to determine, which face will be parallel to the surface. In this respect, the z-axis is defined as perpendicular to the surface [25].

2.2 Introduction to scanning tunnelling microscope

The first among scanning probe microscope types is STM, which was invented by two physicists, Gerd Binnig and Heinrich Rohrer, working at IBM Research Division, who shared the Nobel Prize for Physics in 1986. Then it was Binnig, Rohrer, Gerber, and Weibel, who managed to realise STM practically [29],[30]. The STM is a powerful instrument that allows samples to be visualised at true atomic level in a typical ambient environment, and while capable of handling conducting and semi-conducting materials, it may be used on other material, such as thin insulator films and small samples placed on substrates that are conductive. STM consists of several key components, such as scanning tip, height control using piezoelectrics, sample-to-tip control, and x-y scanner, as well as vibration isolation, and a connection to a computer, as shown in fig. 2.1. STM provides an image resolution whose upper limit is determined by the scanning tip radius of curvature. The situation where the STM tip is not sharp enough, and rather than one has more than two atoms depending on the tip state, leads to artefacts appearing in the image or double-tip imaging as more than one tip is involved in the process of tunnelling [31]. Indeed, the atoms act as a second tip. This underscores the vital importance of having a process to produce tips that are consistently sharp.

Computer control is needed to ensure proper tip to sample positioning, sample scanning, and data acquisition. Quantitative measurements and image enhancement using image processing software may also be done on the computer [32]. Real-space imaging of surfaces at atomic resolution was first made possible using STM applying the quantum tunnelling concept. The idea is that when a bias voltage is applied while bringing a conducting tip into very close proximity to a sample surface, electrons will tunnel between tip and surface. Key variables, such as scanning tip position, voltage applied, and the sample's local density of states (LDOS), determine the magnitude of the tunnelling current produced [33]. As the scanning tip reaches a distance of around 10 Å from the sample, electrons begin to tunnel across this gap, either from the sample to the tip or the reverse, as determined by the bias voltage polarity between tip and sample.

The STM concept depends on electrons flowing between the tip and sample, which means that these have to be either conductors or semiconductors, and so samples from insulating materials cannot be imaged using this method. It has been demonstrated that tunnelling current I, varies exponentially with distance, where according to quantum mechanics, it is given by

$$I = e^{-kr} \tag{2.1}$$

where r is the gap between sample surface and tip, and k is the decay constant which depends on atomic orbitals. This means that a small change in the tip

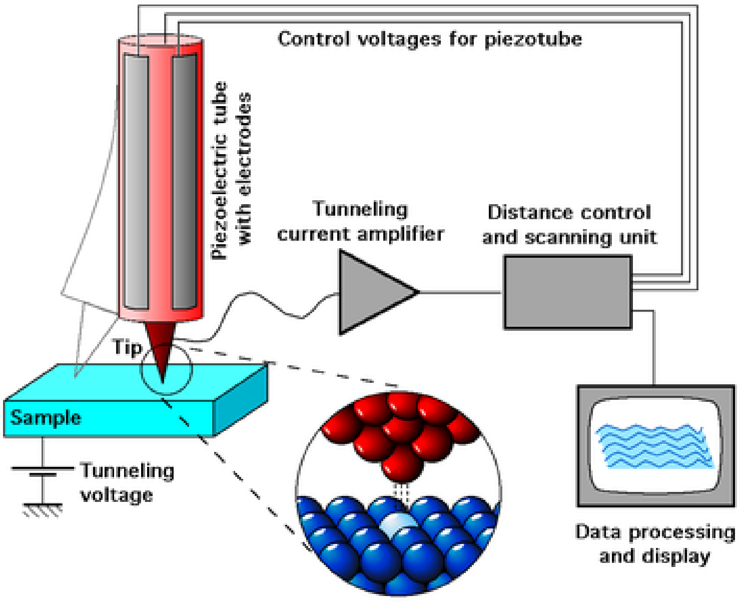

Figure 2.1: The key parts of the scanning tunnelling microscope from *http : //en.wikipedia.org/wiki/Scanning_tunneling_microscope*

to surface distance (such as the order of 1 Å) will cause an order of magnitude change in the tunnelling current. As such, STMs are extremely sensitive, and can resolve sample surface imaging down to atomic resolution in the lateral plane, and to sub-angstrom precision in the vertical plane. In this context, a side resolution of about 0.1 nm and depth resolution about 0.01 nm are deemed good [31]. This allows the electron distributions inside sample materials to be imaged in a straightforward manner.

The STM is quite versatile, as it may be utilised in diverse environmental conditions and fluid media, such as in ultra high vacuum, air, water, and other fluid environments, and wide temperature range (several hundred degrees Celsius to close to zero Kelvin) [33]. The nature of the STM technique, i.e. its sensitivity and resolution, mean that it is quite challenging, because it requires sample surfaces to be exceptionally stable and clean, probe tips to be very sharp, vibration controlled very well, and electronics to be quite complex.

2.2.1 STM Process

In STM, the probe tip is mounted on a piezodrive, made up of three piezoelectric transducers set to act on mutually perpendicular axes, x, y, and z. These piezoelectric transducers contract or expand when a voltage is applied. For the probe tip to scan along the x-y plane, a sawtooth voltage is applied to the piezoelectric on the x-axis, and a voltage ramp to the piezoelectric on the y-axis. Control of the z piezoelectric transducer and the coarse positioner allows the sample and probe tip to be brought close to each other to within a fraction of a nanometre. As the surface electronic wavefunctions of the tip and sample overlap, a finite tunnelling conductance is created. At positive sample bias, tunnelling occurs with electrons moving from the tip's occupied states to the empty surface states to image LUMOs. On the other hand, with $V < 0$, i.e. sample bias negative, the electron flow is the opposite as they move from the occupied states on the sample surface to the probe tip, this allowing an image to be built up for the surfaces HOMOs. So, by using this process, the electron densities will be imaged not the atom positions.

In this arrangement, the amplifier's phase is selected to ensure negative feedback is given, where an absolute tunnelling current value that is larger than the reference causes the voltage driving the z-piezoelectric to move the probe tip away from the surface, while a tunnelling current value smaller than the reference causes the opposite. In this way, an equilibrium position on the z-axis can be established. While the probe travels in the x-y plane, these equilibrium positions on the z-axis are acquired and stored in a 2-dimensional array. This allows the discrete points marking equal tunnelling current to be plotted as a contour surface [33].

As the probe scans the surface along the x-y plane, the current changes due to the variation in density of states and surface height. The change in current allows images to be mapped accordingly. Current may be measured directly, and changes recorded with probe position, in what is called constant height mode (CHM), or alternatively the tip vertical position z, may be varied, and then recorded once a fixed value of current is achieved, in what is called constant current mode (CCM)[34]. Typically, only one of these two modes is selected to collect data in an experiment, where each offers its specific advantages. By its nature, only very smooth surfaces can be imaged using CHM, while for irregular surfaces, the tip is moved up or down with great precision to acquire more highly resolved image and probes the molecule in more detail in CCM.

CHM is relatively quick, and has higher scan speeds compared to CCM, since the surface height does not need to be changed or adjusted. However, CHM can only be used for samples with very low surface roughness, i.e. peaks may not exceed 5-10 Å, otherwise the probe tip may crash into the sample. The tip vertical position is kept fixed.

However, even in CHM, a weak feedback loop exists so as to keep the tip at a fixed average distance from the sample.

In CCM, a set value is chosen for the tunnelling current, and when the measured current is found to be higher, the tip-sample distance is increased automatically, and when the measured current is lower this distance is reduced, and so tunnelling current is kept constant [34]. In the ideal case, this current and the local density of states are proportional, and so the scanning tip follows a constant density of states contour.

However, STM has several disadvantages, including the difficulty in interpreting the results in most cases, as the image of the surface depends, in addition to the surface topography, on the magnitude and polarity of bias voltage, density of states, current magnitude, and other factors.

STM produces all images in grayscale, and colour may be added in a post-processing step, to visually highlight any key feature.

2.3 Group theory of icosahedral symmetry

Many quantum mechanical concepts need to be clarified to understand the effect of JT interactions in C_{60} ions. In addition, this includes the important assumptions made to simplify the modelling processes of some different C_{60} ions, such as C_{60}^{-}, C_{60}^{2-}, C_{60}^{3-}, C_{60}^{4-}. The following sections contain some of these techniques, starting from group theory in the icosahedral symmetry, used in Hückel molecular orbital theory (the main theory used in this thesis) to model the surface interaction and hence, construct the STM images of the different C_{60} ions.

The group theory technique is very useful on high symmetry systems, such as C_{60} ions, in order to explain the degeneracy and how the orbitals would split due to some interactions, which may reduce the symmetry of the undistorted molecule. In fact, one of the methods used to investigate the symmetry in the fullerene molecule is using the icosahedral point group. The point group consists of a complete set of symmetry operations. Indeed, any symmetry operators can form a point group, if it closes under multiplication. In short, when one operator is multiplied by the other, the result is an operator which also one of the group operators.

The symmetry operation sets in each point group refer to geometric operations which have the molecule unaltered. These symmetry operation can be classified into different forms. Table 2.1 represents the Character Table of I_h symmetry. The horizontal group elements at the top of the Table are;

- $E \rightarrow$ Identity
- $15C_2 \rightarrow$ Rotation about 15 twofold axes (about axes joining opposite double bonds at the respective midpoints).
- $20C_3 \rightarrow$ Rotation about 10 threefold axes (about axes through the centres of opposite hexagons).
- $12C_5$ and $12C_5^2 \rightarrow$ Rotation about 6 fivefold axes (about axes passing through the centres of two opposite pentagons).

Table 2.1: The Character Table for I_h symmetry, where ϕ is Golden ratio [14]

I_h	E	$12C_5$	$12C_5^2$	$20C_3$	$15C_2$	P	$12S_{10}^3$	$12S_{10}$	$20S_3$	$15\sigma_v$
A_g	+1	+1	+1	+1	+1	+1	+1	+1	+1	+1
T_{1g}	+3	$+\phi$	1-ϕ	0	-1	+3	ϕ	1-ϕ	0	-1
T_{2g}	+3	1-ϕ	$+\phi$	0	-1	+3	1-ϕ	ϕ	0	-1
G_g	+4	-1	-1	+1	0	+4	-1	-1	+1	0
H_g	+5	0	0	-1	+1	+5	0	0	-1	+1
A_u	+1	+1	+1	+1	+1	-1	-1	-1	-1	-1
T_{1u}	+3	$+\phi$	1-ϕ	0	-1	-3	-ϕ	ϕ-1	0	+1
T_{2u}	+3	1-ϕ	$+\phi$	0	-1	-3	ϕ-1	-ϕ	0	+1
G_u	+4	-1	-1	+1	0	-4	+1	+1	-1	0
H_u	+5	0	0	-1	+1	-5	0	0	+1	-1

- $P \rightarrow$ Inversion element.

These rotation operations C represents how many rotations would be applied on the molecule to rotate one full circle. For example, in radians $\frac{2\pi}{3}$ refers to C_3 and $\frac{2\pi}{5}$ to C_5 rotations, where the subscript denotes the number of rotations. The rest of classes involve elements include rotation and inversion. The inversion operation moves any point in a line through the inversion centre to another point away the same distance far from that inversion centre as a → -a. On the other hand, the reflection operation is through a plane σ, which could be vertical σ_v or horizontal σ_h. However, if the rotation operation is followed by a reflection operation, this would show another rotation named improper rotation (S), and this reflection via a plane is perpendicular to the axis of the rotation.
In fact, the 120 kinds of symmetry operations in the I_h group of three dimensional space, can be reduced due to JT interaction to lower symmetry operations, such as 10 three-fold symmetry D_{3d} (around hexagon), 6 five-fold symmetry D_{5d} (around pentagon), 15 two-fold D_{2h} (placed at the centre of the double bonds) and 30 two-fold C_{2h} of rotations (any point on great circle passing through a double bond).

It is worth turning our attention to describe the physical properties of the molecule, such as the electronic and phonon bases of the ion by using group theory techniques. More specifically, the irreducible representation property of the icosahedral point group of different dimensions. The electronic and vibrational states of the molecule are labeled using the irreducible representations. From group theory, it was found that any irreducible representation associated with basis functions can be defined with appropriate spherical harmonic wave functions [41]. The list of the 10 irreducible representations in the leftmost column of Table 2.1 subscripted depending on even (g) or odd (u) basis of their matrix representation under inversion, which could be used in modelling the point group. The difference between symmetries, u and g, yields the constant factor of 2. Therefore, in this case, the group has 120 elements in total. The character of the identity E shows the dimensionality of each irrepresentation. This kind of representation is in the possible lowest dimensionality. However, in the reducible representation of the point group, the matrix resulting from applying a transformation will take a block diagonal form when applied on a suitable basis, which would then be divided into another two matrices of lower dimension. The decomposition of which leads to irreducible representations designated (A, T_1, T_2, G, H) in relation to dimensionality, (1D, 3D, 3D, 4D and 5D) respectively. The three components of the two T_1 and T_2 irreps labeled as x,y,z, while G irrep has four components, which labeled as a,x,y,z. The other five components represented the H irrepresentation labeled as θ,ϵ,4,5,6 which are defined in eq.(3.7) in the following chapter. Using these labelling conventions, a threefold-degenerate with a symmetric electronic state is denoted by T_{1u}, while a fivefold-degenerate symmetric molecular vibration mode is denoted by h_g [42]. The molecular orbitals of the JT systems associated with the C_{60} molecule will be defined using the I_h irreducible representation point group with uppercase label for the electronic state and lowercase for the vibrational state, such as in $T \otimes h$ system, the uppercase T electronic state couples with the lowercase five-dimensional h_g vibronic state. Further details are given in subsequent sections, regarding these orbitals, including the means by which they make a contribution to the wave function.

2.4 Hückel molecular orbital method

In 1930, Erich Hückel proposed the HMO or Hückel method, as a very simple method based on Linear Combination of Atomic Orbitals (LCAO) [43], which allows the π electrons molecular orbital energies to be determined, as shown in fig. 2.2. Hückel method can be expanded from the Ritz method with assumptions added to the Hamiltonian and the overlap matrices. The highest energy electrons such as the p electrons in conjugated molecules determine the interactive character of molecules. The Hückel method is a very useful approach, including some approximations to describe how many energy levels in the molecule and how the electrons are implicated in molecular bonding. One of these approximations is the most fundamental, and involves only the available π-orbital electrons. In addition, the Hückel Hamiltonian considers only two parameters, α, which represent the single-atom contribution and the two centre contribution β between neighbours, as any other contributions due to any non-neighbouring atoms will not be taken into account [24]. For example, for the ethylene molecule C_2H_4 which contains two π electrons, Hückel theory predicts two energy levels. The low-energy HOMO filled by the two π electrons and the high energy LUMO which

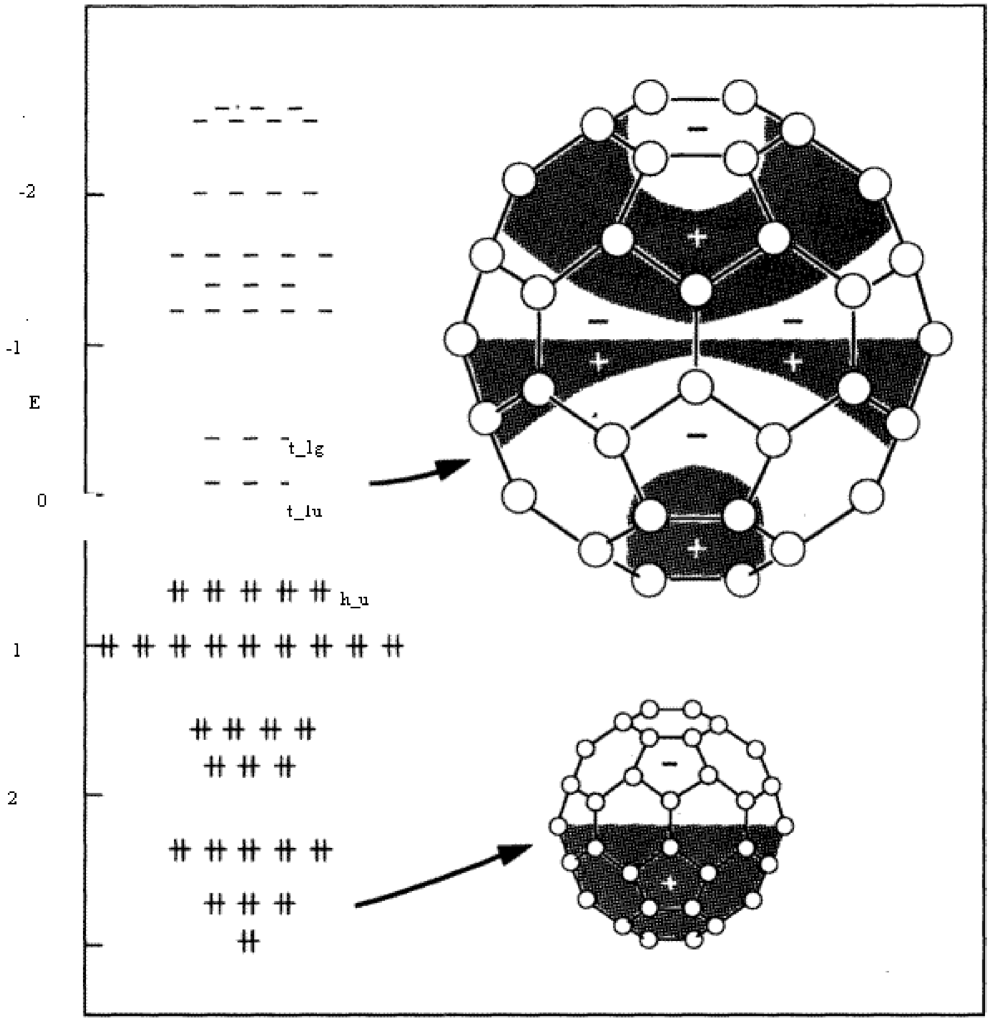

Figure 2.2: Hückel molecular orbitals of some of the electronic wavefunctions reproduced from [43]

in this molecule remains empty. The matrix elements H_{ij} can be written as;

$$\begin{aligned} H_{ij} &= \int \psi_i H \psi_j d\tau \\ S_{ij} &= \int \psi_i \psi_j d\tau \end{aligned} \tag{2.2}$$

which can also parametrised as;

$$\begin{aligned} H_{11} &= H_{22} = \alpha \\ H_{12} &= H_{21} = \beta \end{aligned} \tag{2.3}$$

The overlap between orbitals is an identity matrix which means that the orbitals are orthogonal and the overlap between them is neglected and the orbital overlap will follow;

$$\begin{aligned} S_{11} &= S_{22} = 1 \\ S_{12} &= S_{21} = 0 \end{aligned} \tag{2.4}$$

In case of ethylene the molecular orbital ψ is a linear combination of the atomic orbitals ψ_i such as;

$$\psi = c_1\psi_1 + c_2\psi_2. \tag{2.5}$$

By substituting into the Schrödinger equation, gives;

$$Hc_1\psi_1 + Hc_2\psi_2 = Ec_1\psi_1 + Ec_2\psi_2 \tag{2.6}$$

where E is the energy of the molecular orbital. Then by multiplying eq.(2.6) by ψ_1 and integrating, this will give;

$$c_1(H_{11} - ES_{11}) + c_2(H_{12} - ES_{12}) = 0 \tag{2.7}$$

the same step will be apply on eq.(2.6) with respect to ψ_2 and write them in a matrix form to be;

$$\begin{bmatrix} H_{11} - ES_{11} & H_{12} - ES_{12} \\ H_{21} - ES_{21} & H_{22} - ES_{22} \end{bmatrix} \times \begin{bmatrix} c_1 \\ c_2 \end{bmatrix} = 0 \tag{2.8}$$

then;

$$\begin{bmatrix} \alpha - E & \beta \\ \beta & \alpha - E \end{bmatrix} = 0 \tag{2.9}$$

then after solving eq.(2.9) to determine the values of parameters c_1 and c_2, it is found that $c_1 = \pm c_2$ and, $\psi = \frac{\psi_1+\psi_2}{\sqrt{2}}$ is giving the molecular orbital of the HOMO and $\psi = \frac{\psi_1-\psi_2}{\sqrt{2}}$ corresponding to the LUMO. This method will be used later in section 2.8.1 to explain the molecular orbital wave functions of C_{60} molecule as has been used by Deng and Yang in ref.[28].

More specifically, it is worthwhile to study the individual C_{60} molecule in isolation, in terms of electronic structure, to pave the way for exploring the electronic properties of C_{60}^{n-} ions. In this respect, the HMO calculations presented by Haddon [43], offer the easiest approach. Haddon formed each molecular orbital using the Linear Combination of Atomic Orbitals (LCAO) method [43].

While there are 240 valence electrons in C_{60}, there are three sigma bonds between each carbon atom and the adjacent carbon atoms. This means that 180 electrons are already used, and whose energy is significantly under the Fermi level. Therefore, these electrons ensure that the structure is stabilised, yet make no contribution to electrical conduction. It is the orbitals around the molecule, arising from significantly less tight (C-C) π orbitals, on which the remainder of the valence electrons (60) can be found distributed. Regarding the location of these π electrons, the tendency is for them to be found over less time inside the ball than outside, since the three sigma bonds around an individual C_{60} carbon atom are not on a single plane. Furthermore, the lack of uniformity in the lengths of (C-C) bonds results in the absence of true delocalisation for π electrons about these rings formed by the six carbon atoms.

The C_{60} molecule has two different lengths of C-C bonds, 1.40 Å for double bond and 1.46 Å long for single bond, which implies that across all bonds, the π electrons are not evenly delocalised [46]. As such, the longer C-C bonds are situated along the 60 common edges of adjacent pentagons and hexagons. In contrast, the shorter C-C bonds are found on the 30 edges between adjacent hexagons. A type of double bond, which alternates, along a molecular ring or chain with single bonds is called a conjugated double bond. Molecules with these bond types acquire peculiar chemical characteristics, and possess structures with equivalent resonance.

As such, in doped solids, the band of conduction electrons has specific properties depending on the nature of overlapping orbits between neighbouring molecules. Electron distribution may be determined by first considering the 60 non-interacting electrons. These are held on an orbit, within a sphere, with high n and varying l. Accordingly, the $l = 0$ state is taken by the first two electrons. For higher l values, the available number of states is given by n = $2(2l + 1)$ with the factor 2 relating to electron spin; therefore, as the states, $l = 2, 3, 4$, take up 50 electrons, then the $l = 5$ state takes up the last 10 electrons.

Calculation using the HMO method confirms the above result for $l = (0, 1, 2, 3, 4)$ however, for higher energy states, $l = 5$, the approximation of spherical potential cannot be used, and alternatively, true atomic potentials influencing the energy splitting are considered. The use of l as a quantum number, with respect to real C_{60}, is not particularly appropriate, and therefore, the irreducible representations for the icosahedral symmetry group should be used to classify electronic orbitals. In this context, the last 10 electrons are allocated to the available orbitals by increasing energy level, i.e. to the H_u, T_{1u}, and T_{1g} levels respectively. Indeed, including spin, the degeneracy of the H_u, T_{1u}, and T_{1g} levels, are 10, 6 and 6 respectively. The 10 last electrons completely occupy the H_u level, which as such, is the highest occupied HOMO, while the lowest unoccupied LUMO is the T_{1u} level, with a gap of roughly 2 eV between these molecular orbitals. The spherical approximation considers that all HOMO and LUMO bands relate to quantum number $l = 5$, where part of the character of this quantum number ($l = 5$) is carried by the relevant Hückel molecular wave functions. In the representation of $l = 5$ (denoted in the icosahedral group by T_{2u}), the six remaining states have such high energy that the T_{1g} of the sixfold-degenerate state join the LUMO band. The $l = 6$ character of this level makes it the (LUMO + 1) level. Given their proximity to the Fermi level, the key bands are those stemming from HOMO and LUMO levels in solid C_{60}. More specifically, fig. 2.2[14] shows the two most important HMOs. It can be seen from the figure that the ground state of neutral C_{60} takes possession of a closed shell structure with ten electrons in an electronic quintet orbital labelled by H_u. This highest occupied molecular orbital has the irreducible representation (irrep.) of H_u in the I_h group. In this form, the C_{60} molecule does not exhibit any vibronic interaction, and therefore, JT interaction is unexpected for this structure. The lowest unoccupied molecular orbital is also shown in the figure and this has T_{1u} representation. This is a threefold degenerate orbital, and so can hold up to six electrons. The two lowest excited configurations are each 15-fold degenerate namely $(H_u^9)(T_{1u}^1)$ and $(H_u^9)(T_{1g}^1)$.

Once the isolated C_{60} is charged, either cations C_{60}^{n+} or anions C_{60}^{n-} can be formed. The anions form when n electrons are added to the LUMO of C_{60} to form anions. These molecules can also couple to the vibrational modes and exhibit JT interactions. The other charged form of C_{60} can occur when n electrons are taken from the HOMO of the neutral C_{60} molecule. The removal of electrons will cause vacancies to appear in the HOMO, these holes behave as positively charged particles and can be coupled to a vibrational mode via JT interaction.

In this work, STM represents an excellent technique to explore the C_{60} molecule, since its size means that it can be easily imaged. In addition, the capability of STM to map local areas at very high resolution means that intramolecular features can be readily visualised, and confirm the molecule's icosahedral structure. Yet, imaging the C_{60} molecule requires it to be placed on a solid substrate. This would result in interactions, which reduce the symmetry that preserves the C_{60} icosahedral symmetry, leading to the degeneracy of normally imaged frontier molecular orbitals to be reduced. This issue may be considered in the example, where for C_{60} molecules on a Cu(111) surface, the LUMO is divided into 2-states, yet one state only is seen when potassium is used to a precast Cu(111) [47]. As a result, in STM, the interactions with the substrate on which the sample is placed affect the images acquired, and so may not be neglected. It is the C_{60} molecule's orientation, and the adsorption site's symmetry, which determine the outcome with regard to the images, even though the effect of the latter, (i.e. adsorption site, is only weak) [48]. In STM images, the orientation of the C_{60} molecules must be considered, as the change in atomic positions changes the electron density and thus the STM image. Along the bonds, the electron density depends on the molecular orbitals, such as the double bonds in the degenerate HOMO and the single bonds in the degenerate LUMO, and so if pentagons or hexagons appear in STM images, it would be reasonable to assume that these are uppermost, and nearest to the sample surface. Given the lack of orientations that would produce a pentagonal image, the appearance of pentagons in the STM image indicates their presence [49]. In short, it is more the fact that five fold symmetry is very rare, so observing it, is a strong indication a C_{60} is present.

For isolated molecules, five distinct orientations of single bond, double bond, pentagon, hexagon, and edge atom uppermost, were observed for adsorption on Au(111) by Lu *et al*, near the surface [50]. In order to help interpret the STM images of C_{60}, a variety of prone to the surface orientations have been suggested of which pentagonal and hexagonal face, as well as (C - C) double bond cases are considered. The assumption is that the relevant molecular orbitals or LUMO, HOMO, LUMO+1 in the general case, are split to a sufficiently large extent by the interaction with the surface, such that individual components may be imaged in the absence of interference from neighbouring orbitals. In the current work, HMO theory is employed to acquire simulated images for the imaged C_{60} molecule. The following sections provide further information regarding the method used by Deng and Yang [28], which would introduce the fullerene C_{60} molecule represented in general orbital pictures.

2.5 Jahn-Teller (JT) effect in fullerene systems C_{60}

The properties of the C_{60} molecule make it a perfect system for researchers to investigate symmetry lowering, such as JT interaction. The non-JT-active C_{60} molecule has a fully occupied HOMO with degenerate electronic states. However, for a charged fullerene ion, degenerate electronic states are present, and so the effect of JT interaction will be present.

The splitting of partially occupied degenerate electronic states results in the molecule distorting, and occurrence of the JT effect. The molecular distortion causes a relatively minor perturbation, with upward and downward movement of some electronic energies. The total electronic energy is reduced when electrons move to the low-lying states, while the molecule undergoes quadratic deformation. This effect may be described using the example of an octahedral molecule, with

electrons on p-like orbitals that are threefold-degenerate, where the orbitals point in x, y and z directions in a Cartesian coordinate system. The properties of these orbitals and those of T_{1u} orbitals of the fullerene molecule are similar. Therefore, if the octahedral molecule is subjected to enlargement or symmetrical squeezing, this will result in an upward or downward shift in the three orbitals' energy, but without the levels splitting. The energy shift (upward or downward) due to the squeezing, is determined by the model details. With respect to the JT effect, looking at the octahedral molecule with the threefold-degenerate orbital carrying zero or six electrons, the octahedral shape does not change, even when its size does. On the other hand, in the case of one or two electrons, a favourable change of shape (or distortion) is uniaxial, where the energy of the two empty orbitals increases, as that of the (partially or completely filled) orbit decreases. In the absence of Coulomb repulsion on-site, and all else remaining equal, distortion is greater in the case of two electrons [35].
According to Hückel's theory, a H_u representation, fully filled, fivefold degenerate HOMO is found in the neutral molecule, and so there is no JT effect in this neutral molecule. The LUMO is available to the molecule at a higher energy level of around 2 eV, resulting in a high electron affinity of around 2.7 eV [36]. The usual procedure for C_{60} reduction involves using a highly electropositive group to react with it. The reaction results in a number of JT-active species in the form C_{60}^{n-}, where the T_{1u} orbitals set is partially filled. These T_{1u} orbitals may be coupled to h_g symmetry vibrations. The well known $T_{1u} \otimes h_g$ JT system is the result of the LUMO being occupied by a single electron, which has been investigated in detail in ref. [23] when two different quadratic couplings are included.

The typical JT effect in the LUMO of C_{60}^{-} ion is represented by an electronic T_{1u} interacting with fivefold degenerate nuclear displacements h_g, $T \otimes h$. We start modeling the single C_{60}^{-} ion, by considering a single effective mode of h_g to form a typical $T_{1u}\otimes$ h_g JT system. The problem is identical to a particular case of $T\otimes$ $(e + t_2)$, where the vibronic coupling to the e and t_2 vibrations and their frequencies is the same which is also known as the $T \otimes d$ problem. The five dimensional space of the JT effect in this case can be presented as a combination of the two e coordinates, Q_θ, and Q_ϵ, and the three t_2 coordinates, Q_4, Q_5, and Q_6, of the cubic group.

In 1995, Dunn and Bates [23] investigated the effects of vibronic coupling in icosahedral symmetry, in the particular case of the $T_{1u}\otimes$ h_g JT system. The coupling with the electronic part by using the direct product represents the JT interaction. The basis is taken to be ψ_x, ψ_y, ψ_z, transforming as T_{1ux}, T_{1uy}, T_{1uz} respectively. However, when more electrons occupy the LUMO, this is denoted by p^n $\otimes h$. In addition, due to the reduction in the symmetry of the isolated anions of fullerene, a collection of minima or 'wells' in the lowest APES will be produced. These effects can be seen at atomic resolution on the orbitals using STM, as described briefly in later parts of this chapter.

The diagonalised vibronic Hamiltonian will produce APES sets. In minimising the energy of the system to find the lowest APES, certain values of the five modes will be needed for given values of the JT parameters, such as the linear and quadratic coupling constants. In case of strong coupling, the gap between the APES energy levels is much higher than the vibrational energy $\hbar\omega$. Then, it can be assumed that the nuclear movement may be confined to the lowest adiabatic potential energy surface (LAPES). In icosahedral systems where electrons occupy states represented by T the term, trough, describes a continuous equal energy surface and is formed only in the case of linear coupling parameters [37]. However, this trough will warp in case of adding quadratic coupling constants in order to produce the local minima. This process has effect on the system's behaviour, as it will modify the depth and the distances between existence wells. In fact, two different JT systems will be of interest in this study, which depend on the coupling strengths. The static JT effect may occur in case of infinitely deep wells, where the JT system can be localised in one well. Therefore, the eigenstate of the system is associated with a well state. On the other hand, the dynamic JT system may be able to hop between wells, in the case of finite coupling strengths.

2.6 Pseudorotation process

The pseudorotation is the transition between the energy points [39]. As stated previously, JT distortions are a dynamic effect represented in different forms due to APES characters, and are a function of factors, such as vibronic coupling strength and the Q's values (five modes) of the system [38]. In a free pseudorotation, the system can move freely between equivalent energy points. In this case, the lowest-energy APES is a multidimensional trough of these points. Observed STM images contain equal support from all points on the trough. These full dynamics or free pseudorotations can be eliminated by applying external perturbations [40]. However, when quadratic JT coupling is present, the molecule shows other behaviour, in spending extra time close to the places of the minima instead of in between the points; this corresponds to the dynamic motion associated with hindered pseudorotation where time spent between minima is small. These rotations may occur particularly, in the case of small energy barriers between the minima. The energy barrier between wells depends on the strength of the quadratic JT effects. Therefore, the JT effect becomes static, and the system will be closed in to a well with no pseudorotation when the well depth tends to infinity.

In addition, the system is expected to hop between the wells, when a strong quadratic JT coupling is present. The STM image will be a superposition or overlap of images relative to the individual wells. On the other hand, it is worth mentioning that, in the presence of a substrate, some wells will be favoured due to the surface interaction, quadratic coupling constants and also the molecule orientations. Thus, the surface interaction, will have the effect of preferring a subgroup of the obtainable wells. In short, the ion might be locked into only one specific point, or if more than one well stays equivalent in energy, it may also hop between the remaining equivalent energies. In other words, various JT coupling constants favoured various sets of wells, and different positions of the molecule on the substrate. However, in the case of the low magnitude of quadratic coupling constants, a hindered pseudorotation between the favoured wells will be expected [22]. In addition, the pseudorotation speed is faster than the speed of the tip during the STM imaging. This process should be taken into consideration when imaging using STM, in the simulations in later chapters, as the distinction between the two process will be complicated.

2.7 Overview of fullerene C_{60} electronic and vibronic structure

C_{60} fullerene represents a new type of π-acceptor. In comparison with other acceptors, the C_{60} fullerene molecule has several notable features, such as a bigger size, a highly symmetrical and spherical form, a distinct electron arrangement, and the ability to be polarised. It may also accept 12 electrons or less, with great potential for use in nanotechnology in the future, such as biological applications [51]. Fullerene systems are highly diverse in terms of their properties, mechanical, geometric, and electronic, which represents one of their key strengths [52],[53]. The C_{60} molecule is a good example of the diverse nature of fullerenes, where semiconductor [54], magnetic [55], metal [43],[56], or superconductor [57] behaviour may be achieved in bulk C_{60} through careful control of local levels of charging, while single electron transistors may be made from single C_{60} molecules [58].

Such diversity has led to a concerted research effort aimed at determining C_{60} fullerenes electronic properties when attached to different substrates, paving the way for further applications. As such, C_{60} fullerene has witnessed the majority of fullerene-based solids research focused on it. The C_{60} molecule is a roughly 10 Å diameter sphere, and carbon nuclei are located approximately on a 7 Å diameter, which leaves a cavity 4 Å in diameter within. This molecule structure resembles a truncated icosahedron or soccer ball, with atoms located on 60 vertices. In fact, for all even n, the carbon cage of n atoms must arranged as 12 pentagonal and $\frac{n}{2} - 10$ hexagonal edges [44]. However, for all higher values of n, there is at least one way to put a fullerene polyhedron together [45], and as the number of hexagons rises, the number of ways of packing hexagons together on a sphere increases rapidly; so 20 hexagons for C_{60}.

The 180 modes of the C_{60} molecule may be divided, using group theory, into two, three, five, six, and eight, A_g, T_{1g}, T_{2g}, G_g, and H_g modes respectively, with their antisymmetric (u) counterparts, where 2 (2×1 + 3×3 + 5×3 + 6 ×4 + 8×5) = 180 degrees of freedom (The representation dimensionality and number of degenerate group modes are equal) [59]. Pure rotation and pure translation are represented by one T_{1g} mode and one T_{1u} mode respectively. The total number of vibration modes for the 60 atoms molecule is therefore, given by 3 × 60 - 6 = 174 vibration modes, after subtracting 3 translational and 3 rotational modes [60],[61]. The vibration frequencies have degeneracies as a result of molecule symmetries. The vibration modes are labelled using irreducible representations of the icosahedral group, in the same way as for the electronic orbitals. For C_{60} in the solid state, intramolecular mode frequencies remain relatively unchanged, representing Einstein modes having slight dispersion. The relevant modes are h_g and a_g given the T_{1u} symmetry of the molecule's electrons. Moreover, the three T_{1u} levels are shifted at the same level of energy by an a_g-type distortion, while the ground state is suppressed by other effects including the JT effect.

Group theory shows that $2a_g$ and $8h_g$ modes coupling is likely, and moreover, a reduction to a single effective h_g mode is possible with eight modes coupling. However, the vibronic basis in JT interaction of C_{60} ions makes the modelling of the system more complicated due to the eight vibronic modes. Regardless of this complicating factor, i.e. the multimode nature of the coupling problem, matters may be simplified by assuming a single effective mode, which allows the problem to be treated more easily and reproduces most of its key aspects. In fact, reference [59] found that the corrections, required for the energy levels in case eight modes are involved, are small enough to be neglected.

This will be presented at the review of the electronic structure of C_{60}^{2-} molecule in chapter 4. When electrons are added to C_{60} they begin to fill the triply degenerate orbital. As a result, the added electron in the C_{60}^{-} anion occupies the T_{1u} orbital, which couples to 8 vibrational modes of h_g symmetry. This coupling as mentioned has been denoted as $T \otimes h$ JT effect. In this notation, there is one electron in a T-type electronic orbital coupled to an h-type vibration. In this work, a coupling to a single effective h_g mode, as in ref. [62], only will be considered. Indeed, these facts about vibrational modes are what we would expect in other differently-charged ions C_{60}^{2-}, C_{60}^{3-} and C_{60}^{4-}.

2.8 Deng and Yang group theory technique

The detection of fullerenes led to a huge improvement in the literature in several aspects related to these systems. Deng and Yang, in their paper ref.[28], used the neutral C_{60} and the high symmetry of this molecule to find definitions for the energies and eigenstates for the Hückel Hamiltonian of the system. As known, the symmetry group of the system is the icosahedral group $I \times Z_2$ and the I is the 60-element, while Z_2 indicates the 2-element group holding both the inversion P and the identity I operators. This Hamiltonian has been reduced by applying the icosahedral symmetry from the reducible representation (60×60) into 10 irreducible representations (6×6) Hückel submatrices, which allowed simple calculations to obtain the eigenvalues and eigenvectors of the total Hamiltonian of the system, as shown in ref. [28]. Therefore, the simulations in ref.[28] have been resolved using Hückel molecular orbital theory in the simple form. In fact, 16 irreducible representations have been found by applying the character table of the icosahedral group such as A_u, A_g, T_{1u}, T_{1g}, T_{2u}, T_{2g}, G_u, G_g, H_u, H_g.

$$[A_u \oplus T_{1u} \oplus T_{2u} \oplus 2G_u \oplus 3H_u] \oplus [2T_{1g} \oplus 2T_{2g} \oplus 2G_g \oplus 2H_g] \tag{2.10}$$

Where the 8 odd parity ($p = 1$) representations have been written in the first bracket and the other 8 even parity irreducible representations have been given in the second bracket. The shape of the C_{60} is a truncated icosahedron, which stays fixed after using the I group.

Deng and Yang in ref.[28] have been used a subgroup of $I \times Z_2$ in assigning their ten submatrices. For the icosahedral group,
(H) contains the states m = -2,-1,0,1,2
(G) contains the states m =-2,-1,1,2
(T_2) contains the states m =-2,0,2
(T_1) contains the states m =-1,0,1
(A) contains the states m =0

The later sections illustrate use of this method to simulate STM images for C_{60}, and the charged molecules C_{60}^{-}. In addition, the doubly-charged ion C_{60}^{2-}, and C_{60}^{4-} will be investigated in chapter 4 with a modified treatment. The same method will be applied later on C_{60}^{3-} anion in chapter 5.

2.8.1 Designation of icosahedral and truncated atoms

The Deng and Yang method is the foundation for constructing the MOs, as in ref. [28]. The first step is to set up the undistorted icosahedron defining the 12 corners of the two fold x, y, and z coordinates, as shown in fig. 2.3 [23]. Table 2.2 shows the 6 coordinates of these corners of the icosahedron where ϕ is the golden mean, as given by $\phi = \frac{1}{2}(1 + \sqrt{5})$, and by applying the inversion operation through the icosahedron centre, the other 6 remaining corners coordinates can be obtained. For example, the point labeled A at the corner (0,ϕ,1) is transformed to $\bar{A}$ with coordinate (0,-ϕ,-1). Actually, the same coordinates have been used as the icosahedron coordinates in both references [63],[64]. Then connections between these

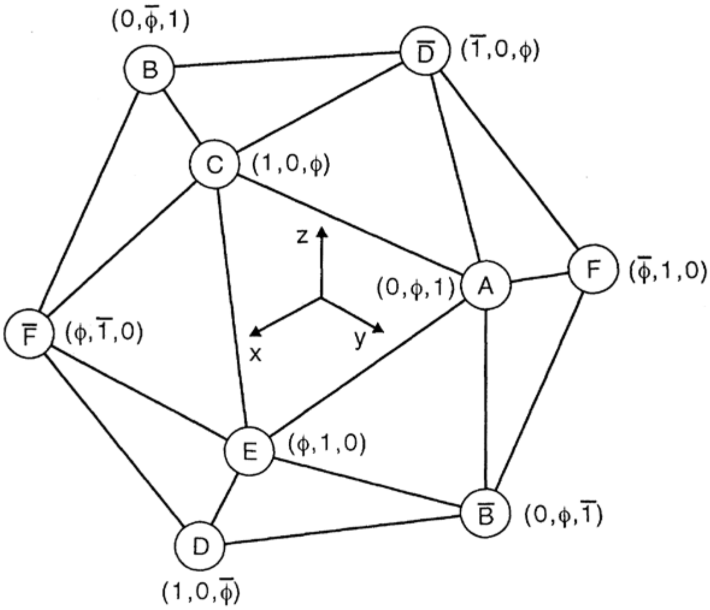

Figure 2.3: The icosahedron corners coordinates reproduced from ref. [23]

Table 2.2: The positions of the pentagonal wells D_{5d} symmetry

Number	Coordinate	Electronic state
A	$(0, \phi, 1)$	$z + \phi y$
B	$(0, -\phi, 1)$	$z - \phi y$
C	$(1, 0, \phi)$	$x + \phi z$
D	$(1, 0, -\phi)$	$x - \phi z$
E	$(\phi, 1, 0)$	$y + \phi x$
F	$(-\phi, 1, 0)$	$y - \phi x$

vertices will be generated.

On the other hand, the designation of truncated icosahedron atoms have been shown in ref. [28]. A particular irrep MO is determined by six parameters, such as (c_1, c_2, c_3, c_4, c_5, c_6), which can be used to construct a linear combination c. Then, assuming that one pentagon with five atoms (1,2,3,4,5) corresponds to one basic set of Deng and Yang atoms, as in ref.[28], such as (1,0,2), (1,0,4),(1,0,6), (1,0,5), (1,0,3),(1,0,1), the coordinates of the other atoms will be determined as Deng's parameters repeat for other atoms by rotation. It has been important to label the 60 truncated atoms, and to consider the origin to be the centre of the molecule and the z-axis is through the top pentagon, as illustrated in fig. 2.4. Then, 6 atoms of 3 numbers, such as (a, b, c), will be used to name each atom, where the first two labels a, b refer to the set to which the atoms belong, and c_i with 6 possibilities (c_1, c_2, c_3, c_4, c_5, c_6), indicates the particular atom in each set a, b. The positive or negative values of a, b refer to the upper $z+$ or

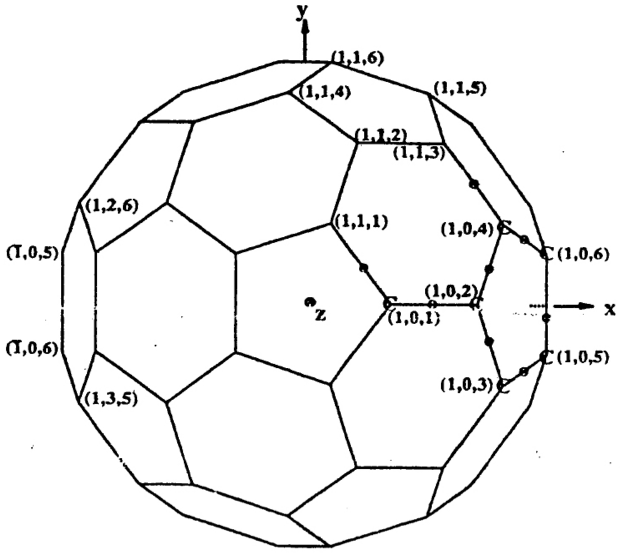

Figure 2.4: The ten sets of Deng and Yang coordinate atoms repreduced from ref. [28].

lower hemisphere z-. On the other hand, other sets can be produced from one set by applying a rotation. For example, the six atoms (1,1,1), (1,1,2),(1,1,3), (1,1,4), (1,1,5),(1,1,6) can be generated from Deng's basic sets above by rotation ρ where ρ is an element in the icosahedral group $I \times \mathrm{Z}_2$ doing a rotation through $\frac{2\pi}{5}$ represented by η^{-m}, where $\eta = \exp((2/5)\pi)i$ and the quantum number m = -2,-1,0,1,2. The atoms (1,2,6) and (1,3,5) from (1,0,6) by applying ρ^2 and ρ^3 rotations respectively. However, the two atoms (1,0,5) and ($\bar{1}$,0,5) are antipodes.

In fact, 60 bonds in C_{60} molecule, which separate a hexagon from a pentagon are denoted as h_p bonds. Also, 30 other bonds, denoted as h_h, are double bonds, which separate two hexagons. The Hückel Hamiltonian discussed in ref. [28] is for the same interaction for all 90 bonds. However, this generalisation guides to a generalized Hamiltonian $H(\alpha)$ with a parameter α in it, as will be discussed. Deng and Yang in ref. [28] observed that for real α, $H_{m_p}(\alpha)$ should be also real. Therefore, its eigenstates ψ would be written as real. Hence:

$$\begin{aligned}
\psi_{1,2} &= \bar{\psi}_{1,2}, \\
\psi_3 &= (1/\sqrt{2})(\bar{\psi}_3 + i\bar{\psi}_4), \\
\psi_4 &= (1/\sqrt{2})(\bar{\psi}_3 - i\bar{\psi}_4) = \psi_3^*, \\
\psi_5 &= (1/\sqrt{2})(\bar{\psi}_5 + i\bar{\psi}_6), \\
\psi_6 &= (1/\sqrt{2})(\bar{\psi}_5 - i\bar{\psi}_6) = \psi_5^*
\end{aligned} \tag{2.11}$$

where ($\psi_{1,2}$, ψ_3, ψ_4, ψ_5, ψ_6) are atomic wavefunctions of sets. Also, the eigenstates ψ of m and $-m$ can be considered as complex conjugates to each other as in [28], which implies,

$$H_{m_p}(\alpha) = H^*_{-m_p}(\alpha) \tag{2.12}$$

From this, the eigenvalues and eigenfunctions of H, for the 6 cases of $p = \pm$, m = 2,1,0, have been derived in [28], while the other four cases $p = \pm$, m = -2,-1 have been obtained by complex conjugations. For an imaginary (complex) wave function, a plot of $|\psi|^2$, i.e. ($\propto \psi\psi^*$), rather than ($\propto \psi\psi$) would be needed, and real combinations produced by combining the eigenfunctions, $m_p = 1$ and $m_p =$ -1. Then, by using suitable computer software the molecular orbitals of C_{60} can be easily evaluated.

The terms formulated for the HMOs in Deng and Yang [28] expressions proposed that the single β_s and the double β_d bonds were equal. Therefore, an improvement to the theory will be needed to consider the more realistic picture, where $\beta_s \neq \beta_d$. In general, the single and double bond are not equal, as shown in fig. 2.5 [65]. The bond lengths will be discussed at the end of this section to provide a realistic picture. The p-orbitals of the 60 carbons of C_{60} molecule, which created the linear combinations of the HMOs have been studied by Deng and Yang in ref.[28]. In their method the C_5 orientation axis synchronized with the z-axis to a pentagon-prone molecule. However, in this work, the C_2 orienta-

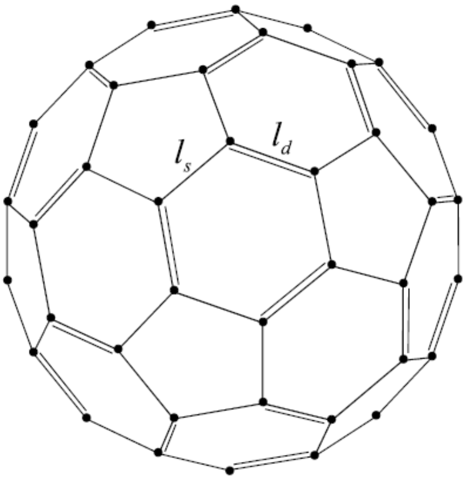

Figure 2.5: The single bonds of length l_s, and the double bonds each of length l_d, joined to form the 12 pentagonal faces and the 20 hexagonal faces of C_{60} where $l_s > l_d$ reproduced from ref. [65].

Table 2.3: The modified Deng and Yang's values for α = 0.8220

	Orb	m	p	c$_1$	c$_2$	c$_3$	c$_4$	c$_5$	c$_6$
LUMO	T_{1uz}	0	-1	-0.264	0.468	0.089	0	-0.838	0
	T_{1ux}	1	-1	-0.463	0.374	0.327	0.623	-0.00087	0.385
HOMO	$H_{u\theta}$	0	-1	0	0	0	-0.398	0	-0.917
	$H_{u\epsilon}$	1	-1	0.530	0.092	-0.480	0.550	0.415	0.066
	H_{u5}	2	-1	-0.368	-0.638	-0.018	-0.468	0.470	0.120

tion axis synchronized with the z-axis to a double bond-prone molecule in order to meet the JT Hamiltonians, which have been used in current work. In order to relate [28] and [65], it will be worthwhile to account for this inequality, taking the expression for the ratio of the resonance integrals for double and single bonds, as in ref. [65] to be:

$$\tau = \frac{\beta_d}{\beta_s} \tag{2.13}$$

According to [28], α has been used for the interaction between single bonds and 2-α has shown the interaction between the double bonds i.e $\tau = \frac{2-\alpha}{\alpha}$. Therefore,

$$\alpha = 2(1+\tau)^{-1} \tag{2.14}$$

rather than $\alpha = \tau = 1$ in the case of the old equal-bond picture. In ref. [25] the value τ = 1.433 was deduced to demonstrated the bond alternation, which has been observed experimentally for (C = C) = 1.391 $\AA$ and (C - C) = 1.455 $\AA$. This, in turn, implies that α = 0.8220. Using this value of α= 0.8220, the following c's parameters have been derived in Table 2.3. Where (T_{1ux},T_{1uy},T_{1uz}) are the three LUMO components of C$_{60}$, and ($H_{u\theta}$,$H_{u\epsilon}$,H_{u4},H_{u5},H_{u6}) are the five HOMO components of the same molecule. T_{1uy} in this case is T^*_{1ux} and similarly, ($H_{u4} = H^*_{u\epsilon}$), and ($H_{u6} = H^*_{u5}$). Then the parameter coefficients required to rebuild the linear combination of the molecular orbitals were calculated from the adjusted consequences of Deng and Yang in their paper [28]. Figures (2.6,2.7) show the density is around pentagons for LUMO (T_{1u}) and the density is around hexagons for HOMO (H_u) electron densities, expressed as sums of the squares, in the case, where both orbitals are degenerate orbitals are present in each irrepresentation.

2.9 Simulated STM images in Fullerene C$_{60}$ molecule

This section follows the approach used by [25] employing specific molecular orbitals to generate simulated C$_{60}$ STM images. The simple tunnelling theory

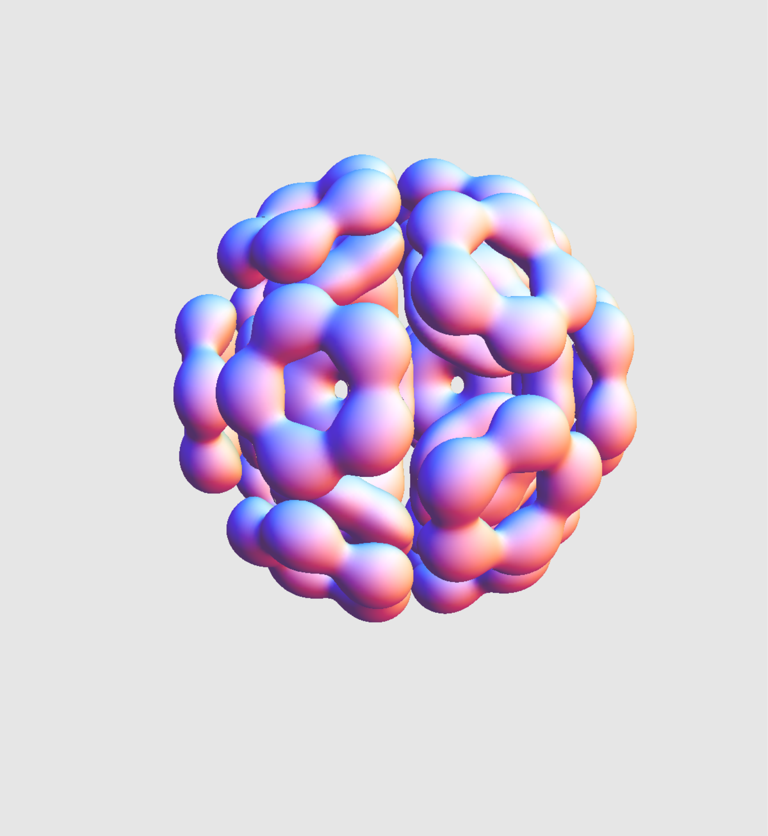

Figure 2.6: The electron distribution of C_{60} related to the LUMO

procedure proposed by Tersoff and Hamann [66] may be used to obtain accompanying STM image simulations. The theory proposes that in STM, the measured tunnelling current I, and the density of the electronic states are nearly proportional, taken at a distance of tip r_0, such that:

$$I \propto \Sigma_v |\psi_v(r_0)|^2 \delta(E_v - E_f) \tag{2.15}$$

where the wave function representing the state of surface energy E_v is given by ψ_v, E_f denotes the Fermi energy, and v is running overall available surface states. When imaging the LUMO, the assumption is that positive bias is applied to the surface, leading to a proportional relationship between the current and electron density $\rho_L(r_0)$ as found at r_0, such that:

$$I(r_0) \propto \rho_L(r_0) = \Sigma_{\alpha=x,y,z} |T_{1u\alpha}(r_0)|^2 \tag{2.16}$$

This sum includes all degenerate orbitals. Equation (2.16) can be easily evaluated in a given plane of any point in the x-y plane to generate a CHM image. CCM may be simulated using extended calculations in ref.[25] to produce plots for tip height satisfying the condition of constant tunnelling current. In addition,

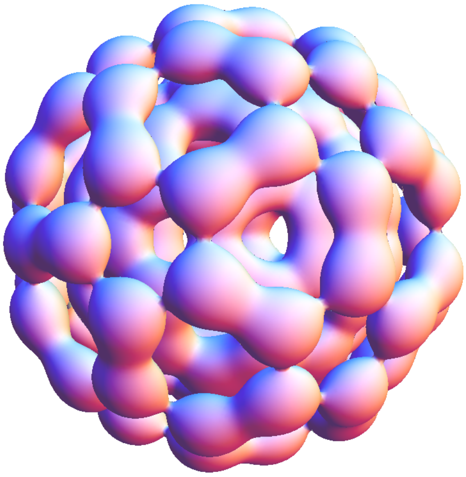

Figure 2.7: The electron distribution of C_{60} related to the HOMO

eq. (2.16) may be generalized quite easily for both HOMO and LUMO+1.

In order to generate STM images, it will be assumed that the HMOs are made from π bonds, which are p-orbitals aligned radially in the direction of unit vector n, where n is a vector from the centre of molecule to atom (i). It assumed that in ref.[21], the wavefunctions will decay, according to e^{-kR}, where for hydrogen like atoms k is related to the Bohr radius a_0 and the effective nuclear charge Z_{eff} in a simple relation $k = \frac{Z_{\text{eff}}}{2a_0}$ [21]. In addition, according to ref. [67], Z_{eff} has been determined to be equal to 3.14, which is associated with $k \approx 3$. Therefore, the value of the p-orbital is $(n.R)\ e^{-3R}$, where R is the distance from atom (i). However, $|r - n|$ is the distance from the centre of the molecule, where $n.R = n.(r - n)$, given by $n.r - n^2$. Then, the wave function describing the HMOs of the molecule will take the form $(n.r - n^2)e^{-3(r-n)}$. In order to deform the normalized wave function of the LUMO, the wave function describing the HMOs will be multiplied with the Deng and Yang parameters of the representation of the electronic state T_{1ux},T_{1uy}, and T_{1uz} of different values of m and p of all over the 60 atoms, as shown in Table 2.3. As found, the T_{1uz} is a real part, while T_{1uy} is a complex conjugate of complex T_{1ux}. Figure 2.8 shows the important three molecular symmetry axes with the rotational angles ϕ needed to rotate the molecule direct to the black upper plane, which denoted the scan region. The black square plane has been fixed at a specific extent from the origin of the molecule. Then the molecule will be rotated around the y-axis with the particular face facing toward the STM tip. The highlighted axes C_n show the double bond facing the surface when $n = 2$, while the hexagonal and pentagonal faces for $n = 3$ and $n = 5$.

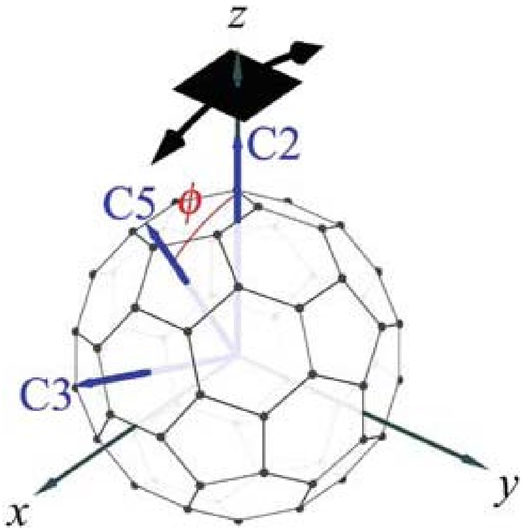

Figure 2.8: The three orientation axes with the rotation angles ϕ, reproduced from ref. [26].

Plotting the electron density provides a good creation of real pictures. To clarify that, the ordinary non-interacting state, sets of orbitals can be investigated. It is noteworthy that identical STM images are generated, for the LUMO and LUMO+1, where only the parity of the T_1 representation is different.

For the idealised STM image, eq.(2.16) is plotted whereby tunnelling current may be set to be constant, while the STM tip height is varied normal to the surface. This will map out the variation of the tip height across the sample plane coordinates for constant current, i.e. simulating constant tunnelling current. The tunnelling current is fixed at a small value, to reflect the observed electron density accurately, while neglecting STM tip effects due to its finite size.

Therefore, for a specified plane, eq.(2.16) may be easily evaluated, and as such, fig. 2.9 which represents the STM image for the LUMO of C_{60} of double bond orientation generated for constant height mode. It is clear that the information provided is very limited compared with fig. 2.10 of constant current mode of the same orientation. Moreover, it is quite straightforward to create plots using simulation for the tip height needed for tunnelling current to be kept constant by extending the calculations in Figures (2.10,2.11,2.12). For example, 2.10 is showing the molecular orbitals in fig. 2.6 in the direction of double bond, so

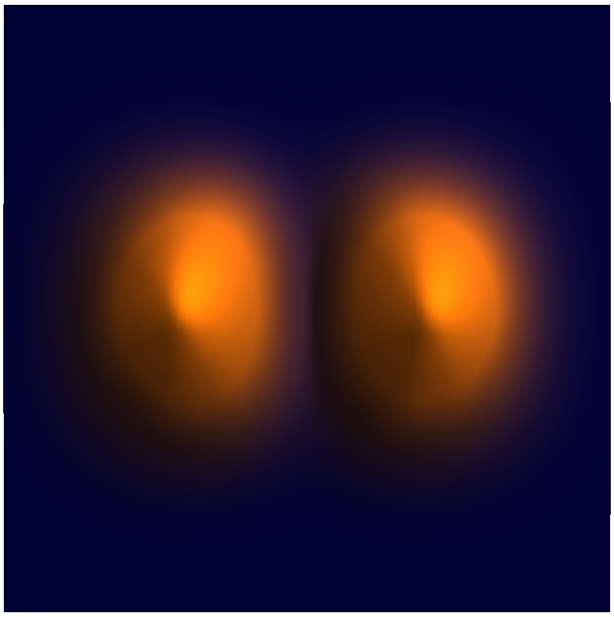

Figure 2.9: The STM constant height image for LUMO of C_{60} when C_2 axis perpendicular to the surface

fig.2.11 around pentagon with C_5 axis perpendicular to the surface and fig. 2.12 around hexagon with C_3 axis perpendicular to the surface.

In conclusion, these simulated C_{60} images are in good agreement with others reported in other theoretical works [25]. Different orientations of STM images of C_{60}^{-} ion will be added in the next chapter, in order to compare them with the images that have been simulated for the doubly-charged ion, in the presence of surface interaction applied equally with JT effect.

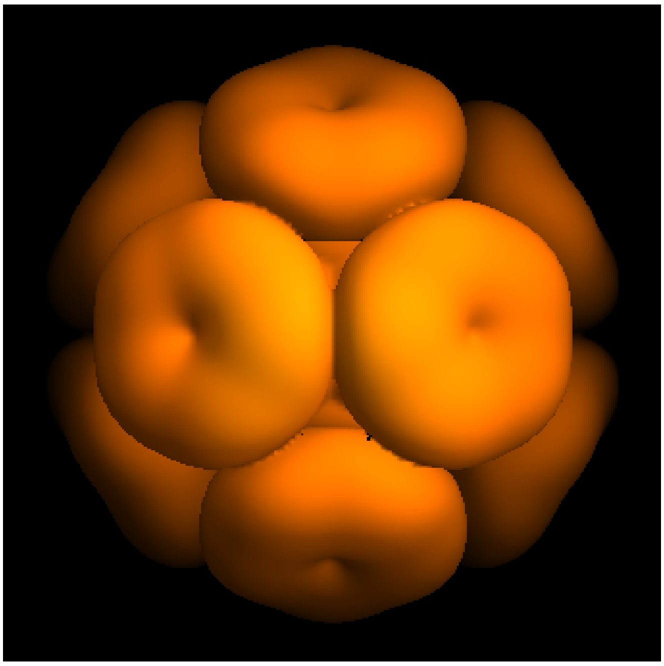

Figure 2.10: STM simulation for fully degenerate LUMO of C_{60} with C_2 axis perpendicular to the surface in case of no JT and surface interaction.

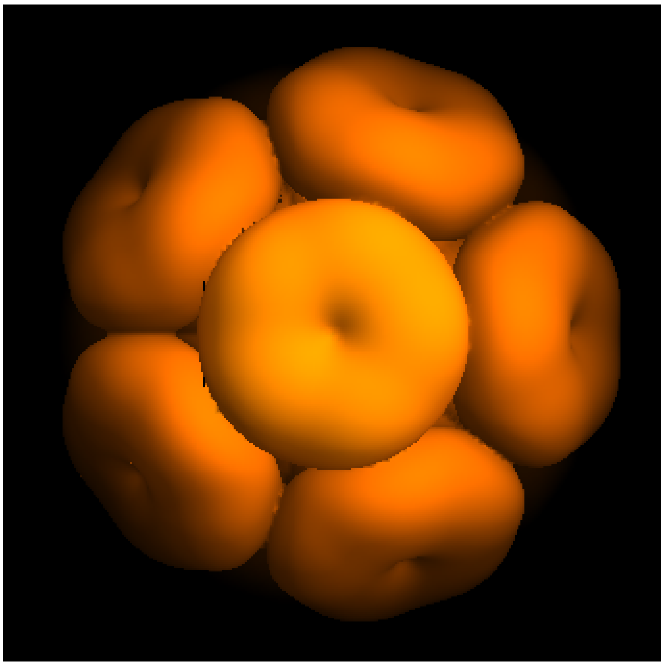

Figure 2.11: The STM image of C_{60} with C_5 axis perpendicular to the surface

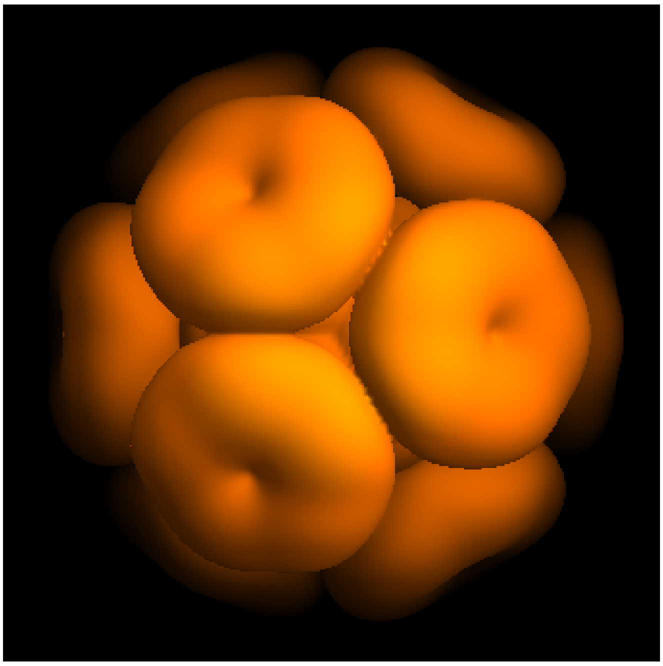

Figure 2.12: The STM image of C_{60} with C_3 axis normal to the surface

Chapter 3

Review of STM images of C_{60}^{-} anions

3.1 Introduction

After successfully reproducing the observed STM images of the C_{60} neutral molecule, it is worth turning attention to charged states, where the static and dynamic JT effect [68], will be presented side by side with other equally important interactions generated by contact with a substrate surface. The neutral molecule is a good acceptor of electrons, and not a good donor. Therefore, it would be easy to start an investigation of JT interaction in the simplest mono-anion, such as C_{60}^{-}, in order to move confidently towards the more complicated charged states, as will be presented in subsequent chapters.
The aim of this chapter is to reproduce observed STM images of the C_{60}^{-} ion, as described in references [26],[22], while considering the JT effect as an internal interaction, and the interaction with the surface as an external interaction. In addition, the splits in the electronic states, which have been observed from JT interaction, as a result of the high degeneracies from the strong electronic and vibronic coupling, will be taken into consideration. The JT effect in this ion is the same as the JT coupling in C_{60}^{5-} [69] [70].

Static and dynamic JT effects are included in this review, and JT distortions are considered in general, in relation to D_{3d} and D_{5d} symmetries. The surface, has another effect on the symmetry reduction. The chapter will be concluded by predicting STM images of mono-anion C_{60}^{-} adsorbed on a surface in different orientations.

3.2 JT effect and surface interaction modelling

In order to model JT effect and the surface interactions with respect to C_{60}^{-}, it is assumed that the C_{60}^{-} ion is adsorbed onto a surface with different orientations. A brief overview of modelling the JT effect in the C_{60}^{-} ion with the external effect generated by the surface is provided. The effect of the molecular orientations on the combination of JT and surface interactions are presented.

3.2.1 JT Hamiltonian in C_{60}^{-} ion

In general, the JT interaction can be formulated by linear and quadratic coupling constants. In the case of the linear JT interaction, the LAPES takes the form of a trough of points of equal energies [71]. However, due to the $H \otimes H$ product, the reduction of the symmetry will not be simple. Therefore, two distinct quadratic coupling constant types are generated.

Following ref. [23], the JT Hamiltonian is written using 2-fold molecular axes (X, Y, Z) through the centre of the double bonds of the molecule located between two hexagons. However, (x, y, z) is used later in case of applying the surface, where the z-axis is defined normal to the surface, and y-axis is between two hexagons to the centre of the double bond. Therefore, the y-axis is associated with the molecule axis Y but x and z are rotated with respect to X and Z. This means that, in order to obtain the symmetry orientations, such as, C_3 and C_5, a rotation of the molecule about the y-axis in the x,z plane is required. However, axes coincide for C_2 orientations.

The full JT Hamiltonian for the system may be shown in the form of 3×3 matrices.

This Hamiltonian can be divided into two parts:

$$\mathcal{H} = \mathcal{H}_{JT} + \mathcal{H}_0 \tag{3.1}$$

where; $\mathcal{H}_0$ is the vibrational Hamiltonian representing the fivefold degenerate vibrations.

If we define an operator $\mathcal{H}_0$ by

$$\mathcal{H}_0 = \frac{1}{2}\sum_i \left[\frac{P_i^2}{\mu} + \mu\omega^2 Q_i^2\right] I \tag{3.2}$$

where,

$$Q_i \;=\; \left(\frac{V_1}{\mu\omega^2}\right) a_i$$

and, the sum is over the five h_g components of normal modes $Q_\epsilon, Q_\theta, Q_4, Q_5, Q_6$.

H_{JT} is the JT interaction Hamiltonian, which has the general form

$$\mathcal{H}_{JT} = V_1 \mathcal{H}_1(Q) + V_2 \mathcal{H}_2(Q^2) + V_3 \mathcal{H}_3(Q^2) \tag{3.3}$$

where $\mathcal{H}_1$ is the linear interaction Hamiltonian, and the two quadratic coupling Hamiltonians are $\mathcal{H}_2$, $\mathcal{H}_3$. The relative importance of these two quadratic terms depends on the magnitude of the quadratic coupling constants V_2 and V_3. These parameters are treated in this system as generally as possible, because no attempts have been made to calculate them.

As for any JT coupling problem, the Hamiltonian that represents the interaction should be found in order to analyse the system. Using the table in [72], which agrees with [23], it can be shown that the linear interaction Hamiltonian of the $T \otimes h$ problem can be written in matrix form with electronic basis (X,Y,Z) as:

$$\mathcal{H}_1 = \begin{bmatrix} \frac{1}{2\sqrt{5}}(\sqrt{3}\,\phi^{-1}\,Q_\theta + \phi^2 Q_\epsilon) & \sqrt{\frac{3}{10}}Q_6 & \sqrt{\frac{3}{10}}Q_5 \\ \sqrt{\frac{3}{10}}Q_6 & \frac{-1}{2\sqrt{5}}(\sqrt{3}\,\phi\,Q_\theta + \phi^{-2}Q_\epsilon) & \sqrt{\frac{3}{10}}Q_4 \\ \sqrt{\frac{3}{10}}Q_5 & \sqrt{\frac{3}{10}}Q_4 & \frac{1}{2}\left(\sqrt{\frac{3}{5}}Q_\theta - Q_\epsilon\right) \end{bmatrix} \tag{3.4}$$

where ϕ is the golden mean, as given by $\phi = \frac{1}{2}(1+\sqrt{5})$.

This linear Hamiltonian by itself produces a trough of points of energy minima in five-dimensional APES, where each point on this continuous trough is matched to a different distortion. The motion of the system consists of rotating around, as well as vibrating across the trough.

The quadratic Hamiltonian matrices $\mathcal{H}_2$ and $\mathcal{H}_3$ for the system in two forms are:

$$\mathcal{H}_2 = \begin{bmatrix} \frac{1}{2}\,\phi^{-1}\sqrt{\frac{3}{5}}A_1 + \frac{\phi^2}{2\sqrt{5}}A_2 & -\sqrt{\frac{3}{5}}Q_\epsilon Q_6 & \frac{1}{2}\sqrt{\frac{3}{5}}(-\sqrt{3}Q_\theta + Q_\epsilon)Q_5 \\ -\sqrt{\frac{3}{5}}Q_\epsilon Q_6 & \frac{-1}{2}\,\phi\sqrt{\frac{3}{5}}A_1 - \frac{\phi^{-2}}{2\sqrt{5}}A_2 & \frac{1}{2}\sqrt{\frac{3}{5}}(\sqrt{3}Q_\theta + Q_\epsilon)Q_4 \\ \frac{1}{2}\sqrt{\frac{3}{5}}(-\sqrt{3}Q_\theta + Q_\epsilon)Q_5 & \frac{1}{2}\sqrt{\frac{3}{5}}(\sqrt{3}Q_\theta + Q_\epsilon)Q_4 & \frac{1}{2}\sqrt{\frac{3}{5}}A_1 - \frac{1}{2}A_2 \end{bmatrix} \tag{3.5}$$

and,

$$\mathcal{H}_3 = \begin{bmatrix} \frac{1}{2}\,\phi^{-1}\,\sqrt{\frac{3}{5}}B_1 + \frac{\phi^2}{2\sqrt{5}}B_2 & \sqrt{\frac{1}{5}}(Q_\theta Q_6 - \sqrt{2}Q_4Q_5) & C_1 \\ \sqrt{\frac{1}{5}}(Q_\theta Q_6 - \sqrt{2}Q_4Q_5) & \frac{-1}{2}\,\phi\,\sqrt{\frac{3}{5}}B_1 - \frac{\phi^{-2}}{2\sqrt{5}}B_2 & D_1 \\ C_1 & D_1 & \frac{1}{2}\sqrt{\frac{3}{5}}B_1 - \frac{1}{2}B_2 \end{bmatrix} \tag{3.6}$$

with,

$$\begin{aligned} A_1 &= \sqrt{\frac{1}{2}}Q_\theta Q_\epsilon + \sqrt{\frac{3}{8}}(Q_4^2 - Q_5^2) \\ A_2 &= \sqrt{\frac{1}{8}}(Q_\theta^2 - Q_\epsilon^2 + Q_4^2 - Q_5^2 - 2Q_6^2) \\ B_1 &= \sqrt{\frac{3}{8}}(Q_\theta^2 - Q_\epsilon^2) - \sqrt{\frac{1}{24}}(Q_4^2 + Q_5^2 - 2Q_6^2) \\ B_2 &= -\sqrt{\frac{3}{2}}Q_\theta Q_\epsilon + \sqrt{\frac{1}{8}}(Q_4^2 - Q_5^2) \\ C_1 &= -\frac{1}{2}\sqrt{\frac{1}{5}}[(Q_\theta + \sqrt{3}Q_\epsilon)Q_5 + 2\sqrt{2}Q_4Q_6] \\ D_1 &= -\frac{1}{2}\sqrt{\frac{1}{5}}[(Q_\theta - \sqrt{3}Q_\epsilon)Q_4 + 2\sqrt{2}Q_5Q_6]. \end{aligned}$$

In order to simplify the form of the minima, the Qs, in terms of d-orbitals can be written as [10]:

$$\begin{aligned} Q_\theta &\sim \frac{\sqrt{3}}{\sqrt{8}}d_{3Z^2-R^2} + \frac{\sqrt{5}}{\sqrt{8}}d_{X^2-Y^2}, \\ Q_\epsilon &\sim \frac{\sqrt{3}}{\sqrt{8}}d_{X^2-Y^2} - \frac{\sqrt{5}}{\sqrt{8}}d_{3Z^2-R^2} \\ Q_4 &\sim d_{YZ} \\ Q_5 &\sim d_{ZX} \\ Q_6 &\sim d_{XY} \end{aligned} \tag{3.7}$$

It will be more useful to write the JT Hamiltonian in the form:

$$\mathcal{H}_{JT} = V_1\mathcal{H}_1 + V_2\mathcal{H}_2 + V_3\mathcal{H}_3 + \frac{\mu\omega^2\sum_i Q_i^2}{2} \tag{3.8}$$

It has been appropriate to remove some of the constants in $\mathcal{H}$ by defining:

$$\begin{aligned}
V_1' &= -V_1/\sqrt{\mu\hbar\omega^3} \\
V_2' &= \frac{V_2}{\mu\omega^2} \\
V_3' &= \frac{V_3}{\mu\omega^2}
\end{aligned}$$

In fact, by substituting the Q_i by $-a_i$, V_2 by V_2', and V_3 by V_3', a dimensionless Hamiltonian $\mathcal{H}_1'$ then can be defined from $\mathcal{H}$. Then, V_1 can be omitted from $\mathcal{H}_1$, and $\mathcal{H}_0$ will be written as $\frac{1}{2}\Sigma a_i^2 \mathrm{I}$ [23], where μ is the mass of the carbon nuclei of the icosahedron, I represents the 3×3 unit matrix, V_1 represents JT coupling constants, which measure the strength of the coupling; and V_2 and V_3 are the quadratic coupling constants where all the parameters H_i', a_i, V_2', V_3' are dimensionless. The energy eigenvalues of this Hamiltonian will be in units of $\hbar\omega$, where ω is the normal mode frequency of oscillation. In general, according to ref. [14], the five a_i can be represented in terms of four angles and one distance. However, for D_{3d} and D_{5d} distortions, these a_i can be written in terms of only θ and ϕ with spherical polar coordinates definitions. Therefore, after converting to our notation, the visual display of the wells by plotting $(\sin\theta\cos\phi, \sin\theta\sin\phi, \cos\phi)$ on a sphere can be obtained as in ref.[23]. Figure fig.3.1 shows the structure of the minima by changing the radial coordinate between wells in order to determine the relative energies of the APES. Due to the vibronic coupling, the JT ion will be distorted in different symmetries such as, six D_{5d} wells, labeled from A to F at the vertices of the icosahedron. These 6 wells have equal distance between each other as in fig.3.1(a).

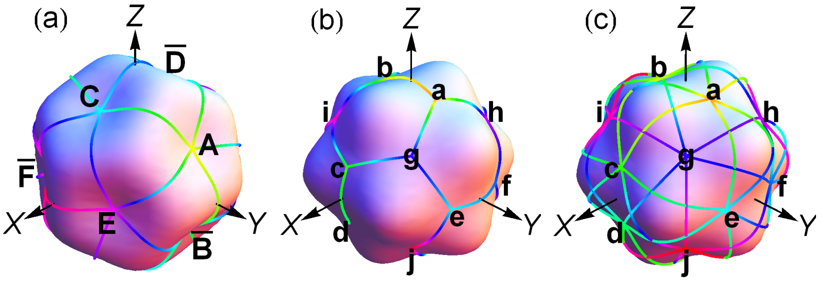

Figure 3.1: (a)The D_{5d} wells, (b) the 3-nearest neighbours of D_{3d} wells and (c)shows the 6 next- nearest neighbours of D_{3d} wells reproduced from ref. [22]

However, the ten D_{3d} wells at the vertices of a dodecahedron labeled from a to j have 3 nearest neighbours as shown in fig.3.1(b) and 6 next nearest neighbours as shown in fig.3.1(c). Then, 15 D_{2h}-type saddle points labeled from A to O at the centres of the edges of either polyhedron.

3.2.2 Introduction to the surface interaction in C_{60}^{-} system

A maximum of six electrons may be taken up by the T_{1u} LUMO. In general, the surface will be treated independently of the surface structure, as the atoms positions are perturbing near that surface. From the knowledge of the symmetry reduction of I_h, group theory will find the remaining orientations of the C_{60} molecule. Then, it will be possible to work out how T_{1u} and H_u can transform as described in [22].

The effect of the surface on the ion will be demonstrated, in removing the parity between the perpendicular z-axis to the surface and the other two axes, x and y, placed on the surface plane. In this treatment, the surface structure will not be considered. However, the strength of the surface interaction depends on the surface structure. Generally, the surface interaction can change the electronic state of the system and the Q_i positions at the APES. Therefore, this will require obtaining the new electronic state of the minimum wells by using the parameters generated from JT and surface interactions.

The STM current according to Tersoff-Haman theory is proportional to the sum of the squares of the equivalence states ψ_i as follows:

$$I = \sum_{i}^{n} \frac{\psi_i^2}{n}$$

However, the overall constant is not relevant as we only know $I \propto \sum_i \psi_i^2$. For normalisation, this sum will be divided by n, which is the number of the minima. In case of the three higher symmetric orientations, the cross terms will be cancelled due to the symmetric distribution of the APES points around z-axis. Therefore, the current will take the form:

$$I = a_x\psi_x^2 + a_y\psi_y^2 + a_z\psi_z^2 \tag{3.9}$$

where (a_x, a_y, a_z) are constant coefficients for a given set of interaction parameters, which can show the contribution from each part of the wavefunction.

3.2.3 The character tables of different orientations

In this orientation, the nearest atoms to the surface are perturbed in different kinds of symmetries. The basis set of the ion in the form of the molecular orbitals can be written in terms of the Cartesian coordinates (x, y, z). However, as an alternative, it is possible to use functions that transform in the same way. In pentagon down orientation, the symmetry operations will survive C_5 rotations about the z–axis normal to the surface.

To find the characters for a basis set that can be written in terms of the cartesian coordinates, we will look at the reduction from I_h symmetry to the different point group symmetry. In case of the C_{5v} point group is made up of the identity, $2C_5$, $2C_5^2$, and reflection symmetry operation $5\sigma_v$. For example, to find the characters for each component of the H_u basis, we will need to find the five fold matrix (M) that acts on this basis, that has the same effect as the symmetry operation. Then, it is straightforward to obtain a series of equations that can be solved for the individul matrix elements. The equations will be solved by looking at the coefficients of the x^2,y^2,z^2,yz,xz,xy components which will construct the symmetry matrix M. The character associated with each component is the corresponding diagonal element of the symmetric matrix M. Then, this character table can be compared with the actual C_{5v} character table to find the groupings. Then, T_{1u} and H_u will transform as;

$$\begin{aligned} T_{1u} &\rightarrow A_1 + E_1 \\ H_u &\rightarrow A_2 + E_1 + E_2 \end{aligned}$$

From the basis functions, which transform in the same way, each individual component will transform as:

C_{5v}	E	$2C_5$	$2C_5^2$	$5\sigma_v$	
T_{1uz}	1	1	1	1	$\rightarrow A_1$
$T_{1ux} + T_{1uy}$	2	ϕ^{-1}	$-\phi$	0	$\rightarrow E_1$
$H_{u\theta}$	1	1	1	-1	$\rightarrow A_2$
$H_{u\epsilon} + H_{u6}$	2	$-\phi$	ϕ^{-1}	0	$\rightarrow E_2$
$H_{u4} + H_{u5}$	2	ϕ^{-1}	$-\phi$	0	$\rightarrow E_1$

where (θ,ϵ) are both referred to the d orbital. It is clear that the singlet component of the T_{1u} is the z–component; this consideration looks acceptable as the z-direction is treated differently. However, x and y are managed in the same way. However, z component in hexagon down orientation is over the centre of a hexagon, while the y component is out of the centre of the bond between two hexagons. In this case, the group is therefore C_{3v}, and $2C_3$ and $3\sigma_v$ are the symmetry operations that are going to survive when the atoms nearest the surface are perturbed. Comparing characteristics of the basis functions, which convert in the same way, gives:

$$\begin{aligned} T_{1u} &\rightarrow A_1 + E \\ H_u &\rightarrow A_2 + 2E \end{aligned}$$

And each individual component will transform as:

C_{3v}	E	$2C_3$	$3\sigma_v$	
T_{1uz}	1	1	1	$\rightarrow A_1$
$T_{1ux}+T_{1uy}$	2	-1	0	$\rightarrow E$
$H_{u\theta}$	1	1	-1	$\rightarrow A_2$
$H_{u\epsilon}+H_{u6}$	2	-1	0	$\rightarrow E$
$H_{u4}+H_{u5}$	2	-1	0	$\rightarrow E$

Also, as has been found in the pentagon orientation, the singlet component of the T_{1u} is the z–component. On the other hand, in the double bond prone orientation, the remaining symmetry operations are C_2 and $\sigma_v(xz)$ and $\sigma_v^{'}(yz)$. Then the group will be C_{2v}, and T_{1u} and H_u will transform as;

$$\begin{aligned} T_{1u} &\rightarrow A_1+B_1+B_2 \\ H_u &\rightarrow A_1+2A_2+B_1+B_2 \end{aligned}$$

Also, each individual component will transform as:

C_{2v}	E	C_2	$\sigma_v(xz)$	$\sigma_v^{'}(yz)$	
T_{1uz}	1	1	1	1	$\rightarrow A_1$
T_{1ux}	1	-1	1	-1	$\rightarrow B_1$
T_{1uy}	1	-1	-1	1	$\rightarrow B_2$
$H_{u\theta}$	1	1	-1	-1	$\rightarrow A_2$
$H_{u\epsilon}$	1	1	-1	-1	$\rightarrow A_2$
H_{u4}	1	-1	1	-1	$\rightarrow B_1$
H_{u5}	1	-1	-1	1	$\rightarrow B_2$
H_{u6}	1	1	1	1	$\rightarrow A_1$

This shows that in this orientation all of the T_{1u} and H_u representations are singlets. This orientation cannot hold the two dimensions representation due to C_{2v} point group.

3.3 The surface interaction Hamiltonian form

The simple Hamiltonian will be needed to model the surface interaction, and then locate other solutions to the combined Hamiltonian in eq.(4.62).

3.3.1 The pentagon and hexagon orientations

Indeed, these two different orientations are common, the z–component being the singlet, and the other, x– and y–components are two dimensions. The labels used for x,y,z here indicate the C_3 or C_5 z–axis.

The surface interaction Hamiltonian for C_5 orientation in the C_5 basis can take the form,

$$H_S = \frac{V_1^2}{\mu\omega^2}\begin{bmatrix} 0 & 0 & 0 \\ 0 & 0 & 0 \\ 0 & 0 & -\Delta_1 \end{bmatrix} \tag{3.10}$$

where, Δ_1 is the energy of the singlet z-state, which can be positive (higher in energy) or negative (lower in energy) than the two dimensions.
In order to write the surface interaction Hamiltonian in terms of (x, y, z) in the 2-fold z-axis to be in the same basis as the JT Hamiltonian using (X, Y, Z), a converter matrix will be needed to convert from C_2 z-axis to a C_3, which is a rotation in the x–z plane by an angle $(\tan^{-1}[\frac{1}{2}(3+\sqrt{5})])$ or C_5, which is a rotation in the x–z plane by an angle $(\tan^{-1}[\frac{1}{2}(-1+\sqrt{5})])$. It is easier to convert from the basis state related to the surface interaction, to the basis relating to JT Hamiltonian, as the latter is the most complex. As is known, if the rotation is in z-direction, the appropriate rotation matrix is;

$$U_T = \begin{bmatrix} \cos\theta & 0 & -\sin\theta \\ 0 & 1 & 0 \\ \sin\theta & 0 & \cos\theta \end{bmatrix} \tag{3.11}$$

However, the inverse rotation matrix, required to convert from C_5 or C_3 to C_2, takes the form:

$$U_T^{-1} = \begin{bmatrix} \cos\theta & 0 & \sin\theta \\ 0 & 1 & 0 \\ -\sin\theta & 0 & \cos\theta \end{bmatrix} \tag{3.12}$$

Then the required Hamiltonian in the 2-fold (X, Y, Z) basis has the form:

$$H_S^{C2} = U_T H_S U_T^{-1} \tag{3.13}$$

In fact, the overall zero in energy is not fixed, so this will not be the only form for the surface Hamiltonian.

3.3.2 Double bond-prone orientation

The surface interaction Hamiltonian in this orientation is easier than the other previous orientations, as it is already in the C_2 basis. The three T_{1u} components are singlets; therefore, the matrix will be diagonal with two surface parameter constants, Δ_1 and Δ_2:

$$H_S = \frac{V_1^2}{\mu\omega^2}\begin{bmatrix} 0 & 0 & 0 \\ 0 & -\Delta_2 & 0 \\ 0 & 0 & -\Delta_1 \end{bmatrix} \tag{3.14}$$

The surface parameters Δ_1 and Δ_2 could be defined in a different way. In this orientation, the basis coincide, so the transformation between these bases is not required.

3.4 Solving combined Hamiltonian of surface and JT interactions

The JT and surface interaction Hamiltonians need to be diagonalized and dealing with the molecule on the same basis. Therefore, it is possible to join them in order to construct one Hamiltonian, which can display the interactions on the molecule. The surface unknown parameters will be treated as generally as possible, because the energy gaps between the orbitals are unknown. The first step in this investigation is to obtain the minimum wells favoured for a specific set of the combined constants, by searching the values of the normal modes positions, which reduce the lowest energy eigenvalue of the lowest Hamiltonian. The same notations for the wells are used as in ref.[23], where only JT interaction is involved, in determining the positions of the D_{3d} and D_{5d} wells. The majority of the results will consider the cases where surface interaction is added to the system with values of $(V_2' = 0.5, V_3' = 0)$ that result in a D_{5d} distortion in absence of surface interaction and $(V_2' = 0, V_3' = 0.5)$ to prefer D_{3d} distortion, in order to be consistent with ref.[22]. The following section will present an approximation method, which will be used in solving the combined Hamiltonian to find the preferred wells for each possible symmetry operation for different orientations, and then compare them with what has been done previously in ref.[22].

3.4.1 The approximation method

The appropriate technique, which was discussed in the section above, concentrated on minimizing the whole system energy in order to find the normal mode coordinates Q_i. The five variables (a_θ, a_ϵ, a_4, a_5, a_6) for any option of parameters after the surface and JT interactions are added, require minimising the lowest eigenvalues of the total Hamiltonian, which included the sum of the interaction, considering $\mathcal{H}_{JT}$ and $\mathcal{H}_S$. However, this approximation method, will keep the normal modes coordinate Q_i fixed, while the surface interaction is added in. On the other hand, this method will speed up the calculations of finding eigenvectors rather than using the full theory. Therefore, it is possible to work out the required form of the JT Hamiltonian from the eigenvalues, or solve the JT Hamiltonian directly, while fully ignoring surface parameters. This approximation method is followed by defining the new eigenvectors from the lowest eigenvalues of the 3×3 JT Hamiltonian without resetting the normal mode coordinate values Q_i. Similar results were found either way [22], and the wells position would keep the same path [22]. This similarity can be seen between fig. 3.3 which has been done by using approximation method and the diagram in fig. 3.2(b) which have been done by using proper method. The proper method shows the positions of the wells as

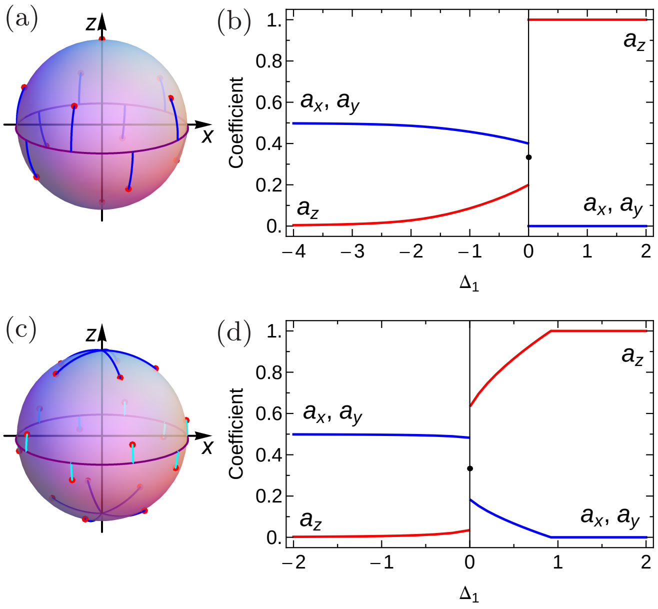

Figure 3.2: (a)The position of the wells of C_{60}^- for D_{5d} symmetry (b) the current coefficients for parameters preferring a D_{5d} symmetry (c) the position of the wells of C_{60}^- for D_{3d} symmetry (d) the same as in b, but for D_{3d} symmetry reproduced from ref. [22]

a curve towards the equator, and indeed, the line paths are in the same direction for the approximation method. In addition, the coefficients of the current a_x, a_y, and a_z cover the same ranges in both methods, whether the surface interaction is weak or strong. This approximate method is very useful in saving time in order to do further investigations of any higher charged fullerene ions with higher dimensional matrices, such as 6 dimensional matrices for C_{60}^{2-} and C_{60}^{4-}. Also, the more complicated C_{60}^{3-} triply charged ion, which is represented by a 8 dimensional matrix, where more wells in this ion make the situation more complicated, as the wells are likely to favour either D_{2h} or C_{2h}, as will be discussed in chapter 5. Indeed, it is worth promoting some chosen values as needed by using the proper method.

The most useful application of the approximation method in this matter is to minimise the time and effort, needed to work out the different ranges of JT and surface strengths parameters to achieve good potential matches with the published experimental images, as presented in later chapters. However, in order to match the published results confidently, the proper method is needed.

3.4.2 Pentagon-prone orientation

In this orientation, one parameter from the surface interaction Δ_1, and two parameters from JT effect V_2', V_3' will join to consider case where surface interaction is added to the system that result in a D_{5d} distortion in absence of surface interaction. For the positive value of Δ_1, the global minimum in energy will be given by well C only, which is equivalent to electronic state ψ_z. However, there are five equivalent lowest energy wells, namely (A,B,D,E,F) for Δ_1 less than zero, with electronic states coordinates direct to the $x-y$ plane. Figure 3.3 shows the effect of the surface on the coefficients a_x,a_y,a_z in eq. (3.9) for positive and negative surface parameters. From the diagram in fig. 3.3, it will be possible to predict the STM images for any given set of parameters. It is clear that the curves do not join up at the z-axis, which indicates a change in the lowest energy wells, so the coefficients change suddenly to give a discontinuous curve.

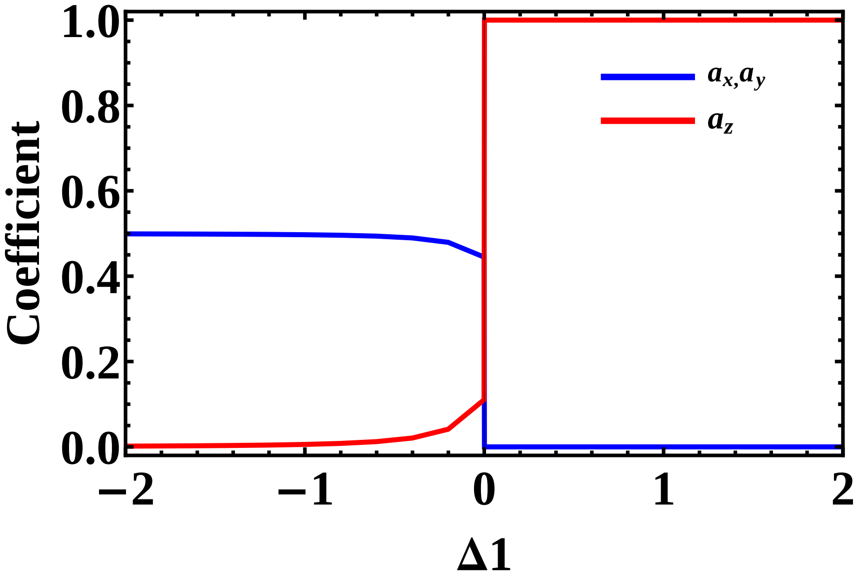

Figure 3.3: The plot of the coefficients a_x,a_y, and a_z of the parameters preferring D_{5d} symmetry distortion via a range of surface strengths for the C_5 orientation of parameters V_2'=0.5,V_3'=0 of the C_{60}^- ion (by using approximation method)

On the other hand, there are JT parameters that prefer a D_{3d} symmetry, as a result of negative Δ_1. Similar to the D_{5d} distortion, another five minima will result, such as (d, e, f, h, j) towards the $x-y$ plane.

In the same way, the change in coefficients values due to the change in the strength of the surface is illustrated in fig. 3.4.

Well d is one of the five expected STM images when the system is locked into one of the wells, as shown in fig. 3.5(a). The images of the other wells (e, f, h, j) are $\frac{2\pi}{5}$ rotations.

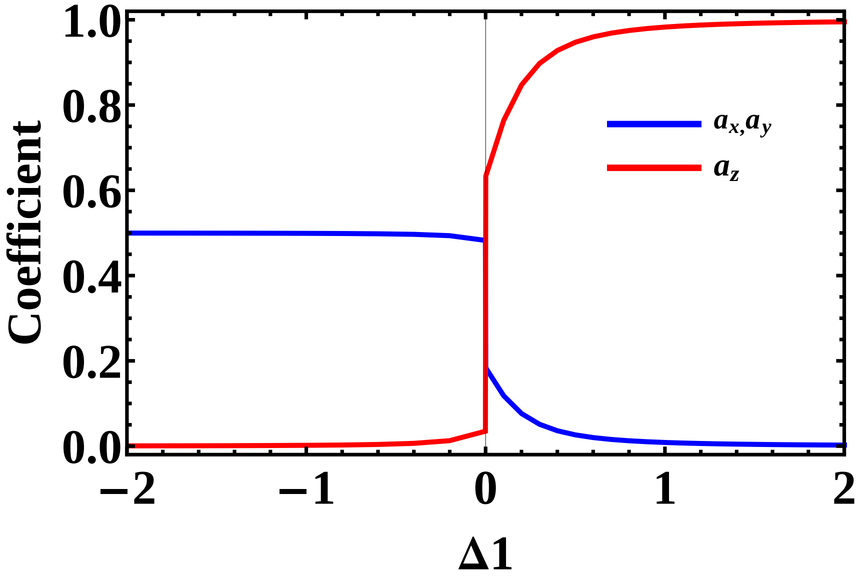

Figure 3.4: The plot of the coefficients a_x,a_y, and a_z of the parameters preferring D_{3d} symmetry distortion via a range of surface strengths for the C_5 orientation of the C_{60}^- ion (by using approximation method)

However, the image fig. 3.5(b), which is the superposition of the five minima, will be expected to be shown in case of the system hopping between the wells in a timescale shorter than the required time of the STM process. This superposed image is evidence of the JT effect in the STM experiment. For the other case, when Δ_1 greater than zero, the five wells (a, b, c, g, i) will form the points of the minimum, and direct toward the z-axis. These paths of pentagon prone of different values of surface have been shown in fig. 3.2. Therefore, the STM image would involve only ψ_z^2. The expected STM images in this case will be provided in fig. 3.6(a) for well g, and again the superposition of all of the wells in fig. 3.6(b). Similarly, the images of wells (a, b, c, i) are $\frac{2\pi}{3}$ rotations. Additional images of just pure ψ_x^2,ψ_y^2 and ψ_z^2 in order to show how resultant image is a superposition of the individual images have been shown in fig.3.7.

It is clear that from fig. 3.5(c) and fig. 3.6 that while images of separate wells are clearly different, the combined image is rather similar. In fact, high current used in produce the STM image in fig. 3.5(c), while the STM image in fig. 3.6 simulated by using lower current. These, images with different resolution can be distinguish theoretically according to the size of the images and how much detail has been provided.

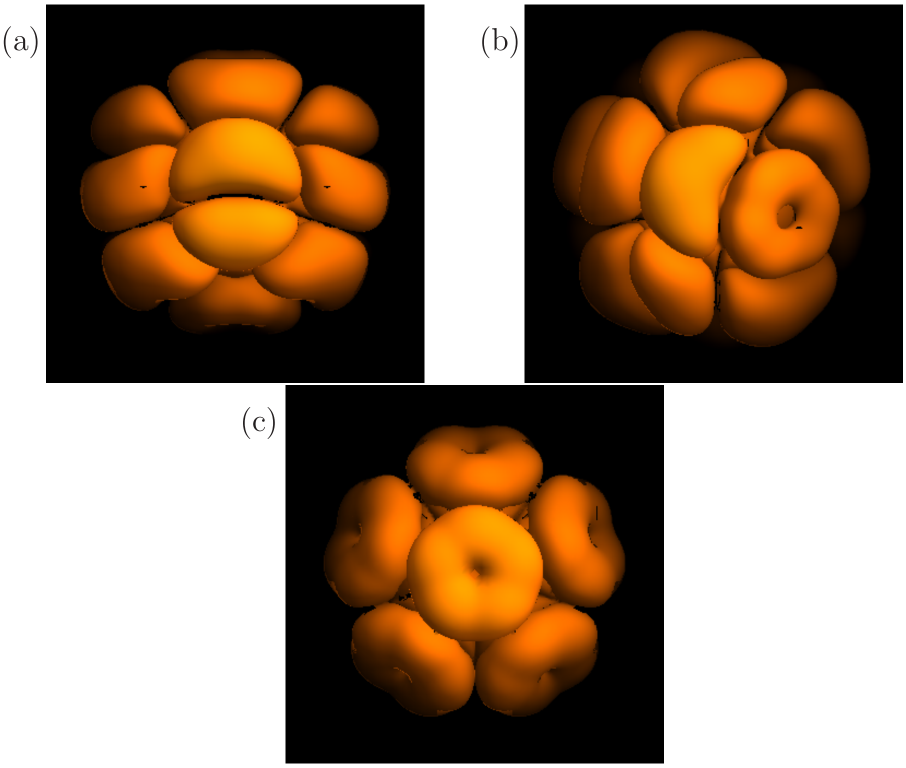

Figure 3.5: (a)The STM image of well d of the parameters preferring D_{3d} symmetry distortion of C_5 orientation of C_{60}^{-} ion of parameters V_2'=0,V_3'=0.5 for Δ_1 less than zero, (b) well g for Δ_1 greater than zero, and (c) is the expected STM image of the superposition of the five wells for the same distortion for Δ_1 less than zero.

.

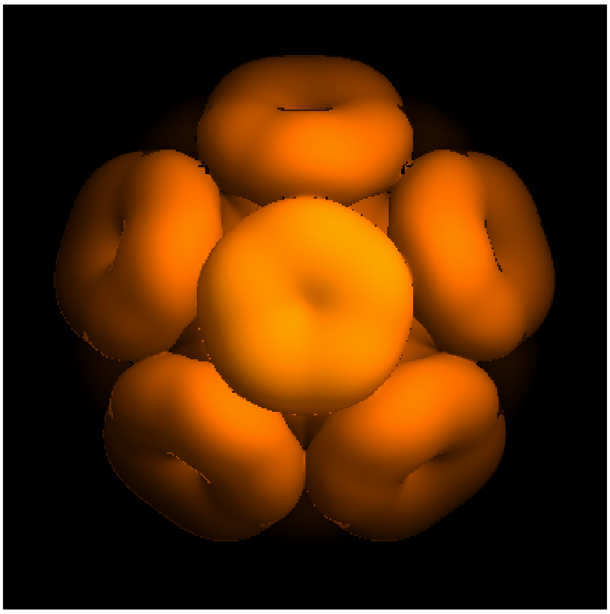

Figure 3.6: The expected STM image of the superposition of the five wells for Δ_1 greater than zero of the parameters preferring D_{3d} symmetry distortion of C_5 orientation of V_2'=0,V_3'=0.5 of C_{60}^- ion.

.

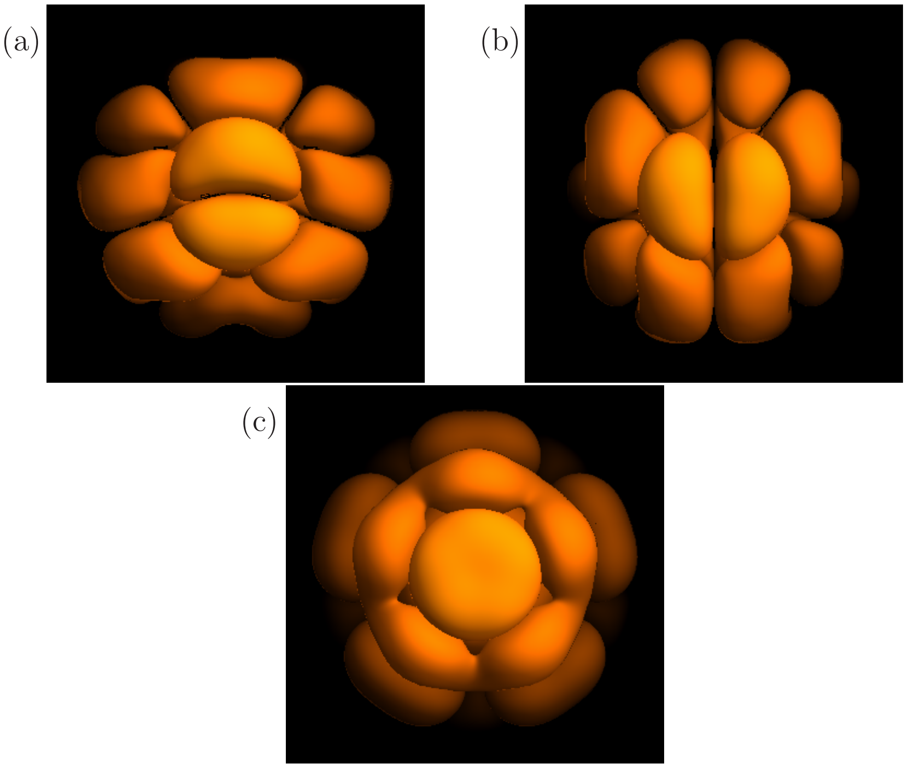

Figure 3.7: The expected STM images of pure (a) ψ_x^2 (b)ψ_y^2 (c)ψ_z^2 of C_{60}^{-} ion of C_5 orientation

.

3.4.3 Hexagon-prone orientation

In this orientation, the z-axis refers to the C_3 rotation axis aligned with the centre of hexagon. Similar to what was done in the pentagon-prone orientation, in $\Delta_1 < 0$, three wells (A,B,C) result when JT parameters prefer the D_{5d} symmetry, and the effect of the surface on the three coefficients, is as shown in fig. 3.8. However, when $\Delta_1 > 0$, the behaviour will be changed, and the system will prefer (C,E,F) wells. Therefore, we turn our attention to the system, when JT constants prefer the D_{3d} distortion, the global minimum will be well c only for $\Delta_1 > 0$, and the behaviour of the three coefficients a_x,a_y, and a_z, is as shown in fig.3.9.

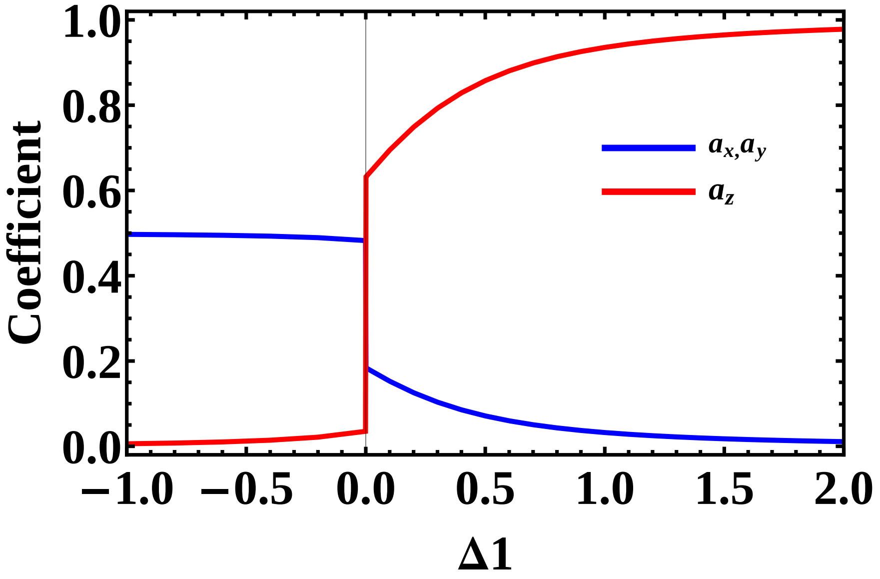

Figure 3.8: The plot of the coefficients a_x,a_y, and a_z of the parameters preferring D_{5d} symmetry distortion via a range of surface strengths in the C_3 orientation of V_2'=0.5,V_3'=0 of the C_{60}^- ion (by using approximation method)

In addition, six wells labeled (a, b, e, f, h, j) has been favoured, when $\Delta_1 < 0$. Some of these wells are displayed in fig.3.10. Again, these resultant images are superposition of the individual images that have been provided in fig. 3.11.

The same method has been applied to the double bond-prone in references [26],[22] with two surface parameters Δ_1,Δ_2.

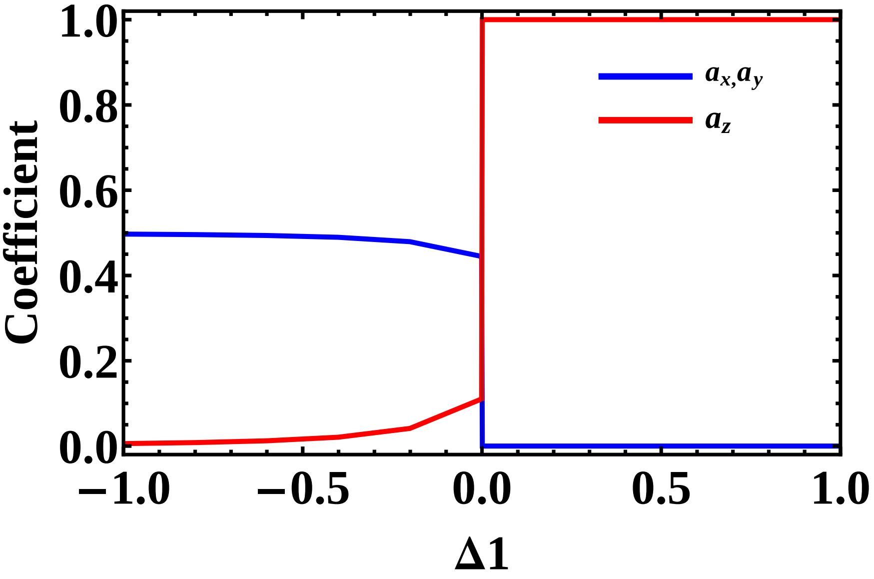

Figure 3.9: The plot of the coefficients a_x,a_y, and a_z of the parameters preferring D_{3d} symmetry distortion via a range of surface strengths in the C_3 of V_2'=0,V_3'=0.5 orientation of the C_{60}^- ion (by using approximation method)

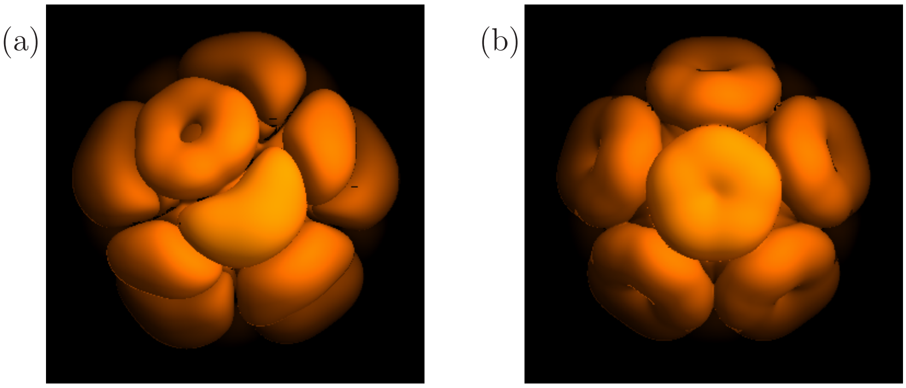

Figure 3.10: (a)The STM image of well b of the parameters preferring the D_{3d} symmetry distortion of the C_3 orientation of C_{60}^- ion, for Δ_1 less than zero (b) is the superposition of the wells.

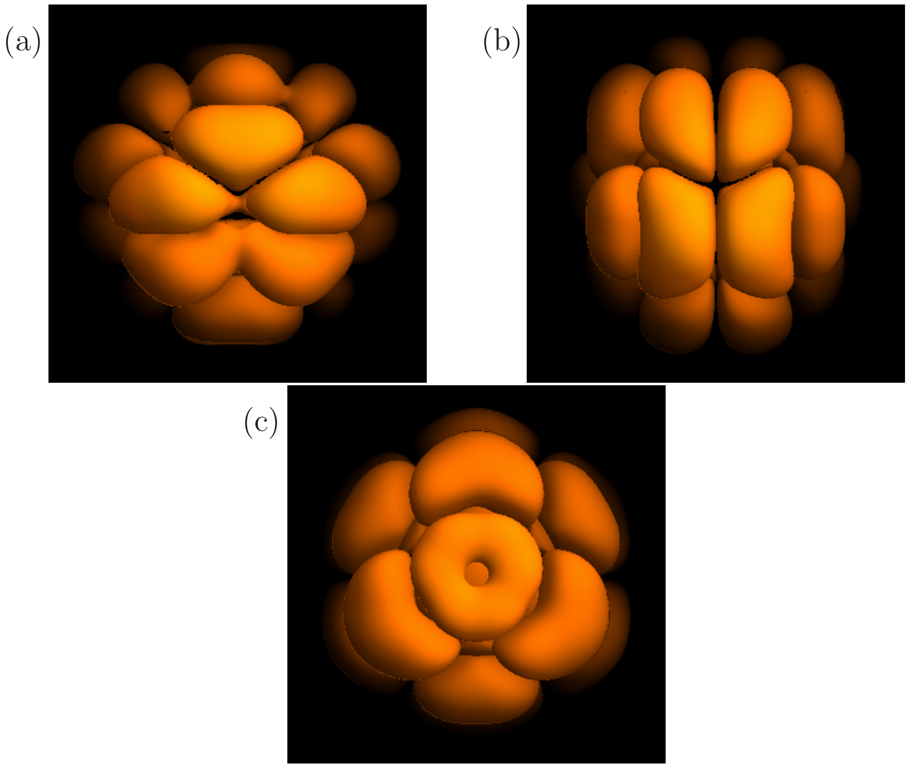

Figure 3.11: The expected STM images of pure (a) ψ_x^2 (b)ψ_y^2 (c)ψ_z^2 of C_{60}^- ion of C_3 orientation

.

3.5 Conclusion

The surface interaction makes the actual symmetry lower than D_{5d} and D_{3d} distortion. C_{60}^{-} is subject to a JT effect, and the additional electron occupies the T_{1u} orbital. This chapter provided a brief review of how the combined surface interactions and JT interaction Hamiltonians have been solved basically for a C_{60}^{-} ion using Hückel molecular orbital theory with the symmetry arguments, in order to explain the STM images of the ion following references [26],[22]. This has been obtained by determining the values of the normal modes (a_θ, a_ϵ, a_4, a_5, a_6).

The STM images have been considered from the lowest unoccupied molecular orbital of the single electron state system, where the LUMO was composed of a linear combination of T_{1ux},T_{1uy} and T_{1uz}.

The tunnelling currents have been calculated in terms of ψ_x^2,ψ_y^2,ψ_z^2 with no cross terms found. Also, pseudorotation and hopping between the equivalent minimum wells was considered.

Some solutions for the C_{60}^{-} ion facing the surface in different orientations have been included. In addition, STM images of chosen wells for given sets of parameters have been reproduced. Some diagrams have indicated that different values of surface strengths have produced different STM images, which in addition, have included the cases where the system was assumed to hop between wells in the pseudorotation process.

More STM images of this ion will be shown in the next chapter, in order to compare between C_{60}^{-}, C_{60}^{2-}, and C_{60}^{4-} ions. Theoretically, the simulated STM results are similar to each other, such that the small difference between them cannot be noticed experimentally.

Chapter 4, next, will present different treatment for higher charged systems, which will need further modifications to the treatment presented in this chapter.

Chapter 4

The STM images of C$_{60}^{2-}$ and C$_{60}^{4-}$ molecules on surfaces

4.1 Introduction

The structure and chemistry or spectroscopy of fullerides has received significant attention from many researchers. Electron-vibration interactions of the C$_{60}$ molecule are highly influenced by the charge state, and the effects of doping are ideally explored using STM. As has been discussed in the previous chapter, laying the molecule onto a surface can shift the MOs energy, and vary the tunnelling current. On the other hand, the other inherent effect due to JT interaction, causing degeneracy in the electronic state and resulting in different symmetry distortion, can also be studied through STM.

In 1997, Chancey and O'Brien in [14] extended the work on the fullerene anion, C$_{60}^{n-}$ by calculating the result of addition of electrons at the strong JT coupling position in the C$_{60}$ molecule.
Simulation has managed to generate images of both neutral C$_{60}$ and singly-charged ion C$_{60}^{-}$, as reported in ref.[25] and ref.[26]. These matched and successfully described the experimentally observed images in ref.[13], and have also been reproduced in sections of this work.
This study aims to progress new work relating to the doubly-charged ion, C$_{60}^{2-}$, which at system-level involves adsorbing an isolated C$_{60}^{2-}$ ion onto a substrate surface. In addition, it also includes the other charged ion, C$_{60}^{4-}$, which is similar to the doubly-charged ion as it contains two holes (rather than two electrons), as stated in ref. [73]. In this respect, interactions due to the general JT coupling model $p^2 \otimes h_g$, considered proper in dealing with the C$_{60}^{2-}$ dianion, and those due

to the substrate surface, are taken into account.

As was found, it seems that the JT effect is a significant factor dictating the particular combinations to be made, yet without ignoring the possible equally important involvement of other interactions, such as surface interaction. The combination of the JT interaction and the surface interaction Hamiltonians will be investigated by using Hückel molecular orbital theory and group theory techniques.

On doping a fullerene ion, such as C_{60}^{2-}, the additional electrons occupy the T_{1u} orbital. The main most complicated interactions of the fullerene physics, such as the JT effect, are discussed. These effects have been investigated in detail when second order quadratic coupling is added to the system, as in ref. [16]. The theory of modelling the surface interaction for $T \otimes h_g$ in [22] will be applied in case of $p^2 \otimes h_g$ and the surface Hamiltonian forms for each orientation will be derived. The subsequent sections provide an outline of the basis states involving many electrons, which are used in this study, as well as presenting the $p^2 \otimes h_g$ system Hamiltonian. It is also essential to demonstrate the system electronic states that may form the bases for representing the interaction Hamiltonian on a matrix, as derived by [16] using tables compiled by Fowler and Ceulemans in ref. [72]. Moreover, proposed modifications to the multi-electron method [74] to enable simulated STM images to be obtained are presented in detail that will be used in calculating the total current for tunnelling into T_{1g}, A_{1g}, and H_g states in order to model the STM images for C_{60}^{2-} as simply as has been done in Tersoff and Hamann in [66].

The work will go further to modify the theory for multi-electron states by using the direct integration method to write the current in the simplest forms, in terms of single electron state, as a linear combination of ψ_x^2,ψ_y^2 and ψ_z^2 [75].

This chapter will also include certain assumptions to show the behaviour of the ion when adsorbed pentagon-prone to the surface for positive and negative surface interaction. Then the same method will be extended to be applied to the same ion in the hexagon and double bond-prone orientations. Some images will be simulated by using the constant current mode to show the appearance of the double-charged ion as might be recorded by STM. This will take into consideration the hopping or the pseudorotation between wells, and how the solutions can be affected by the new electronic state corresponding to each well that results from including the external effect of the surface.

The same calculations will be applied to the C_{60}^{4-} ion in order to explain what has been published in 2005 in ref. [18]. Also, a theoretical comparison between published STM images of C_{60}^{-} with C_{60}^{2-} is provided.

The chapter ends by including a summary of the key results and discussion of the points raised.

4.2 JT and surface interactions of C_{60}^{2-} ion

The $p^2 \otimes h_g$ interaction model can be used to describe C_{60}^{2-} ions, since those electrons that are added move into the C_{60} LUMO having T_{1u} representation. As found in C_{60} negatively charged ions, the JT effect exists due to the orbitals comprising the LUMO, and as such these were the focus of the study. The C_{60} anion vibrations interact, and may cause the energy levels of the triply degenerate state to split, leading to a reduction in energy. This means that ion distortion occurs spontaneously, and a consequent departure from icosahedral symmetry is favourable from an energy perspective. This work will look at the key problem in a number of its general aspects. It is assumed that adsorption of the active JT molecule onto the substrate surface has been performed ahead of STM imaging. The aim is to find out, as simply as possible, and under ideal conditions, those effects related to JT, which may manifest in the image captured, such as the surface interaction.

Similarly, as has been considered in the $T \otimes h$ problem, to model the surface interaction, it will be assumed that the C_{60}^{2-} ion is adsorbed onto a surface as an isolated ion. Both the surface and JT interactions will be joined to investigate the effect of possible orientations on the JT ion. The combined Hamiltonian will be needed to obtain the interaction minima of APES.

4.2.1 Jahn-Teller Hamiltonian of C_{60}^{2-} ion

Compared to the linear $p\otimes h_g$ system, the current model suffers further complications due to the added electron. A discussion of the C_{60}^{2-} molecule electronic structure will be worthwhile ahead of applying any interactions, including surface or JT interactions. In the notation, consistent with that of ref. [14], the superscript indicates that the p-type electronic orbital is occupied by two electrons coupled to the h_g-type mode.

C_{60} is distinguished by its high symmetry, where a potentially large set of electron-vibration coupling systems (of interest) may be established through doping the molecule. As adsorption of the C_{60}^{2-} anion (with two electrons added), onto a substrate occurs, the likeliest doping event to happen is of electron density transfer to the LUMO. As such, the remainder of the chapter focuses on LUMO-derived images. Accordingly, to create images for the C_{60}^{2-} ion, which is adsorbed onto a substrate surface, the same methods in ref. [22] are used.

It is worthwhile to discuss the electronic structure of the C_{60}^{2-} molecule before applying interactions, such as JT or surface interactions. In case of multi-electron systems, the JT effects were usually investigated from the electronic parts in order to simplify the interpretation of Coulomb effects.

The electronic basis to allow formulating the $p^2 \otimes h_g$ system Hamiltonian needs to be derived first. The partially filled LUMO T_{1u} is occupied by the two electrons [76], and these electrons experience Coulomb interaction between them, which needs to be considered. This interaction results in terms that are derived from coupling the two electron orbital and spin angular momenta. The coupling of the electrons spin angular momentum is considered first, where total spin state is given by $S = 1$, or high-spin (symmetric) triplet spin state. On the other hand, $S = 0$ represents a low-spin (antisymmetric) singlet spin state. These two spin states are also coupled to the two electrons states of orbital momentum. The Kronecker product $T\otimes$ T = (A $\oplus$ H)$_S$ $\oplus$ (T)$_A$ allows prediction of the electrons orbital momentum states [16]. The high spin term $^3\mathrm{T}_{1g}$ is the result of the coupling of the Kronecker product's antisymmetric part with the symmetric triplet spin state. At the same time, the low spin states $(^1A_g,^1H_g)$ are product of the coupling between the Kronecker product's symmetric part with the antisymmetric singlet spin states. According to the tables, given the total wavefunction, the A_{1g} orbital plays an equally important part as the H_g orbitals. In fact, for high positive contribution of term splitting between A_{1g} and H_g states, the H_g will only be contributed. However, A_{1g} and H_g can both be involved in case small amounts of have been considered.

Moreover, a $T \otimes h$ interaction is the basis on which h_g vibrations and the high-spin term $^3\mathrm{T}_{1g}$ are coupled [38]. The multiplication of the spin and orbital states results in wavefunctions, which are associated with these terms. In accordance with the Pauli exclusion principle, the wavefunctions that result need to be antisymmetric.

Modelling the C_{60}^{2-} ion correctly, means that spin interactions, in this context, must be accounted. This is especially true, since factors regarding the density of electron states and spin states are taken into account in STM images. Therefore, the final orbital basis states are written as in ref. [16].

$$\begin{aligned}
|A_{1g}\rangle &= \frac{-1}{\sqrt{3}}[|T_{1ux}\rangle_1|T_{1ux}\rangle_2 + |T_{1uy}\rangle_1|T_{1uy}\rangle_2 + |T_{1uz}\rangle_1|T_{1uz}\rangle_2] \\
|T_{1gx}\rangle &= \frac{1}{\sqrt{2}}[|T_{1uy}\rangle_1|T_{1uz}\rangle_2 - |T_{1uz}\rangle_1|T_{1uy}\rangle_2] \\
|T_{1gy}\rangle &= \frac{1}{\sqrt{2}}[-|T_{1ux}\rangle_1|T_{1uz}\rangle_2 + |T_{1uz}\rangle_1|T_{1ux}\rangle_2] \\
|T_{1gz}\rangle &= \frac{1}{\sqrt{2}}[-|T_{1ux}\rangle_1|T_{1uy}\rangle_2 - |T_{1uy}\rangle_1|T_{1ux}\rangle_2] \\
|H_{g\theta}\rangle &= \frac{\phi^{-1}}{2}|T_{1ux}\rangle_1|T_{1ux}\rangle_2 - \frac{\phi}{2}|T_{1uy}\rangle_1|T_{1uy}\rangle_2 + \frac{1}{2}|T_{1uz}\rangle_1|T_{1uz}\rangle_2 \\
|H_{g\epsilon}\rangle &= \frac{\phi^2}{2\sqrt{3}}|T_{1ux}\rangle_1|T_{1ux}\rangle_2 - \frac{\phi^{-2}}{2\sqrt{3}}|T_{1uy}\rangle_1|T_{1uy}\rangle_2 - \frac{\sqrt{5}}{2\sqrt{3}}|T_{1uz}\rangle_1|T_{1uz}\rangle_2 \\
|H_{g4}\rangle &= \frac{1}{\sqrt{2}}[|T_{1uy}\rangle_1|T_{1uz}\rangle_2 + |T_{1uz}\rangle_1|T_{1uy}\rangle_2] \\
|H_{g5}\rangle &= \frac{1}{\sqrt{2}}[|T_{1ux}\rangle_1|T_{1uz}\rangle_2 + |T_{1uz}\rangle_1|T_{1ux}\rangle_2] \\
|H_{g6}\rangle &= \frac{1}{\sqrt{2}}[|T_{1ux}\rangle_1|T_{1uy}\rangle_2 + |T_{1uy}\rangle_1|T_{1ux}\rangle_2] \qquad (4.1)
\end{aligned}$$

In these expressions, $|T_{1ux}\rangle_1$ $|T_{1uy}\rangle_2$ represents the product state where electron (1) is in the $|T_{1ux}\rangle_1$ orbit and electron (2) is in the $|T_{1uy}\rangle_2$ orbit. Utilising basic quantum mechanics rules, allows the spin wavefunctions to be derived. For example, two electrons having spins of ($s_1 = s_2 = 1/2$)) and ($m_{s1} = m_{s2} = \pm\ 1/2$), are coupled giving a spin maximum value of (S=1) with (M_s = 1, 0, -1). As was explained previously, anti-symmetry governs the overall states. This leads to multiplication of antisymmetric orbital wavefunctions by triplet symmetric spin wavefunctions, and multiplication of singlet antisymmetric spin states by symmetric orbital wavefunctions. As was discussed previously, for the product $T_{1u} \otimes T_{1u}$, the tables in ref. [72] were used to derive the orbital wavefunction's CG coefficients [16]. The presence in the T_{1u} LUMO of these two electrons, results in spin terms, both high and low, as an outcome of the mechanisms for electron-electron interaction, such as Coulomb repulsion. This process ensures that the angular momenta and spin coupling results in degenerate electronic states or terms, even where there is a lack of interactions due to JT.

$$\begin{aligned}
S^t_a(1,2) &= S_1^+ S_2^+ \\
S^t_b(1,2) &= S_1^- S_2^- \\
S^t_c(1,2) &= \frac{1}{2}(S_1^+ S_2^- + S_1^- S_2^+) \qquad (4.2) \\
S^s(1,2) &= \frac{1}{2}(S_1^+ S_2^- - S_1^- S_2^+)
\end{aligned}$$

where, $S^t(1,2)$ is the spin triplet state, and $S^s(1,2)$ is the spin singlet state. The three subscripts (a,b,c) indicate the different spin states of the triplet spins. The

notations (1) and (2) are used to represent the two electrons.
More explicitly, the fully antisymmetric orbital and spin states of the two-electron orbital states $A^{(2e)}(1,2)$, $H_\theta^{(2e)}(1,2)$, and $T_{1x}^{(2e)}(1,2)$...etc, will take the forms:

$$\begin{aligned} &A^{(2e)}(1,2)S^s(1,2) \\ &H_i^{(2e)}(1,2)S^s(1,2) \\ &T_{1i}^{(2e)}(1,2)S^t(1,2) \end{aligned} \tag{4.3}$$

where (i) represents the state, and the superscript (2e) represents the two electron states. Then, the overall state is antisymmetric after multiplying by the spin states. There are three possible symmetric spin states and one antisymmetric state.
So, this will give:

- One A_{1g} state, consistent with low spin ^{1}S→ where, L=0, and S=0
- Nine T_{1u} state, consistent with high spin ^{3}P→ where, L=1, and S=1
- Five H_g state, consistent with low spin ^{1}D→ where, L=2, and S=0

The required states will be in forms of an orbital states × a spin state. Also, H_g states have five antisymmetrised combinations from (θ,ϵ,4,5,6).
However, T_{1u} states are triple spin states with $S = 1$; therefore, there will be 6 antisymmetrised combinations from (x,y,z).
If the minimum energy is found from the eigenvalues of a 6×6 matrix $(A_{1g} + H_g)$ or 3×3 matrix T_{1g}, then the eigenvector will only involve the $(A_{1g} + H_g)$ part or T_{1g} part, depending on which has the minimum energy. Since the T_{1g} components are at higher energy, and there are no matrix elements mixing the T_{1g} state with the A_{1g} and H_g states, they can be treated as two different problems. However, the one corresponding to the highest in energy would have zero contribution to the current. In the case of C_{60}^{2-}, the $(A_{1g}+H_g)$ part is the lowest in energy. Then, only the coupling between the $^1A_{1g}+\,^1H_g$ and h_g modes of vibration is considered. In fact, it is necessary to find electronic states of the form $(^1A_{1g}+^1H_g)$ to describe this coupling. So, the Hamiltonian will be a 6×6 matrix with six fold degenerate states. After the Hamiltonian has been written in terms of this basis, and by using the CG coefficients as in ref. [72], the two-electron states for our electronic basis can be formulated as shown above in eq.(4.1). The JT Hamiltonian is defined with two fold axes normal to the centre of a double bond between two hexagons. The total Hamiltonian of the system is written generally as:

$$\mathcal{H} = \mathcal{H}_{vib} + \mathcal{H}_{JT} + \mathcal{H}_S \tag{4.4}$$

This consists of terms generated from the isolated h$_g$ vibronic five fold degenerate mode and energies due to the JT interaction $\mathcal{H}_{JT}$ and surface interaction H_S

respectively. Again the vibronic term will take the form

$$\mathcal{H}_0 = \frac{1}{2}\sum_i [\frac{P_i^2}{\mu} + \mu\omega^2 Q_i^2] I \tag{4.5}$$

As shown in previous sections, the sum is over the five normal mode components Q_θ, Q_ϵ, Q_4, Q_5, Q_6, while P_i is the momentum operator conjugate to Q_i; μ here is the mass and ω is the frequency of the h_g mode of vibration, while I in eq.(4.5) represents the identity matrix.

$\mathcal{H}_S$ is a matrix that arises from the surface interaction, and represents the interaction between the sample and the substrate. The components of this matrix represent the energy difference between the states A_{1g} and H_g, as is shown in subsequent sections about adding surfaces. The JT Hamiltonian is formed of three parts given by,

$$\mathcal{H}_{JT} = V_1\mathcal{H}_1(Q) + V_2\mathcal{H}_2(Q^2) + V_3\mathcal{H}_3(Q^2) \tag{4.6}$$

In eq.(4.6), $\mathcal{H}_i$ are interaction matrices, and V_i are vibronic coupling constants. These vibronic constants usually determine the amount of contribution of each part to the coupling. In addition, the values of these parameters are still unknown for C_{60}^{2-}, so are treated as generally as possible.

The linear interaction matrix for the system uses the basis states arising from the coupling between A_{1g} and H_g terms. From the tables in ref. [72], this takes the form:

$$\mathcal{H}_1(Q) = \begin{bmatrix} 0 & Q_\theta & Q_\epsilon & Q_4 & Q_5 & Q_6 \\ Q_\theta & f_1 & f_2 & \frac{\sqrt{3}}{4\phi}Q_4 & \frac{-\sqrt{3}\phi}{4}Q_5 & \frac{\sqrt{3}}{4}Q_6 \\ Q_\epsilon & f_2 & -f_1 & \frac{\phi^2}{4}Q_4 & \frac{-1}{4\phi^2}Q_5 & \frac{-\sqrt{5}}{4}Q_6 \\ Q_4 & \frac{\sqrt{3}}{4\phi}Q_4 & \frac{\phi^2}{4}Q_4 & f_3 & \frac{-\sqrt{3}}{\sqrt{8}}Q_6 & \frac{-\sqrt{3}}{\sqrt{8}}Q_5 \\ Q_5 & \frac{-\sqrt{3}\phi}{4}Q_5 & \frac{-1}{4\phi^2}Q_5 & \frac{-\sqrt{3}}{\sqrt{8}}Q_4 & f_4 & \frac{-\sqrt{3}}{\sqrt{8}}Q_4 \\ Q_6 & \frac{\sqrt{3}}{4}Q_6 & \frac{-\sqrt{5}}{4}Q_6 & \frac{-\sqrt{3}}{\sqrt{8}}Q_5 & \frac{-\sqrt{3}}{\sqrt{8}}Q_4 & -(f_3+f_4) \end{bmatrix} \tag{4.7}$$

where;

$f_1 = \frac{\left(3\sqrt{3}Q_\theta+\sqrt{5}Q_\epsilon\right)}{8}$,

$f_2 = \frac{\left(\sqrt{5}Q_\theta-3\sqrt{3}Q_\epsilon\right)}{8}$,

$f_3 = \frac{\left(\sqrt{3}Q_\theta+\phi^3 Q_\epsilon\right)}{4\phi}$,

$f_4 = -\frac{\left(\sqrt{3}\phi^3 Q_\theta+Q_\epsilon\right)}{4\phi^2}$

This linear interaction Hamiltonian has been studied in more detail in ref. [10]. Generally, for unknown vibronic coupling constants, (in this case), then all the potential combinations of the two CG coefficient sets must be considered. The quadratic interaction matrices can be written by making simple substitutions in the linear matrix of the form:

$$H_2(Q^2) \rightarrow H_1(Q \mapsto A)$$

$$H_3(Q^2) \rightarrow H_1(Q \mapsto B)$$

with A_i and B_i components, which have been derived in ref. [72], where;

$$A_\theta = \frac{1}{2\sqrt{6}} \left(3Q_\theta^2 - 3\mathrm{Q}\epsilon^2 - Q_4^2 - Q_5^2 + 2Q_6^2\right)$$

$$A_\epsilon = \frac{-1}{2\sqrt{2}} \left(2\sqrt{3}Q_\theta \, \mathrm{Q}\epsilon - Q_4^2 + Q_5^2\right)$$

$$A_4 = \frac{-1}{\sqrt{6}} \left(Q_\theta \, Q_4 - \sqrt{3}\mathrm{Q}\epsilon \, Q_4 + 2\sqrt{2}Q_5 \, Q_6\right)$$

$$A_5 = \frac{-1}{\sqrt{6}} \left(Q_\theta \, Q_5 + \sqrt{3}\mathrm{Q}\epsilon \, Q_5 + 2\sqrt{2}Q_4 \, Q_6\right)$$

$$A_6 = \frac{2}{\sqrt{6}} \left(Q_\theta \, Q_6 - \sqrt{2}Q_4 Q_5\right)$$

and,

$$B_\theta = \frac{1}{2\sqrt{2}} \left(2Q_\theta \mathrm{Q}\epsilon + \sqrt{3}Q_4^2 - \sqrt{3}Q_5^2\right)$$

$$B_\epsilon = \frac{1}{2\sqrt{2}} \left(Q_\theta^2 - \mathrm{Q}\epsilon^2 + Q_4^2 + Q_5^2 - 2Q_6^2\right)$$

$$B_4 = \frac{1}{\sqrt{2}} \left(\mathrm{Q}\epsilon + \sqrt{3}Q_\theta\right) Q_4$$

$$B_5 = \frac{1}{\sqrt{2}} \left(\mathrm{Q}\epsilon - \sqrt{3}Q_\theta\right) Q_5$$

$$B_6 = -\sqrt{2}\mathrm{Q}\epsilon Q_6$$

At this stage, in order to compare the results of different charged states, redefining the JT constants with a $\sqrt{10}$ will be added to the JT parameters of C_{60}^{2-} system to be consistent with how they were written in previous papers [23],[22].

Now, including quadratic terms in the problem, the JT effect has known results in the dynamic equipotential energy points on the trough to be warped to form minima. These icosahedral subgroups are found to be ten minima of D_{3d}

Table 4.1: The electronic states of the Pentagonal wells of D_{5d} symmetry and D_{3d} symmetry of C_{60}^{2-} of term splitting=0 with respect to basis $(A, H_\theta, H_\epsilon, H_4, H_5, H_6)$

Label	Electronic state
D_{5d}	
A	$(\frac{-1}{\sqrt{3}}, \frac{-1}{\sqrt{5}}, \frac{-1}{\sqrt{15}}, \frac{\sqrt{2}}{\sqrt{5}}, 0, 0)$
B	$(\frac{-1}{\sqrt{3}}, \frac{-1}{\sqrt{5}}, \frac{-1}{\sqrt{15}}, \frac{-\sqrt{2}}{\sqrt{5}}, 0, 0)$
C	$(\frac{-1}{\sqrt{3}}, \frac{1}{\sqrt{5}}, \frac{-1}{\sqrt{15}}, 0, \frac{\sqrt{2}}{\sqrt{5}}, 0)$
D	$(\frac{-1}{\sqrt{3}}, \frac{1}{\sqrt{5}}, \frac{-1}{\sqrt{15}}, 0, \frac{-\sqrt{2}}{\sqrt{5}}, 0)$
E	$(\frac{-1}{\sqrt{3}}, 0, \frac{2}{\sqrt{15}}, 0, 0, \frac{\sqrt{2}}{\sqrt{5}})$
F	$(\frac{-1}{\sqrt{3}}, 0, \frac{2}{\sqrt{15}}, 0, 0, \frac{-\sqrt{2}}{\sqrt{5}})$
D_{3d}	
a	$(\frac{-1}{\sqrt{3}}, \frac{1}{3}, \frac{-1}{\sqrt{3}}, \frac{\sqrt{2}}{3}, 0, 0)$
b	$(\frac{-1}{\sqrt{3}}, \frac{1}{3}, \frac{-1}{\sqrt{3}}, \frac{-\sqrt{2}}{3}, 0, 0)$
c	$(\frac{-1}{\sqrt{3}}, \frac{1}{3}, \frac{1}{\sqrt{3}}, 0, \frac{\sqrt{2}}{3}, 0)$
d	$(\frac{-1}{\sqrt{3}}, \frac{1}{3}, \frac{1}{\sqrt{3}}, 0, \frac{-\sqrt{2}}{3}, 0)$
e	$(\frac{-1}{\sqrt{3}}, \frac{-2}{3}, 0, 0, 0, \frac{\sqrt{2}}{3})$
f	$(\frac{-1}{\sqrt{3}}, \frac{-2}{3}, 0, 0, 0, \frac{\sqrt{2}}{3})$
g	$(\frac{-1}{\sqrt{3}}, 0, 0, \frac{\sqrt{2}}{3}, \frac{\sqrt{2}}{3}, \frac{\sqrt{2}}{3})$
h	$(\frac{-1}{\sqrt{3}}, 0, 0, \frac{-\sqrt{2}}{3}, \frac{\sqrt{2}}{3}, \frac{-\sqrt{2}}{3})$
i	$(\frac{-1}{\sqrt{3}}, 0, 0, \frac{-\sqrt{2}}{3}, \frac{\sqrt{2}}{3}, \frac{-\sqrt{2}}{3})$
j	$(\frac{-1}{\sqrt{3}}, 0, 0, \frac{-\sqrt{2}}{3}, \frac{-\sqrt{2}}{3}, \frac{\sqrt{2}}{3})$

symmetry or six minima of D_{5d}. In the current work, we will focus on what effects the presence of a JT interaction may have on STM images observed from C_{60}^{2-} anions adsorbed on surfaces. The values of the minimum points for the wells have been obtained theoretically in ref. [16] by applying the symmetry operators on one of them then the same method can be applied for both symmetries D_{5d} and D_{3d}. The electronic states due to JT effect alone for D_{3d} and D_{5d} symmetries are tabulated in Table 4.1 [16]. These will be modified when term splitting and Coulomb interactions are included.

4.3 Theory of tunnelling for multiple particles [Bardeen's theory]

The tunnelling phenomenon is one of the fundamental aspect of quantum mechanics, which distinguishes it from classical mechanics. It plays a vital role in many categories of modern physics. The most widely applied theory for the tunnelling phenomenon in solids, as well as in STM, is Bardeen's theory. This theory is very useful for modelling the STM images of multi-electron states in the general case. Interestingly, this approach simplifies to the Tersoff and Hamann method, which has been used in the case of neutral fullerene, in the simple case, as in ref. [66]. In two electron states, it would be worth extending what has already been done for single-electron states, as in ref. [26] using the method in ref. [74]. This method supposed that the boundary extended from x_a toward x_b. More specifically, in the case of tunnelling into a two electron state, metal 'a' (tip) and 'b' (sample) represent the initial state with one electron each, then the final state will have both electrons in the sample, which in our case formed the doubly-charged ion C_{60}^{2-}. The results do not involve the tip states explicitly (although the tip states have been assumed to be s-type).

Before looking at the multi-electron case, it is useful to review how to obtain the result, as reported in references [25], [26], where an STM tip at a position $\mathbf{r}_0$ detects a current I, which is,

$$I \propto \sum_{\mu} |W_\mu(\mathbf{r}_0)|^2 \tag{4.8}$$

where the $W_\mu(\mathbf{r_0})$ are wavefunctions of the sample at the position of the tip, and the sum is over all degenerate states. This assumes that the tip can be modelled as a s-wave to represent tip wavefunctions in the gap region, which is the simplest choice. This means that the angular dependence of the tip wavefunction is the same as for the spherical harmonics Y_{lm}. The spherical harmonic expansion is used extensively in solid state physics for describing the electronic states. The current in eq. (4.8) obtained by Tersoff and Hamann by applying a two dimensional Fourier transformation. Alternatively, Chen in ref. [33] used Green's function in order to detect the tunnelling current. Green's function, is defined by the differential equation, such that the tip wavefunction χ_ν is proportional to $G(\mathbf{r}-\mathbf{r}_0)$, where G satisfies;

$$\left[\nabla^2 - \kappa^2\right] G(\mathbf{r}-\mathbf{r}_0) = -\delta(\mathbf{r}-\mathbf{r}_0) \tag{4.9}$$

For both tip states and sample states near the Fermi level, the sample wavefunctions W_μ satisfy the Schrödinger equation in the vacum:

$$\nabla^2 W_\mu = \kappa^2 W_\mu \tag{4.10}$$

in the gap region (where there is no potential). Here, κ is the decay constant. A central issue of the application of Bardeen's tunnelling theory is the evaluation of the tunnelling matrix element, which is a surface integral of the wavefunctions of the tip and the sample on a separation surface. From Bardeen's theory of tunnelling [33], the tunnelling current is proportional to the sum of the square of matrix elements $M^2_{\mu\nu}$ over all degenerate states, where:

$$M_{\mu\nu} = \frac{\hbar^2}{2m} \int_{\Omega_T} \left(\chi^*_\nu \nabla^2 W_\mu - W_\mu \nabla^2 \chi^*_\nu\right) \, d\tau \tag{4.11}$$

This matrix element involves integrals with the tip states, and Ω_T is the volume of the tip over which to integrate. The matrix element has the dimension of energy, which is the interaction energy due to the overlap of the two unperturbed states. By substituting for χ_ν, and using eq.(4.9) and eq.(4.10) the matrix element will have the form:

$$M_{\mu\nu} \propto \int_{\Omega_T} \left[G(\mathbf{r}-\mathbf{r}_0)\kappa^2 W_\mu - W_\mu \left(\kappa^2 G(\mathbf{r}-\mathbf{r}_0) - \delta(\mathbf{r}-\mathbf{r}_0)\right)\right] \, d\tau \tag{4.12}$$

The first two equal terms in this relation will cancel each other, and from the fundamental property of a δ function,

$$\int f(\mathbf{r})\delta(\mathbf{r}-\mathbf{r}_0) \, d\tau \;\; = \;\; f(\mathbf{r}_0). \tag{4.13}$$

So, the final term gives $f_\mu(\mathbf{r}_0)$ (the wavefunctions of the sample at the position of the tip for any function $f(\mathbf{r})$).

However, similar theory to that above in case of an electron tunnelling into a multielectron state. The theory modified for the multi-electron state, has been used in ref. [74]. In this case, the matrix elements can be written as:

$$M_{\mu\nu} = \frac{\hbar^2}{2m} \sum_i \int \ldots \int_{\Omega_T} \left(\chi^*_\nu \nabla^2_i W_\mu - W_\mu \nabla^2_i \chi^*_\nu\right) \, d\tau_1 \ldots d\tau_N. \tag{4.14}$$

where, ∇^2_i is the ∇^2 operator acting on the coordinates of electron i.
For these multi-electron systems, χ_ν is the wavefunction of the whole system before the tunnelling takes place (initial wave function). Similarly, W_μ is the wavefunction of the whole system after the tunnelling. Both relate to the same number of electrons in total, but one electron has moved from a state (tip) to a state (sample).
This case of tunnelling can be more specific, in studying the two electron state and that summation above, in eq. (4.14), will expand into initial and final states such as:

$$\begin{aligned} M_{\mu\nu} &= \frac{\hbar^2}{2m}\int\int_{\Omega_T}\left(\chi^*_\nu\nabla^2_1 W_\mu - W_\mu\nabla^2_1\chi^*_\nu\right)\,d\tau_1 d\tau_2 \\ &\quad+\frac{\hbar^2}{2m}\int\int_{\Omega_T}\left(\chi^*_\nu\nabla^2_2 W_\mu - W_\mu\nabla^2_2\chi^*_\nu\right)\,d\tau_1 d\tau_2 \end{aligned} \tag{4.15}$$

This relationship can be applied to other specific cases, such as (T_{1gx}, T_{1gy}, T_{1gz}). It is very important at this stage to confirm that by applying this relationship to previous squares of wave functions (ψ^2_x, ψ^2_y, ψ^2_z), it gives the same results as the one electron state. This theory will be used in order to obtain matrix elements for the two electron functions of C_{60}^{2-} and C_{60}^{4-}.

4.3.1 Tunnelling into the T_{1gx} two-electron state

From what has been discussed in section 4.3, consider W_μ to be the state of the system when one electron has tunnelled from the tip to the sample to be the two-electron state T_{1gx}; so from the basis state in eq. (4.1), ψ_μ the two electron state T_{1gx} is:

$$\psi_\mu = \frac{1}{\sqrt{2}}\left[|\psi_y(1)\psi_z(2) - \psi_z(1)\psi_y(2)\right] \tag{4.16}$$

where ψ_y is the single-electron T_{1u} state transforming as y, and the (1) means that the function is written in terms of the coordinates of electron (1). We assume that the initial state before the tunnelling has one electron in the ψ_z state of the sample and one electron in the state F_ν, Therefore, the initial state of the system is

$$F_\nu = \frac{C}{\sqrt{2}}\left[G(\mathbf{r}_1-\mathbf{r}_0)\psi_z(2) - \psi_z(1)G(\mathbf{r}_2-\mathbf{r}_0)\psi_z(2)\right] \tag{4.17}$$

where C is a constant (from converting the tip wavefunction to a Green's function). Substituting the ψ_x and F_ν into the first line of eq. (4.15), the matrix elements $M_{T_{1gx}\nu}(1)$ for the two electron state ψ_x will be proportional to:

$$\begin{aligned} &\int\int_{\Omega_T}\big(\left[G(\mathbf{r}_1-\mathbf{r}_0)\psi_z(2) - \psi_z(1)G(\mathbf{r}_2-\mathbf{r}_0)\psi_z(2)\right]\nabla^2_1\big[\psi_y(1)\psi_z(2) \\ &\quad-\psi_z(1)\psi_y(2)\big] - \left[\psi_y(1)\psi_z(2) - \psi_z(1)\psi_y(2)\right]\nabla^2_1\big[G(\mathbf{r}_1-\mathbf{r}_0)\psi_z(2) \\ &\qquad-\psi_z(1)G(\mathbf{r}_2-\mathbf{r}_0)\psi_z(2)\big]\big)\,d\tau_1 d\tau_2 \end{aligned} \tag{4.18}$$

Then applying eq. (4.9) and eq. (4.10), as for the single-electron case, the matrix elements above will be proportional to:

$$\int\int_{\Omega_T} \Big([G(\mathbf{r}_1-\mathbf{r}_0)\psi_z(2)-\psi_z(1)G(\mathbf{r}_2-\mathbf{r}_0)\psi_z(2)]\,\kappa^2\,[\psi_y(1)\psi_z(2)-\psi_z(1)\psi_y(2)] \\ -[\psi_y(1)\psi_z(2)-\psi_z(1)\psi_y(2)]\,\kappa^2\,[G(\mathbf{r}_1-\mathbf{r}_0)\psi_z(2)-\psi_z(1)G(\mathbf{r}_2-\mathbf{r}_0)\psi_z(2)] \\ +[\psi_y(1)\psi_z(2)-\psi_z(1)\psi_y(2)]\,\delta(\mathbf{r}_1-\mathbf{r}_0)\psi_z(2)\Big)\; d\tau_1 d\tau_2 \tag{4.19}$$

Only the third part (with the δ function) will remain, as the first two will cancel each other out. The integral over the coordinates of electron (1) just picks out specific values for ψ_y and ψ_z, with the result that

$$M_{T_{1gx}\nu}(1) \propto \psi_y(\mathbf{r}_0)\int_{\Omega_T}\psi_z(2)^2 d\tau_2 - \psi_z(\mathbf{r}_0)\int_{\Omega_T}\psi_y(2)\psi_z(2)d\tau_2. \tag{4.20}$$

Additionally, the label (2) can be dropped from the integrals after the other parts have been cancelled, because at this stage the relationship will be related to one electron only. Therefore, the second line of eq. (4.15) then gives exactly the same contribution as the first line.
Then,

$$M_{T_{1gx}\nu} \propto \psi_y(\mathbf{r}_0)\int_{\Omega_T}\psi_y^2 d\tau - \psi_z(\mathbf{r}_0)\int_{\Omega_T}\psi_y\psi_z d\tau. \tag{4.21}$$

Because the single-electron states are normalised $\int_{\Omega_T}\psi_z^2 d\tau \sim 1$, and the integral over $\int_{\Omega_T}\psi_y\psi_z\, d\tau \sim$ zero as the single-electron states are orthogonal; so eq. (4.21) will be proportional to,

$$M_{T_{1gx}\nu} \propto \psi_y(\mathbf{r}_0). \tag{4.22}$$

Similarly, the matrix elements for the other two electron states:

$T_{1gy} \rightarrow$

$$M_{T_{1gy}\nu} \propto \psi_z(\mathbf{r}_0). \tag{4.23}$$

and
$T_{1gz} \rightarrow$

$$M_{T_{1gz}\nu} \propto \psi_x(\mathbf{r}_0). \tag{4.24}$$

Then in order to calculate the total current, we should add up appropriate wavefunction squares over all degenerate states, and according to eq. (4.8) this gives:

$$I \propto \psi_x(\mathbf{r}_0)^2 + \psi_y(\mathbf{r}_0)^2 + \psi_z(\mathbf{r}_0)^2 \tag{4.25}$$

This implies that we can get the same STM images for C_{60}^{2-} both by applying integrals involving tip states, or without doing integrals, although that does involve some approximations. In the next section, we can use the approximation confidently, in order to make these calculations much easier. Then, we can apply the following rules,

- If initiated with one electron in the tip and one electron in the T_{1uz} single electron state of the sample, and the electron in the tip, then tunnelling into the $T_{1ux} \rightarrow$ single electron state of the sample, the current contribution is proportional to $\psi_x(\mathbf{r}_0)^2$.

- The same result is given if the electron in the T_{1uz} single-electron state of the sample has been neglected; then an electron in the tip tunnelling into the T_{1uy} single-electron state of the sample would remain, and the current contribution would be proportional to $\psi_y(\mathbf{r}_0)^2$.

These two rules can be applied if the electron exists in other possibilities, T_{1ux}, and T_{1uy}. For example:

- Sample electron in T_{1ux} + Tip electron tunnelling into $T_{1uy} \rightarrow$ the current contribution is $\propto \psi_y(\mathbf{r}_0)^2$.

- Sample electron in T_{1ux} + Tip electron tunnelling into $T_{1uz} \rightarrow$ the current contribution is $\propto \psi_z(\mathbf{r}_0)^2$.

- Sample electron in T_{1uy} + Tip electron tunnelling into $T_{1uz} \rightarrow$ the current contribution is $\propto \psi_z(\mathbf{r}_0)^2$.

- Sample electron in T_{1uy} + Tip electron tunnelling into $T_{1ux} \rightarrow$ the current contribution is $\propto \psi_x(\mathbf{r}_0)^2$.

However, in the special case of one electron in T_{1uz} throughout; Another electron tunnelling into $T_{1uz} \rightarrow$ etc, has no contributions here as that relates to a final sample state with a different energy.

It might be necessary to consider combinations, where the electron that is not tunnelling changes its state, e.g. initial state has one electron in T_{1ux} state of sample and one in the tip; final state has one electron in T_{1uy} and one in T_{1uz}. These contributions equal zero when the approximation is applied of as they are essentially higher-order contributions, which could change a state, while the two states only altered in the movement of an electron from tip to sample [74].

4.3.2 Tunnelling into the A_{1g} two-electron state

Now, W_μ is the two-electron state A_{1g}, so the basis state from eq. (4.1) show that:

$$A_{1g} = -1/\sqrt{3}(\psi_x(1)\psi_x(2) + a_y\psi_y(1)\psi_y(2) + a_z\psi_z(1)\psi_z(2)) \tag{4.26}$$

After following the same theory as for T_{1g}, and applying the approximation, it is obvious that the terms in κ^2 will still cancel and all that will be left are the contributions from the δ-functions.

For the case where one electron remains in a T_{1ux} single - electron state of the sample, throughout and the other electron tunnels into a T_{1ux} state,

$$\begin{aligned} M_{A_{1gx}\nu}(1) \propto \psi_x(\mathbf{r}_0)\int_{\Omega_T}\psi_x(2)^2 d\tau_2 + \psi_y(\mathbf{r}_0)\int_{\Omega_T}\psi_y(2)\psi_x(2)d\tau_2 \\ +\psi_z(\mathbf{r}_0)\int_{\Omega_T}\psi_z(2)\psi_x(2)d\tau_2 \end{aligned} \tag{4.27}$$

Again, the label (2) can be dropped from the integrals. The second line of eq. (4.15) then gives exactly the same contribution as the first line. Therefore,

$$\begin{aligned} M_{A_{1gx}\nu} &\propto \psi_x(\mathbf{r}_0)\int_{\Omega_T}\psi_x^2 d\tau + \psi_y(\mathbf{r}_0)\int_{\Omega_T}\psi_y\psi_x d\tau \\ &+ \psi_z(\mathbf{r}_0)\int_{\Omega_T}\psi_z\psi_x d\tau \end{aligned} \tag{4.28}$$

which is;

$$M_{A_{1gx}\nu} \propto -1/\sqrt{3}\psi_x(\mathbf{r}_0) \tag{4.29}$$

Similarly, if the other electron tunnels into the T_{1uy} then
$A_{1gy} \rightarrow$

$$M_{A_{1gy}\nu} \propto -1/\sqrt{3}\psi_y(\mathbf{r}_0). \tag{4.30}$$

and, in case of the other electron tunnels into T_{1uz} gives:

$A_{1gz} \rightarrow$

$$M_{A_{1gz}\nu} \propto -1/\sqrt{3}\psi_z(\mathbf{r}_0) \tag{4.31}$$

Finally, the total current for these cases is

$$I \propto (-1/\sqrt{3})^2(\psi_x(\mathbf{r}_0)^2 + \psi_y(\mathbf{r}_0)^2 + \psi_z(\mathbf{r}_0)^2) \tag{4.32}$$

Which is in short, the current proportional to

$$I \propto \psi_x(\mathbf{r}_0)^2 + \psi_y(\mathbf{r}_0)^2 + \psi_z(\mathbf{r}_0)^2 \tag{4.33}$$

4.3.3 Tunnelling into H_g two-electron states

The final result for the H_g states will be the sum over all degenerate states. Similar to the T_{1g} and A_{1g} states.
The A_{1g} state and the $H_{g\theta}$ and $H_{g\epsilon}$ states are all of the same form so,

- The contributions from $H_{g\theta}$ are $\frac{\phi^{-2}}{4}\psi_x^2 + \frac{\phi^2}{4}\psi_y^2 + \frac{1}{4}\psi_z^2$.
- The contributions from $H_{g\epsilon}$ are $\frac{\phi^4}{12}\psi_x^2 + \frac{\phi^{-4}}{12}\psi_y^2 + \frac{5}{12}\psi_z^2$.

However, the H_{g4}, H_{g5} and H_{g6} states will have the same pattern as for the T_{1g} states. By using the approximation, the results will be the same, although the change of the sign from minus to a plus makes no difference.

- The contributions from H_{g4} are $\frac{1}{2}\psi_y^2 + \frac{1}{2}\psi_z^2$.
- The contributions from H_{g5} are $\frac{1}{2}\psi_z^2 + \frac{1}{2}\psi_x^2$.
- The contributions from H_{g6} are $\frac{1}{2}\psi_x^2 + \frac{1}{2}\psi_y^2$.

After adding up all components up, the coefficients of ψ_x^2, ψ_y^2 and ψ_z^2 are all the same $= 5/3$.

4.3.4 Total current of non degenerate wavefunction

The total wavefunction of doubly-charged ion C_{60}^{2-} is a linear combination of the 6 components of the LUMO, which have been given in an earlier section. These six components are:

$$W_L = aA_{1g} + a_\theta H_{g\theta} + a_\epsilon H_{g\epsilon} + a_4 H_{g4} + a_5 H_{g5} + a_6 H_{g6} \tag{4.34}$$

where, W_L is the wavefunction of the C_{60}^{2-} LUMO state and, a, a_θ, a_ϵ, a_4, a_5, a_6 are the coefficients of the linear combination (the eigenvectors of the Hamiltonian of the doubly-charged C_{60}^{2-} ion).
By substituting W_L in to eq. (4.15) and by using the final basis states form of

$(A_{1g} + H_g)$ from eq. (4.1), and after following what has been done in the earlier section 4.3.1, the matrix element of C_{60}^{2-} will be calculated with respect to $(T_{1ux}$, T_{1uy}, $T_{1uz})$ as follows,

$$\begin{aligned}
M_{L\nu 2} \propto & \int_{\Omega_T} \psi_z(2)[a(\frac{1}{\sqrt{3}}[\psi_x(1)\psi_x(2) + \psi_y(1)\psi_y(2) + \psi_z(1)\psi_z(2)])]d\tau_2 \\
& + \int_{\Omega_T} \psi_z(2)[a_\theta(\frac{\phi^{-1}}{2}\psi_x(1)\psi_x(2) - \frac{\phi}{2}\psi_y(1)\psi_y(2) + \frac{1}{2}\psi_z(1)\psi_z(2))]d\tau_2 \\
& + \int_{\Omega_T} \psi_z(2)[a_\epsilon(\frac{\phi^2}{2\sqrt{3}}\psi_x(1)\psi_x(2) - \frac{\phi^{-2}}{2\sqrt{3}}\psi_y(1)\psi_y(2) - \frac{\sqrt{5}}{2\sqrt{3}}\psi_z(1)\psi_z(2))]d\tau_2 \\
& + \int_{\Omega_T} \psi_z(2)[a_4(\frac{1}{\sqrt{2}}[\psi_y(1)\psi_z(2) + \psi_z(1)\psi_y(2)])]d\tau_2 \\
& + \int_{\Omega_T} \psi_z(2)[a_5(\frac{1}{\sqrt{2}}[\psi_x(1)\psi_z(2) + \psi_z(1)\psi_x(2)])]d\tau_2 \\
& + \int_{\Omega_T} \psi_z(2)|[a_6(\frac{1}{\sqrt{2}}[\psi_x(1)\psi_y(2) + \psi_y(1)\psi_x(2)]))]d\tau_2
\end{aligned} \tag{4.35}$$

First, with respect to $\psi_z(2)$, where $\psi_z(2)$ is the contribution of the wavefunction from the z component with respect to the second electron. In this case, the matrix element will be:

$$M_{L\nu 2} \propto \frac{a}{\sqrt{3}}\psi_z + \frac{a_\theta}{2}\psi_z - (\frac{\sqrt{5}}{2\sqrt{3}})a_\epsilon\psi_z + \frac{a_4}{\sqrt{2}}\psi_y + \frac{a_5}{\sqrt{2}}\psi_x \tag{4.36}$$

Applying the same method above with respect to $\psi_z(1)$, again $\psi_z(1)$ is the contribution of the wavefunction from the z component with respect to the first electron. Then, the matrix element for the first electron will be:

$$\begin{aligned}M_{L\nu 1} \propto \int_{\Omega_T} &\psi_z(1)[a(\frac{1}{\sqrt{3}}[\psi_x(1)\psi_x(2)+\psi_y(1)\psi_y(2)+\psi_z(1)\psi_z(2)])]d\tau_1\\ +\int_{\Omega_T} &\psi_z(1)[a_\theta(\frac{\phi^{-1}}{2}\psi_x(1)\psi_x(2)-\frac{\phi}{2}\psi_y(1)\psi_y(2)+\frac{1}{2}\psi_z(1)\psi_z(2))]d\tau_1\\ +\int_{\Omega_T} &\psi_z(1)[a_\epsilon(\frac{\phi^2}{2\sqrt{3}}\psi_x(1)\psi_x(2)-\frac{\phi^{-2}}{2\sqrt{3}}\psi_y(1)\psi_y(2)-\frac{\sqrt{5}}{2\sqrt{3}}\psi_z(1)\psi_z(2))]d\tau_1\\ +\int_{\Omega_T} &\psi_z(1)[a_4(\frac{1}{\sqrt{2}}[\psi_y(1)\psi_z(2)+\psi_z(1)\psi_y(2)])]d\tau_1\\ +\int_{\Omega_T} &\psi_z(1)[a_5(\frac{1}{\sqrt{2}}[\psi_x(1)\psi_z(2)+\psi_z(1)\psi_x(2)])]d\tau_1\\ +\int_{\Omega_T} &\psi_z(1)[a_6(\frac{1}{\sqrt{2}}[\psi_x(1)\psi_y(2)+\psi_y(1)\psi_x(2)]))]d\tau_1\end{aligned} \tag{4.37}$$

$$M_{L\nu 1} \propto \frac{a}{\sqrt{3}}\psi_z + \frac{a_\theta}{2}\psi_z - (\frac{\sqrt{5}}{2\sqrt{3}})a_\epsilon\psi_z + \frac{a_4}{\sqrt{2}}\psi_y + \frac{a_5}{\sqrt{2}}\psi_x \tag{4.38}$$

This implies that the current with respect to z component of the two electrons will be:

$$I \propto 2(\frac{a}{\sqrt{3}}\psi_z + \frac{a_\theta}{2}\psi_z - (\frac{\sqrt{5}}{2\sqrt{3}})a_\epsilon\psi_z + \frac{a_4}{\sqrt{2}}\psi_y + \frac{a_5}{\sqrt{2}}\psi_x)^2 \tag{4.39}$$

By applying the same method, with respect to x the above, the result will take the form:

$$\begin{aligned}M_{L\nu 2} \propto \int_{\Omega_T} &\psi_x(2)[a(\frac{1}{\sqrt{3}}[\psi_x(1)\psi_x(2)+\psi_y(1)\psi_y(2)+\psi_z(1)\psi_z(2)])]d\tau_2\\ +\int_{\Omega_T} &\psi_x(2)[a_\theta(\frac{\phi^{-1}}{2}\psi_x(1)\psi_x(2)-\frac{\phi}{2}\psi_y(1)\psi_y(2)+\frac{1}{2}\psi_z(1)\psi_z(2))]d\tau_2\\ +\int_{\Omega_T} &\psi_x(2)[a_\epsilon(\frac{\phi^2}{2\sqrt{3}}\psi_x(1)\psi_x(2)-\frac{\phi^{-2}}{2\sqrt{3}}\psi_y(1)\psi_y(2)-\frac{\sqrt{5}}{2\sqrt{3}}\psi_z(1)\psi_z(2))]d\tau_2\\ +\int_{\Omega_T} &\psi_x(2)[a_4(\frac{1}{\sqrt{2}}[\psi_y(1)\psi_z(2)+\psi_z(1)\psi_y(2)])]d\tau_2\\ +\int_{\Omega_T} &\psi_x(2)[a_5(\frac{1}{\sqrt{2}}[\psi_x(1)\psi_z(2)+\psi_z(1)\psi_x(2)])]d\tau_2\\ +\int_{\Omega_T} &\psi_x(2)[a_6(\frac{1}{\sqrt{2}}[\psi_x(1)\psi_y(2)+\psi_y(1)\psi_x(2)]))]d\tau_2\end{aligned} \tag{4.40}$$

First, with respect to $\psi_x(2)$, where $\psi_x(2)$ is the contribution of the wavefunction from the x component with respect to the second electron. In this case the matrix element will be:

$$M_{L\nu 2} \propto \frac{a}{\sqrt{3}}\psi_x + \frac{a_\theta}{2}\phi^{-1}\psi_x + \frac{\phi^2}{2\sqrt{3}}a_\epsilon\psi_x + \frac{a_5}{\sqrt{2}}\psi_z + \frac{a_6}{\sqrt{2}}\psi_y \tag{4.41}$$

Applying the same method above with respect to $\psi_x(1)$, and again $\psi_x(1)$ is the contribution of the wavefunction from the x component with respect to the first electron. Then, the matrix element will be:

$$\begin{aligned} M_{L\nu 1} \propto & \int_{\Omega_T} \psi_x(1)[a(\frac{1}{\sqrt{3}}[\psi_x(1)\psi_x(2) + \psi_y(1) + \psi_z(1)\psi_z(2)])]d\tau_1 \\ & + \int_{\Omega_T} \psi_x(1)[a_\theta(\frac{\phi^{-1}}{2}\psi_x(1)\psi_x(2) - \frac{\phi}{2}\psi_y(1)\psi_y(2) + \frac{1}{2}\psi_z(1)\psi_z(2))]d\tau_1 \\ & + \int_{\Omega_T} \psi_x(1)[a_\epsilon(\frac{\phi^2}{2\sqrt{3}}\psi_x(1)\psi_x(2) - \frac{\phi^{-2}}{2\sqrt{3}}\psi_y(1)\psi_y(2) - \frac{\sqrt{5}}{2\sqrt{3}}\psi_z(1)\psi_z(2))]d\tau_1 \\ & + \int_{\Omega_T} \psi_x(1)[a_4(\frac{1}{\sqrt{2}}[\psi_y(1)\psi_z(2) + \psi_z(1)\psi_y(2)])]d\tau_1 \\ & + \int_{\Omega_T} \psi_x(1)[a_5(\frac{1}{\sqrt{2}}[\psi_x(1)\psi_z(2) + \psi_z(1)\psi_x(2)])]d\tau_1 \\ & + \int_{\Omega_T} \psi_x(1)[a_6(\frac{1}{\sqrt{2}}[\psi_x(1)\psi_y(2) + \psi_y(1)\psi_x(2)]))]d\tau_1 \end{aligned} \tag{4.42}$$

$$M_{L\nu 1} \propto \frac{a}{\sqrt{3}}\psi_x + \frac{a_\theta}{2}\phi^{-1}\psi_x + \frac{\phi^2}{2\sqrt{3}}a_\epsilon\psi_x + \frac{a_5}{\sqrt{2}}\psi_z + \frac{a_6}{\sqrt{2}}\psi_y \tag{4.43}$$

Finally, this integration with respect to y component of the wavefunction for the same two electron system will be:

$$
\begin{aligned}
M_{L\nu 2} \propto \int_{\Omega_T} & \psi_y(2)[a(\frac{1}{\sqrt{3}}[\psi_x(1)\psi_x(2)+\psi_y(1)\psi_y(2)+\psi_z(1)\psi_z(2)])]d\tau_2 \\
+\int_{\Omega_T} & \psi_y(2)[a_\theta(\frac{\phi^{-1}}{2}\psi_x(1)\psi_x(2)-\frac{\phi}{2}\psi_y(1)\psi_y(2)+\frac{1}{2}\psi_z(1)\psi_z(2))]d\tau_2 \\
+\int_{\Omega_T} & \psi_y(2)|[a_\epsilon(\frac{\phi^2}{2\sqrt{3}}\psi_x(1)\psi_x(2)-\frac{\phi^{-2}}{2\sqrt{3}}\psi_y(1)\psi_y(2)-\frac{\sqrt{5}}{2\sqrt{3}}\psi_z(1)\psi_z(2))]d\tau_2 \\
+\int_{\Omega_T} & \psi_y(2)[a_4(\frac{1}{\sqrt{2}}[\psi_y(1)\psi_z(2)+\psi_z(1)\psi_y(2)])]d\tau_2 \\
+\int_{\Omega_T} & \psi_y(2)[a_5(\frac{1}{\sqrt{2}}[\psi_x(1)\psi_z(2)+\psi_z(1)\psi_x(2)])]d\tau_2 \\
+\int_{\Omega_T} & \psi_y(2)[a_6(\frac{1}{\sqrt{2}}[\psi_x(1)\psi_y(2)+\psi_y(1)\psi_x(2)]))]d\tau_2
\end{aligned}
$$

First, with respect to $\psi_y(2)$, where $\psi_y(2)$ is the contribution of the wavefunction from the y component with respect to the second electron. In this case the matrix element will be:

$$
M_{L\nu 2} \propto \frac{a}{\sqrt{3}}\psi_y - \frac{a_\theta}{2}\phi\psi_y - \frac{\phi^{-2}}{2\sqrt{3}}a_\epsilon\psi_y + \frac{a_4}{\sqrt{2}}\psi_z + \frac{a_6}{\sqrt{2}}\psi_x \tag{4.44}
$$

Applying the same method above with respect to $\psi_y(1)$, again $\psi_y(1)$ is the contribution of the wavefunction from the y component with respect to the first electron. Then, the matrix element will be:

$$
\begin{aligned}
M_{L\nu 1} \propto \int_{\Omega_T} & \psi_y(1)[a(\frac{1}{\sqrt{3}}[\psi_x(1)\psi_x(2)+\psi_y(1)\psi_y(2)+\psi_z(1)\psi_z(2)])]d\tau_1 \\
+\int_{\Omega_T} & \psi_y(1)[a_\theta(\frac{\phi^{-1}}{2}\psi_x(1)\psi_x(2)-\frac{\phi}{2}\psi_y(1)\psi_y(2)+\frac{1}{2}\psi_z(1)\psi_y(2))]d\tau_1 \\
+\int_{\Omega_T} & \psi_y(1)[a_\epsilon(\frac{\phi^2}{2\sqrt{3}}\psi_x(1)\psi_x(2)-\frac{\phi^{-2}}{2\sqrt{3}}\psi_y(1)\psi_y(2)-\frac{\sqrt{5}}{2\sqrt{3}}\psi_z(1)\psi_z(2))]d\tau_1 \\
+\int_{\Omega_T} & \psi_y(1)[a_4(\frac{1}{\sqrt{2}}[\psi_y(1)\psi_z(2)+\psi_z(1)\psi_y(2)])]d\tau_1 \\
+\int_{\Omega_T} & \psi_y(1)[a_5(\frac{1}{\sqrt{2}}[\psi_x(1)\psi_z(2)+\psi_z(1)\psi_x(2)])]d\tau_1 \\
+\int_{\Omega_T} & \psi_y(1)[a_6(\frac{1}{\sqrt{2}}[\psi_x(1)\psi_y(2)+\psi_y(1)\psi_x(2)]))]d\tau_1
\end{aligned}
\tag{4.45}
$$

$$M_{L\nu 1} \propto \frac{a}{\sqrt{3}}\psi_y - \frac{a_\theta}{2}\phi\psi_y - \frac{\phi^{-2}}{2\sqrt{3}}a_\epsilon\psi_y + \frac{a_4}{\sqrt{2}}\psi_z + \frac{a_6}{\sqrt{2}}\psi_x \tag{4.46}$$

This form of the non-degenerate wavefunction will be used later to simulate the STM images for C_{60}^{2-} in later sections.

4.4 The direct integration

As known, the standard Tersoff-Hamann method in ref.[66] shows that the tunnelling current in an STM in s-type tip is given by $I \propto \psi_x^2$. This result according to Bardeen's theory of tunnelling in ref.[77]. However, in case of multielectron states, the theory can be extended in order to obtain the tunnelling current as proportional to the probability of finding one of the electrons in given space whatever the positions of the other electrons (direct integration).

The direct integration method is an alternative approach to be applied in order to calculate the STM current for multi-electron states as simply as has been done in the single electron state case. In this method, the distribution of one electron around the ion depends on the other electron position. Therefore, it is possible to apply the integration over all coordinates for one electron to obtain the current in terms of single electron function.

Then the current can be obtained by integrating over all coordinates of all electrons except one. In this case, different rules for each electron will be applied. Using knowledge that the orbital and spin wavefunctions are normalised and orthogonal. The results of applying the orthonormality conditions which ensures that the integrals of the products of states tend to zero or one, can be written in terms of spin rules as:

$$\begin{aligned} S_a^t &= S_1^+ S_2^+ \to 1, \\ S_b^t &= S_1^- S_2^- \to 1, \\ S^s &= S_1^+ S_2^- \to 0 \end{aligned} \tag{4.47}$$

and orbital rules as,

$$Orb^{(i)} = \left\{x_i^2 \to 1, y_i^2 \to 1, z_i^2 \to 1, x_i y_i \to 0, x_i z_i \to 0, y_i z_i \to 0\right\} \tag{4.48}$$

where, $x_i^2 = \int \psi_x^2(i) d\tau$, i= 1 to 4 and s and t refer to the singlet and triplet cases respectively. The subscripts a,b refer to the different spin states of the triplets. For more details, to avoid confusion, similar to what has been done in section

4.3.4, square the total wavefunction in eq. (4.34) of the doubly-charged ion C_{60}^{2-}, which has the 6 components of the LUMO. Then integrate over all coordinates of electrons, except electron one (1) with respect to (ψ_x,ψ_y,ψ_z) after applying the spin-orbital rules above. Then apply the same method with respect to the second electron (2).

At the end, by assuming that, the initial x, y, and z states are degenerate, the current is the same as that current obtained using Bardeen's method. As expected, the different spin values end up with the same result for the current. An extra justification is the square of the minimum energy eigenstate, which is written in terms of the spin-orbit state will be written in terms of one electron orbital state only. In other words, the current at the end will be proportional to the basis set (ψ_x, ψ_y, ψ_z), and has the form (a_{2x} $\psi_x\psi_x$, a_{2y} $\psi_y\psi_y$,a_{2z} $\psi_z\psi_z$), where a_{2x}, a_{2y}, and a_{2z} are some functions of the parameters. This means that the current in the higher charged molecules can be written as a linear combination of single electron state with no cross terms. Furthermore, these types of notations x^2=$\psi_x\psi_x$, y^2=$\psi_y\psi_y$, z^2=$\psi_z\psi_z$ will be used to express the current in terms of single electron state basis.

By using Fowler and Ceulemans Tables in ref.[72], the multi-electron states can be generated from a single-electron subscript T_{1u} states with the right transformation properties. However, the result does not have the required properties of being antisymmetric under exchange of two electrons. Such as the orbital states A_{1g} and H_g are symmetric, while T_{1u} state is antisymmetric. At the end, the final state (spin+orbit) should be antisymmetric. Hence, different permutations of the electron labels of linear combinations of the non-symmetric results should be considered.

As discussed above, from group theory, $T_{1u} \otimes T_{1u}$ is a combination between A_{1g}, H_g, and T_{1u}. Then, A_{1g} and H_g will still have singlets spin (S = 0), and the triplet spin (S = 1) for T_{1u}. More specifically, because the states can be formulated as a direct multiplication between spin and orbital parts, therefore, the singlet and the triplet spin states will be taken into account. The advantage of the direct integration method is to display the current simply into single electron basis to allow more investigations in higher charged systems.

4.5 Theoretical technique of modelling the surface interaction

This section will focus on studying the effects of the substrate surface on the position of the atoms of the C_{60}^{2-} cage nearest to the surface independently of the surface structure. In fact, the icosahedral symmetry of an isolated ion will reduce due this interaction, also different interactions will arise from different

substrates. This is far from a trivial extension as it is necessary to include interactions between the two electrons, interactions between the molecule and the surface substrate and JT interactions between the electrons and vibrations of the C_{60} cage. It is necessary to write a Hamiltonian describing the interaction with the surface, as no suitable form has been formulated previously. This Hamiltonian will be combined with the JT Hamiltonian in order to determine the LAPES positions, which is affected by this external interaction. As there is a reduction in symmetry, the rotation and reflection symmetry operations will reduce associated with the parallel axis to the surface. Then the only symmetry operations, which remain, are associated with C_{5v}, C_{3v}, or C_{2v} point groups when adsorbed with a pentagon, hexagon or double bond facing the surface, as with C_{60}^{-}.
Currently, this study will concentrate on modelling the surface interaction in C_{60}^{2-} ion, including the three orientations in detail. The modelling will focus on how the underlying surface can reduce the degeneracies in the molecular orbitals of the system. The calculation is a bit tricky, because the surface interaction is more readily written in ref. [28], using a basis with the z-axis normal to the surface, whereas the JT Hamiltonian, which is used is written down in terms of a C_2 z-axis. These are only the same for the double bond prone orientation. However, it should not be the same basis for the other orientations. Also the definitions of the *d*-orbital basis are the same as Ceulemans and Fowler's basis, which have been used previously in References [72],[16]. In light of this, a transformation to the surface interaction Hamiltonian in order to write it in the Ceulemans and Fowler basis will be needed. This is easier than applying a transformation into the JT Hamiltonian to be in the *d*-orbital basis, as this Hamiltonian is the most complicated. Indeed, it should give the same result, whichever approach is used. The surface interaction cannot be ignored, as the observed STM images are affected by such interactions. Therefore, the effect of different orientations will be considered. In order to determine how the molecular orbital will split, character tables are needed. However, before that, the coordinate system needs to be defined to specify the surface interaction, which is different to that usually used for a JT interaction. In order to be consistent with what has been used in ref. [25], as in fig. 2.8, in this work, the z-axis has been defined to be normal to the surface, through the double bond of the C_{60}^{2-} molecule, while the y-axis will be through the centre between two hexagons of the double bond, i.e the z-axis will be considered as the normal to the surface through the orientation axis. However, the y-axis remains static for different values of the rotation angles ϕ as;

$$T_{1uY} = T_{1uy} \tag{4.49}$$

So, by rotating the sample in the x-z plane through the y-axis, the highest symmetry orientations C_2,C_3,C_5 will be produced. In this way, the basis states for the LUMO of C_{60}^{2-} will be (T_{1gx}, T_{1gy}, T_{1gz}, A_{1g}, $H_{g\theta}$, $H_{g\epsilon}$, H_{g4}, H_{g5}, H_{g6}). The T_{1g} orbitals will transform as *p*-orbitals range along (x, y, z), and A_{1g} will transform as a s-orbital. Finally, H_g orbitals will transform as the d-orbital with the basis (θ, ϵ, 4, 5, 6). These definitions will be used in the following section for the three different orientations above. The surface interaction is modelled by assuming its effect as perturbing the positions of the atoms of the C_{60}^{2-} molecule nearest to the surface in which it is independent of the structure of the surface. This is different to how it has been described in ref.[25], as each C_{60} molecule sits on the surface. Thus, it is very necessary to define the remaining symmetry operations of I_h for the various orientations of the C_{60}^{2-} ion by using group theory, to work out the symmetry reductions in an easier and accurate way.

The new treatment for the surface in the next section is different to that done in ref. [25]. They considered possible point group symmetries for the surface with the symmetry C_{6v}, which is not a subgroup of I_h. Therefore, they have assumed that the molecular orbitals of C_{60} would be subject to a reduction to C_{6v} symmetry, with the symmetry axes defined to be those appropriate to the surface. This implies that it would not be possible to work out splittings of degenerate states by calculating reduction of the characters. On the other hand, they have looked for states having the same characters (the same transformation properties) for each of the allowed group operations. However, there are other combinations of states, have not been included, where transfer occurs in the same way.

4.6 The forms of the surface interaction Hamiltonian

In the same way, in order to model a molecule on any surface, the side facing that surface is very high important to be considered. Therefore, the following subsections will clarify how the direction, which is parallel to the surface, will be affected. For example, in the case of a surface, the LUMO unoccupied 3-fold states can reduce to singlet or a singlet and a doublet states according to the molecular orientation.

4.6.1 Orbital splittings of different orientations

- Pentagon-prone orientation

Now we concentrate on the LUMO surface interaction of C_{60}^{2-}. The point group C_{5v} contains the symmetry operations that survive when the atoms nearest the surface are perturbed in some kind of symmetry, including the C_5 rotations about the z-axis (normal to the surface), $2C_5$, $2C_5^2$, and the five reflections in planes $5\sigma_v$, parallel to the surface. There are no C_3, C_2, i, S_{10} or S_3 operations. From either the actual MOs or from the basis functions, the transformation of individual components could be shown, which are built from ($T_{1u}\otimes$ T_{1u}) single electron states, given in Table 4.2. As usual, ϕ is the golden mean and θ,ϵ have been defined in the d-orbital basis.

Table 4.2: The transformation of the individual components of the pentagon-prone orientation of C_{60}^{2-}

C_{5v}	E	$2C_5$	$2C_5^2$	$5\sigma_v$	
T_{1gz}	1	1	1	-1	$\rightarrow A_2$
$T_{1gx}+T_{1gy}$	2	ϕ^{-1}	$-\phi$	0	$\rightarrow E_1$
A_g	1	1	1	1	$\rightarrow A_1$
$H_{g\theta}(d-orbital)$	1	1	1	1	$\rightarrow A_1$
$H_{g\epsilon}(d-orbital)+H_{g6}$	2	$-\phi$	ϕ^{-1}	0	$\rightarrow E_2$
$H_{g4}+H_{g5}$	2	ϕ^{-1}	$-\phi$	0	$\rightarrow E_1$

Table 4.3: The transformation of individual components of the hexagon-prone orientation of C_{60}^{2-}

C_{3v}	E	$2C_3$	$3\sigma_v$	
T_{1gz}	1	1	-1	$\rightarrow A_2$
$T_{1gx}+T_{1gy}$	2	-1	0	$\rightarrow E$
A_{1g}	1	1	1	$\rightarrow A_1$
$H_{g\theta}$ (d-orbital)	1	1	1	$\rightarrow A_1$
$H_{g\epsilon}$(d$-orbital$)$+H_{g6}$	2	-1	0	$\rightarrow E$
$H_{g4}+H_{g5}$	2	-1	0	$\rightarrow E$

Because the A_{1g} and H_g at different energies, the Hamiltonian of the surface interaction will have two parameters for pentagon-prone orientation. Also, due to repeated representations, the group theory is not enough alone to derive a form for the surface Hamiltonian. The result above in Table 4.2 can be used to construct a form for a surface Hamiltonian H_S^p describing the surface interaction for a given orbital in cases of pentagon orientation.

- Hexagon-prone orientation

For an isolated C_{60}^{2-}, the interaction with the surface have been used to record imaging to wells adsorbed onto a surface. For this orientation, z-axis is through the centre of a hexagon and y-axis to the centre of the bond between two hexagons (or two triangles on an icosahedron). The group is C_{3v}, and both $2C_3$ and $3\sigma_v$ are the symmetry operations that survive when the atoms nearest the surface are perturbed.

In this case, the transformation of individual components are shown in Table 4.3. The Hamiltonian of the surface interaction will have two parameters for the hexagon-prone orientation. These parameters because A_{1g} and the $H_{g\theta}$ will both transform as A_1, while $(H_{g4}+H_{g5})$ and $(H_{g\epsilon}+H_{g6})$ will transform as E.

Again $A_1 \rightarrow A_2$ for the z–component of T_1. $(H_{g4}+H_{g5})$, and $(H_{g\epsilon}+H_{g6})$ form two dimensions E, which cannot be distinguished on symmetry grounds. The same components pair together as with H_u in ref. [25]. These repeated representations

Table 4.4: the transformation of individual components of the double-prone orientation of C_{60}^{2-}

C_{2v}	E	C_2	$\sigma_v(xz)$	$\sigma_v^{'}(yz)$	
T_{1gz}	1	1	-1	-1	$\rightarrow A_2$
T_{1gx}	1	-1	-1	1	$\rightarrow B_2$
T_{1gy}	1	-1	1	-1	$\rightarrow B_1$
A_{1g}	1	1	1	1	$\rightarrow A_1$
$H_{g\theta}$	1	1	1	1	$\rightarrow A_1$
$H_{g\epsilon}$	1	1	1	1	$\rightarrow A_1$
H_{g4}	1	-1	-1	1	$\rightarrow B_2$
H_{g5}	1	-1	1	-1	$\rightarrow B_1$
H_{g6}	1	1	-1	-1	$\rightarrow A_2$

imply that there are two states that should have different energies. Actually, the resultant splitting of the LUMO is always the same for both pentagon- and hexagon-prone orientations.

- Double bond-prone orientation

In this case, the group is therefore C_{2v}. The symmetry operations that survive when the atoms nearest the surface are perturbed are C_2, $\sigma_v(xz)$, and $\sigma_v^{'}(yz)$. In the case of double-prone orientation, the transformation of individual components will take the form as in Table 4.4.

This double bond case is different than the pentagon- and hexagon-prone cases, as the two dimensions does not support. Currently, calculations have been done, adopting the Hückel approach, which indicate that the difference in energy between B_1 and B_2 is small (compared to the difference in energy to A_1), because no mechanism can distinguish between x and y as in ref. [22]. In general, A_{1g}, $H_{g\theta}$ and $H_{g\epsilon}$ all will transform to the same A_1. In fact, the surface and Coulomb interactions work in a different way. Coulomb interactions make the A and H states into eigenstates. However, the surface interactions makes the combinations (xx,yy,zz) combinations of the single electron (x,y,z) states, into eigenstates.

4.6.2 The general surface Hamiltonian

The z–component of T_{1g} has switched to A_2, compared to A_1 for T_{1u} in ref. [25]. Similarly, $H_{g\theta}$ has switched to A_1, compared to A_2 for $H_{u\theta}$. $H_{g\epsilon}$ and H_{g6} will form two dimensions transformation and H_{g4}, H_{g5} will form the other two dimensions transformation. However, A_{1g} and $H_{g\theta}$ cannot be distinguished by using group theory alone, as they both transform to the same form A_1. So, in this case, they can have different energies due to Coulomb interaction, but the surface can still mix between them. Then, assuming that the effects of the Coulomb and the surface interactions on the states are given by;

$$\begin{aligned} \psi_{1p} &= \cos\alpha A_{1g} + \sin\alpha H_{g\theta} \\ \psi_{2p} &= -\sin\alpha A_{1g} + \cos\alpha H_{g\theta} \end{aligned} \tag{4.50}$$

where the mixing angle α is an unknown parameter. According to the basis above, an appropriate Hamiltonian H_S^p of the pentagon-prone molecule can be constructed as a diagonal matrix H_S^p in the bases $\psi_m =(\psi_{1p}, \psi_{2p}, H_{g\epsilon}, H_{g4}, H_{g5}, H_{g6})$ of the form:

$$H_S^p = \begin{bmatrix} 0 & 0 & 0 & 0 & 0 & 0 \\ 0 & 0 & 0 & 0 & 0 & 0 \\ 0 & 0 & \Delta_1 & 0 & 0 & 0 \\ 0 & 0 & 0 & \Delta_2 & 0 & 0 \\ 0 & 0 & 0 & 0 & \Delta_2 & 0 \\ 0 & 0 & 0 & 0 & 0 & \Delta_1 \end{bmatrix} \tag{4.51}$$

The term splitting will be modelled by considering a diagonal matrix, which divided the A_{1g}, H_g orbitals into two different energy levels of δ'. δ' is the splitting between A_{1g} and H_g, and this matrix takes the form;

$$H_{term} = \begin{bmatrix} \delta' & 0 & 0 & 0 & 0 & 0 \\ 0 & 0 & 0 & 0 & 0 & 0 \\ 0 & 0 & 0 & 0 & 0 & 0 \\ 0 & 0 & 0 & 0 & 0 & 0 \\ 0 & 0 & 0 & 0 & 0 & 0 \\ 0 & 0 & 0 & 0 & 0 & 0 \end{bmatrix} \tag{4.52}$$

But (Δ_1, Δ_2) are constants parameters of the surface determining the strength of the surface interaction, which give the energy of the orbital relative to the zero energy state (i.e Δ_1 is the splitting between $H_{g\epsilon} + H_{g6}$ and $H_{g\theta}$, while Δ_2 is the splitting between $H_{g4} + H_{g5}$ and $H_{g\theta}$). In addition, they can be positive or negative. It also includes the linear JT constant factor $V_1^2/\mu\omega^2$, which implies dimensionless strength of the surface interaction. There are many other possibilities for contrasting this matrix depending on the overall zero in energy, which is not fixed. Actually, the surface interaction will prefer various wells depending on the sign of the strength of the surface interaction Δ_i. This form of the surface of H_S^p is only valid for the considered orientations, such as C_5, C_3 and C_2. However, a modified form of H_S^p, including additional parameters, will be required for more general orientations.

This implies that, the singlet of T_{1g} is z–component and the degenerate states are some linear combinations of $T_{1gx}+T_{1gy}$, $H_{g\epsilon}+H_{g6}$, and $H_{g4}+H_{g5}$. Then it should apply the transformation matrix, which have been contrasted to convert from ψ_p to the d-orbital basis ψ_c, which is $= (A_{1g}, H_{g\theta}, H_{g\epsilon}, H_{g4}, H_{g5}, H_{g6})$

where, ψ_p=S_p ψ_c

then:

$$S_p = \begin{bmatrix} \cos\alpha & \sin\alpha & 0 & 0 & 0 & 0 \\ -\sin\alpha & \cos\alpha & 0 & 0 & 0 & 0 \\ 0 & 0 & 1 & 0 & 0 & 0 \\ 0 & 0 & 0 & 1 & 0 & 0 \\ 0 & 0 & 0 & 0 & 1 & 0 \\ 0 & 0 & 0 & 0 & 0 & 1 \end{bmatrix} \tag{4.53}$$

In fact, this transformation could be defined the other way round as the mixed angle can be negative.

The second transformation needed is a matrix that could be used to convert from the C_5 definitions of the H components to the C_2 with the same definitions of θ and ϵ. Obviously, by using the relations:

$\theta \sim \frac{1}{2}\left(2z^2 - x^2 - y^2\right)$,

$\epsilon \sim \frac{\sqrt{3}}{2}\left(x^2 - y^2\right)$

$4 \sim \sqrt{3}yz$

$5 \sim \sqrt{3}zx$

$6 \sim \sqrt{3}xy$

and the matrix U_T to convert from a C_2 to C_5 (by rotating in the x-z plane by an angle $\theta = \tan^{-1}(\phi^{-1})$) is:

$$U_T = \begin{bmatrix} \cos\theta & 0 & -\sin\theta \\ 0 & 1 & 0 \\ \sin\theta & 0 & \cos\theta \end{bmatrix} \tag{4.54}$$

As the basis forms a complete set, some linear combination of the original basis to obtain the new basis will be needed to define the rotation matrix. Each row of the rotation matrix is defined by the solutions where the linear combination is equal to the appropriate component of the new basis, such as $\psi = c_1 H_\theta + c_2 H_\epsilon + c_3 H_4 + c_4 H_5 + c_5 H_6$. To solve it, we can use the appropriate coefficients for each term $(x^2, y^2, z^2, xy, xz, yz)$. For example, the first element in the 5×5 rotation matrix will be calculated as the x^2 components will be equal in the relation $\psi = c_1 H_\theta$.

Then, at the end, we can collect the results to form the final matrix elements. This will give the required Hamiltonian U_H in the C_2 basis used to express the JT Hamiltonian, with two fold z-axis:

$$U_H = \begin{bmatrix} 1 & 0 & 0 & 0 & 0 & 0 \\ 0 & \frac{1}{2}\left(3\cos\theta^2 - 1\right) & \frac{1}{2}\sqrt{3}\sin\theta^2 & 0 & \sqrt{3}\cos\theta\sin\theta & 0 \\ 0 & \frac{1}{2}\sqrt{3}\sin\theta^2 & \frac{1}{2}\left(1 + \cos\theta^2\right) & 0 & -\cos\theta\sin\theta & 0 \\ 0 & 0 & 0 & \cos\theta & 0 & \sin\theta \\ 0 & -\sqrt{3}\cos\theta\sin\theta & \cos\theta\sin\theta & 0 & \cos\theta^2 - \sin\theta^2 & 0 \\ 0 & 0 & 0 & -\sin\theta & 0 & \cos\theta \end{bmatrix} \tag{4.55}$$

However, this is not the end of the road, as the JT Hamiltonian for $p^2 \otimes h$ is written using the Ceulemans and Fowler definitions of θ and ϵ, rather than d-orbital definitions [16]. Therefore, another transformation matrix will be used to convert to the new basis ψ_{CF}, which is equal to $S_{CF}\ \psi_{C2}$ where;

$$S_{CF} = \begin{bmatrix} 1 & 0 & 0 & 0 & 0 & 0 \\ 0 & \frac{\sqrt{3}}{\sqrt{8}} & \frac{\sqrt{5}}{\sqrt{8}} & 0 & 0 & 0 \\ 0 & -\frac{\sqrt{5}}{\sqrt{8}} & \frac{\sqrt{3}}{\sqrt{8}} & 0 & 0 & 0 \\ 0 & 0 & 0 & 1 & 0 & 0 \\ 0 & 0 & 0 & 0 & 1 & 0 \\ 0 & 0 & 0 & 0 & 0 & 1 \end{bmatrix} \tag{4.56}$$

The final expression of the required surface interaction Hamiltonian after adding the three transformations will take the last form:

$$H_P^{C_2} = S_{CF} U_H S_P^T H_S^P S_P U_H^T S_{CF}^T \tag{4.57}$$

which have been evaluated by using mathematica program, which is too long to be represented here.

In case of the hexagon-prone orientation, due to the repetition of transformation, it will be complicated for this orientation to derive a unique Hamiltonian of the surface. Exactly, as has been done for the pentagon-prone orientation, it will be possible to mix the A_{1g} and $H_{g\theta}$ with a different definition of θ. Then, the appropriate Hamiltonian for the surface interaction H_S^h of the hexagon-prone molecule in the ψ_m basis will be:

$$H_S^h = \begin{bmatrix} 0 & 0 & 0 & 0 & 0 & 0 \\ 0 & 0 & 0 & 0 & 0 & 0 \\ 0 & 0 & \Delta_1 & 0 & 0 & 0 \\ 0 & 0 & 0 & \Delta_2 & 0 & 0 \\ 0 & 0 & 0 & 0 & \Delta_2 & 0 \\ 0 & 0 & 0 & 0 & 0 & \Delta_1 \end{bmatrix} \tag{4.58}$$

This Hamiltonian looks similar to the pentagon-prone surface in eq. (4.51), but with different basis. Again, δ' is the splitting between A_{1g} and H_g, Δ_1 is the splitting between $H_{g\epsilon} + H_{g6}$ and $H_{g\theta}$, Δ_2 is the splitting between $(H_{g4} + H_{g5})$ and $H_{g\theta}$. Then, with this H_S^h, the required surface and Coulomb interaction Hamiltonian could obtained in the same way, as the pentagon prone above:

$$H_h^{C_2} = S_{CF} U_H S_h^T H S_h U_H^T S_{CF}^T \tag{4.59}$$

In the double bond case, the appropriate Hamiltonian for the surface interaction H_S^{db} of the double-bond Prone molecule in the basis will be:

$$H_S^{db} = \begin{bmatrix} 0 & 0 & 0 & 0 & 0 & 0 \\ 0 & 0 & 0 & 0 & 0 & 0 \\ 0 & 0 & \Delta_1 & 0 & 0 & 0 \\ 0 & 0 & 0 & \Delta_2 & 0 & 0 \\ 0 & 0 & 0 & 0 & \Delta_3 & 0 \\ 0 & 0 & 0 & 0 & 0 & \Delta_4 \end{bmatrix} \tag{4.60}$$

There are many equivalent forms to H_S^{db} depending on different zeros in energy. This more complicated surface interaction Hamiltonian for double prone orientation has five different parameters, (δ' the splitting between A_{1g} and H_g, and the remaining five Δ_1, Δ_2, Δ_3, Δ_4 between H_g components). These parameters will split the LUMO into six singlets independent of each other. In this case, the approach is unlikely to work out, because the degeneracy and group theory cannot be used alone. However, in this orientation, one transformation will be needed as the same definitions of (x,y,z) and ($H_{g\theta}$, $H_{g\epsilon}$) both transform in the same way. In short, the work in Ceulemans and Fowler basis form the origin. Actually, many unknown parameters [δ',Δ_1,Δ_2,Δ_3,Δ_4] and about three mixed angles make the orientation more complicated. Specifically, the work in this orientation will be taken into account in case of matching our results with Wachowiak *et al* in ref. [18].

The surface interaction Hamiltonian will be included together with the JT Hamiltonian to find positions of minima and electronic states numerically. In addition, the images from the T states in C_{60}^{2-} will look the same as those from the T states in C_{60}^{-} (have been proved in the earlier section by using Bardeen's method). After finding the lowest in energy, the eigenvectors will be used to show STM images of the C_{60}^{2-} molecule in different orientations.

4.6.3 Pentagon and hexagon orientations from $T \otimes h$

Instead of working out the surface interaction in general, it is useful to work it out as simply as possible, starting from the surface interaction of the $T \otimes h$ single electron state. Basically, this idea comes from the fact that the Hamiltonian of the multi-electron systems can be produced from the single electron Hamiltonian. This alternative method can overcome the previous complex form relating to the surface interaction with less unknown parameters. Indeed, this allows more investigations to be conducted for higher charged systems, as the number of parameters is completely dependent on the orientation of the molecule and independent of the charged state.

In order to construct the surface Hamiltonian of $p^2 \otimes h$ two electron states from the $T \otimes h$ one electron case, it can be assumed that H_S is the surface interaction Hamiltonian for the doubly-charged ion $p^2 \otimes h$ in terms of the general Hermitian matrix with respect to the basis (x_i,y_i,z_i) of one electron state, which will take the form below, where a= H_{11}, b= H_{22} and c= H_{33} as;

$$H_S = \begin{bmatrix} a & H_{12} & H_{13} \\ H_{12} & b & H_{23} \\ H_{13} & H_{23} & c \end{bmatrix}$$

For example, by using eq.(4.1), and the rule $(x_i^2 \rightarrow H_{11}, x_i y_i \rightarrow H_{12}, x_i z_i \rightarrow H_{13}, y_i^2 \rightarrow H_{22}, y_j z_i \rightarrow H_{23}, z_i^2 \rightarrow H_{33}, x_j^2 \rightarrow 1, y_j^2 \rightarrow 1, z_j^2 \rightarrow 1, x_j y_j \rightarrow 0, x_j z_j \rightarrow 0, y_j z_j \rightarrow 0)$ to expand the basis in eq.(4.1) to a 6 × 6 matrix, then the matrix element associated with the first electron (1) will be:

$$
\begin{aligned}
\langle A_g(1,2)|H_S^1|H_{g4}(1,2)\rangle &= \langle\frac{-1}{\sqrt{3}}(x_1x_2+y_1y_2+z_1z_2)|H_S^1|\frac{1}{\sqrt{2}}(z_1y_2+y_1z_2)\rangle \\
&= \frac{-1}{\sqrt{6}}[\langle y_1|H_S^1|z_1\rangle+\langle z_1|H_S^1|y_1\rangle] \\
&= -\frac{2}{\sqrt{6}}H_{23}
\end{aligned}
\tag{4.61}
$$

Then, because of the orthogonality of the basis functions for the other electron (2), the other terms will disappear. The total matrix elements after including the other electron will be double the result above in eq.(4.61), which equals $\frac{2}{\sqrt{6}}H_{23}$ as there is a factor of 2 to cover the second electron. Now it is easy to produce the rest of the matrix elements by applying the same method. The total matrix is:

$$
H_S = \begin{bmatrix}
A_1 & A_2 & A_3 & -2\sqrt{\frac{2}{3}}H_{23} & -2\sqrt{\frac{2}{3}}H_{13} & -2\sqrt{\frac{2}{3}}H_{12} \\
A_2 & A_4 & \frac{-a+b}{\sqrt{3}} & \frac{H_{23}}{\sqrt{3}} & \frac{H_{13}}{\sqrt{3}} & -\frac{2H_{12}}{\sqrt{3}} \\
A_3 & \frac{-a+b}{\sqrt{3}} & a+b & -H_{23} & H_{13} & 0 \\
-2\sqrt{\frac{2}{3}}H_{23} & \frac{H_{23}}{\sqrt{3}} & -H_{23} & b+c & H_{12} & H_{13} \\
-2\sqrt{\frac{2}{3}}H_{13} & \frac{H_{13}}{\sqrt{3}} & H_{13} & H_{12} & a+c & H_{23} \\
-2\sqrt{\frac{2}{3}}H_{12} & -\frac{2H_{12}}{\sqrt{3}} & 0 & H_{13} & H_{23} & a+b
\end{bmatrix}
\tag{4.62}
$$

where;

$A_1 = \frac{2}{3}(a+b+c)$
$A_2 = \frac{1}{3}\sqrt{2}(a+b-2c)$
$A_3 = \sqrt{\frac{2}{3}}(-a+b)$
$A_4 = \frac{1}{3}(a+b+4c)$

The definition of Δ_1,Δ_2 in this treatment is the same as has been used in the $T\otimes h$ single electron problem. The surface interaction Hamiltonian for the single electron problem from eq.(3.10), which has one parameter in the pentagon and hexagon orientations as Δ_2=0 and two parameters in the double-bond prone, will be used to construct the surface Hamiltonian for $p^2\otimes h$ from comparing the matrix elements in eq.(4.61) with eq.(3.14) and substituting into eq.(4.62). As a result, most of the matrix elements will be zero.

In addition, the term splitting δ' due to the Coulomb interaction should be taken into account as a main part of this treatment of the surface, so its contribution will be added to the first element of the surface Hamiltonian as;

$$H_S = \begin{bmatrix} \delta' - \frac{2(\Delta_1+\Delta_2)}{3} & \frac{\sqrt{2}(2\Delta_1-\Delta_2)}{3} & \frac{-\sqrt{2}\Delta_2}{\sqrt{3}} & 0 & 0 & 0 \\ \frac{\sqrt{2}(2\Delta_1-\Delta_2)}{3} & -\frac{4\Delta_1+\Delta_2}{3} & -\frac{\Delta_2}{\sqrt{3}} & 0 & 0 & 0 \\ \frac{-\sqrt{2}\Delta_2}{\sqrt{3}} & -\frac{\Delta_2}{\sqrt{3}} & -\Delta_2 & 0 & 0 & 0 \\ 0 & 0 & 0 & -\Delta_1 - \Delta_2 & 0 & 0 \\ 0 & 0 & 0 & 0 & -\Delta_1 & 0 \\ 0 & 0 & 0 & 0 & 0 & -\Delta_2 \end{bmatrix} \tag{4.63}$$

Finally, the specific form of the combined surface interaction, and the term splitting Hamiltonian in case of Δ_2=0 will written as:

$$H_S = \begin{bmatrix} \delta' - \frac{2\Delta_1}{3} & \frac{2\sqrt{2}\Delta_1}{3} & 0 & 0 & 0 & 0 \\ \frac{2\sqrt{2}\Delta_1}{3} & \frac{-4\Delta_1}{3} & 0 & 0 & 0 & 0 \\ 0 & 0 & 0 & 0 & 0 & 0 \\ 0 & 0 & 0 & -\Delta_1 & 0 & 0 \\ 0 & 0 & 0 & 0 & -\Delta_1 & 0 \\ 0 & 0 & 0 & 0 & 0 & 0 \end{bmatrix} \tag{4.64}$$

In fact, both the pentagon-prone and hexagon-prone orientations share the same form of surface Hamiltonian; however, the rotation angle is different to obtain the form with the 2-fold z-axis, which is used in H_{JT}.
The general form (S_g) from the symmetry aspect will have the diagonal elements (Δ_a,Δ'_a,Δ_b,Δ_c,Δ_c,Δ_b), and we will need to replace 0 in the diagonal with Δ'_a due to the overall energy zero will not be the same.

$$S_g = \begin{bmatrix} \Delta_a & 0 & 0 & 0 & 0 & 0 \\ 0 & \Delta'_a & 0 & 0 & 0 & 0 \\ 0 & 0 & \Delta_b & 0 & 0 & 0 \\ 0 & 0 & 0 & \Delta_c & 0 & 0 \\ 0 & 0 & 0 & 0 & \Delta_c & 0 \\ 0 & 0 & 0 & 0 & 0 & \Delta_b \end{bmatrix} \tag{4.65}$$

which correspond to the basis with unknown combinations between A_g and $H_{g\theta}$. This form will generally be written with more parameters, such as $H_S = S_p^T.S_g.S_p$ as given in eq. (4.53), then;

$$H_S = \begin{bmatrix} \Delta_a \cos^2\alpha + \Delta'_a \sin^2\alpha & (\Delta_a - \Delta'_a)\cos\alpha\sin\alpha) & 0 & 0 & 0 & 0 \\ (\Delta_a - \Delta'_a)\cos\alpha\sin\alpha) & \Delta'_a\cos^2\alpha + \Delta_a\sin^2\alpha & 0 & 0 & 0 & 0 \\ 0 & 0 & \Delta_b & 0 & 0 & 0 \\ 0 & 0 & 0 & \Delta_c & 0 & 0 \\ 0 & 0 & 0 & 0 & \Delta_c & 0 \\ 0 & 0 & 0 & 0 & 0 & \Delta_b \end{bmatrix} \tag{4.66}$$

where again α is the mixed angle between A_g and $H_{g\theta}$, and there are a number of possibilities for Δ_a, Δ'_a and α depending on the quadrant we choosen for α.
It is possible to match the general form of the surface matrix with the more specific one by setting Δ_c to be equal to $-\Delta_1$, and Δ_b to be zero.
Then, to convert from the C_5 definitions of the H components to the C_2 ones, and from the d-orbital definitions of θ and ϵ, the Ceulemans and Fowler basis is still needed.
In order to be in the Fowler and Ceulemans basis, it will be necessary to keep the same basis in eq.(4.1) for θ and ϵ as they are different to what is usually used in the d-orbital basis. However, x, y and z will still be the same in both definitions. Therefore, the rotation matrix U_H in eq.(4.55) by using the relations θ and ϵ in eq.(4.56)
And the same matrix to convert from C_2 to C_5 as in eq.(4.54). After using the same method to construct eq.(4.55).
The last form of the required surface interaction Hamiltonian will be;

$$H^{c2} = S_{CF} U_H H_S U_H^T S_{CF}^T \tag{4.67}$$

which is too long to be represented here. Indeed, this surface interaction Hamiltonian will combine with the JT Hamiltonian to determine the position of the wells and the electronic states. Then, the eigenvectors will be required in producing the current to predict the STM images of different orientations, as is shown in the following sections for both C_{60}^{2-} and C_{60}^{4-} molecules. By using this method, it will be easy to solve the Hamiltonian of the system with less unknown parameters, and with no need to consider more mixing angles.

4.6.4 Double bond-prone orientation from $T \otimes h$

As this orientation is with respect to a C_2 z-axis, no rotation transformation will be required.
The surface interaction Hamiltonian will be a more specific form of the general expression in the previous section in eq.(4.66) and will take the form;

$$H_S = \begin{bmatrix} \delta' - \frac{2(\Delta_1+\Delta_2)}{3} & \frac{\sqrt{2}(2\Delta_1-\Delta_2)}{3} & \frac{-\sqrt{2}\Delta_2}{\sqrt{3}} & 0 & 0 & 0 \\ \frac{\sqrt{2}(2\Delta_1-\Delta_2)}{3} & -\frac{4\Delta_1+\Delta_2}{3} & -\frac{\Delta_2}{\sqrt{3}} & 0 & 0 & 0 \\ \frac{-\sqrt{2}\Delta_2}{\sqrt{3}} & -\frac{\Delta_2}{\sqrt{3}} & -\Delta_2 & 0 & 0 & 0 \\ 0 & 0 & 0 & -\Delta_1-\Delta_2 & 0 & 0 \\ 0 & 0 & 0 & 0 & -\Delta_1 & 0 \\ 0 & 0 & 0 & 0 & 0 & -\Delta_2 \end{bmatrix} \tag{4.68}$$

The extra parameters in this orientation is more complicated to be displayed in terms of the currents coefficients, as the relation between the two surface parameters is still unknown. However, we still should be able to move further with the matching process. The Hamiltonian, which will be used in later sections to match these results with the results, which have been published previously in 2005, will take the form;

$$H^{c2} = S_{CF} H_S S_{CF}^T \tag{4.69}$$

4.7 The STM images of C_{60}^{2-} due to surface and JT interactions

The Hamiltonian of the C_{60}^{2-} system in eq. (4.4) will be investigated to find the minima and the energy associated by displacing each of the coordinates (Q_θ, Q_ϵ, Q_4, Q_5, Q_6) by an amount equal to (a_θ, a_ϵ, a_4, a_5, a_6). This can be accomplished by solving the total Hamiltonian of the system using a numerical minimisation program. In fact, the basic meaning of the number of certain minima refers to the distortion symmetry. The Hamiltonian H_{a_i} then, is a function of the parameters (a_θ, a_ϵ, a_4, a_5, a_6), where a_i are dimensionless values. Then, the eigenvectors corresponding to these parameters can be derived using the minimisation program. In addition, the energy in the isolated ion is the same for the wells in any symmetry type.
However, this picture will not remain in case of placing the ion onto a substrate. This additional effect due to the surface will distort the molecule in an equally important way, as JT coupling constants have done. In order to model these two interactions, it is necessary to derive the values of normal modes (Q_θ, Q_ϵ, Q_4, Q_5, Q_6), which minimise the energy of the total Hamiltonian of the system and then determine the associated eigenvectors. Our focus is to carry out these calculations using particular orientations, such as (C_2,C_3,C_5) depending on the form of rotational axis, which is aligned to the surface as mentioned previously. In addition, as the strength of the surface interaction increases relative to the JT interaction, the electronic coordinates will change. As a result, the positions of the minimum will also change accordingly.

Bardeen's method concentrated on how to use this information to work out each contribution caused from the square of the wavefunction ($aA_{1g}+$ $a_\theta H_{g\theta}+$ $a_\epsilon H_{g\epsilon}+$ $a_4 H_{g4}+$ $a_5 H_{g5}+$ $a_6 H_{g6}$) of each well after normalisation (i.e. divided by the number of minimum wells). The results obtained depend on the two JT dimensionless quadratic coupling constants interaction (V_2', and V_3') with the symmetry of the wells after the surface interaction is applied. However, the direct integration method will be the more useful alternative solution as the current will involve contributions from (a_{2x},a_{2y},a_{2z}) or (a_{4x},a_{4y},a_{4z}) in case of C_{60}^{4-} only, where no cross terms remain. Then, the STM images would be estimated and all of these qualitatively provided information will be used to show how these images will appear.

4.7.1 Pentagon-prone orientation

The STM images appearing from the LUMO, consist of a linear combination of A_{1g}, $H_{g\theta}$, $H_{g\epsilon}$, H_{g4}, H_{g5}, H_{g6}. Starting with JT parameters preferring D_{5d} symmetry C_5 orientation for positive surface interactions, there will be one well (C), which will give a global minimum of the energy in the system as along as the z-axis is written in Table 4.5, so the molecule will not pseudorotate. This implies that the magnitude of the surface interaction has no effect on the wavefunction; as an outcome, the STM images are independent of the surface interaction. Figure 4.1 shows the effect of the surface interaction for both positive and negative surface interaction of D_{5d} symmetry, C_5 orientation.

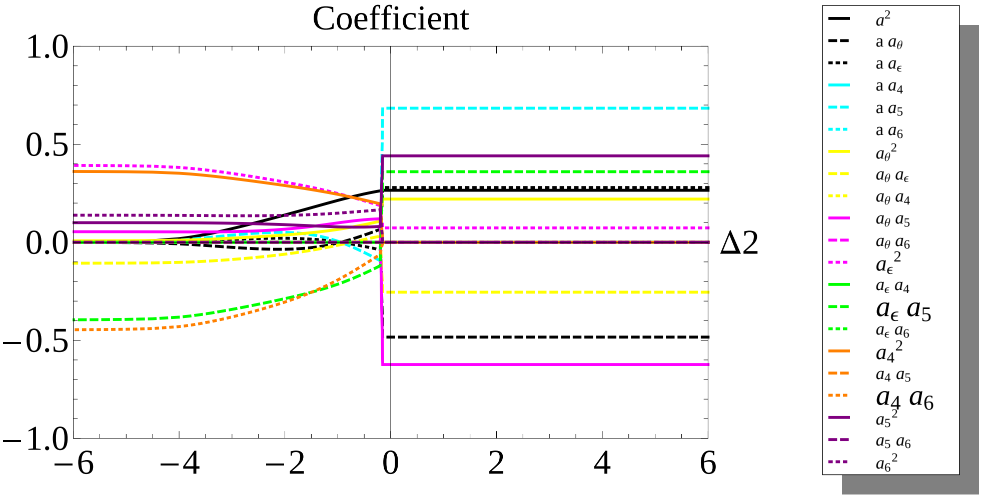

Figure 4.1: The contribution from each coefficient of the wavefunction of C_{60}^{2-} of D_{5d} symmetry, C_5 orientation for different strengths of the surface Δ_2 for δ'=1, Δ_1=0.2, α=π (Bardeen's method)

This diagram, which has been done by applying Bardeen's method, will be used to explain the results calculated for JT distorted C_{60}^{2-} ion hopping between minima with equivalent energies' configuration. Thus, the coefficients in this diagram shows the contribution from each part of the components of the squared wavefunction of C_{60}^{2-} molecule. In other words, the squared wavefunction of this system $(aA_g + a_\theta H_{g\theta} + a_\epsilon H_{g\epsilon} + a_4 H_{g4} + a_5 H_{g5} + a_6 H_{g6})^2$ involves 21 different terms. By extending the squared wavefunction of the system, these terms will take the form, a^2, aa_θ, aa_ϵ, aa_4, aa_5, aa_6, a_θ^2, $a_\theta a_\epsilon$, $a_\theta a_4$, $a_\theta a_5$, $a_\theta a_6$, a_ϵ^2, $a_\epsilon a_4$, $a_\epsilon a_5$, $a_\epsilon a_6$, a_4^2, $a_4 a_5$, $a_4 a_6$, a_5^2, $a_5 a_6$, a_6^2. For example, in fig. 4.1, the terms labelled in large font a_ϵ^2, $a_\epsilon a_5$, a_4^2, $a_4 a_6$ have the highest contribution to the wavefunction in the negative surface interaction. These small gaps between the surviving components a_ϵ^2, a_4^2 and $a_\epsilon a_5$, $a_4 a_6$ in the negative strength of fig. 4.1 could be due to numerical calculation from the Mathematica program, which has been used. In addition, the cross terms, which appeared in this diagram indicate that the negative coefficient terms of the multiplied coefficients of the square wavefunction of C_{60}^{2-} molecule, subtracting from the positive coefficient terms contributions, which make the sum of overall coefficients of the squared wavefunction add up to 1 after normalisation. These coefficients at the end, will show which parts of the squared wavefunction will be involved in the STM images of the system for different strengths of surfaces because of the large number of terms involved. Indeed, the method above is actually not very useful in giving enough prediction of the behaviour of the molecule after adding the interaction of the surface. However, the direct integration approach overcomes this problem, and provides qualified diagrams representing all symmetry cases with successful cancellation of any cross term. Then Figures (4.2, 4.3) show the contributions of the three coefficients (a_{2x},a_{2y},a_{2z}) of LUMO components (ψ_x^2,ψ_y^2,ψ_z^2) for different values of the surface Δ_1 and term splitting δ, in terms of single electron states. A comparison between C_{60}^{-} and C_{60}^{2-} molecules on a surface will be considered in case of δ'=0 as there is no parameter in the single electron system equivalent to δ' in the other higher charged JT molecules C_{60}^{2-}. It was found that the systems show a similar behaviour to fig. 4.3(a)(b) and the other following symmetry operations of different orientations. Different wells positions have been found around Δ_1= -0.16 due to different minima energy in fig. 4.3 which is not an artifact. These energies are very close to each other.

The majority of the results in this work represent the case V_2'=0.1, and V_3'=0 for D_{5d} symmetry, and these will be swapped for the D_{3d} case.

The different negative values of the term splitting δ' between A_g and H_g, as shown in fig.4.3, have no significant effect on the contribution of each coefficient of the wavefunction of C_{60}^{2-}. However, Figures (4.7,4.8) show the opposite picture, when altering the values of the term splitting with positive amounts. This distinct exchange between these coefficients due to the JT effect in H_g state, which is not in A_g in the diagonal matrix. Therefore, lowering or raising the energy between them can make them different. Some estimates done in the literature show that the value of the splitting term δ' is approximately equal to 1 [78]. Some results will be provided by taking this value into consideration.

It was not possible to plot the positions of the wells on the sphere in the case of the C_{60}^{2-} molecule, as has been done in the three dimension $T \otimes h$ problem in ref.[22] (as in fig.3.2), which shows the positions of the wells for the pentagon-prone orientation, parameters preferring D_{5d} symmetry and D_{3d} symmetry and the wavefunction coefficients of C_{60}^{-} molecule, because of the extra dimensions.

Although, Reference [16] showed that the five components of H_g orbital ($H_{g\theta}$, $H_{g\epsilon}$, H_{g4}, H_{g5}, H_{g6}) are in the same form as the $Q's$ for $T \otimes h$ in ref. [23], corresponding to ref. [14]. These components can be formulated in terms of two angles satisfying their equation (3.3). After applying this method, we found that it was not possible to show these wells on the surface of a sphere as shown in fig. 3.2 by using two different ways, either the vibronic or electronic state in eq.(E.2) in ref. [14].

This is because the six components eigenvectors (a,a_θ,a_ϵ,a_4,a_5,a_6) of the six orbital states of the LUMO of the C_{60}^{2-} molecule will make the solution for the Hamiltonian of the system more complicated. As a result, the wells will not lie on the surface of a sphere after adding surface interaction.

STM images for D_{5d} pentagon prone for C_{60}^{2-} molecule, as shown in fig. 4.4. One well (C) only gives the global minimum. However, five wells with equal global minima energy (A,B,D,E,F) in Table 4.5, will appear for the negative surface interaction of the C_{60}^{2-} molecule.

Table 4.5: The minimum wells of the D_{5d} and D_{3d} symmetry of the C_{60}^{2-} molecule in case surface interaction is applied; here C_5, and C_3 is perpendicular to the surface

Ori	D_{5d}		D_{3d}	
	Positive Δ_1	Negative Δ_1	Positive Δ_1	Negative Δ_1
C_5	C	A, B, D, E, F	a, b, c, g, i	d, e, f, h, j
C_3	C, E, F	A, B, D	c	a, b, e, f, h, j

This result was expected as all the five wells were distributed in an equivalent manner with respect to the z-axis. The figures between the coefficient for the strength of the surface show greater increase in surface interaction, the more these wells move towards the x-y plane. This result was accepted, as it was consistent with what was done in ref. [22]. For example, in case of the $T \otimes h$ 3D problem, as in References [26], [22], it was found that for negative surface interaction, of the parameters preferring a D_{5d} distortion, five wells equivalent to (A, B, D ,E and F), are all distributed in an equivalent manner along the z-direction and have equal energy. In general, the minimum wells of the D_{5d} or D_{3d} symmetry of C_{60}^{2-} and C_{60}^{-} molecules in case the surface interaction is applied, are in the same positions. In short, C_{60}^{-} and C_{60}^{2-} show the same behavior for the D_{5d} pentagon prone orientation. Increasing the surface interaction drives the coordinates of the electronic states of these wells to the x-y plane. However, the other STM image in fig. 4.5 shows how the individual wells look like in case of negative surface interaction for D_{5d} of the same orientation. These separate images in fig. 4.5 are associated with the permanent image expected of the ion to be locked into one of these five wells.

The image in the middle shows how the STM image would be seen when the C_{60}^{2-} molecules hop between the global minima. On the other hand, fig. 4.6 shows different expected STM images for C_{60}^{-} representing the same case as described above in fig. 4.5.

The diagrams for the C_{60}^{2-} molecule, which show the coefficient for Δ_1 for the D_{5d} pentagon prone, are very similar to each other for the same quadratic coupling constant value of V_2'=0.1, and the asymptotic limit for the parameters is 0.6. Thus, there is no point adding more diagrams. In other words, different strengths of surface interaction give different predicted STM images due to the different distribution of the wells.

The other kind of symmetry for JT parameters prefer D_{3d} distortion, the system shows a picture similar to the case considered above as shown in Figures (4.7,4.8) with quadratic coupling constant value of V_3'=0.1. These diagrams again show the effect of the positive and negative energy gap between A_g,H_g as has been shown in the D_{5d} symmetry. However, fig. 4.8 shows different sets of local minima with very similar energy in a very small values of positive Δ_1 around 0.063.

Again, the asymptotic limit for the parameters up to 1. The STM images in fig. 4.9(a) for D_{3d} symmetry are similar to D_{5d} for the same orientation as D_{3d} always shows five wells of equal global energy minima for both positive and negative strength of the surface, as in Table 4.5, which corresponds to one of the five equivalent distortions for positive surface interaction.
However, the images in fig. 4.9(b) show the STM images have been simulated as in ref. [26] for C_{60}^{-} molecule for positive surface interaction as one of five equivalent distortions.
The system in this case is allowed to hop between the five wells. As a result of increased dynamic freedom, the system is able to hop between different equivalent wells. For increasing the surface interaction, the STM images of the double charged ion will be similar to the single electron ion.
A similar conclusion for both D_{3d} and D_{5d} distortions is that it is not possible to distinguish between surface interaction and pseudorotation effects. This consideration of a negative surface interaction of these distortions is consistent with the earlier work reported by ref. [22].

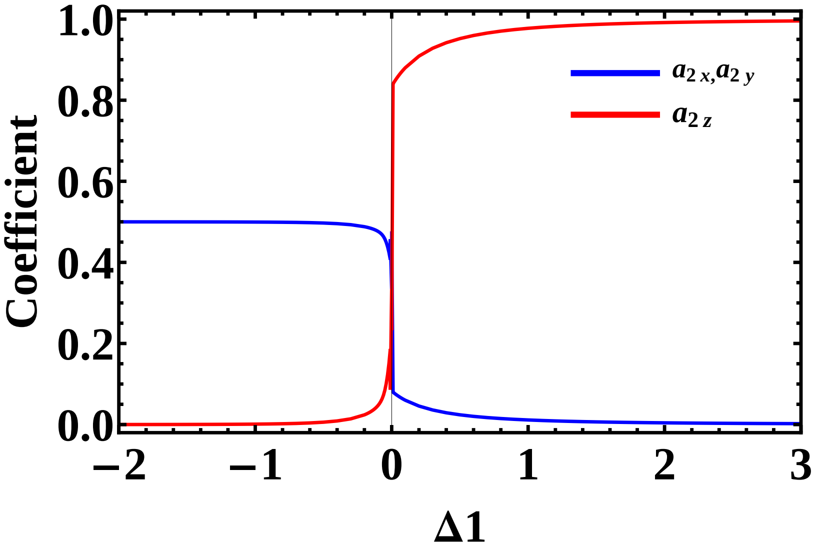

(a)

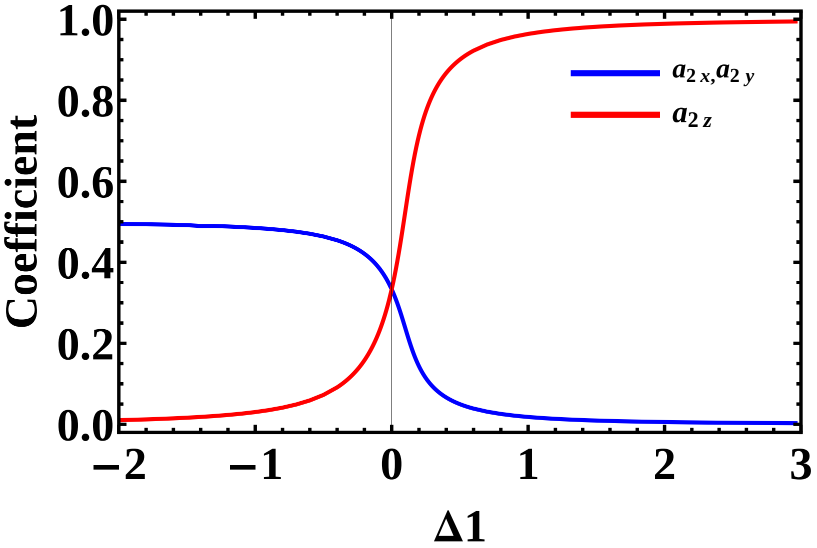

(b)

Figure 4.2: (a) The contribution from ψ_x^2,ψ_y^2,and ψ_z^2 of the wavefunction of C_{60}^{2-} of D_{5d} symmetry, C_5 orientation for different strengths of the surface Δ_1 for δ'=1, (b) the same case for δ'=-1

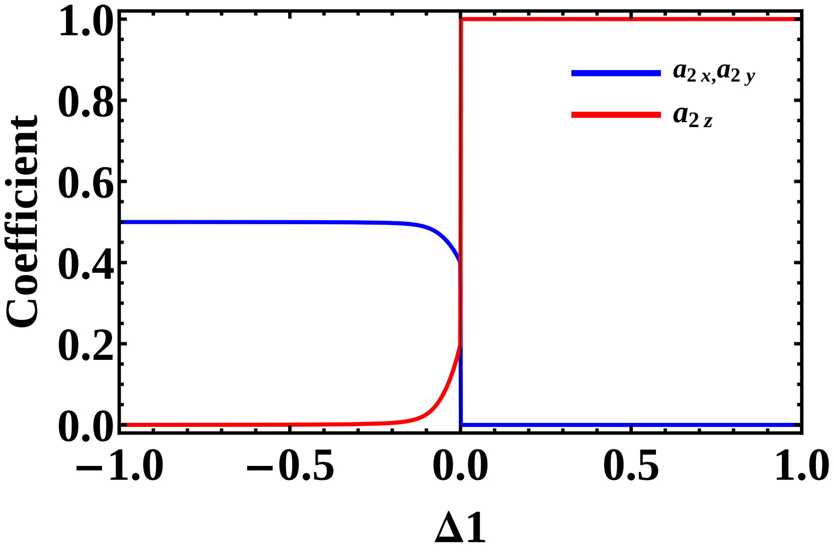

(a)

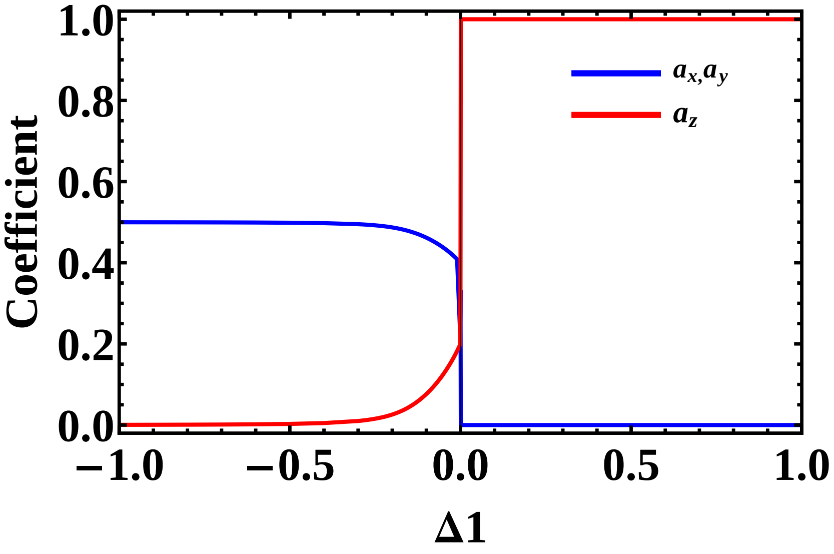

(b)

Figure 4.3: The contribution of ψ_x^2,ψ_y^2,and ψ_z^2 of the wavefunction of C_{60}^{2-} molecule pentagon-prone distorted into D_{5d} symmetry, for different strengths of the surface Δ_1, when δ'= 0 in (a) and the same parameters of C_{60}^{-} in (b)

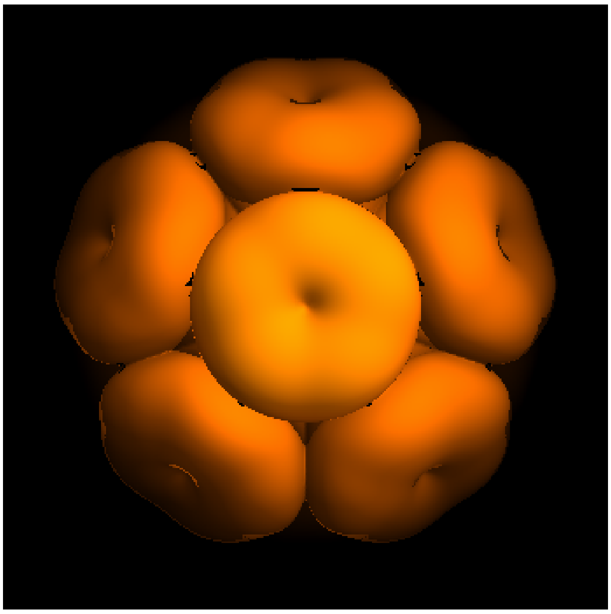

Figure 4.4: The theoretical STM image of well C for the C_{60}^{2-} molecule pentagon-prone distorted into D_{5d} symmetry for positive surface interaction

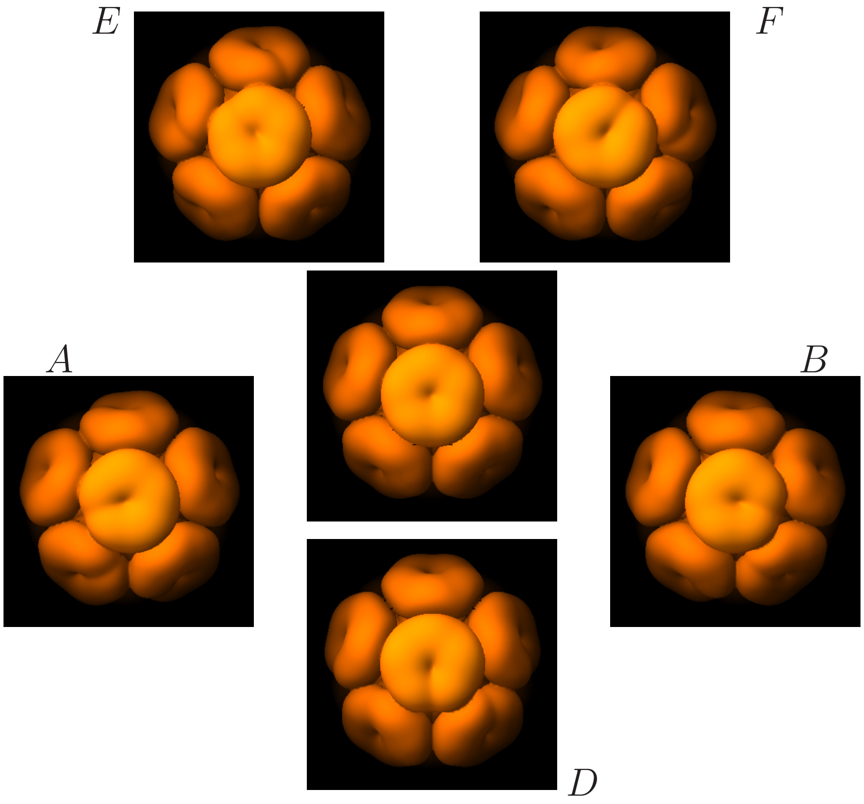

Figure 4.5: The five individual wells of the STM images for the pentagon-prone C_{60}^{2-} molecule distorted into the D_{5d} symmetry of negative surface interaction, while the image in the middle is the STM image expected when the system hops between its five global energy minima.

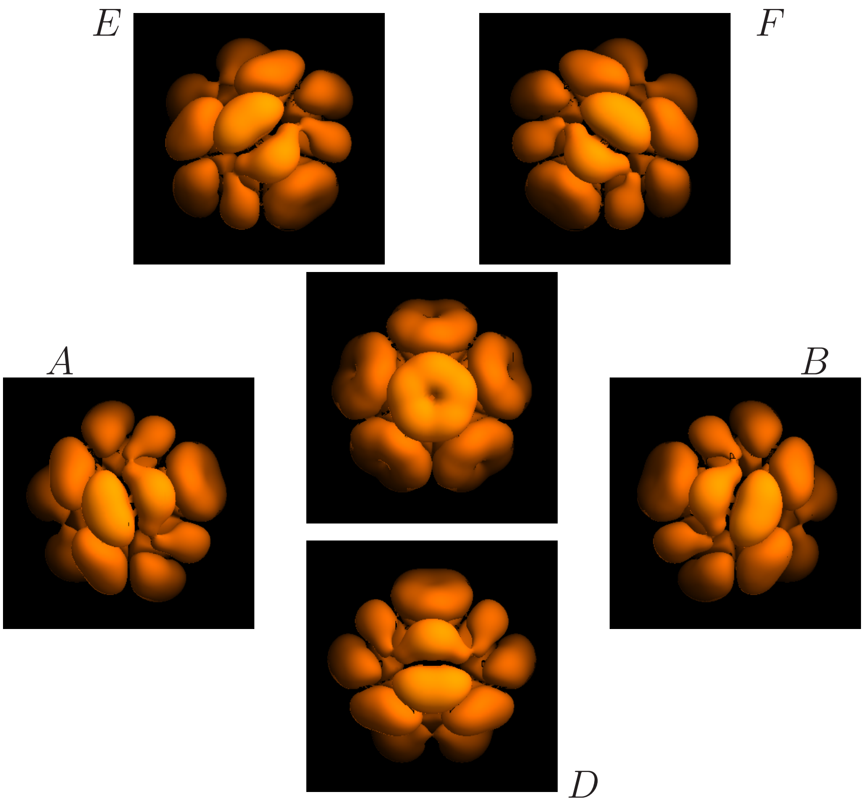

Figure 4.6: The central STM image for the C_{60}^{-} molecule pentagon-prone distorted into D_{5d} symmetry, when the system hops between its five global energy minima in case of negative surface interaction, and the five images around are the five individual wells of the same symmetry, i.e. same negative surface interaction.

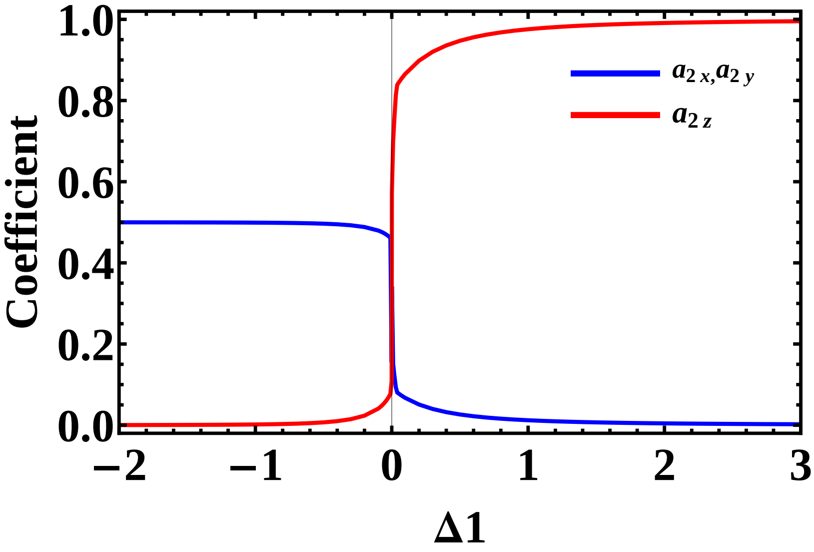

(a)

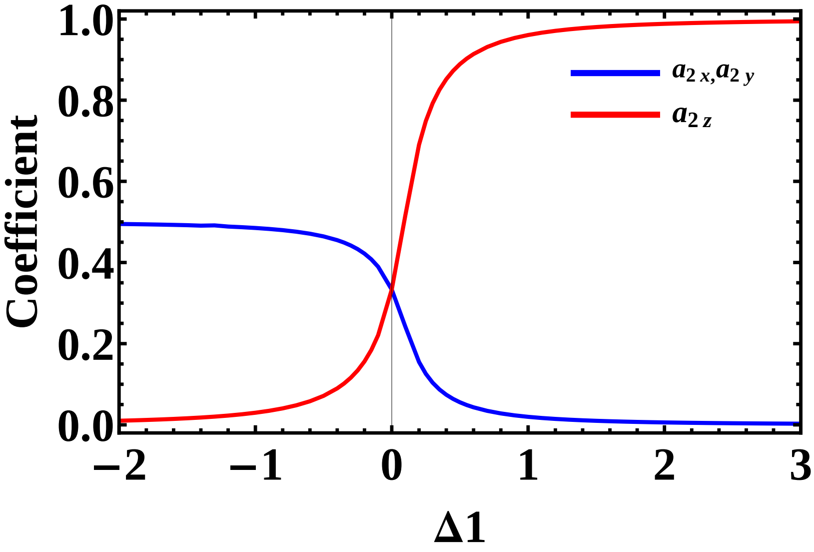

(b)

Figure 4.7: (a) The contribution from ψ_x^2,ψ_y^2,and ψ_z^2 of the wavefunction of C_{60}^{2-} of D_{3d} symmetry, C_5 orientation for different strengths of the surface Δ_1 for δ'=1 of V_2'=0 and V_3'=0.1(b) the same case with δ'=-1

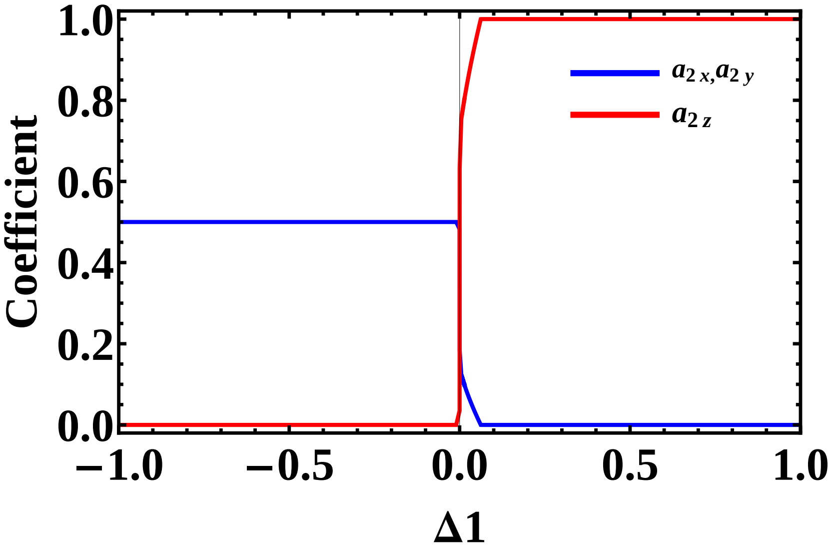

(a)

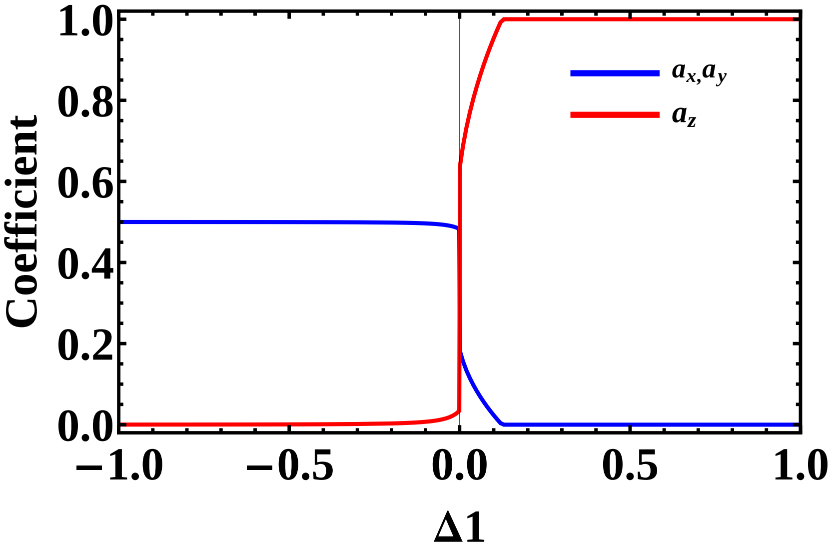

(b)

Figure 4.8: (a) The contribution fromψ_x^2,ψ_y^2,and ψ_z^2 of the wavefunction of C$_{60}^{2-}$ of D_{3d} symmetry, C_5 orientation for different strengths of the surface Δ_1 for δ'=0 of V_2'=0 and V_3'=0.1(b) the same case of C$_{60}^{-}$

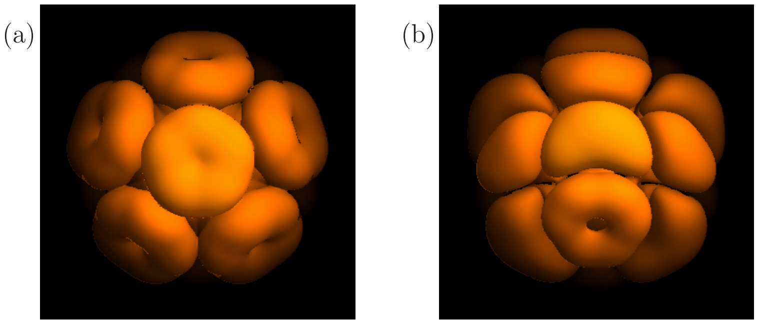

Figure 4.9: (a)The STM image of C_{60}^{2-} for D_{3d} symmetry of a pentagon-prone molecule for well c for positive surface interaction, (b) the STM images reproduced for C_{60}^{-} molecule for well (c) for positive surface.

4.7.2 Hexagon-prone orientation

Another case will be investigated, when the system with JT coupling parameters preferring D_{5d} distortion is adsorbed onto a surface with a hexagonal face of the molecule directed towards the surface. Similar to the pentagon-prone orientation, hopping between the wells is taken into account. The negative surface interaction shows three minima all the time, as in Table 4.5, which implies that increasing the magnitude of the surface strength has a very small effect in the wavefunction or the positions of the wells as shown in fig. 4.10.

The change in the coefficients in fig. 4.10, has no noticeable effect on the images. This result matches ref. [22], as three wells are favoured (A,B,D), and they are always close to the equator.

However, a rather different behaviour has been seen in the positive interaction in fig. 4.10(a) of δ'=1, as the surface interaction increases at the point $\Delta_1 \sim 0.35$ for the quadratic constant V_2'=0.1; the coordinate of the electronic states will head to $x-y$ plane. Only one well (c) will give a global minimum energy as calculated, which implies the same STM images as fig. 4.4 for pentagon-prone; so again the molecule will not pseudorotate. A real behaviour shown in fig.4.14 in about Δ_1 around 0.057 when the system has two sets of wells with two solutions of different Qs due to the high similarity of their energies. The first solution involving a pure ψ_z while the other solutions is a combinations of ψ_x,ψ_y,ψ_z. This behaviour is not unusual as it has been observed in the single electron system in ref. [22]. A final point worth discussing is the system preferring D_{3d} adsorbed onto a surface with a hexagonal face of the molecule directed toward the surface, as in fig. 4.12.

For all positive values of Δ_1 and whatever the strength of the surface, the results will remain the same. On the other hand, the expected STM images will be as in fig. 4.12.

The image is not the same for the single ion C_{60}^- in fig. 4.12(b). Again, it is not possible to distinguish between the surface interaction and the other effect from the pseudorotation during the STM process. Also, no other different images will be seen.

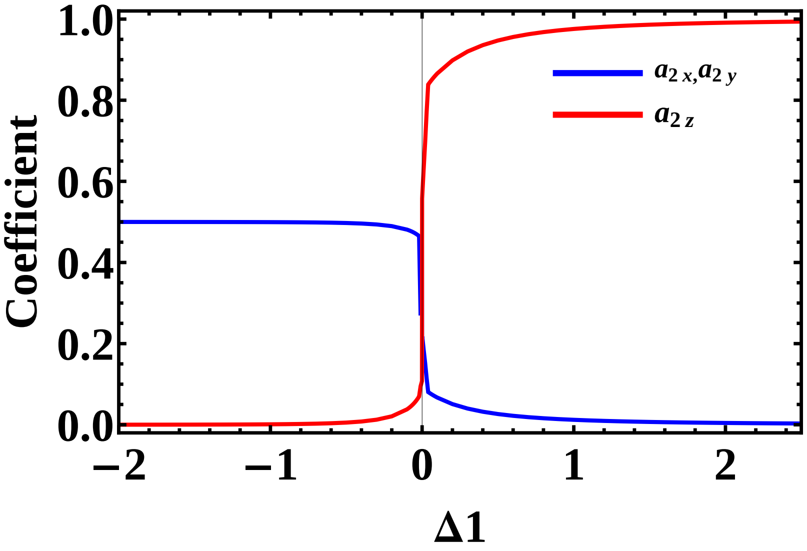

(a)

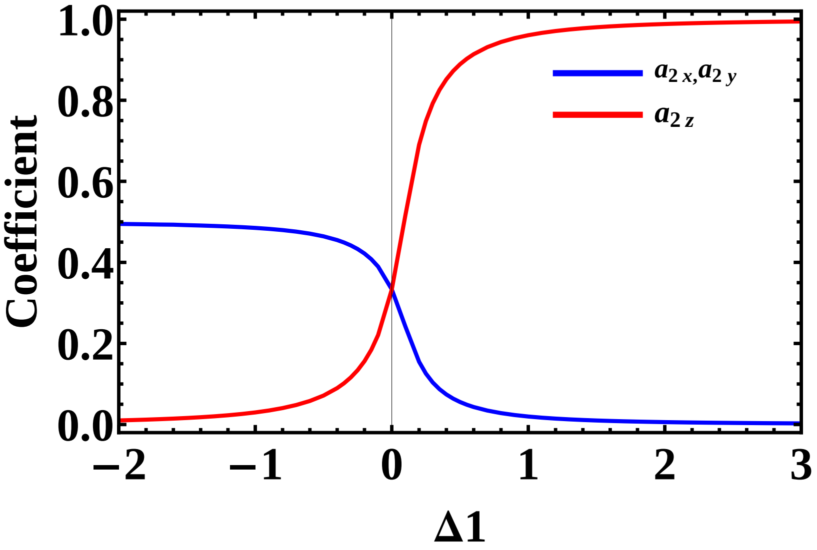

(b)

Figure 4.10: (a) The contribution from ψ_x^2,ψ_y^2,and ψ_z^2 of the wavefunction of the C_{60}^{2-} for D_{5d} symmetry, C_3 orientation for different strengths of the surface Δ_1 for δ'=1 of V_2'=0.1 and V_3'=0(b) the same case for δ'=-1

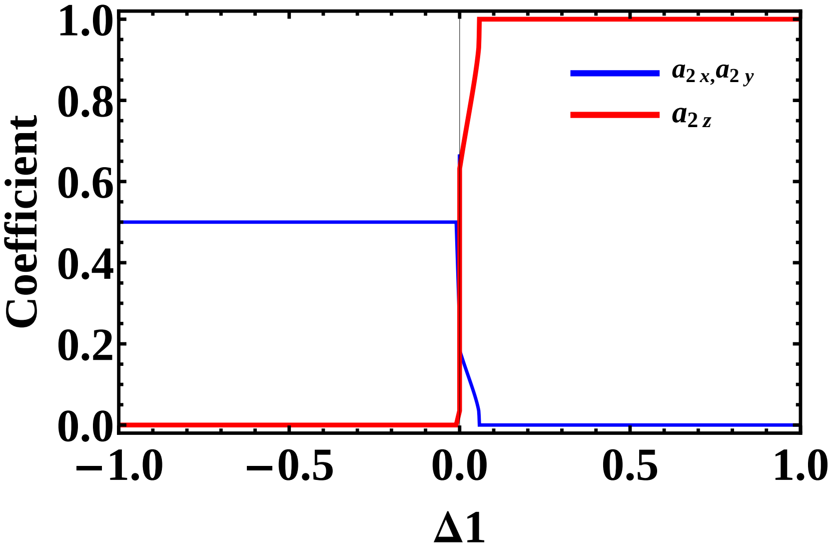

(a)

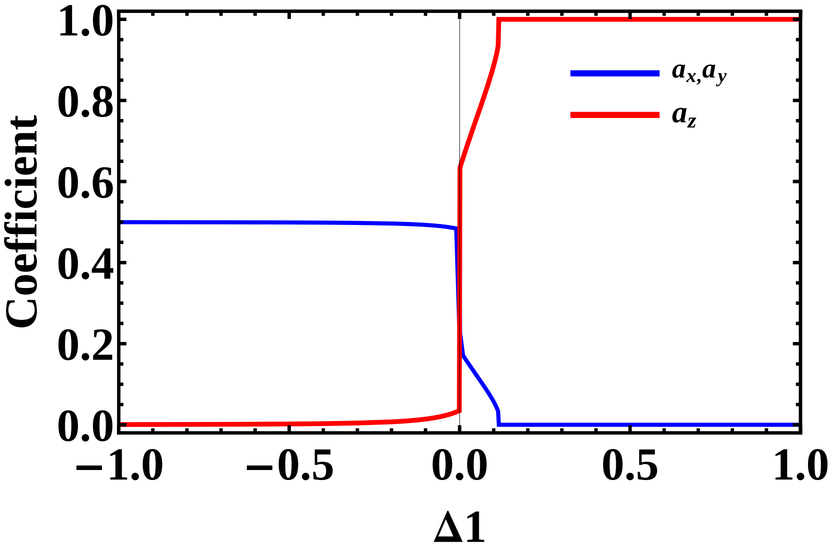

(b)

Figure 4.11: (a) The contribution from each coefficient ψ_x^2,ψ_y^2,and ψ_z^2 of the wavefunction of the C_{60}^{2-} for D_{5d} symmetry, C_3 orientation for different strengths of the surface Δ_1 for δ'=0 of V_2'=0 and V_3'=0.1 (b) the same case for C_{60}^{-}

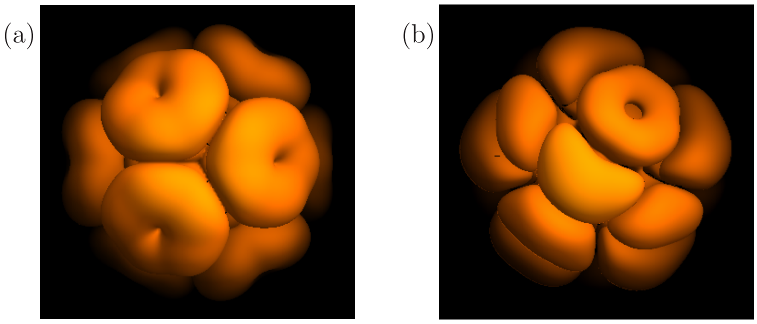

Figure 4.12: (a) The STM image of C_{60}^{2-} of D_{3d} symmetry of a hexagon-prone for negative surface interaction for individual well (b) is the reproduced STM image for the single ion C_{60}^{-} for the same symmetry for the well (a).

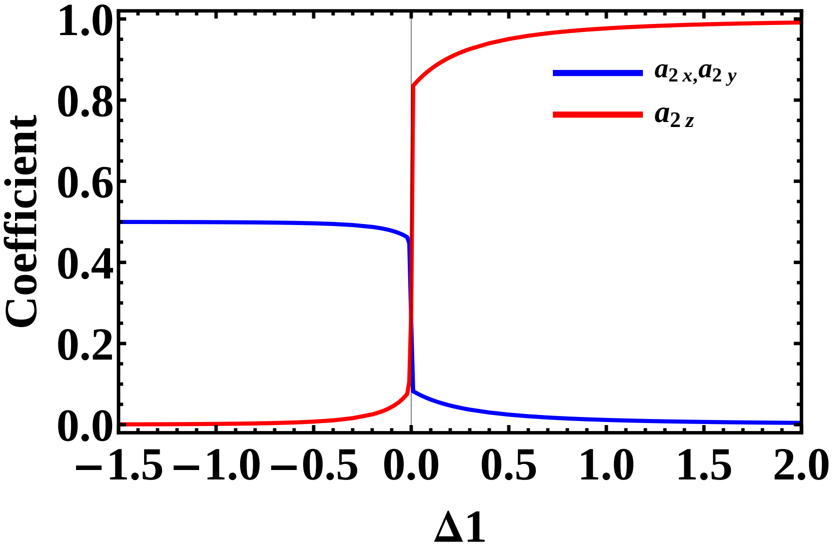

(a)

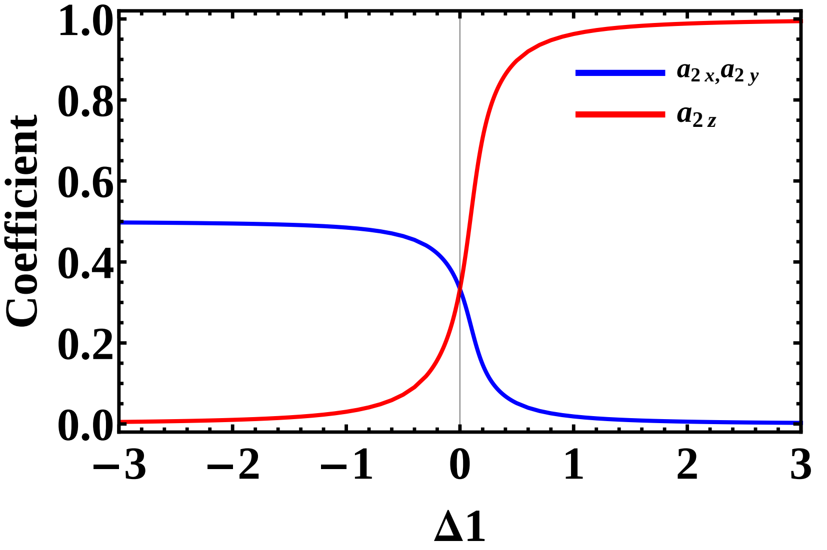

(b)

Figure 4.13: (a)The contribution from ψ_x^2,ψ_y^2,and ψ_z^2 of the wavefunction of C_{60}^{2-} of D_{3d} symmetry, C_3 orientation for different strengths of the surface Δ_1 for δ'=1 of V_2'=0.1 and V_3'=0(b) δ'=-1

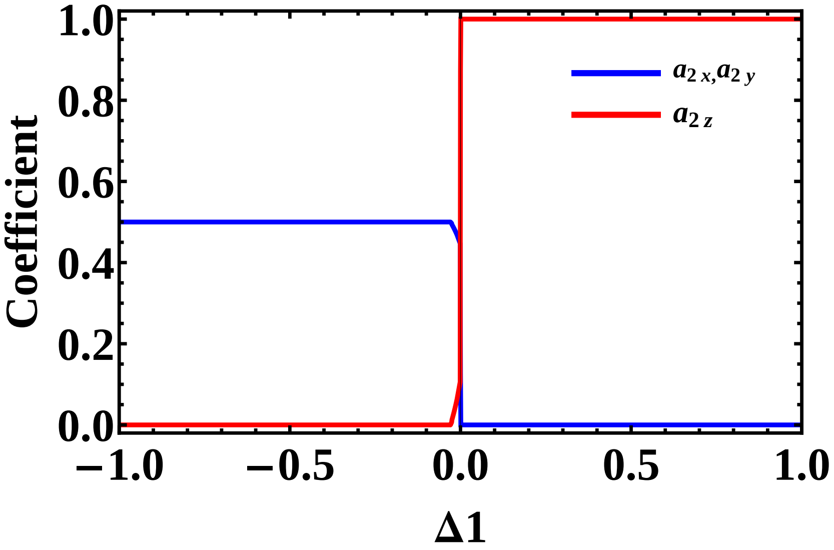

(a)

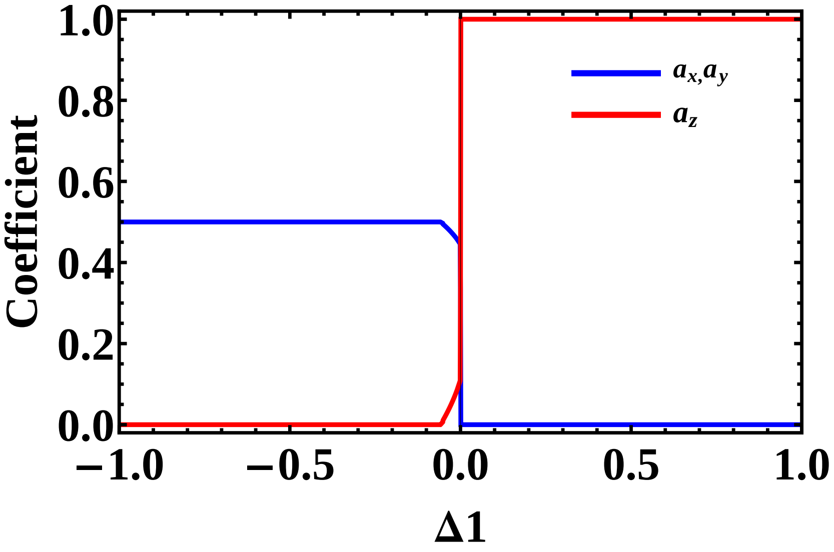

(b)

Figure 4.14: (a)The contribution from ψ_x^2,ψ_y^2,and ψ_z^2 of the wavefunction of C_{60}^{2-} of D_{3d} symmetry, C_3 orientation for different strengths of the surface Δ_1 for δ'=0 of V_2'=0 and V_3'=0.1(b)the same case of C_{60}^{-}

4.8 Further investigation of multi-electron states: C_{60}^{4-} ion

In general, the fullerene ion with four electrons added C_{60}^{4-}, can be distorted to D_{3d} or D_{5d} symmetry as in References [79],[80]. However, no evidence indicates the possible distortion [81]. In fact, the doped ion can be formed when these electrons occupy T_{1u} state in the LUMO. This model can be related to the doubly-charged ion C_{60}^{2-} by the symmetry numbers of the electrons and holes [73]. Then, C_{60}^{4-} can be modelled as an anion with two holes instead of the four electrons [14]. Therefore, the Hamiltonian for this ion will be the same as those used in C_{60}^{2-}. Then, in this case, it will be easy to apply the same Q_i's, which minimised the energy of our previous ion C_{60}^{2-} in earlier sections. This indicates that C_{60}^{4-}, therefore, has also a singlet spin ${}^1A_g$ and ${}^1H_g$ in the ground state and a triplet ${}^3T_1$ in the excited state. This section will highlight the behaviour, which will be shown by C_{60}^{4-} ion on some surfaces. In addition, the JT effect will be taken into account when higher order quadratic coupling constants are applied. Similarly, as has been done in the C_{60}^{2-} problem, Fowler and Ceulemans tables will be used to derive the bases for the energy Hamiltonian of the system. The target of this section is to apply the surface interaction on C_{60}^{4-} ion as has been done in C_{60}^{2-} system, and represent some diagrams for pentagon-prone and hexagon-prone orientations. These diagrams, in general, show the behaviour of this doped ion on different substrates. The same values for quadratic constants from C_{60}^{2-} will be used. In fact, the STM images are very similar in both C_{60}^{2-} and C_{60}^{4-}, although the expression for the current is different due to the use of 4-electron (rather than 2-electron) states as shown in Tables (4.6,4.7) of different symmetry operations.

Table 4.6: Comparison between the STM current values of the C_{60}^{2-} and C_{60}^{4-} molecules for D_{3d} (V_2'=0,V_3'=0.1) symmetry of C_3 and C_5 orientation in case surface interaction is applied for δ'=1 ,Δ_1=0.2

Ori	D_{3d}	
	C_{60}^{2-}	C_{60}^{4-}
C_5	$0.2610\,\psi_x^2+0.2610\psi_y^2+0.3858\psi_z^2$	$0.2574\psi_x^2+0.2574\psi_y^2+0.4851\psi_z^2$
C_3	$0.4191\psi_x^2+0.4191\psi_y^2+0.1616\psi_z^2$	$0.4986\psi_x^2+0.4986\psi_y^2+0.002724\psi_z^2$

4.8.1 Pentagon and hexagon orientations for C_{60}^{4-} ion

For this orientation, Figures (4.15, 4.16) will show the contribution from each coefficient of the current (a_{4x},a_{4y},a_{4z}) in case of D_{5d} and D_{3d} symmetries for different strengths of the surface and term splittings in one of the symmetry

Table 4.7: Comparison between the STM current values of the C_{60}^{2-} and C_{60}^{4-} molecules for D_{5d} (V_2'=0.1,V_3'=0) symmetry of C_3 and C_5 orientation in case of surface interaction is applied for δ'=1 ,Δ_1=0.2

Ori	D_{5d}	
	C_{60}^{2-}	C_{60}^{4-}
C_5	$0.4191\psi_x^2+0.4191\psi_y^2+0.1616\psi_z^2$	$0.4969\psi_x^2+0.4969\psi_y^2+0.006154\psi_z^2$
C_3	$0.2875\psi_x^2+0.2878\psi_y^2+0.4249\psi_z^2$	$0.2574\psi_x^2+0.2574\psi_y^2+0.4851\psi_z^2$

distortion D_{5d}. In these figures, there is a swap between the minimum wells around Δ_1=0.2 in most of the cases where H_g is the lowest in energy.

Also, the asymptotic limit for the parameters is about 0.5 due to the electronic distributions of the four electrons. In short, if the contribution of one of the single electron states equal zero i.e x=0, two electrons will occupy each of the other states equally. Therefore, the STM images will be a combination from y and z. However, the minimum possibility of each state will be $\frac{1}{4}$ if none of these states equal zero.

The STM images are similar to the images produced in the $p^2 \otimes h$ problem. However, different current is involved as in Tables (4.6,4.7).

However, Figures (4.17, 4.18) are good enough to give some information about the C_{60}^{4-} system on the hexagon prone perpendicular to the surface for D_{5d} and D_{3d} distortion. Again, as in C_{60}^{2-} system, the sets of minima of small values of Δ_1 around 0.033, changed as shown in Figures 4.16 and 4.17.

In fact, different substrates have been used to show the contribution from each coefficient of the wavefunction of the system, which shows the current used. These Figures (4.17, 4.18) represents both D_{5d} and D_{3d} symmetries for different strengths of the term splitting and surface interaction for fixed value of quadratic constants, as mentioned before (V_2'=0.1,V_3'=0) for D_{5d} and (V_2'=0,V_3'=0.1) for D_{3d}. These values for the coupling parameters are in systems and all orientations and symmetries in order to provide a fair comparison in all cases. Again, no difference in the STM images deserves discussion, even though different currents have been used as in Tables (4.6,4.7).

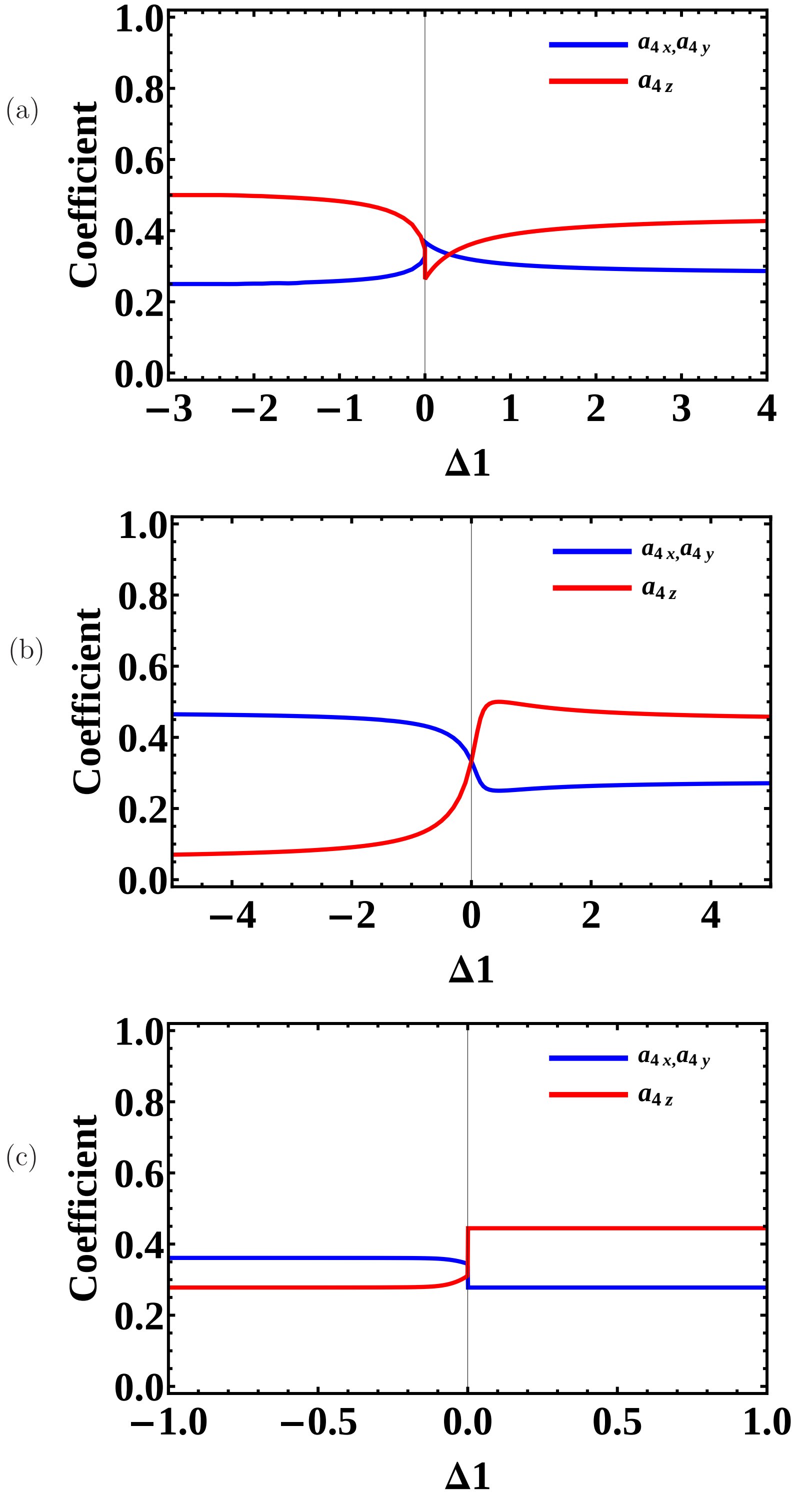

Figure 4.15: (a) The contribution from ψ_x^2,ψ_y^2,and ψ_z^2 of the wavefunction of C_{60}^{4-} of D_{5d} symmetry, C_5 orientation for different strengths of the surface Δ_1 for δ'=1,of V_2'=0.1 and V_3'=0 (b) δ'=-1, (c) δ'=0

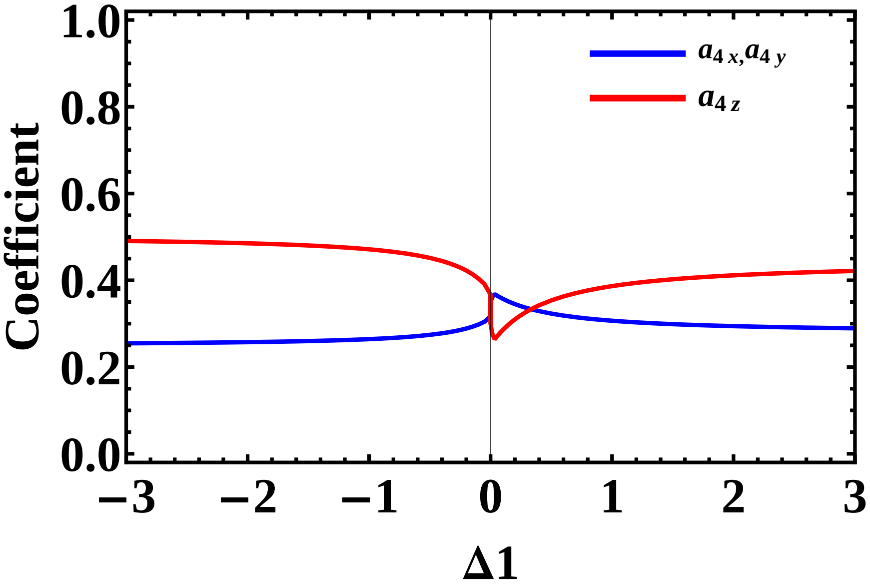

Figure 4.16: The contribution from ψ_x^2,ψ_y^2,and ψ_z^2 of the wavefunction of C_{60}^{4-} of D_{3d} symmetry, C_5 orientation for different strengths of the surface Δ_1 for δ'=1 of V_2'=0 and V_3'=0.1

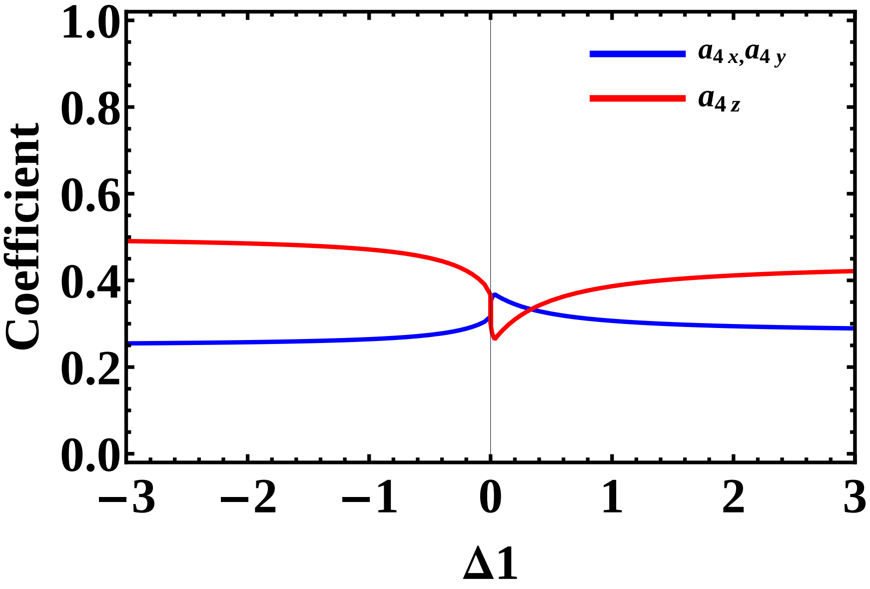

Figure 4.17: The contribution from ψ_x^2,ψ_y^2,and ψ_z^2 of the wavefunction of C_{60}^{4-} of D_{5d} symmetry, C_3 orientation for different strengths of the surface Δ_1 for δ'=1 of V_2'=0.1 and V_3'=0

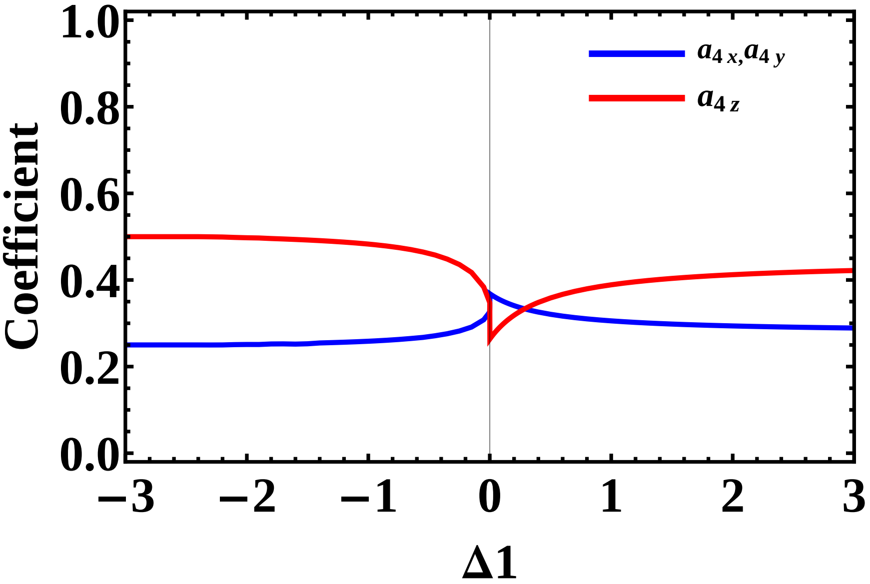

Figure 4.18: The contribution from ψ_x^2,ψ_y^2,and ψ_z^2 of the wavefunction of C_{60}^{4-} of D_{3d} symmetry, C_3 orientation for different strengths of the surface Δ_1 for δ'=1 of V_2'=0 and V_3'=0.1

4.9 The regions of validity

It is very important to focus on the region of validity of quadratic coupling constants, which keep the system stable from breaking down. The strength of the quadratic constants, describing the electronic and nuclear coupling plays a vital role in the stability of the system. In short, the energy of the system can be strongly affected by the nuclear vibrations. However, overcoming this limit can diverge the JT energy E_{JT} associated with this coupling to -∞, with the amplitudes of the vibrations also becoming infinite which could be the end of the stable molecule. According to the Hermitian matrices properties in ref. [82], the energy of the system included term splitting should be the same or smaller than the sum of the E_{JT} and the minimum energy of the term splitting Hamiltonian. As found in ref.[38], Q_4= Q_5=0 can be found in at least one of the lowest eigenvalues through the minimisation of D_{3d},D_{5d},D_{2h} and C_{2h} symmetry distortions. Therefore, the electron states will be associated with A_g,$H_{g\theta}$,$H_{g\epsilon}$,H_{g6}, which decrease the calculations of the Hamiltonian from 6D to 4D. Then, applying the minimisation and covering all the positive and negative ranges of both V_2' and V_3' of large grid points in all directions by fixing one coupling constant and altering the other, the region of validity will be determined.

The bounded JT energies have been located inside the contour; however, all the points out side the contour show the unbounded JT energies, i.e. an unstable system. So, the increase of the coupling parameters has significant effect on the overall energy of the system. Some more numerical calculations added promised that the boundary is independent of any other parameters, such as the term splitting and the surface parameters.

Actually, the region of validity for $p^2 \otimes h$ is similar to what has been found in ref. [26] of single electron state, however, a different $T \otimes h$ JT system has been applied. The different symmetry reduction types of $T \otimes h$ JT molecule have been shown in fig.4.19. The mathematical form, which has been used analytically on $T \otimes h$ for different types of symmetry (D_{2h},D_{3d},D_{5d}) is much easier than what should be used in the two electron states system. In fact, it is quite a challenge to find the analytical forms, in the case of $p^2 \otimes h$, which have been done for D_{5d} and D_{3d} symmetry only and ignoring the Coulomb factor δ' in ref. [16].

As a fact, it was found numerically that the region of validity is independent of non-zero term splitting and surface interaction. Finally, it is worth exploring further the comparison between $T \otimes h$ and $p^2 \otimes h$, in order to find the JT energy for a D_{2h} symmetry type of interest in case of matching this work with ref.[18]. This analytical calculations will include the minimum positions along with the electronic states of this distortion with no surface added to avoid complicated calculations. The 15 minima labeled from A to O will be tabulated in Table 4.8 to be consistent with the expressions have been presented in ref. [83] for $(h_u^+)^2 \otimes h_g$system. However, different definitions of ξ and κ between the two

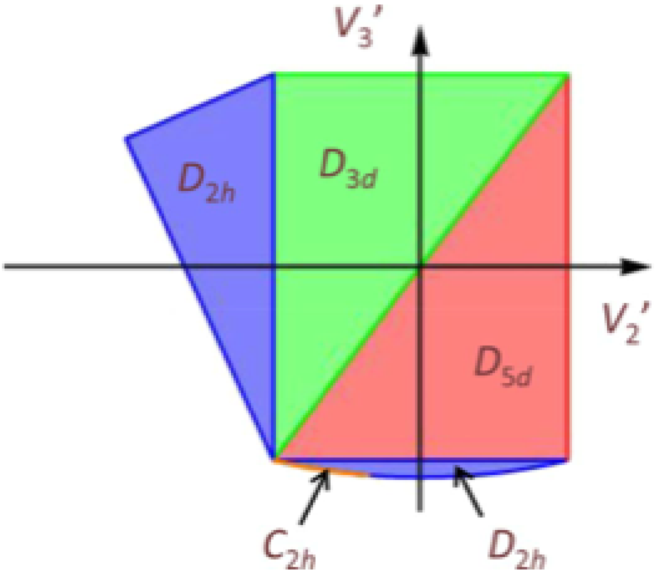

Figure 4.19: The calculated region of validity in Jahn-Teller parameter space for $T \otimes h$ reproduced from ref. [26]

systems, where:

$$\xi = \frac{-\sqrt{3}}{\sqrt{2}} \frac{1 - \sqrt{5}V_3' - V_2'}{1 - 2V_3'^2 - 6V_2'^2}$$

$$\kappa = \frac{\sqrt{5}}{\sqrt{2}} \frac{1 + \frac{V_3'}{\sqrt{5}} - 3V_2'}{1 - 2V_3'^2 - 6V_2'^2}$$

Table 4.8: The positions of the wells of D_{2h} symmetry of C_{60}^{2-}

Label	a_θ	a_ϵ	a_4	a_5	a_6
A	$\frac{\xi}{2}$	$-\frac{\kappa}{2}$	$-\frac{\sqrt{3}\kappa+\xi}{2\sqrt{2}}$	$\frac{-\sqrt{6}\kappa+\sqrt{2}\xi}{4}$	$\frac{\xi}{\sqrt{2}}$
B	$\frac{\xi}{2}$	$-\frac{\kappa}{2}$	$\frac{\sqrt{3}\kappa+\xi}{2\sqrt{2}}$	$\frac{+\sqrt{6}\kappa-\sqrt{2}\xi}{4}$	$\frac{\xi}{\sqrt{2}}$
C	$\frac{-\sqrt{3}\kappa-\xi}{4}$	$\frac{\kappa-\sqrt{3}\xi}{4}$	$\frac{\sqrt{6}\kappa-\sqrt{2}\xi}{4}$	$\frac{\xi}{\sqrt{2}}$	$\frac{\sqrt{3}\kappa+\xi}{2\sqrt{2}}$
D	$\frac{-\sqrt{3}\kappa-\xi}{4}$	$\frac{\kappa-\sqrt{3}\xi}{4}$	$\frac{\sqrt{6}\kappa-\sqrt{2}\xi}{4}$	$-\frac{\xi}{\sqrt{2}}$	$-\frac{\sqrt{3}\kappa+\xi}{2\sqrt{2}}$
E	$\frac{\sqrt{3}\kappa-\xi}{4}$	$\frac{\kappa+\sqrt{3}\xi}{4}$	$-\frac{\xi}{\sqrt{2}}$	$-\frac{\sqrt{3}\kappa+\xi}{2\sqrt{2}}$	$\frac{\sqrt{6}\kappa-\sqrt{2}\xi}{4}$
F	$\frac{\sqrt{3}\kappa-\xi}{4}$	$\frac{\kappa+\sqrt{3}\xi}{4}$	$-\frac{\xi}{\sqrt{2}}$	$-\frac{\sqrt{3}\kappa+\xi}{2\sqrt{2}}$	$\frac{-\sqrt{6}\kappa+\sqrt{2}\xi}{4}$
G	$\frac{\xi}{2}$	$-\frac{\kappa}{2}$	$-\frac{\sqrt{3}\kappa+\xi}{2\sqrt{2}}$	$\frac{\sqrt{6}\kappa-\sqrt{2}\xi}{4}$	$-\frac{\xi}{\sqrt{2}}$
H	$\frac{\xi}{2}$	$-\frac{\kappa}{2}$	$\frac{\sqrt{3}\kappa+\xi}{2\sqrt{2}}$	$\frac{-\sqrt{6}\kappa+\sqrt{2}\xi}{4}$	$-\frac{\xi}{\sqrt{2}}$
I	$\frac{-\sqrt{3}\kappa-\xi}{4}$	$\frac{\kappa-\sqrt{3}\xi}{4}$	$\frac{-\sqrt{6}\kappa+\sqrt{2}\xi}{4}$	$\frac{\xi}{\sqrt{2}}$	$\frac{-\sqrt{3}\kappa+\xi}{2\sqrt{2}}$
J	$\frac{-\sqrt{3}\kappa-\xi}{4}$	$\frac{\kappa-\sqrt{3}\xi}{4}$	$\frac{-\sqrt{6}\kappa+\sqrt{2}\xi}{4}$	$-\frac{\xi}{\sqrt{2}}$	$\frac{\sqrt{3}\kappa+\xi}{2\sqrt{2}}$
K	$\frac{\sqrt{3}\kappa-\xi}{4}$	$\frac{\kappa+\sqrt{3}\xi}{4}$	$\frac{\xi}{\sqrt{2}}$	$\frac{\sqrt{3}\kappa+\xi}{2\sqrt{2}}$	$\frac{\sqrt{6}\kappa-\sqrt{2}\xi}{4}$
L	$\frac{\sqrt{3}\kappa-\xi}{4}$	$\frac{\kappa+\sqrt{3}\xi}{4}$	$-\frac{\xi}{\sqrt{2}}$	$\frac{\sqrt{3}\kappa+\xi}{2\sqrt{2}}$	$\frac{-\sqrt{6}\kappa+\sqrt{2}\xi}{4}$
M	$\frac{-\sqrt{3}\kappa-\xi}{2}$	$\frac{-\kappa+\sqrt{3}\xi}{2}$	0	0	0
N	$\frac{\sqrt{3}\kappa-\xi}{2}$	$\frac{-\kappa-\sqrt{3}\xi}{2}$	0	0	0
O	ξ	κ	0	0	0

4.9.1 The symmetry regions of $p^2 \otimes h$ system

After the region of validity has been found, the relationship between the JT coupling constants, and the symmetry reduction of JT effect can be established. From group theory, the I_h symmetry can reduce to D_{3d}, D_{5d}, D_{2h} and C_{2h} and further to C_i point groups. The rest of this section will show how the JT effect can reduce the symmetry of the system for different values of term splitting δ'. As has been found previously in the comparisons between $T \otimes h$ and $p^2 \otimes h$, the same regions of symmetry have been found as in the single electron state case without the C_{2h} region. The relationship between the quadratic coupling constants and the symmetry regions inside the region of validity can be established by applying the minimisation in 3D with Q_θ,Q_ϵ and Q_6 of chosen a value of term splitting over a large range of points. In addition, the separate boundaries in between the different symmetry types can be calculated in an easier way, such as in 1D for D_{3d}, D_{5d} and 2D for D_{2h} as in ref. [84]. The symmetry regions for $p^2 \otimes h$ system will be shown in fig.4.20 for the case of interest δ'=0. In addition, the boundaries between these regions have been calculated analytically to be:

$$V_3' = \frac{3}{\sqrt{5}} V_2', \qquad V_2' = \frac{-5}{8\sqrt{2}} \qquad \text{and}$$

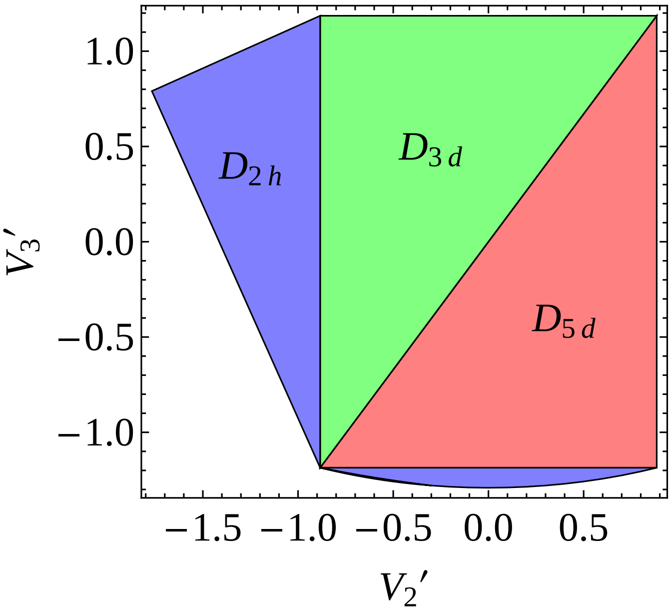

Figure 4.20: The symmetry region for $p^2 \otimes h$ in case of non zero splitting term

On the other hand, different possible values can be estimated for the term splitting parameter that can be calculated from the non-JT model in [78]. For example, δ'=2.4 is a chosen value from the middle of the range. The three kinds of symmetries in fig.4.20 meet each other at the point in the bottom left of the plot when the term splitting is zero. This point moves up the central line of the boundary as the value of the term splitting increases. The unlabelled region shows the D_{2h} symmetry in fig.4.20. The change in this boundary is shown clearly in fig.4.21. Different term splittings can make a change in the symmetry of the region, as

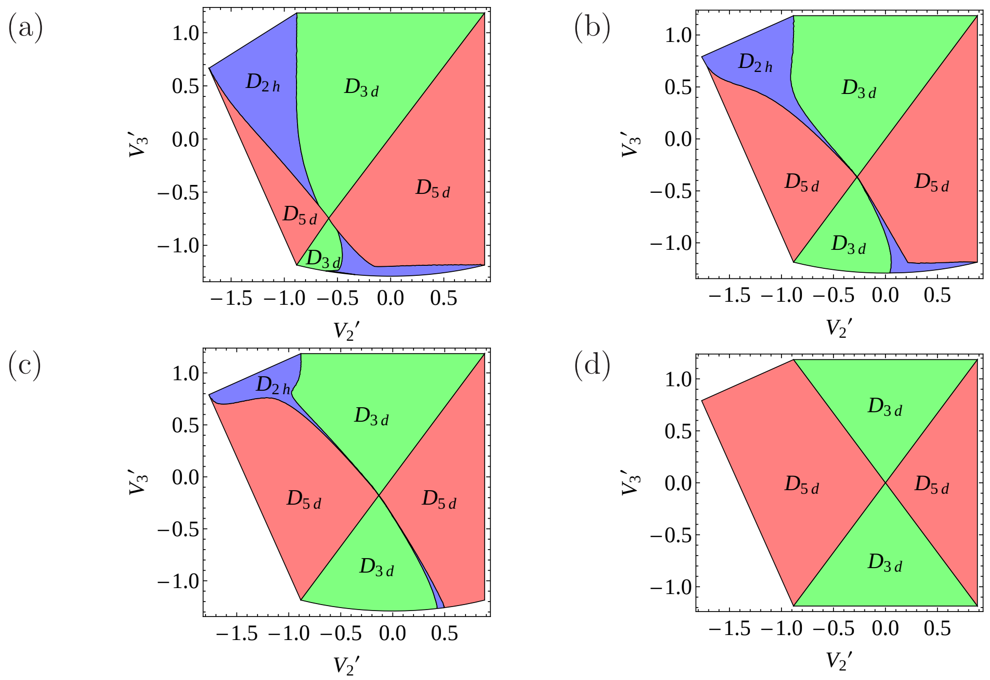

Figure 4.21: The symmetry region for $p^2 \otimes h$ with term splittings (a) δ'=0.24, (b)0.96, (c)2.4, (d)∞ reproduced from ref.[85]

shown in ref. [85]. Figure 4.21 shows the effects of different values of term splittings on the distortion region of the low spin of C_{60}^{2-}. It was found that, any decrease in a distortion region corresponds to increase in the other regions. Some regions get excluded when δ' is negative because the A state is lowest.

In fact, in these plots of different term splittings in the fig. 4.21, the symmetry region of C_{2h} is very small between V_2'= -0.88 and -0.3 which can be neglected as these values are very unlikely to place the molecule in this particular region. On the other hand, if the energy of the A_g tends to infinity, the regions will look like fig. 4.21(d). Furthermore, increasing the values of the term splitting can change the symmetry region distribution. For example, increasing from zero can add more size to the D_{5d} and D_{3d} with equivalent decreasing in the D_{2h} regions which would disappear in very high values of term splitting. This information about the regions of validity in the JT parameter plane followed by the symmetry regions is enough to start thinking about the way to match the theoretical results of this work with the published images in ref. [18] in chapter 6.

4.10 Discussion and conclusion

C_{60}^{2-} is subject to a JT effect that prefers either a D_{3d} or D_{5d} distortion, depending on the values of quadratic JT coupling constants. The STM images have been considered from the lowest unoccupied molecular orbital of the doubly-charged ion. On charging the fullerene ion, such as C_{60}^{2-}, the additional electrons occupy the T_{1u} orbital. In fact, STM images generated from the LUMO is a sum of linear combinations (A_{1g}, $H_{g\theta}$, $H_{g\epsilon}$, H_{g4}, H_{g5}, H_{g6}), due to superposition of results from different wells whatever the prone symmetry or the strength of the surface. These effects have been investigated in detail when a second order quadratic coupling is included in the system, as in ref. [16]. The calculations of STM images in the C_{60}^{-} anion, which have been investigated in an earlier work in ref. [26] have been extended. However, in ref. [26], the JT effect was considered to be the effective interaction and the surface interaction was treated as a perturbation. As a final result on this matter, JT effects cannot be ignored even in cases where C_{60}^{2-} can be decoupled efficiently from the surface.
The results here have been different to those for C_{60}^{-} in ref. [26], as the JT interaction Hamiltonian is different to theirs, and so electron states and the energy of the system have been rearranged due to surface interaction in most of the cases. Another consideration is that the effect of the substrate has made the structure of C_{60}^{n-} more complicated than C_{60}^{-} after the second electron is added. This factor influenced the appearance of the STM images. The Hückel molecular orbital approach has been improved by simplifying the way of modelling STM images of fullerene molecules, such as C_{60}^{2-}, adsorbed onto surfaces, as given by Deng and Yang in ref. [28]. Furthermore, the theory was modified for multi-electron functions (Bardeen's theory) where the two electron case (which is a new method used here for the first time in order to distinguish between two tunnelling electrons) has been used to get the total current for tunnelling into the T_{1g}, A_{1g}, and H_g states. The surface Hamiltonian forms for each orientation have been extended from the simpler $T \otimes h$ system, to determine the values of the (a_θ, a_ϵ, a_4, a_5, a_6), which have been combined with the JT Hamiltonian later to evaluate the eigenvalues and eigenvectors of the system. However, an alternative method (the direct integration method) has been used in order to simplify the current to be a linear combinations of the single electron state, making the calculations simpler with no cross terms. This was followed by an approximation method, which promised similar results with less calculation time.

This work has been concluded with certain assumptions (included in diagrams) to show the behaviour of the molecule and the contributions from each part of the LUMO wavefunction when a pentagonal face is prone to the surface, for positive and negative surface interaction of both D_{3d} and D_{5d} symmetries. The results have been given when the same method has been applied to C_{60}^{2-} molecules in the hexagonal orientation. These diagrams have indicated that different values of surface strengths presented different STM images for the same molecule, which in one way or another illustrated that JT effect and surface interaction are both significant. This included the cases where the system was assumed to hop between wells in a pseudorotation process, which cannot be distinguished from surface effect. Some images have been simulated using the constant current mode to show the appearance of the double-charged ion as might be recorded by STM. It is found that, the STM images of the C_{60}^{2-} ion will be similar to the images of the single electron state ion of different orientations as Δ_1 increasing. These images have a clear signature of a surface interaction being present. A comparison between the theoretical images for C_{60}^{-} molecules obtained earlier in ref. [26] and currently simulated images for C_{60}^{2-} molecules has been done. This difference between both molecules gave a strong motive to find out how the simulated images for C_{60}^{3-} molecules will look like. Extra work has been done on the C_{60}^{2-} ion in order to give further analytical information about the region of validity, which shows the boundary limit and the symmetry regions.

Chapter 5, next, will present a different treatment, since the symmetry will change to C_{2h} and D_{2h}, which makes the situation more complicated.

Chapter 5

JT and surface interactions in C_{60}^{3-} ions

5.1 Introduction

The $p^3 \otimes h$ Jahn-Teller effect applicable to C_{60}^{3-} trianion has been studied in relation to linear coupling in References [86], [14] and quadratic coupling in ref.[87]. Additional doping by co-deposition has the advantage of producing charged ions with three electrons. Therefore, recording the JT effect through STM is made possible. Changing the number of electrons can have a small effect on the strength of the coupling. There is an estimate in ref. [88] that the JT coupling in case of three electrons ion such as Cs_3C_{60} is strong. It is also interesting to consider C_{60}^{3-} anions theoretically, because it is of interest to assess whether it is possible that the experimentally-observed images can be due to a JT distortion, as proposed by ref. [18], or other interaction. The triply charged ion C_{60}^{3-} will be different to the other charge states, as the wells are likely to favour either D_{2h} or C_{2h}. More wells in this ion make the situation more complicated, due to the additional electrons. This is of particular interest, because materials containing this ion can be superconducting, as in ref. [89]. Therefore, the aim of this chapter, in the next stage of this research, is to present further investigation of this ion, in order to simulate images for ions adsorbed at various geometries. The work will start with finding out the electronic basis of three electrons, followed by the JT interaction Hamiltonian in linear and quadratic distortions. This will cover all the possible remaining symmetry types. The new treatment of the surface will be extended from the previous chapter to form the surface interaction Hamiltonians in various orientations. Then, a combined Hamiltonian between the JT and surface interactions will be needed. Finally, solving this Hamiltonian will be the main step in order to discover how the surface and JT interactions can manifest themselves in STM images.

5.2 The JT effect in fullerene trianion

Before we turn our attention to the JT Hamiltonian of this more complicated system, it is worthwhile providing information about how to construct the electronic basis of the system in the Fowler and Ceulemans basis.

5.2.1 The electronic basis

The three electron states T_{1u} and H_u are not written according to symmetry transformation properties as orbital and spin parts multiplied by each other but as a sum of products of orbitals and spin contributions. Therefore, while states with the right transformation properties can be obtained by using Fowler and Ceulemans tables. This is not enough to write the components in antisymmetric form, which takes into account the exchange of two electrons. Hence, this requires linear combinations of the non-symmetric results for different alternation of the electron labels.

Group theory shows that, $T_{1u} \otimes T_{1u} = A_g + H_u + T_{1u}$, with A and H_u orbitals are singlets and have zero spin $S = 0$, while T_{1u} is triplet spin with $S = 1$. The singlet A_g is in high spin and is not a subject to JT coupling. However, T_{1u} and H_u orbitals are in low spin with half filled T_{1u}. In addition, there is no JT effect within both states, but there is still a coupling between them [14][90]. As has been done in $p^2 \otimes h$, the two electron states could be written as a product of an orbital and a spin part, as shown in eq.(4.2). However, in case of three electrons, these two electron states should multiply with T_{1u} then,

- $T_{1u} \otimes A$

This multiplication is equal T_{1u}, and the right transformation properties of the 6 T_1 states can be obtained by multiplying the two-electron $A^{(2)}(1,2)\ S^s_{1,2}$ state by appropriate orbital and spin wavefunctions for electron 3, for the orbit $T_{1\gamma}(3)$, where γ=x,y,z, and spin S_3^+ and S_3^-. Linear combinations of these six basis states should build up in order to derive the right antisymmetry properties.

- $T_{1u} \otimes T_{1u}$

From group theory, $T_{1u} \otimes T_{1u} = A + H_u + T_{1u}$. Then, the required states can be obtained again by using Fowler and Ceulemans tables with one of the sets of states $T_{1\gamma}(3)S^{\pm}$ and the other sets will be $T^{(2)}_{1\gamma}(1,2)\ S^t_{1,2}$.

First, A states have six anti-symmetrised combinations multiplied by two spin possibilities $S^{\pm}$, all in the required form of an orbital state × a spin state, however, with four distinct results only. Two of them are spin combinations with

m_s=$\frac{3}{2}$ and the other with m_s=$\frac{1}{2}$.
Second, T_{1u} is a triplet with $S = 1$ spin state. This has 18 possible unsymmetrised basis states due to the combination of (x,y,z × n=(1,2,3) × $S^{\pm}$). In addition, these 18 states are equal to the six T_{1u} three electron states caused from $T_{1u} \otimes A$ or linear combinations of them.
The last term, H_u, has 30 possible unsymmetrised states coming from $\gamma(\theta, \epsilon, x, y, z)$.

- $T_{1u} \otimes H_u$

Again from group theory, $T_{1u} \otimes H_u$= T_{1u}+T_{2u}+G_{1u}+H_u, and Fowler and Ceulemans tables are used. Actually one of the sets of states will be $T_{1\gamma}(k)$ $S^{\pm}$ and $H_{\gamma}^{(2)}(i,j)S_{i,j}^{s}$ will form the other. As a result, ten possible states of H_u will remain from γ=(θ, ϵ,x,y,z) × $S^{\pm}$, which is consistent with a ^2D. On the other hand, every antisymmetric combination for T_{2u} and G_u will vanish. The basis of this system are too long to display here.

The only coupling between the $^1T_{1u}$+ ^1H_u and h_u modes of vibration are considered. In fact, the electronic basis of the form ($^1T_{1u}$+^1H_u) have been adapted to describe this coupling.
Then, the Hamiltonian of the system is an 8 × 8 matrix with an eight fold degenerate basis set. After writing the Hamiltonian in forms of this basis, and by using the CG coefficients in ref. [72], the three-electron states for our electronic basis can be formulated as shown above. The JT Hamiltonian is defined with two fold axes perpendicular to the centre of the double bond as is explained in the next section.

5.2.2 The linear and quadratic Hamiltonians of the system

In the same way, the Clebsch-Gordan coefficients have been used to construct the JT Hamiltonian of the three electron system. The additional term (term splitting) of the energy between T_{1u} and H_u states has been added to the total Hamiltonian of the ion due to the Coulomb interaction between the two electronic states T_{1u} and H_u as shown in ref.[83]. Then, the full Hamiltonian will take the form [91]:

$$\mathcal{H}_{JT} = \mathcal{H}_0 + V_1\mathcal{H}_1(Q) + V_2\mathcal{H}_2(Q^2) + V_3\mathcal{H}_3(Q^2) \tag{5.1}$$

The matrix representation of the Hamiltonian for the term splitting will be a 3 × 3 diagonal matrix, which represent the energy of the orbital T_{1u} at an energy δ' which can be positive or negative to be higher or lower in energy than the other electronic state H_u. This matrix will take the form:

$$H_{term} = \begin{bmatrix} \delta' & 0 & 0 & 0 & 0 & 0 & 0 & 0 \\ 0 & \delta' & 0 & 0 & 0 & 0 & 0 & 0 \\ 0 & 0 & \delta' & 0 & 0 & 0 & 0 & 0 \\ 0 & 0 & 0 & 0 & 0 & 0 & 0 & 0 \\ 0 & 0 & 0 & 0 & 0 & 0 & 0 & 0 \\ 0 & 0 & 0 & 0 & 0 & 0 & 0 & 0 \end{bmatrix} \tag{5.2}$$

This Coulomb term has not much effect on the JT symmetry. However, in the previous different charge states C_{60}^{2-} and C_{60}^{4-}, the distortion symmetries over a large range of JT parameters, depend on the values of the Coulomb term. This implies that adding more electrons can have effects on the JT distortion symmetry, but does not give any information about any other different system of different charge states [77].

The vibrational Hamiltonian will again take the same form as has been shown in previous systems. However, the linear Hamiltonian $\mathcal{H}_1$ has the form;

$$-\sqrt{\frac{3}{10}} \begin{bmatrix} 0 & 0 & 0 & \frac{\phi^2}{\sqrt{2}}Q_4 & -\frac{\sqrt{3}}{\sqrt{2}}\frac{1}{\phi}Q_4 & A_1 & Q_6 & -Q_5 \\ 0 & 0 & 0 & -\frac{1}{\phi^2\sqrt{2}}Q_5 & \frac{\sqrt{3}}{\sqrt{2}}\phi Q_5 & -Q_6 & B_1 & Q_4 \\ 0 & 0 & 0 & -\frac{\sqrt{5}}{\sqrt{2}}Q_6 & -\frac{\sqrt{3}}{\sqrt{2}}Q_6 & Q_5 & -Q_4 & C_1 \\ \frac{\phi^2}{\sqrt{2}}Q_4 & -\frac{1}{\phi^2\sqrt{2}}Q_5 & -\frac{\sqrt{5}}{\sqrt{2}}Q_6 & 0 & 0 & 0 & 0 & 0 \\ -\frac{\sqrt{3}}{\sqrt{2}}\frac{1}{\phi}Q_4 & \frac{\sqrt{3}}{\sqrt{2}}\phi Q_5 & -\frac{\sqrt{3}}{\sqrt{2}}Q_6 & 0 & 0 & 0 & 0 & 0 \\ A_1 & -Q_6 & Q_5 & 0 & 0 & 0 & 0 & 0 \\ Q_6 & B_1 & -Q_4 & 0 & 0 & 0 & 0 & 0 \\ -Q_5 & Q_4 & C_1 & 0 & 0 & 0 & 0 & 0 \end{bmatrix} \tag{5.3}$$

where;

$$\begin{aligned} A_1 &= \frac{\sqrt{3}}{\sqrt{2}}\frac{1}{\phi}Q_\epsilon - \frac{\phi^2}{\sqrt{2}}Q\theta \\ B_1 &= \frac{1}{\phi^2\sqrt{2}}Q_\theta - \frac{\sqrt{3}}{\sqrt{2}}\phi Q\epsilon \\ C_1 &= \frac{\sqrt{5}}{\sqrt{2}}Q_\theta + \frac{\sqrt{3}}{\sqrt{2}}Q\epsilon \end{aligned}$$

This linear interaction Hamiltonian has been studied in more detail in ref. [10], and was constructed using the basis states arising from the coupling between T_{1u} and H_u terms. However, the quadratic interaction matrices can be written by making simple substitutions in the linear matrix of the form:

$\mathcal{H}_2(Q^2) \to \mathcal{H}_i(Q \mapsto A_i)$

$\mathcal{H}_3(Q^2) \to \mathcal{H}_i(Q \mapsto B_i)$

with A_i and B_i components, which have been derived again as in ref. [72]

$$\begin{aligned}
A_\theta &= \frac{1}{2\sqrt{6}}(3Q_\theta^2 - 3Q_\epsilon^2 - Q_4^2 - Q_5^2 + 2Q_6^2) \\
A_\epsilon &= -\frac{1}{2\sqrt{2}}(2\sqrt{3}Q_\theta Q_\epsilon - Q_4^2 + Q_5^2) \\
A_4 &= -\frac{1}{\sqrt{6}}(Q_\theta Q_4 - \sqrt{3}Q_\epsilon Q_4 + 2\sqrt{2}Q_5 Q_6) \\
A_5 &= -\frac{1}{\sqrt{6}}(Q_\theta Q_5 + \sqrt{3}Q_\epsilon Q_5 + 2\sqrt{2}Q_4 Q_6) \\
A_6 &= \frac{2}{\sqrt{6}}(Q_\theta Q_6 - \sqrt{2}Q_4 Q_5)
\end{aligned}$$

and,

$$\begin{aligned}
B_\theta &= \frac{1}{2\sqrt{2}}(2Q_\theta Q_\epsilon + \sqrt{3}Q_4^2 - \sqrt{3}Q_5^2) \\
B_\epsilon &= \frac{1}{2\sqrt{2}}(Q_\theta^2 - Q_\epsilon^2 + Q_4^2 + Q_5^2 - 2Q_6^2) \\
B_4 &= \frac{1}{\sqrt{2}}(Q_\epsilon + \sqrt{3}Q_\theta)Q_4 \\
B_5 &= \frac{1}{\sqrt{6}}(Q_\epsilon - \sqrt{3}Q_\theta)Q_5 \\
B_6 &= -\sqrt{2}Q_\epsilon Q_6
\end{aligned}$$

Later, we will find it useful to relate the quadratic interactions to each other with a fixed coefficient V'_{tot} and a mixed angle β by the relations;

$$\begin{aligned}
V'_2 &= V'_{tot}\cos\beta \\
V'_3 &= V'_{tot}\sin\beta
\end{aligned} \tag{5.4}$$

5.2.3 The C_{2h} and D_{2h} symmetry distortions

Similarly, as has been obtained previously for the other differing ions of fullerene, the minimum APES forms a trough of different symmetries in linear coupling.

Table 5.1: The positions of the wells of D_{2h} symmetry of C_{60}^{3-}

Label	a_θ	a_ϵ	a_4	a_5	a_6
A	a_θ	a_ϵ	0	0	0
B	$-s_1$	s_4	0	0	0
C	s_2	$-s_3$	0	0	0
D	$\frac{1}{2}a_\theta$	$-\frac{1}{2}a_\epsilon$	$\frac{1}{\sqrt{2}}s_1$	$\frac{1}{\sqrt{2}}s_2$	$\frac{1}{\sqrt{2}}a_\theta$
E	$\frac{1}{2}a_\theta$	$-\frac{1}{2}a_\epsilon$	$\frac{1}{\sqrt{2}}s_1$	$-\frac{1}{\sqrt{2}}s_2$	$\frac{1}{\sqrt{2}}a_\theta$
F	$\frac{1}{2}a_\theta$	$-\frac{1}{2}a_\epsilon$	$-\frac{1}{\sqrt{2}}s_1$	$\frac{1}{\sqrt{2}}s_2$	$\frac{1}{\sqrt{2}}a_\theta$
G	$\frac{1}{2}a_\theta$	$-\frac{1}{2}a_\epsilon$	$-\frac{1}{\sqrt{2}}s_1$	$-\frac{1}{\sqrt{2}}s_2$	$\frac{1}{\sqrt{2}}a_\theta$
H	$-\frac{1}{2}s_1$	$-\frac{1}{2}s_4$	$\frac{1}{\sqrt{2}}s_2$	$\frac{1}{\sqrt{2}}a_\theta$	$\frac{1}{\sqrt{2}}s_1$
I	$-\frac{1}{2}s_1$	$-\frac{1}{2}s_4$	$\frac{1}{\sqrt{2}}s_2$	$\frac{1}{\sqrt{2}}a_\theta$	$-\frac{1}{\sqrt{2}}s_1$
J	$-\frac{1}{2}s_1$	$-\frac{1}{2}s_4$	$-\frac{1}{\sqrt{2}}s_2$	$\frac{1}{\sqrt{2}}a_\theta$	$\frac{1}{\sqrt{2}}s_1$
K	$-\frac{1}{2}s_1$	$-\frac{1}{2}s_4$	$-\frac{1}{\sqrt{2}}s_2$	$\frac{1}{\sqrt{2}}a_\theta$	$-\frac{1}{\sqrt{2}}s_1$
L	$\frac{1}{2}s_2$	$\frac{1}{2}s_3$	$\frac{1}{\sqrt{2}}a_\theta$	$\frac{1}{\sqrt{2}}s_1$	$\frac{1}{\sqrt{2}}s_2$
M	$\frac{1}{2}s_2$	$\frac{1}{2}s_3$	$\frac{1}{\sqrt{2}}a_\theta$	$\frac{1}{\sqrt{2}}s_1$	$-\frac{1}{\sqrt{2}}s_2$
N	$\frac{1}{2}s_2$	$\frac{1}{2}s_3$	$\frac{1}{\sqrt{2}}a_\theta$	$-\frac{1}{\sqrt{2}}s_1$	$\frac{1}{\sqrt{2}}s_2$
O	$\frac{1}{2}s_2$	$\frac{1}{2}s_3$	$\frac{1}{\sqrt{2}}a_\theta$	$-\frac{1}{\sqrt{2}}s_1$	$-\frac{1}{\sqrt{2}}s_2$

Adding the quadratic coupling constants warps the surface in order to form distinct wells at some minima associated with the symmetry of the distortion. From what has been stated in the previous section, the I_h symmetry may be reduced due to the JT effect, in symmetries like D_{3d},D_{5d},D_{2h} and C_{2h} point groups in ref.[14]. Each symmetry type has a form of the transformed (a_θ, a_ϵ,a_4,a_5,a_6) coordinates, substituted into the Hamiltonian of the system. For example, in ref.[38], it was found that by assuming that a_4=a_5=0 and the other three coordinates are free, gives C_{2h} symmetry and (a_θ, a_ϵ,0,0,0) represents a point of D_{2h} symmetry. In fact, it has been found in ref.[87] that the molecular distortion of the trianion may only represented by D_{2h} or C_{2h} point groups. However, the additional independent coordinate a_6 in C_{2h} distortion can make the analytical expressions for this symmetry more complicated. In addition, most of the quadratic coupling constants gave the C_{2h} distortion and other certain combinations represented the D_{2h} symmetry.

As is known, C_{2h} is a subgroup of the D_{3d}, D_{5d} and D_{2h} point groups, and the remaining coordinates have restrictions in finding minima in the Q space of each symmetry. Tables (5.1,5.2) show the positions of the wells of D_{2h} symmetry, and the complete sets of coordinates of D_{2h} and C_{2h} symmetries as defined in ref. [83]. In these tables,

$$s_1 = \frac{1}{2}(\sqrt{3}a_\epsilon + a_\theta), s_2 = \frac{1}{2}(\sqrt{3}a_\epsilon - a_\theta), s_3 = \frac{1}{2}(\sqrt{3}a_\theta + a_\epsilon), s_4 = \frac{1}{2}(\sqrt{3}a_\theta - a_\epsilon)$$

and;

$$\begin{aligned}
a &= \frac{1}{4}(2a_6 + \sqrt{6}a_\epsilon + \sqrt{2}a_\theta) \\
b &= \frac{1}{4}(2a_6 - \sqrt{6}a_\epsilon + \sqrt{2}a_\theta) \\
c &= \frac{1}{4}(2a_6 - \sqrt{6}a_\epsilon - \sqrt{2}a_\theta) \\
d &= \frac{1}{4}(2a_6 + \sqrt{6}a_\epsilon - \sqrt{2}a_\theta) \\
e &= \frac{1}{4}(\sqrt{6}a_6 - a_\epsilon + \sqrt{3}a_\theta) \\
f &= \frac{1}{4}(\sqrt{6}a_6 + a_\epsilon + \sqrt{3}a_\theta) \\
g &= \frac{1}{4}(\sqrt{6}a_6 + a_\epsilon - \sqrt{3}a_\theta) \\
h &= \frac{1}{4}(\sqrt{6}a_6 - a_\epsilon - \sqrt{3}a_\theta)
\end{aligned}$$

Those wells are identical to the wells defined in ref. [92] of C_{60}^{2+} molecule. By substituting these values of the coordinates, the Hamiltonian associated with each distortion may be constructed. Then, it will be possible to find the minimum energy of the particular distortion by diagonalising the Hamiltonian. This will result in forming eight eigenvalues by considering the distortion given by the C_{2h} subgroup.
The symmetry of the distorted C_{60}^{3-} ion has been found for different values of term splittings δ' in fig. 5.1. It shows the region of validity of the energy function of C_{60}^{3-} ion with D_{2h} and C_{2h} kinds of symmetry. This plot has been calculated numerically by substituting the values of the independent coordinates for C_{2h} distortion into the Hamiltonian system to find the eight eigenvalues. There are no JT distortions inside the solid area for the given values of δ'. Furthermore, the first solid line region around the centre of the plot of term splitting $\delta'=\pm 2.5$ with no JT effects. Then, $\delta'=\pm 3$ for the next outer solid line region, and $\delta'=\pm 4$ for the outer next solid line. The fourth solid lines is the region of validity of the three electrons system. Therefore, the symmetry regions of this ion are independent of the term splitting as in ref. [85].

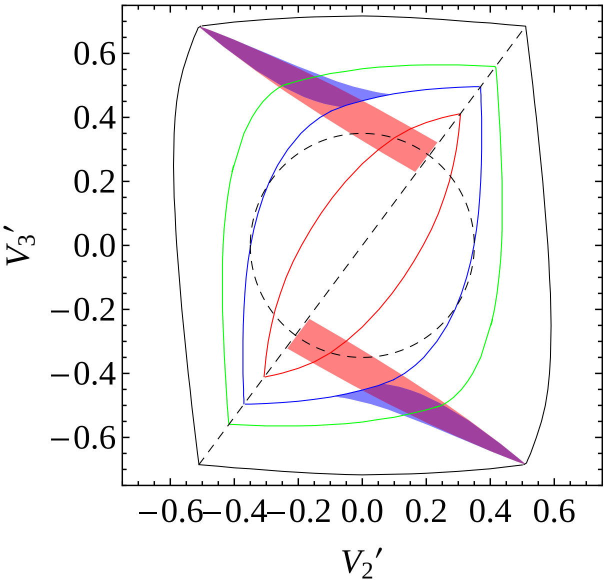

Figure 5.1: The symmetry region of C_{60}^{3-}, where D_{2h} is displayed by colored regions. The pink color displays the D_{2h} symmetry for $\delta'=\pm2.5$ and the blue is for $\delta'=\pm3$. However, the uncolored regions show the molecular distortion of C_{2h} point group, while the rest of the region represents the boundary of the system reproduced from ref. [85].

Table 5.2: The positions of the wells of C_{2h} point group of C_{60}^{3-}

Label	a_θ	a_ϵ	a_4	a_5	a_6
C_1	a_θ	a_ϵ	0	0	a_6
C_2	a_θ	a_ϵ	0	0	$-a_6$
C_3	$\frac{1}{2}(\sqrt{3}a_\epsilon - a_\theta)$	$\frac{1}{2}(-a_\epsilon - \sqrt{3}a_\theta)$	0	a_6	0
C_4	$\frac{1}{2}(\sqrt{3}a_\epsilon - a_\theta)$	$\frac{1}{2}(-a_\epsilon - \sqrt{3}a_\theta)$	0	$-a_6$	0
C_5	$\frac{1}{2}(-\sqrt{3}a_\epsilon - a_\theta)$	$\frac{1}{2}(-a_\epsilon + \sqrt{3}a_\theta)$	a_6	0	0
C_6	$\frac{1}{2}(-\sqrt{3}a_\epsilon - a_\epsilon)$	$\frac{1}{2}(-a_\epsilon + \sqrt{3}a_\theta)$	$-a_6$	0	0
C_7	$\frac{1}{2}(-\sqrt{2}a_6 + a_\theta)$	$-\frac{1}{2}a_\theta$	a	b	$-\frac{1}{\sqrt{2}}a_\theta$
C_8	$\frac{1}{2}(-\sqrt{2}a_6 + a_\theta)$	$-\frac{1}{2}a_\theta$	$-a$	$-b$	$-\frac{1}{\sqrt{2}}a_\theta$
C_9	$\frac{1}{2}(-\sqrt{2}a_6 + a_\theta)$	$-\frac{1}{2}a_\theta$	$-a$	b	$\frac{1}{\sqrt{2}}a_\theta$
C_{10}	$\frac{1}{2}(-\sqrt{2}a_6 + a_\theta)$	$-\frac{1}{2}a_\theta$	a	$-b$	$\frac{1}{\sqrt{2}}a_\theta$
C_{11}	$\frac{1}{2}(\sqrt{2}a_6 + a_\theta)$	$-\frac{1}{2}a_\theta$	c	d	$-\frac{1}{\sqrt{2}}a_\theta$
C_{12}	$\frac{1}{2}(\sqrt{2}a_6 + a_\theta)$	$-\frac{1}{2}a_\theta$	$-c$	$-d$	$-\frac{1}{\sqrt{2}}a_\theta$
C_{13}	$\frac{1}{2}(\sqrt{2}a_6 + a_\theta)$	$-\frac{1}{2}a_\theta$	$-c$	d	$\frac{1}{\sqrt{2}}a_\theta$
C_{14}	$\frac{1}{2}(\sqrt{2}a_6 + a_\theta)$	$-\frac{1}{2}a_\theta$	c	$-d$	$\frac{1}{\sqrt{2}}a_\theta$
C_{15}	$-\frac{1}{\sqrt{2}}a$	$-e$	$-d$	$\frac{1}{\sqrt{2}}a_\theta$	c
C_{16}	$-\frac{1}{\sqrt{2}}a$	$-e$	$-d$	$-\frac{1}{\sqrt{2}}a_\theta$	$-c$
C_{17}	$-\frac{1}{\sqrt{2}}a$	$-e$	d	$\frac{1}{\sqrt{2}}a_\theta$	$-c$
C_{18}	$-\frac{1}{\sqrt{2}}a$	$-e$	d	$-\frac{1}{\sqrt{2}}a_\theta$	c
C_{19}	$-\frac{1}{\sqrt{2}}b$	f	$-\frac{1}{\sqrt{2}}a_\theta$	c	d
C_{20}	$-\frac{1}{\sqrt{2}}b$	f	$-\frac{1}{\sqrt{2}}a_\theta$	$-c$	$-d$
C_{21}	$-\frac{1}{\sqrt{2}}b$	f	$\frac{1}{\sqrt{2}}a_\theta$	c	$-d$
C_{22}	$-\frac{1}{\sqrt{2}}b$	f	$\frac{1}{\sqrt{2}}a_\theta$	$-c$	d
C_{23}	$\frac{1}{\sqrt{2}}c$	g	$-b$	$\frac{1}{\sqrt{2}}a_\theta$	a
C_{24}	$\frac{1}{\sqrt{2}}c$	g	$-b$	$-\frac{1}{\sqrt{2}}a_\theta$	$-a$
C_{25}	$\frac{1}{\sqrt{2}}c$	g	b	$\frac{1}{\sqrt{2}}a_\theta$	$-a$
C_{26}	$\frac{1}{\sqrt{2}}c$	g	b	$-\frac{1}{\sqrt{2}}a_\theta$	a
C_{27}	$\frac{1}{\sqrt{2}}d$	$-h$	$-\frac{1}{\sqrt{2}}a_\theta$	a	b
C_{28}	$\frac{1}{\sqrt{2}}d$	$-h$	$-\frac{1}{\sqrt{2}}a_\theta$	$-a$	$-b$
C_{29}	$\frac{1}{\sqrt{2}}d$	$-h$	$\frac{1}{\sqrt{2}}a_\theta$	a	$-b$
C_{30}	$\frac{1}{\sqrt{2}}d$	$-h$	$\frac{1}{\sqrt{2}}a_\theta$	$-a$	b

Table 5.3: The transforming of individual components in pentagon-prone orientation of C_{60}^{3-}

C_{5v}	E	$2C_5$	$2C_5^2$	$5\sigma_v$	
T_{1uz}	1	1	1	-1	$\rightarrow A_2$
$T_{1ux}+T_{1uy}$	2	ϕ^{-1}	$-\phi$	0	$\rightarrow E_1$
$H_{u\theta}$	1	1	1	1	$\rightarrow A_1$
$H_{u\epsilon}+H_{u6}$	2	$-\phi$	ϕ^{-1}	0	$\rightarrow E_2$
$H_{u4}+H_{u5}$	2	ϕ^{-1}	$-\phi$	0	$\rightarrow E_1$

Table 5.4: The transforming of individual components of hexagon-prone orientation for C_{60}^{3-}

C_{3v}	E	$2C_3$	$3\sigma_v$	
T_{1uz}	1	1	-1	$\rightarrow A_2$
$T_{1ux}+T_{1uy}$	2	-1	0	$\rightarrow E$
$H_{u\theta}$	1	1	1	$\rightarrow A_1$
$H_{u\epsilon}+H_{u6}$	2	-1	0	$\rightarrow E$
$H_{u4}+H_{u5}$	2	-1	0	$\rightarrow E$

5.3 The surface interaction

Similar to what was done for C_{60}^{2-}, the surface interaction Hamiltonian will be included together with the JT Hamiltonian to find positions of minima and electronic states numerically. After finding the lowest in energy, the eigenvectors will be used to show STM images for the C_{60}^{3-} molecule in different orientations. This will be investigated in this section.
Again, using group theory is very useful to determine how the LUMO orbitals in case of C_{60}^{3-} molecule will split. The following will give an idea about the transformation of each orbital in several orientations.

- Pentagon-prone orientation

Concentrating on the LUMO of C_{60}^{3-}, From either the actual MOs or from the basis functions, the transformation of individual components is given in Table 5.3 where LUMO components transform to u rather than g in C_{60}^{2-} and C_{60}^{4-} ions.
The z–component of T_{1u} has switched to A_2, compared to A_1 for T_{1u} in case of C_{60}^{-} in ref.[25]. Similarly, $H_{u\theta}$ has switched to A_1, compared to A_2 for $H_{u\theta}$, as in Table 5.3. $H_{u\epsilon}$ and H_{u6} will form the first two dimensions and H_{u4}, H_{u5} will form the other two dimensions.

- Hexagon-prone orientation

In this orientation, the transforming of individual components will be shown in Table 5.4.

Table 5.5: The transforming of individual components of double-prone orientation of C_{60}^{3-}

C_{2v}	E	C_2	$\sigma_v(xz)$	$\sigma_v^{'}(yz)$	
T_{1uz}	1	1	-1	-1	$\rightarrow A_2$
T_{1ux}	1	-1	-1	1	$\rightarrow B_2$
T_{1uy}	1	-1	1	-1	$\rightarrow B_1$
$H_{u\theta}$	1	1	1	1	$\rightarrow A_1$
$H_{u\epsilon}$	1	1	1	1	$\rightarrow A_1$
H_{u4}	1	-1	-1	1	$\rightarrow B_2$
H_{u5}	1	-1	1	-1	$\rightarrow B_1$
H_{u6}	1	1	-1	-1	$\rightarrow A_2$

Again $A_1 \rightarrow A_2$ for the z–component of T_1. $(H_{u4} + H_{u5})$, and $(H_{u\epsilon} + H_{u6})$ form two dimensions transformation E, which cannot be distinguished on symmetry grounds. The same components pair together, as with H_u in ref. [25]. This repeated representation implies that there are two states that should have different energies. Actually, the resultant splitting of the LUMO is always the same for both pentagon and hexagon-prone cases.

- Double bond-prone orientation

In the case of double bond-prone orientation, the transforming of individual components take the form as in Table 5.5.
This double bond case is different than the pentagon and hexagon-prone cases, as the reduced symmetry of the molecule does not support the two dimensions transformation.

5.4 STM pictures of C_{60}^{3-} due to surface and JT interactions

Similarly, the Hamiltonian of the C_{60}^{3-} system will be investigated to find the minima and the associated energy. Again, The external effect from the surface that distorts the molecule is as important as the JT interaction.

Our focus as mentioned previously, is to continue with these investigations using the same possible particular orientations, such as (C_2,C_3,C_5) depending on the form of rotational axis, which is aligned to the surface . As a result, the positions of the minima will also change due to the change in the electronic coordinates. At the end, the STM images will be generated and interpreted, as well as compared with images taken from observation.

By applying the same method as described in the previous chapter for the double-charged ion, the surface Hamiltonian will take a very simple form after deleting the constant $(-\Delta_1 - \Delta_2)$ for each diagonal element, which is only alters the zero energy, then the form will be;

$$H_S = \begin{bmatrix} 0 & 0 & 0 & 0 & 0 & \Delta_2-\Delta_1 & 0 & 0 \\ 0 & 0 & 0 & 0 & 0 & 0 & \Delta_1 & 0 \\ 0 & 0 & 0 & 0 & 0 & 0 & 0 & -\Delta_2 \\ 0 & 0 & 0 & 0 & 0 & 0 & 0 & 0 \\ 0 & 0 & 0 & 0 & 0 & 0 & 0 & 0 \\ \Delta_2-\Delta_1 & 0 & 0 & 0 & 0 & 0 & 0 & 0 \\ 0 & \Delta_1 & 0 & 0 & 0 & 0 & 0 & 0 \\ 0 & 0 & -\Delta_2 & 0 & 0 & 0 & 0 & 0 \end{bmatrix} \tag{5.5}$$

This specific form has already been calculated directly from the basis states of Fowler and Ceulemans; in short, there is no need for any other additional transformation, and the off diagonal terms due to T_{1u} and H_u have common representation. This is except the rotation matrix U_H in eq. (4.55), which needs to transform to the Fowler and Ceulemans basis, in order to rotate to pentagon or hexagon basis. This new rotation matrix can be written in block form as;

$$U_{TH} = \left[\begin{array}{c|c} U_T & 0 \\ \hline 0 & S_{CF}.U_H.S_{CF}^T \end{array}\right] \tag{5.6}$$

where U_T and U_H are given in eq.(3.12) and eq.(4.55). So that the required Hamiltonian is $U_{TH}H_SU_{TH}^T$. In case of pentagon and hexagon prone Δ_2 in eq. (5.5) is equal zero. In addition, in double-prone orientation, all singlets (A_1, A_2, B_1, B_2) are repeated twice, so this allows any required mixing between T_{1u} and H_u in general. This very simple form will be used in the following section to match the published results in ref.[18], when the hexagon prone faces the surface.

5.4.1 Pentagon and hexagon orientations

The C_{60}^{3-} STM images, which appear from the LUMO, are linear combinations of T_{1ux}, T_{1uy}, T_{1uz}, $H_{u\theta}$, $H_{u\epsilon}$, H_{u4}, H_{u5}, H_{u6}. Starting with the parameters preferring C_{2h} symmetry, the wells generated depend on the values of the quadratic coupling constants; this makes the identification of these wells more complicated. The results in C_{2h} symmetry display different JT strengths in direction due to different form of the wells, such as centred around pentagon, where V_2'=-0.4,V_3'=0; around double bond in direction of pentagon, where V_2'=0,V_3'=0.2; around double bond in direction of hexagon V_2'=0,V_3'=0.5; and around hexagon V_2'=0.2,V_3'=0.6 as in fig. 5.1. On symmetry grounds, the 30 wells representing this distortion, as defined by the T-components of the electronic parts, should be placed on one of the circles along the two vertices of the double bond. For the allowed ranges of JT parameters, the wells will be shown in the same grouping of different orientations. In case of C_5 orientation, the equal global minima energy wells, are in two groups of ten points, and another two of five. On the other hand, the C_3 orientation is represented by four groups of points, where each has six wells, and the other two groups with three wells each. Therefore, the molecule will pseudorotate and hop between these global minima.

From fig. 5.1, it is clear that the term splitting has no noticeable effect on the coefficient contribution of the wave function. Therefore, as long as δ' increases, the JT coupling between T_{1u} and H_u will decrease at large positive or negative values of the surface.

Figure 5.2 showing the contributions of the three coefficients (a_{3x},a_{3y},a_{3z}) of LUMO components (ψ_x^2,ψ_y^2,ψ_z^2), for different values of the surface interactions parameter Δ_1, will be used to investigate the results obtained for the JT distorted C_{60}^{3-} ion moving between equivalent wells.

From these results in fig. 5.2, it is clear that, the STM images depend on the strength of the surface interaction and that two of the electrons occupy the z state when the surface interaction tends to infinity. As a consequence, in this case, the JT effect has a weak contribution and can be neglected.

The figures between the coefficient via the strength of the surface show that the greater the increase in surface interaction, the more these wells move toward x-y plane. But we cannot represent the states on a sphere because of their high dimensionality.

The diagrams for C_{60}^{3-} molecule, which show the coefficient via Δ_1 for C_{2h} pentagon prone, are very similar to each other, and the asymptotic limit for the parameters is 0.66. From the electron distribution, if the contribution of any state equal zero, the possibilities of the other two around $\frac{1}{3}$ and $\frac{2}{3}$. Therefore, purely x or y or z STM images of this ion are unexpected.

The dominant a_{3z} coefficients are in the positive surface interaction, while a_{3x} and a_{3y} will be dominant in the negative values of the surface interaction. All the

Table 5.6: The groups of minimum wells of D_{2h} symmetry of the C_{60}^{3-} molecule, where surface interaction is applied, here C_3,C_5 and C_2 is perpendicular to the surface respectively

Orientation	D_{2h}
C_5	(A,B,C,G,H),(D,E,L,M,O),(F,I,J,K,N)
C_3	(A,J,K),(B,M,I),(C,F,L),(D,E,N),(G,H,O)
C_2	A,N,O,[(B,D),(C,E)],[(F,H),(G,I)],[(J,L),(K,M)]

other diagrams have a very small dependence on the quadratic coupling constants, thus no more diagrams will be added. It also shows that the contributions from a_{3x} and a_{3y} are equal, which is in agreement with that expected in pentagon and hexagon orientations. Part (b) of fig. 5.2 shows a sharp jump between different sets of minima in case where the pentagon face the surface. This further jump around Δ_1=6, implies that, different sets of minima wells have equivalent energies which allow a free pseudorotation between the wells.
Therefore, different strengths of surface interaction will produce different predicted STM images due to different distributions of the wells.

The other kind of symmetry for JT parameters prefers D_{2h} distortion in fig. 5.3, the system displays a picture similar to the case considered above, as shown in fig. 5.2 over all the JT coupling constants region of D_{2h} symmetry.
The 15 different wells of D_{2h} in the centre of the double bond are shown in fig. 5.4. The surface acting on this ion along the z axis can pick different groups of equivalent wells according to the face down orientation. Table 5.6 displays these groupings in the $x - z$ plane, which was defined from the T-parts of the eigenvectors to be visualized in 3-dimentions as was discussed for the previous symmetry C_{2h}. This distribution is confirmed after H-part added as shown in fig. 5.3. Each group of vertices in each orientation in the table can be reflected to the others, according to the direction of the rotation in the $x - z$ plane.
Again, the asymptotic limit for the parameters is the same as C_{2h} symmetry. The STM images for C_{2h} symmetry in fig.5.5 are similar to D_{2h} for the same orientation as D_{2h} always shows five wells equal global minima energy for both positive and negative strengths of the surface interaction as in Table 5.6, which corresponds to one of the five equivalent distortions for positive surface interaction. As a result of increased dynamic freedom, the system is allowed to hop between different equivalent wells. Another case will be studied, when the system with JT coupling parameters preferring C_{2h} distortion is adsorbed onto a surface with a hexagonal face of the molecule directed towards the surface. Similar to the pentagon-prone orientation, hopping between the wells is taken into account. The contributions of the different coefficients are similar as in the pentagon prone orientation with also a very small alterations in the numerical values

of their coefficients.

For all positive values of Δ_1, and whatever the strength of the surface, the results will remain the same. However, the change in the coefficients in fig. 5.5 has no effect on the images, which is similar to C_{60}^{2-} for the same orientation. A similar conclusion for both D_{2h} and C_{2h} distortions was reached, in that it is not possible to distinguish between surface interaction and pseudorotation effects.

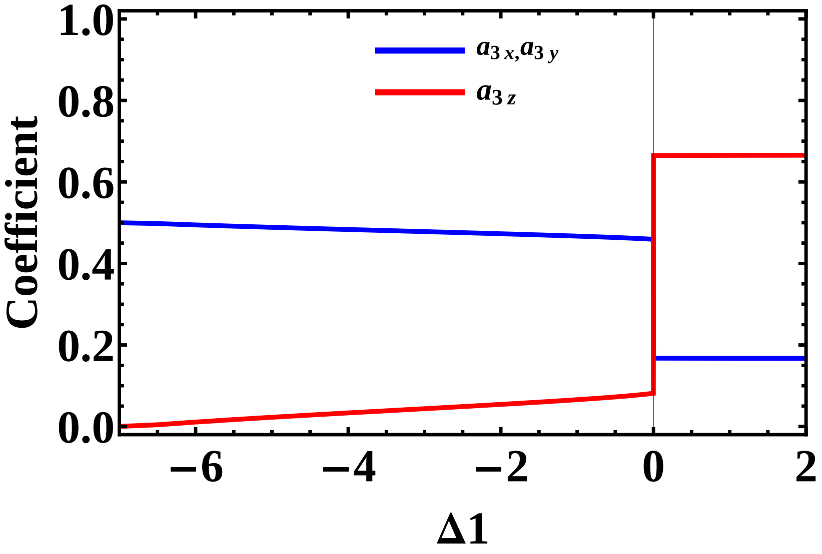

(a)

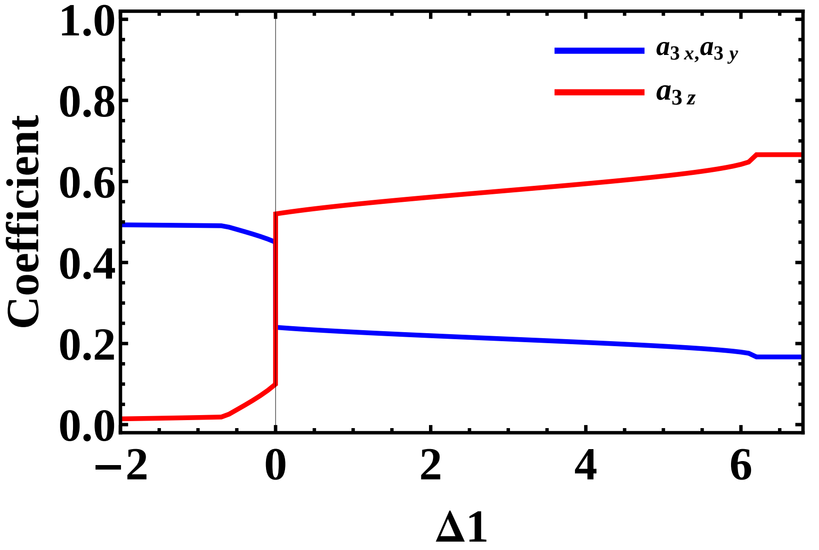

(b)

Figure 5.2: (a)The contribution of ψ_x^2,ψ_y^2,and ψ_z^2 of the wavefunction of C_{60}^{3-} of C_{2h} symmetry, C_3 orientation via different strengths of the surface Δ_1 for δ'=1, V_2'=0.2, V_3'=0.6(b) for C_5 orientation

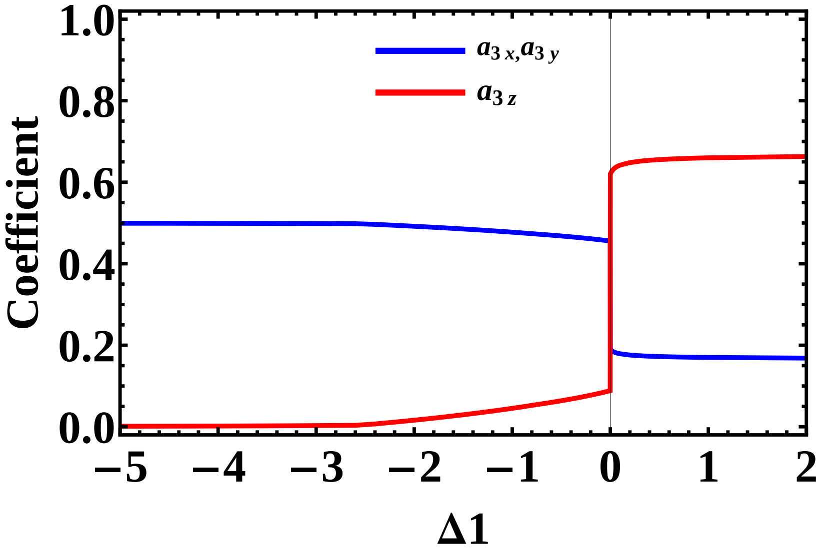

(a)

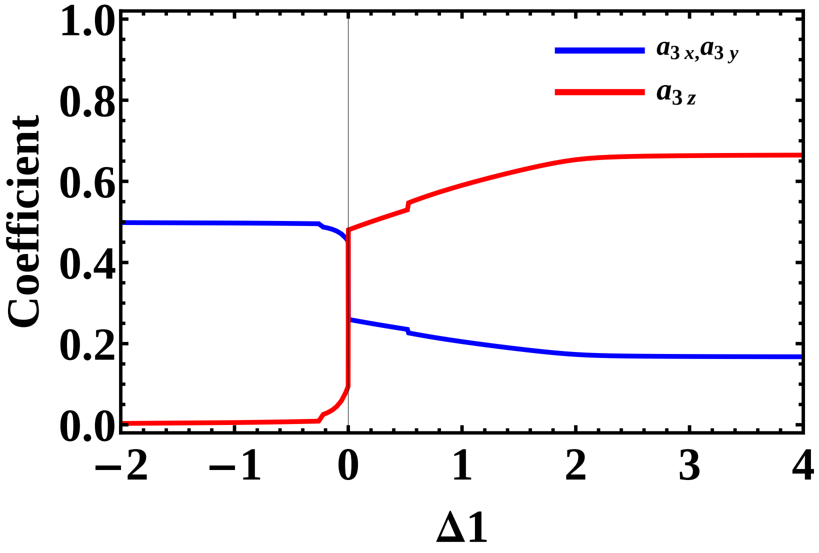

(b)

Figure 5.3: (a) The contribution from ψ_x^2,ψ_y^2,and ψ_z^2 of the wavefunction of C_{60}^{3-} of D_{2h} symmetry, C_3 orientation of V_2'=0.4, V_3'=0, via different strengths of the surface Δ_1 for δ'=1, (b)C_5 orientation

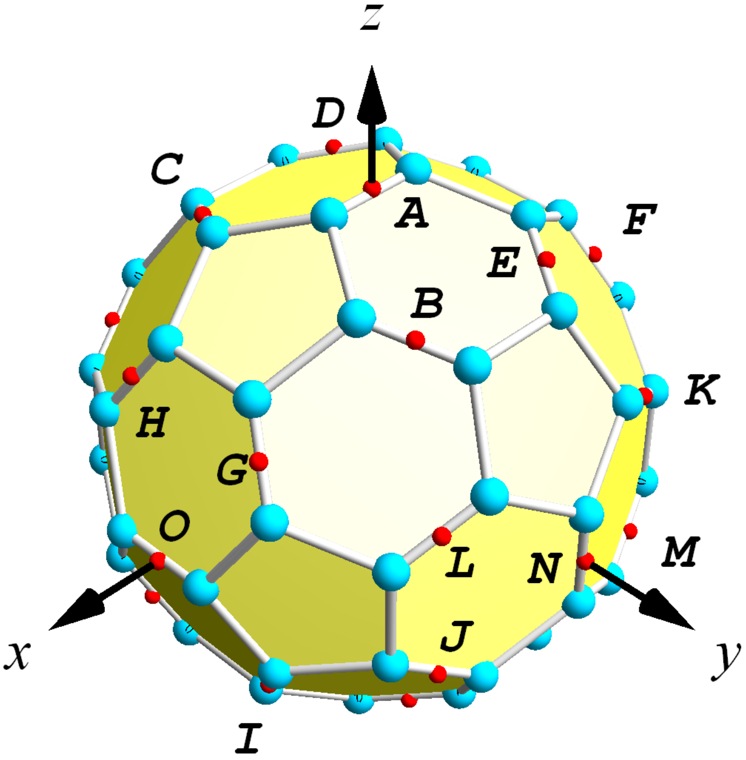

Figure 5.4: The D_{2h} wells distribution in the centre of the double bond reproduced from ref. [77]

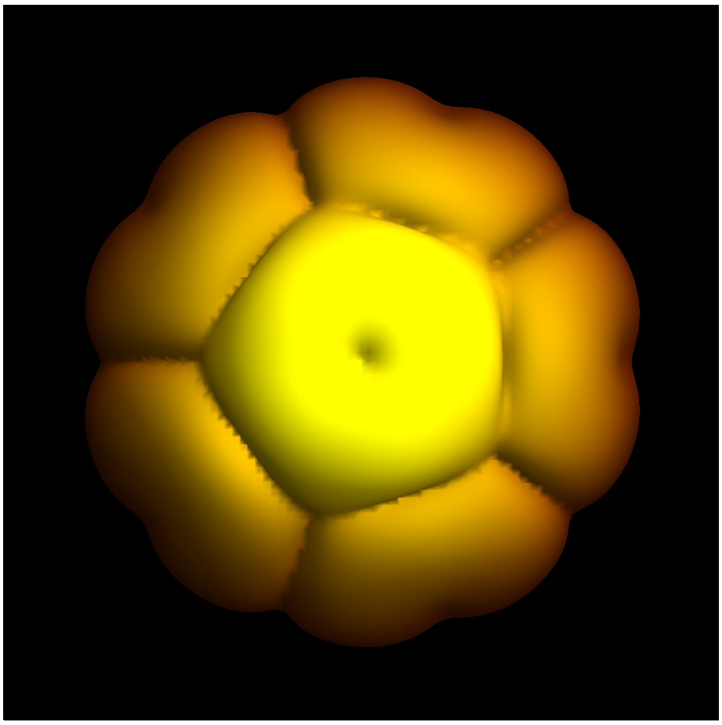

Figure 5.5: The expected STM image of the C_{60}^{3-} ion of C_{2h} symmetry of C_5 orientation of parameters V_2'=0.2, V_3'=0.6, δ'= 1,Δ_1'= 1

5.4.2 Double bond-prone orientation

The more complicated aspect in this type of orientation consists of the two unknown parameters of the surface Δ_1 and Δ_2, in addition to the term splitting δ' and the two coupling constants parameters. In order to manage the system of this complicated orientation, it will be worth considering the special case, when Δ_2 is equal to zero first, then examine the contribution from each coefficient of the wavefunction.

Therefore, in this special case of the system, when Δ_2=0 and $\Delta_1 < 0$, the parameters preferring C_{2h} distortion will favour different sets of wells. In fact, six groups of four points and three other groups each with two points have been shown in the orientation through the double bond, as described in previous section. However, other sets of patterns for the D_{2h} symmetry exist, as in Table 5.6.

The surface parameter Δ_1 as shown in fig. 5.6(a) has not much effect, and the expected STM consists of combinations of x and y with a very small amount of z, as in fig. 5.7.

On the other hand, in case of $\Delta_1 > 0$, when the parameters prefer C_{2h} distortion, the wells will be toward the z-axis in both planes $x - z$ and $y - z$. Whereas, with $\Delta_1 < 0$, the contributions from each coefficient of the wavefunction of C_{60}^{3-} of C_{2h} and D_{2h} symmetries to the STM images depend on the Δ_2 parameter.

Additional results are observed in the case where Δ_2 is taken into account as shown in fig. 5.6(b). For $\Delta_1 < 0$ of C_{2h} distortion, the results will be affected by the presence of Δ_2. Then, the minimum wells this time will track in the $x - y$ plane to the x-axis and the contribution from ψ_x will be more dominant when Δ_2 decreases compared with ψ_y, which decreases with the more negative Δ_2. Also, most of the contributions will be for ψ_y for positive Δ_2 with different values from Δ_1.

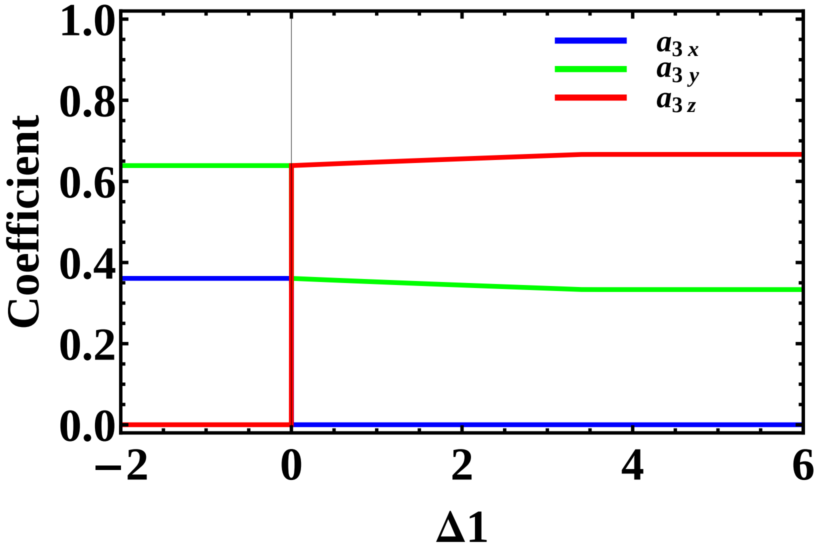

(a)

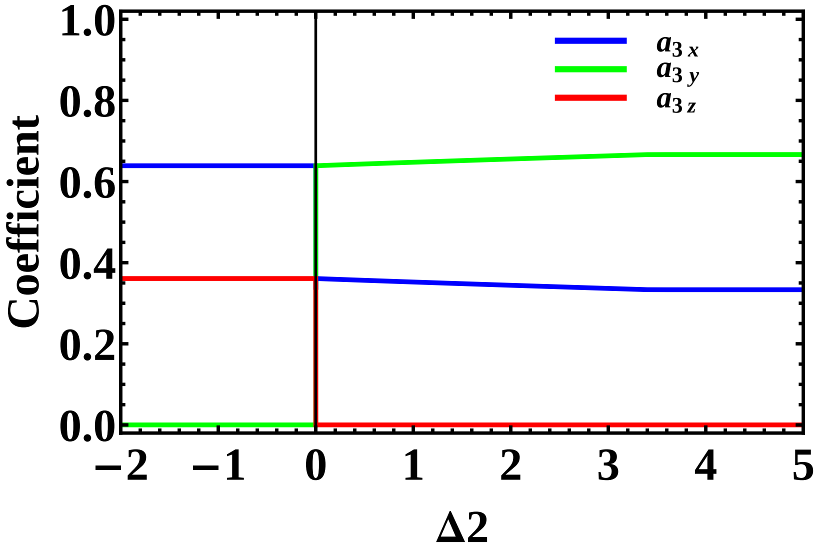

(b)

Figure 5.6: (a) The contribution from ψ_x^2,ψ_y^2,and ψ_z^2 of the wavefunction of C_{60}^{3-} of C_{2h} symmetry, C_2 orientation of V_2'=0.2, V_3'=0.6, via different strengths of the surface Δ_1 for δ'=1, Δ_2=0 (b) the same case for different range of Δ_2 when Δ_1=0

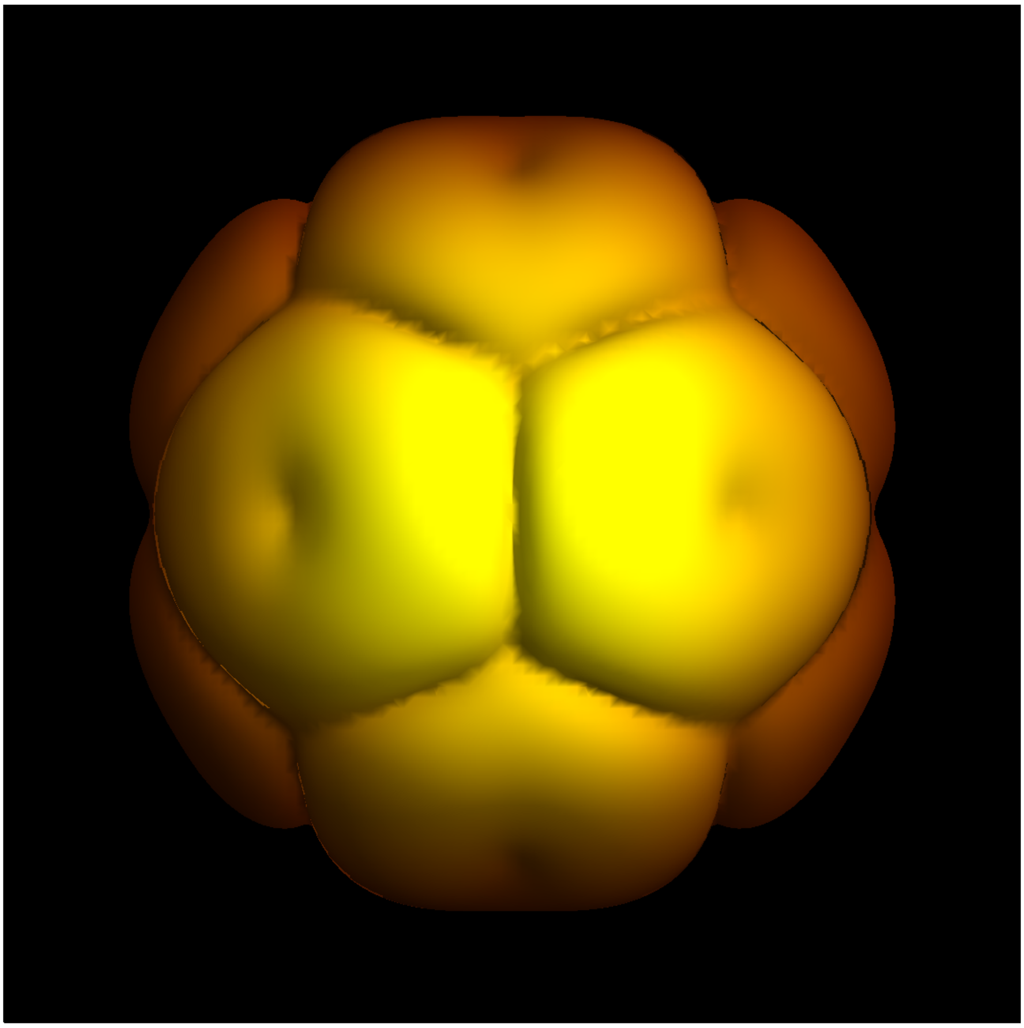

Figure 5.7: The expected STM image of the C_{60}^{3-} ion of C_{2h} symmetry of C_2 orientation of parameters V_2'=0.2, V_3'=0.6, δ'= 1,Δ_1= 0.5

5.5 Discussion and conclusion

In this chapter, work on the trianion fullerene C_{60}^{3-} in references [86],[14],[87] has been extended. In order to make it simpler, the Hückel molecular orbital approach has been used to simplify the calculations. The electronic basis of the system followed by the JT interaction Hamiltonian in linear and quadratic distortions have been investigated as a first step.

It was found that for all of the orientations of interest, any observed STM images generated from the LUMO have been composed of some linear combination of electronic basis (T_{1ux}, T_{1uy}, T_{1uz} ,$H_{u\theta}$, $H_{u\epsilon}$, H_{u4}, H_{u5}, H_{u6}), whatever the symmetry or the strength of the surface interaction.

The wells in this triply charged ion C_{60}^{3-} favoured two kinds of distortions, D_{2h} or C_{2h}, depending on the values of quadratic JT coupling constants. The surface interaction Hamiltonians for the pentagon, hexagon and double-bond prone have been defined simply from $T \otimes h$ single electron problem. This work has been included some diagrams to introduce the behavior of the anion and the contributions from each part of the LUMO wavefunction when a pentagonal prone face to the surface for positive and negative surface interaction of both D_{2h} and C_{2h} symmetries. Then the results have been given when the same method was used for C_{60}^{3-} molecules in the hexagonal orientation, which have also included the cases where the system was assumed to hop between wells in pseudorotation process, which cannot be distinguished from surface effect.

STM images have been simulated for different orientations in order to match what has been published with filled and empty states in ref. [18] with orientation along the hexagon-prone C_3. We expect, the values of the coupling constants in terms of matching with ref. [18] almost the same in the different charged states because they are not dependent on the number of electrons. However, the symmetry of the distorted ions which related to the Coulomb interactions is alter between different systems. For example, Figures 4.21 and 4.20 show the case of changing the symmetry from D_{3d} to D_{5d} after adding other electron for the same values of JT coupling V_2'=V_3'=-0.6.

Chapter 6

Matching the theoretical results to Wachowiak *et al*

6.1 Introduction

Most of the measurements of STM images involve the neutral molecule C_{60}, which is not subject to the JT effect as known. As charge transfer may potentially occur in any system in which C_{60} is adsorbed onto a metallic surface, therefore, it is worth looking at STM images in the literature that may match those obtained in this work using any substrate combination or doping level. In fact, the theoretical results can help provide a good explanation about the images observed experimentally.

The agreement between the simulated images of C_{60}^{4-} molecule, which have been made using DFT and other approaches, is generally consistent with References [19],[20]. The theoretical images for C_{60}^{2-} and C_{60}^{4-} are different to C_{60}^{-}, if the JT effect is considered as a means of generating wells of a given symmetry. The term splitting does not alter the symmetry of the wells. However, Wachowiak *et al* in ref. [18] seems to get results for C_{60}^{4-} due to JT effect in D_{2h} wells. The JT effect alone is not expected to produce D_{2h} wells. However, any splitting in addition to JT effects could also explain their results, e.g surface interaction or nearest-neighbour interaction could have caused the additional splittings in C_{60}^{4-}.

The aim of this section is to match our theoretical results to the experimental images published in 2005 as shown in Wachowiak's image in fig.6.1 of the empty states of C_{60}^{4-}, should equivalent to those of the filled states of the doubly charged C_{60}^{2-} ion. In fact, as was discussed before, because the Hamiltonians of $p^2 \otimes h$ and $p^4 \otimes h$ are the same, thus the Q's, which minimise C_{60}^{2-} energy will be used. This will require setting up the unknown JT and the surface interaction parameters to specify the C_{60}^{4-} isolated molecule. These parameters will include (V_2', V_3'),

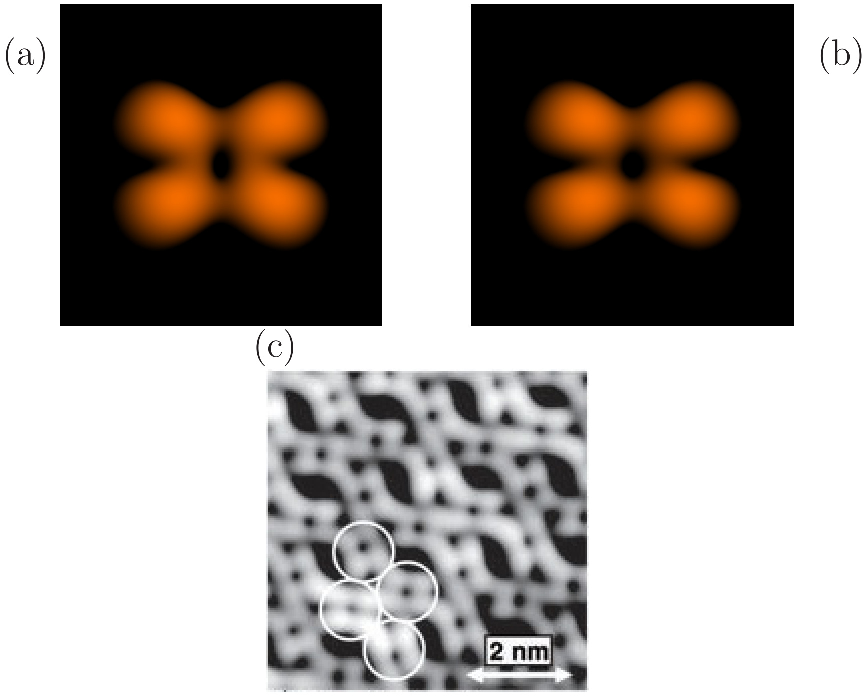

Figure 6.1: (a) and (b) show the STM images for C_{60}^{2-} molecule double bond-prone distorted into D_{3d} symmetry, for currents $I = 0.0139x^2 + 0.8765y^2 + 0.1095z^2$ and $I = 0.0365x^2 + 0.9627y^2 + 0.0007z^2$, while the image in (c) is the experimental STM image expected of Au[111] as in ref. [18].

which represent both the type and the strength of the quadratic JT effect, and also the Coulomb splitting term δ' of the two electron states. In addition, other parameters for different orientations (C_2,C_3,C_5) will be needed in case a surface is applied. The image in the Science paper in ref. [18] appears to be of the double bond prone orientation. The plan of the work will concentrate on finding the regions of validity of the JT parameters, which are valid to describe the ion with different circumstances covering all types of distortion. On the other hand, the surface interaction parameters equally will involve producing the theoretical image, which will reveal more secrets about the image published in ref. [18] and reproduced in fig.6.1(c). However, our target in this part is to concentrate on interpreting our theoretical results compared to the experimental images published in the same paper in ref. [18].

6.2 C_{60}^{4-} on some surfaces

The Wachowiak *et al* STM images in the Science paper [18] belong to the C_{60}^{4-} ion with a positive sample bias of the empty states. It seems to have two reflection plane of symmetry in the image, which represents the orientation along the double-bond C_2. The more complicated part in this type of orientation involves the two unknown parameters of the surface. From the calculations, which have been done regarding the basis, it was assumed that the interaction from the surface splits these basis sets (x_1x_2,y_1y_2,z_1z_2,H_{g4},H_{g5},H_{g6}), with two parameters from the surface, two coupling parameters from the JT effect and one term splitting from the two electron states. The matching process depends on altering these parameters in order to find the possible regions of matching. Mathematically, from the wells distribution in the JT problem, the possible combination of states, which would interact to produce these possible regions of matching are the contribution of (A_g,$H_{g\theta}$,$H_{g\epsilon}$); in other words, (x_1x_2,y_1y_2,z_1z_2) states only without any other states and any cross terms involved, as the elements of the off diagonal matrix are zero. This leads us to set Q_4=Q_5=Q_6=0, so it might be possible to consider these non-contributing states at very high energy, and then any surface parameters associated can go to ∞.

However, in the case of any other contributions from different basis, then two equivalent minima are expected in order to cancel any cross terms. Therefore, the three eigenvalues will need be to checked so as not to be the lowest in energy. This will make the system more manageable as the number of unknown parameters is reduced, which also has an effect on the matrix dimension, reducing from six to three. Then, at the end, the three surface parameters will remain, the δ', describing the term splitting between (A_g and H_g) and Δ_1, Δ_2. More specifically, the direct integration method will be used here and possible ranges of combinations of a_{2x}, a_{2y} and a_{2z}, which promise that a good match to the published STM images will be found numerically. In the end, from the basis states, the STM current should be almost in ψ_y^2 in the rate between 86% and 97%, and at least 70%, from the remaining contribution will go to ψ_x^2 and there is a very small chance for ψ_z^2 to be involved as shown in fig.6.2. In Wachowiak's *et al* work, the D_{2h} theoretical simulation is only of y^2. However, it was found theoretically in this model that the matching with experimental data could be obtained from the D_{3d}, D_{5d} and D_{2h} JT lowest energy symmetry distortions where their energies are equal at $V_3' = \frac{2}{\sqrt{5}} V_3'$ line as in fig. 6.2. These plots are very similar to each other for different values of JT coupling constants. In fact, along this line, is a continuous trough of equivalent wells and the agreement between our calculations with the experimental evidence can put the JT parameters around the equally energy line above. In addition, References [93] [94] assumed that the energies of these symmetry distortions are very near to each other. The following section will include the steps of the matching process.

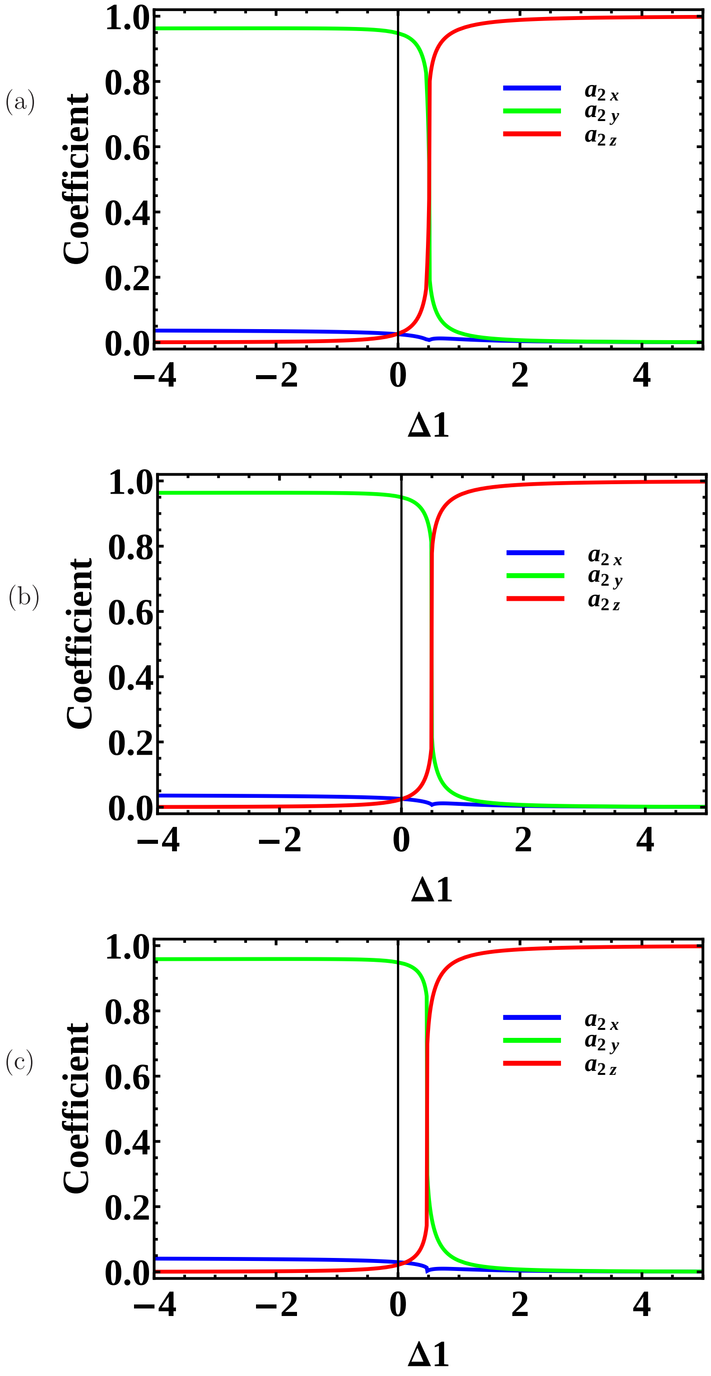

Figure 6.2: The contribution from each coefficient of the current of C_{60}^{2-}, C_2 orientation for different strengths of the surface Δ_1 for δ'=1 and Δ_2=0.5, (a) for D_{3d} symmetry of V_2'=0, V_3'=0.1 ,(b) for D_{5d} symmetry of V_2'=0.1, V_3'=0 and (c) for D_{2h} symmetry of V_2'=-0.5, V_3'=0.1

6.2.1 A finite contribution of z^2

In order to have further discussions of the term splitting parameters effect, it will be useful to consider the case in which the $(z_1 z_2)$ state is really high in energy as $\Delta_2 \rightarrow \infty$. This will reduce the parameters to four, and the eigenvalue matrix order will decrease to 2D. As a result, only $0.86 \leq a_{4y} \leq 0.97$ will need to be considered, as the contribution from ψ_z^2 is zero. By normalisation, the contribution from a_{4x} + the contribution from a_{4y} =1.
After the relaxation made in the previous section from the zero contribution of ψ_z^2, the finite energy ψ_z^2 state will need to be taken into consideration. This means that there will be an additional parameter Δ_2 to be added, and the three dimensional matrix eigenvalue should be solved. In fact, not much rich information is expected. However, it is worth displaying a region in the Δ_1-Δ_2 plane, in which matching could be possible in the V_2'-V_3' plane. The upper bound of this region can be caused by allowing each possible contribution of each part of the current, such as a_{4y} that is between 86%-97% and so a_{4x} can take 70% of the remaining amount, and then a_{4z} should keep the relationship between these 3 parameters, which is that a_{4x}+ a_{4y}+a_{4z}=1. It is necessary to agree that it is unlikely to find any negative values for the surface parameters, Δ_1-Δ_2, because at the final state there should be enough contribution from ψ_y^2 state to allow the matching process go further. As a result, the ψ_y^2 state should always be in the lower energy of the final state, in order to collect most of electrons. This assumption has been proved numerically with the term splitting about 1, overall a big range of surface parameters is less than zero. Also, due to the maximum and minimum possibility in the condition describing a_{4y}, this leads to an interval in Δ_1, which can support the match, and an interval out of the matching area.

In general, for a big range of the term splitting, the numerically calculated regions of validity have shown that Δ_1 is always less than Δ_2 and also the region of validity with Δ_2=20 is similar to the intervals found in case of $\Delta_2 \rightarrow \infty$. Extra calculations have been done showing that the matching regions in the JT parameter plane lie across the symmetry boundaries, which make any display of any matching points in the space of JT parameter meaningless. Finally, the size of the matching area is not the same in the different parameter points of the $(V_2'$,$V_3')$ plane. In short, it is possible to get matches either with V_2' or V_3' dominant. This implies that from the way of modelling C_{60}^{2-} and C_{60}^{4-}, it is possible to match our currents with that published either from D_{3d} wells with Δ_2 greater than zero or can be small negative values, or from D_{5d} wells with Δ_2 less than zero or small values greater than zero. In addition, non-conclusive evidence has indicated that $T \otimes h$ JT system preferred D_{3d} distortions [22]; however, the presence of the surface or the different charged state could create a difference in the quadratic constants, which is unlikely. However, due to the dynamic JT interaction, it would be expected for the surface interaction to prefer two minima for further lowering their symmetry to C_{2h} distortions.

6.3 C_{60}^{3-} on some surfaces

The theoretical images for C_{60}^{2-} and C_{60}^{4-} are similar to C_{60}^{3-} images, if we consider the JT effect as the main generator of the wells for given symmetries.

Now, the Q's which minimise C_{60}^{3-} energy will be used, and then setting up the unknown JT and the surface interaction parameters to specify the C_{60}^{3-} isolated molecule will be required.

We now consider the Wachowiak *et al* STM observations, in the published paper [18], that belong to the C_{60}^{3-} anion with filled and empty states. These two empty and filled states look similar to each other due to the half filled *p*-orbital state. Also, the JT effect is the same in both states. However, the only change could be in the strength of the surface interaction, which can affect the brightness of the images. This observation is different to the filled and empty images of C_{60}^{4-}, where they are different to each other. It seems that the orientation is along the hexagon-prone C_3 due to the threefold symmetry.

The calculations of the basis assumed that interaction from one parameter from the surface and the two coupling parameters from JT effect and one term splitting between the combination T_{1u} and H_u. The matching process depends on altering these parameters in order to find the possible regions of matching. Mathematically, from the wells distribution in JT problem, the possible combination of states, which would interact to produce these possible regions of matching are a contribution of $(\psi_x^2, \psi_y^2, \psi_z^2)$ states.

The limited unknown parameters make the system more manageable; the one surface parameter Δ_1, which shows the splitting between x and z and the term splitting δ' with the JT coupling constants, will remain. It was found that the term splitting is unlikely to alter the symmetry of the wells.

More specifically, the direct integration method will be applied and the possible combinations of a_{3x}, a_{3y} and a_{3z} will be found numerically, which will show a good match to the published STM images.

Qualitative matching calculations should start by seeking possible values for the current coefficients a_{3x}, a_{3y} and a_{3z}. From the basis states, the possible STM current should be almost in ψ_z^2, while the contribution from a_{3z} can vary between 33% and 66 %, and the remaining will go to ψ_x^2 and ψ_y^2 with equal chance for $a_{3x} = a_{3y}$ to be involved in maintaining the relationship between these 3 parameters, which is that $a_{3x}+ a_{3y}+a_{3z}=1$. These results are expected and associated with the Pauli principle of the three electrons distribution in states, as the state could have up to $\frac{2}{3}$ chance, more than the other two, to be in the lowest state of energy.

Now the eight dimensional matrix eigenvalue should be solved. It was found that the best match values for the surface parameter Δ_1 should always be positive, in order to collect enough contribution from the ψ_z^2 state to promote the matching calculations forward and to keep ψ_z^2 state at the lowest energy compared to the other states ψ_x^2 and ψ_y^2, in order to shift the coordinates towards the z-axis. Because the distinct states are at different energies, due to the extra dimensions of the basis for the higher charged states, determining the available region of the splitting term δ' will be required. This interpretation has been proved numerically with a large region of δ', indeed, big positive ranges overall of surface parameter Δ_1. The interpretation with experimental data is possible in any regions. Moreover, similar to C_{60}^{4-}, the size of the matching area is not the same in the different parameter points of the (V_2',V_3') plane. In short, it is possible to get matches either with V_2' or V_3' dominant, and these can be chosen to prefer the type of the symmetry for the anion. Then, determining the allowed combinations between JT and the surface parameters, which can produce the required current for matching. Indeed, the parameters, which set the ψ_z^2 state in the lowest energy of the hexagon-prone, have been found in fig. 6.3. It was determined that the interpretation with the experimental results can be generated from C_{2h} and D_{2h} symmetry operations. Figure 6.3(c) shows the best match when $a_{3z}=\frac{1}{3}$, giving the current $I = \frac{1}{3}(x^2+y^2+z^2)$, which can match the dark image (a) for the filled states, while the image in (d) represents the same case associated with the light empty states image in (b) when the coordinates are shifted to maximum possible value towards the z-axis to generate a current $I = 0.1682x^2+0.1682y^2+0.6634z^2$. The alternation in the brightness of the observed images depends on the strength of the surface interaction. However, image (c) showing how the molecular orbitals will look like the LUMO in the neutral molecule. These images are in low current which is to be expected from the size of the images of individual molecules. It seems that, Wachowiak *et al* did not try to match their images. However, the higher resolution images of these will look like fig. 4.12(a).

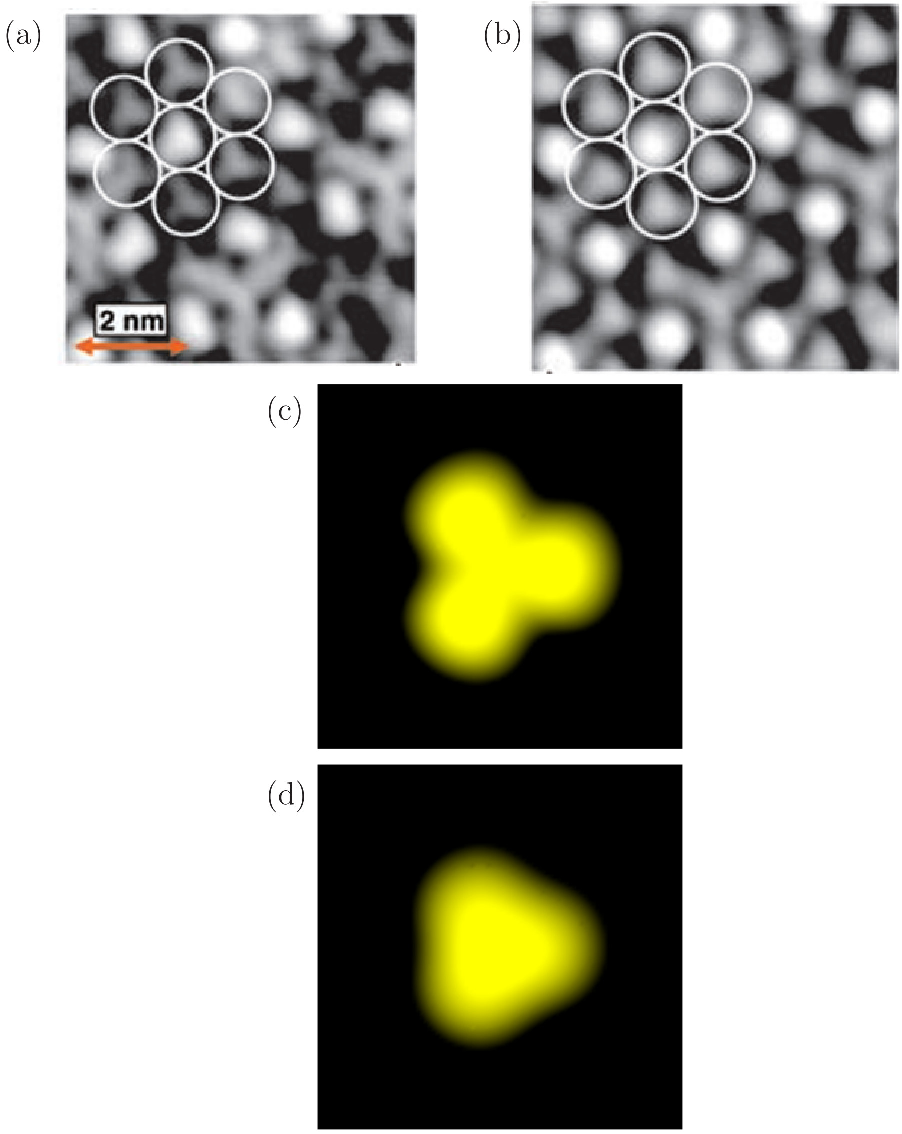

Figure 6.3: (a) represent the experimental STM image of the filled states for the C_{60}^{3-} molecule hexagon-prone, distorted as in [18], and (b) shows the recorded STM images for the empty states, (c) shows the surface as $a_{3z}=\frac{1}{3}$ for the filled state, and $\frac{2}{3}$ for the empty state in (d)

6.4 Discussion and conclusion

Simulated images showed good agreement with those for double-bond images of C_{60}^{4-} and hexagon prone of C_{60}^{3-} as in ref. [18]. It was established that the Hückel process is a sufficient way to produce images of the molecule more simply than other complicated methods. It was found that, the STM images are hopping between equivalent wells taking all of these minima into account. Then, it was possible to determine the values of the three components of the current ψ_x^2,ψ_y^2, and ψ_z^2 in order to match the experimental images published in ref. [18] with no cross terms in the STM current. Then, these currents have been related to the results obtained theoretically to deduce some information about the possible ranges of the JT coupling constants and the strength of the surface applied. In addition, by looking at these different images, it can be possible to observe the possible orientations used.

For C_{60}^{3-} molecules, different strengths of surface interaction can produce two types of images such as, three lobed and a more rounded brighter images. These images are 3-fold symmetric which indicates that the orientation is a hexagon down face. Due to the half filled of the p-orbital, these two images are very similar. However, they can be generated by using different STM currents. In addition, the current values of the theoretical images have been illustrated to give the size of the experimental recorded images.

On the other hand, in case of C_{60}^{4-} ions, the filled and empty states images have been produced almost from ψ_y^2 component of the current with a small contributions from ψ_x^2 and ψ_z^2. It was found that, in this ion the filled and empty images are different due to the different current used between the empty orbitals (two electron states) and filled orbitals (four electron states). Also, the strength of the surface interaction has a significant effect. Our calculations show that, JT in this problem should be a dynamic effect and the D_{3d} symmetry which can be obtained by a very large range of JT parameters can be reduced to D_{2h} with a surface added. These surface interaction parameters should keep the relation $\Delta_1<\Delta_2$. Various models estimated that the value of the term splitting δ' is positive around 1. However, in order to relate the results of different charged states, it can show that less parameters have been used in the case of C_{60}^{3-} ions. Changing the values of the term splitting has little effect on the contribution of the resultant currents. A large region of JT and surface interaction parameters will reduce the symmetry of both systems C_{60}^{3-} and C_{60}^{4-} to D_{2h}. In fact, our model is different to that of the Sience paper [18], who assumed that D_{2h} distortion in C_{60}^{4-} ions was due to the JT effect only, and who did not have a model at all for the C_{60}^{3-} images.

Further attempts at finding the quadratic coupling constants will be studied in the following chapter.

Chapter 7

The width of transition lines of C_{60}^{-} ion

7.1 Introduction

As is known, the vibronic coupling between electronic and vibrational motion in fullerene anions C_{60}^{n-} can reduce the symmetry of the molecule from icosahedral symmetry (neutral molecule symmetry) to lower symmetry. This distortion can be determined mathematically in the linear and quadratic coupling constants for JT effect. Understanding the molecule properties as far as possible requires knowledge of the coupling constant values. However, experimental data are not enough to calculate these coupling constant values and to date, in the literature, some estimates of linear coupling constants have been reported. On the other hand, there are no estimates for quadratic coupling constants, and whether they are positive or negative. STM matching leads to some estimates.

The interaction between atoms or molecules with a single photon usually produces spectral lines, which are a combination of allowed emitted radiation. A photon with enough energy can be absorbed by the atomic system to change the energy state of electrons in order to allow the electrons to move between orbitals. As a result, the photon will be re-emitted either with its original frequency or an organised cascade, where the overall energies at the end will be the same as the original absorbed, assuming that the quantum system will respond to the main state. In fact, the type of spectral line, such as an absorption or emission lines, which are produced depends on the gas or liquid used. The spectral line, more specifically, is very useful for investigating the properties of the system by allowing light to pass through the molecule. Also, the temperature of the medium can affect the breadth of the spectral lines. Each of the molecular orbitals e.g.

T_{1u}, T_{1g} states etc, have an energy associated with them. Therefore, the orbitals have been ordered in the way such as the HOMO below and the LUMO (Hückel method). However, each of the energies isn't an exact value though, as quantum mechanically, it cannot be possible to know the exact energy of the electrons associated with them. Probably we just know how likely it is that it has a certain energy (the uncertainty in the energy levels). So basically, the transition line produced because an electron has had its energy increased and has jumped from one state to another. For example, If the ground state has energy E_u, and the excited state has energy E_g, obviously the most likely energy change is E_g - E_u, and it is at that point we get a peak on the observed spectra. However, it's also possible that the energies weren't exactly E_u and E_g , so there is a probability that the transition was slightly greater and slightly less in energy, and it is this that gives line widths. The width of the transition line is the width of the energy distribution of each state added together. So, if we assume that the width of the ground state is Γ_u, and the width of the excited state is Γ_g, then obviously the width of the transition line is Γ_u $+\Gamma_g$. In short, the widths of transition line will be the sums of the widths of the two energy levels concerned. This relates to the biggest energy jump occurs when the first energy is E_g -Γ_u, and the second energy is E_g $+\Gamma_g$, giving a total energy difference (E_g $+\Gamma_g$) - (E_g -Γ_u) = (E_g-E_u)+(Γ_u+Γ_g), and the lowest energy change when the opposite occurs (E_g -Γ_g) - (E_g $+\Gamma_u$) = (E_g-E_u)-(Γ_u+Γ_g), giving the width as the most likely energy (E_g-E_u) plus or minus the width (Γ_u+Γ_g). This uncertainty in the energy levels leads to the width of the observed transition lines as will be seen in later sections.

The JT C_{60}^- ion has been generated electrochemically in solution which performed under N_2 atmosphere at room temperature by using Ocean Optics HR2000 as in ref.[27]. The spectrum of the transition lines of the C_{60}^- ion near infrared have been recorded over a wide range, between 9000 cm^{-1} to 30000 cm^{-1}, which corresponding to a transition between the ground T_{1u} and excited T_{1g} states as shown in Figures (7.1,7.2)[27].

The solid line in fig.7.2 shows where the Gaussian fits overall, while the dotted lines represent the four Gaussian data lines, namely from 0-III. The highest peak in fig.7.2 produced from the transition between T_{1u} and T_{1g} near infrared at 9294 cm^{-1} around (1.15 eV). However, fig.7.1 shows the energy difference between the allowed vibronic transitions ($T_{2u}\rightarrow G_g$,$G_u\rightarrow G_g$,$G_u\rightarrow T_{2g}$) associated with T_{1u} and T_{1g} states of C_{60}^- ion.

It was found in ref. [27] that two modes are expected to be combined into the four band spectrum.

We will look at the quantum mechanical line widths to see if any information on quadratic constants can be obtained that can then be compared to the STM results. We will consider the transition between the ground T_{1u} and excited states

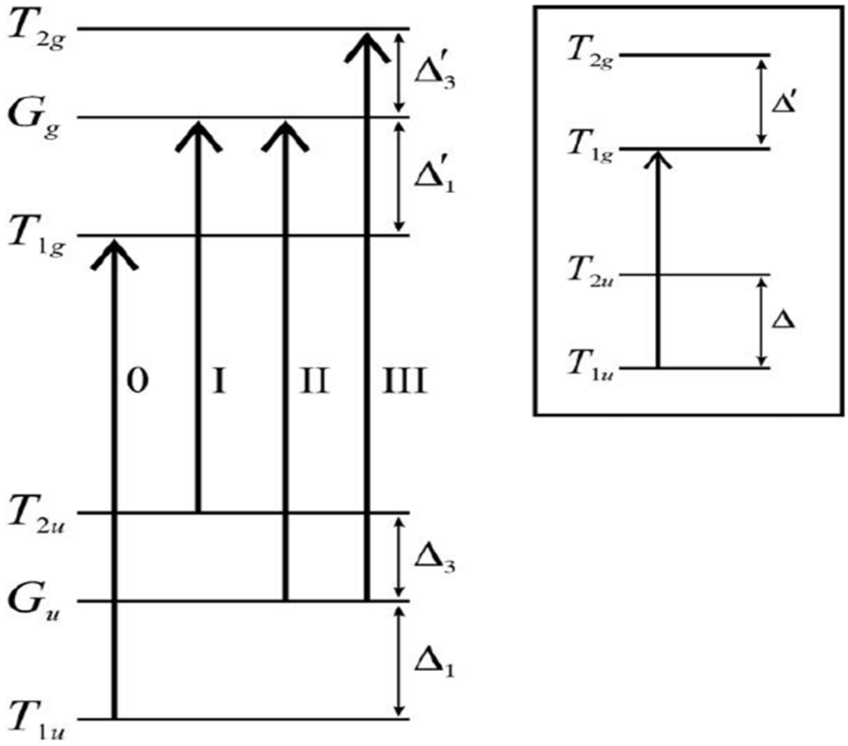

Figure 7.1: The transitions between the ground and the excited states of D_{3d} distortion of C_{60}^- ion near infrared reproduced from ref. [27]

T_{1g} of the JT Hamiltonian. In addition, the jump between the allowed vibronic transitions associated with T_{1u} and T_{1g} states of C_{60}^- anion will be taken into account.

The data of electronic spectrum of C_{60}^- molecule has been fitted in ref. [27] by using Gaussian distribution which often gives a good description of the width of transition lines as in fig.7.2. Also, the range of the quadratic coupling constants of this ion is known. Therefore, simply we are going to match the experimental data by assuming that the energy has Gaussian distribution rather than using any other method such as Lorentzian.

There are more parameters to evaluate than the recorded data in order to find links to compare the theoretical method with the experimental data given. Once we can investigate these transition lines, we can calculate many unknown variables, such as the approximate values for the linear and the quadratic coupling constants of the $T_1 \otimes h$ system.

This part of this research related to calculations, can in some way or another lead to information regarding these values. Firstly, the matrix elements of the Hamiltonian squared for the $T_{1u} \otimes h$ JT system of different symmetries D_{3d} and

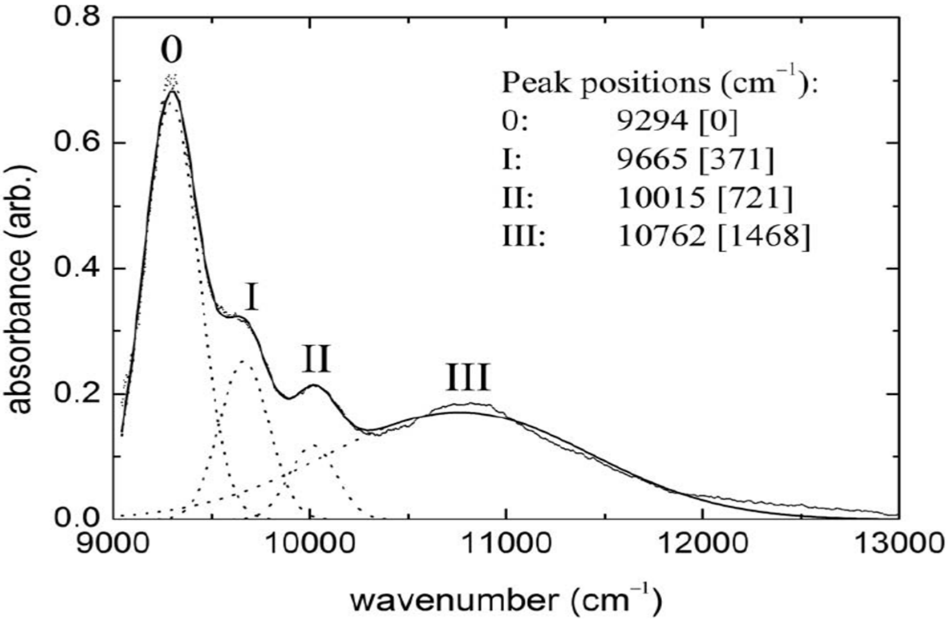

Figure 7.2: The spectrum of the transition lines of C_{60}^{-} ion near infrared reproduced from ref. [27]

D_{5d} is used to analyse the widths of the transition lines Γ. The method adopted is very similar to that used earlier in ref. [23] for D_{3d} trigonal minima. Symmetry adapted states for the ground levels appropriate for finite couplings are used to evaluate the energy squared of the system. The uncertainty principle is applied to find the expectation values of the energy minima. This is used for the first and second order coupling constants. Then, values for the uncertainty in line widths spectra are estimated, following the literature, as in References [27] and [96]. It was found that both line widths of gas and liquid are similar [95], which indicates that much of the line widths could be intrinsic to the ions. In fact, in addition to ΔE, many factors contribute to the widths of spectral lines. Therefore, ΔE would be expected to be less than the observed line widths. Finally, ranges for the JT coupling constants could be determined by comparing the measured values to the calculated width of four transitions, and then combined with knowledge of the positions of the spectral lines.

7.2 The unitary shift transformation method

Obviously, the general Hamiltonian, usually used to describe any JT system, is very complicated and difficult to diagonalise, and hence, cannot be solved easily to determine the lowest energy due to the electronic and vibrational parts. Therefore, approximations will be needed for simplification. Indeed, the unitary shift transformation, developed by Bates and Dunn in 1987 [24], is one of the approximations that can be used to solve the vibronic Hamiltonian. The unitary shift operator is given by;

$$U = \exp\left(i\sum_j \alpha_j P_j\right) \tag{7.1}$$

which implies that;

$$U^{-1}Q_jU = -\hbar\alpha_j \tag{7.2}$$

where α_j are free parameters indicating the locations of the minima on the APES, also, P_j is the momentum operator, which is joined to the normal mode coordinate Q_j, over all the coordinates of the vibronic parts j. This relation shows that the effect of the shift operator is to shift the Q_j coordinate by $\hbar\alpha_j$. This transformation operator technique shifts the phonon coordinates Q_j to a new point $\hbar\alpha_j$. However, given the chosen values of α_j, it is necessary to minimise the energy of the system with respect to each variable for the shifted coordinates. In addition, by using this transformation operator, the interaction Hamiltonian will then transform into five variables α_j, which are not a function of phonon operators. This will make the Hamiltonian simpler to analyse.
Some examples of the transformation operators, e.g. from quantum mechanics, would be useful to simplify the Hamiltonian in later sections:
if,

$[Q_i, U] = Q_iU - UQ_i$ and $U_u^\dagger U_u = 1$

so,

$$\begin{aligned} U_u^\dagger Q_i U_u &= U_u^\dagger([Q_i, U_u] + U_uQ_i) \\ &= U_u^\dagger[Q_i, U_u] + Q_i \\ &= U_u^\dagger(-\hbar\alpha_i U_u) + Q_i \\ &= -\hbar\alpha_i + Q_i \end{aligned}$$

where $[Q_i, U] = -\hbar\alpha_i U$, then by applying these in $Q(i)$ which defined in section 3.2.1, we can find,

$$\begin{aligned} Q(i) &= \left\langle u; 0 \left| U_u^\dagger Q_i U_v \right| v; 0 \right\rangle \\ &= \left\langle u; 0 \left| U_u^\dagger([Q_i, U_v] + U_vQ_i) \right| v; 0 \right\rangle \\ &= \left\langle u; 0 \left| U_u^\dagger([-\hbar\alpha_i, U_v] + U_vQ_i) \right| v; 0 \right\rangle \\ &= -\hbar\alpha_i \left\langle u; 0 \left| U_u^\dagger U_v \right| v; 0 \right\rangle + \left\langle u; 0 \left| U_u^\dagger U_v Q_i \right| v; 0 \right\rangle \end{aligned}$$

where $\langle u$ and $\langle v$ are the electronic parts (positions of the wells), while $0\rangle$ refers to the phonon part.

From;

$$\alpha_i = \frac{\kappa u_i}{\hbar}$$

where $\kappa = -V_1'\sqrt{\hbar/\mu\omega}$ and u_i shows the electronic parts and;

Q_i, in terms of the creation b_i and annihilation $b_i^\dagger$ operators, can be written as:

$$Q_i = -\sqrt{\frac{\hbar}{2\mu\omega}}\left(b_i + b_i^\dagger\right) = \frac{\kappa}{\sqrt{2}V_1'}\left(b_i + b_i^\dagger\right) \tag{7.3}$$

where b_i and $b_i^\dagger$ work on the states as follows:

$$\begin{aligned} b_i\left|n\right\rangle &= \sqrt{n}\left|n-1\right\rangle \\ b_i^\dagger\left|n\right\rangle &= \sqrt{n+1}\left|n+1\right\rangle \end{aligned} \tag{7.4}$$

then,

$$\begin{aligned} Q(i) &= \left\langle u;0\left|U_u^\dagger Q_i U_v\right|v;0\right\rangle \\ &= \left\langle u;0\left|U_u^\dagger([Q_i,U_v]+U_vQ_i)\right|v;0\right\rangle \\ &= -\hbar\alpha_i S + \left\langle u;0\left|U_u^\dagger U_v Q_i\right|v;0\right\rangle \\ &= -ku_i^v S + \frac{k}{\sqrt{2}V_1'}\left\langle u;0\left|U_u^\dagger U_v\right|v;1\right\rangle \end{aligned}$$

where, the phonon overlaps $S = \left\langle 0\left|U_u^\dagger U_v\right|0\right\rangle$.

so,

$$\begin{aligned} -\kappa u_i^v S + \frac{\kappa}{\sqrt{2}V_1'}\left\langle u;0\left|U_u^\dagger U_v\right|v;1\right\rangle &= -\kappa u_i^v S + \frac{\kappa}{\sqrt{2}V_1'}(\frac{u_i^u - u_i^v}{\sqrt{2}}(-V_1'S)) \\ &= -\kappa u_i^v S - \frac{\kappa}{2}(u_i^u - u_i^v)S \\ &= -\kappa S(u_i^v + \frac{1}{2}u_i^u - \frac{1}{2}u_i^v) \\ &= \frac{-\kappa S}{2}\left(u_i^{(u)} + u_i^{(v)}\right) \end{aligned}$$

which implies that,

$$\left\langle u;0\left|U_u^\dagger Q_i U_v\right|v;0\right\rangle = \frac{-\kappa S}{2}\left(u_i^{(u)}+u_i^{(v)}\right)$$

The phonon overlaps between any wells is:

$$S=\left\langle u;0\left|U_u^\dagger U_v\right|v;0\right\rangle \;=\; \exp\left(-\frac{1}{4}(V_1')^2\sum_i\left(u_i^{(u)}-u_i^{(v)}\right)^2\right)$$

Evaluating this phonon overlap can be achieved simply, with the help of the following commutators:

$$U_u=\exp\left(i\sum_i \alpha_i^{(u)}P_i\right)=\exp\left(\frac{i\kappa}{\hbar}\sum_j u_i^{(u)}P_i\right)$$

This is expressed in terms of creation and annihilation operators b_i and $b_i^\dagger$ from eq.(7.4) as,

$$P_i=-\mathrm{i}\hbar\frac{\partial}{\partial Q_i}=\mathrm{i}\sqrt{\frac{\hbar\mu\omega}{2}}\left(b_i-b_i^\dagger\right)$$

with these useful relations:

$$\left[b_i,b_j^\dagger\right]=\delta_{ij}$$

$$\begin{aligned}\mathrm{e}^{(A+B)} &= \mathrm{e}^{A}\mathrm{e}^{B}\mathrm{e}^{-[A,B]/2}\\ &= \mathrm{e}^{B}\mathrm{e}^{A}\mathrm{e}^{[A,B]/2}\end{aligned}$$

The phonon overlaps between any wells S can be easily verified by direct calculation.

Similarly, we can show the effect of the unitary shift operator on $\mathcal{H}_0$ as;

$$\begin{aligned}\langle\mathcal{H}_0\rangle &= \left\langle u;0\left|U_u^\dagger\mathcal{H}_0U_v\right|v;0\right\rangle\\ &= \frac{1}{2}\hbar\omega S\sum_i\left(1+\left(V_1'\right)^2u_i^{(u)}u_i^{(v)}\right)\end{aligned}$$

and for Q_iQ_j to be;

$$\begin{aligned} &= \left\langle u;0 \left| U_u^{\dagger} Q_i Q_j U_v \right| v;0 \right\rangle \\ &= \frac{\hbar S}{2\mu\omega} \left[\delta_{ij} + \frac{1}{2} \left(V_1' \right)^2 \Sigma u_i^{uv} \Sigma u_j^{uv} \right] \end{aligned}$$

where $\Sigma u_i^{uv} \equiv u_i^{(u)} + u_i^{(v)}$ and δ_{ij} is the kronecker delta function.
In the end, the values of α_j are necessary to minimise the eigenvalues and their associated eigenvectors. This can be achieved using the method introduced by Öpik and Pryce in ref. [4].

7.3 The analysis of C_{60}^- spectra techniques

In this work, (Γ) represents the full line width measured at half maximum, as in ref. [97].
The expected value of the energy is often used to determine the width of transition lines of the system. The uncertainty principle relation for the total energies of the T_{1u} states is thus found to be

$$\Delta E_{T_{1u}}^2 = \langle E_{T_{1u}}^2 \rangle - \langle E_{T_{1u}} \rangle^2 \tag{7.5}$$

By assuming that the energy has a Gaussian distribution so;

$$P(E) = \frac{k}{\sqrt{\pi}} e^{[-(kE)^2]} \tag{7.6}$$

The energy distribution P(E) drops to half, as shown in fig. 7.3, when $E = \pm\,\Gamma/2$ where Γ is the width of the half maximum.

$$P(E = \pm\Gamma/2) = \frac{k}{\sqrt{\pi}} e^{[-(\frac{k\Gamma}{2})^2]} = \frac{k}{2\sqrt{\pi}} \tag{7.7}$$

At half maxima;

$$e^{[-(\frac{k\Gamma}{2})^2]} = \frac{1}{2} \tag{7.8}$$

or

$$(\frac{k\Gamma}{2})^2 = \ln 2 \tag{7.9}$$

then the decay constant will be;

$$k = \frac{2\sqrt{\ln 2}}{\Gamma} \tag{7.10}$$

so, the uncertainty of the energies of $T \otimes h$ JT system is given as

$$\Delta E = \sqrt{\langle E^2 \rangle - \langle E \rangle^2} \tag{7.11}$$

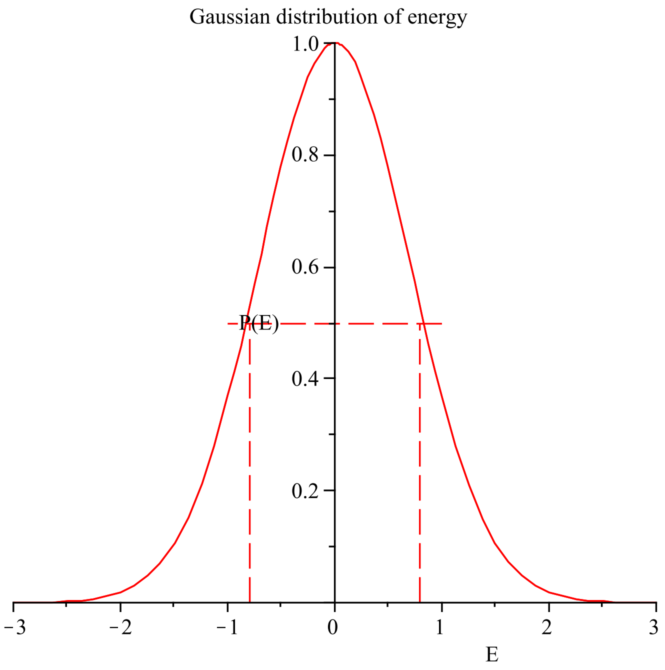

Figure 7.3: Gaussian distribution of $T \otimes h$ JT system in C_{60}^{-}

where;

$$\langle E \rangle = \int_{-\infty}^{\infty} EP(E)dE = 0 \tag{7.12}$$

$$\langle E^2 \rangle = \int_{-\infty}^{\infty} E^2 P(E)dE = \frac{1}{2k^2} \tag{7.13}$$

which implies that;

$$\Delta E = \frac{1}{\sqrt{2}k} \tag{7.14}$$

Therefore, from eq.(7.10) and eq.(7.14) the width of the half maximum is a function of the expectation value of the energy given by the relation:

$$\Gamma = 2\sqrt{2}\sqrt{\ln 2}\Delta E \tag{7.15}$$

This relationship will be used to calculate the width of the transition lines, by applying the unitary transformation method, with calculations to define the matrix elements of the squared Hamiltonian of the system. It is also used later to evaluate the expected values of JT linear and quadratic parameters of the C_{60}^{-} JT system.

7.4 The symmetry adapted state energies of D_{3d} and D_{5d} symmetries

- Energies of trigonal minima D_{3d}

Similar to what was reported in ref.[23], evaluating the matrix elements is required to determine the energies of the symmetry adapted state (SAS). By applying the unitary transformation method, and after some calculations to define the matrix elements of the full Hamiltonian, it was found, as in ref.[23], that for D_{3d} minima, the matrix elements of H corresponding to the trigonal minima with itself H_{11} take the form;

$$H_{11} = 3\hbar\omega\left[\frac{5}{2}-\frac{\sqrt{30}}{10}\gamma(V_1')^2\right],$$

where γ is related to the quadratic coupling constant V_3' by;

$$\gamma = \frac{\sqrt{2}}{\sqrt{15}-4\sqrt{\frac{2}{3}}V_3'} \tag{7.16}$$

Also, the matrix elements of H between the nearest neighbouring states is $\pm\, H_{12}$, which can be written as;

$$H_{12} = \sqrt{5}S\hbar\omega\left[\frac{5}{2}-\frac{V}{10}(\gamma V_1')^2\right];$$

where;

$$V = 25+\sqrt{2}V_2'-5\sqrt{10}V_3'$$

Then, for next-nearest neighbours, the overlap is $\pm\, H_{13}$

$$H_{13} = S^2\hbar\omega\left[\frac{5}{2}-\frac{W}{10}(\gamma V_1')^2\right];$$

where;

$$W = 35+5\sqrt{2}V_2'-7\sqrt{10}V_3'$$

Table 7.1: The values of $\langle\psi\,|H|\,\psi\rangle$ D_{3d} minima of $\langle u';0|to|v';0\rangle$

	a'	b'	c'	d'	e'	f'	g'	h'	i'	j'
a'	H_{11}	H_{12}	H_{13}	$-H_{13}$	H_{13}	H_{13}	H_{12}	H_{12}	H_{13}	$-H_{13}$
b'		H_{11}	H_{13}	$-H_{13}$	$-H_{13}$	$-H_{13}$	H_{13}	H_{13}	H_{12}	$-H_{12}$
c'			H_{11}	H_{12}	H_{13}	$-H_{13}$	H_{12}	$-H_{13}$	H_{12}	H_{13}
d'				H_{11}	H_{13}	$-H_{13}$	H_{13}	$-H_{12}$	H_{13}	H_{12}
e'					H_{11}	H_{12}	H_{12}	H_{13}	$-H_{13}$	H_{12}
f'						H_{11}	H_{13}	H_{12}	$-H_{12}$	H_{13}
g'							H_{11}	H_{13}	H_{13}	H_{13}
h'								H_{11}	$-H_{13}$	$-H_{13}$
i'									H_{11}	$-H_{13}$
j'										H_{11}

Then, Table 7.1 shows the matrix elements of the Hamiltonian between the state associated with the wells for D_{3d} minima of H labeled from a' to j'. In the same way, Table 7.2 represents the phonon overlaps for D_{3d} minima of H.

By using the same method, thus, the matrix elements for the D_{3d} minima overlaps of the squared Hamiltonian H^2 are: $H_{11}^{(2)}$, $H_{12}^{(2)}$, and $H_{13}^{(2)}$.

$$H_{11}^{(2)} = 3(\hbar\omega)^2[A + B_{11}(\gamma V_1')^2 + C_{11}(\gamma V_1')^4]:$$

where,

$$A = \frac{1}{4}[25 + 2(V_2')^2 + 2(V_3')^2];$$

$$B_{11} = \frac{1}{60}[-315 + 90\sqrt{2}V_2' + 54\sqrt{10}V_3' - 60\sqrt{5}V_2'V_3' + 54(V_2')^2 + 94(V_3')^2];$$

$$C_{11} = \frac{1}{20}(3\sqrt{5} - 4\sqrt{2}V_3')^2;$$

Table 7.2: The phonon overlaps for D_{3d} minima of H

	a'	b'	c'	d'	e'	f'	g'	h'	i'	j'
a'	3	$\sqrt{5}S$	S^2	$-S^2$	S^2	S^2	$\sqrt{5}S$	$\sqrt{5}S$	S^2	$-S^2$
b'		3	S^2	$-S^2$	$-S^2$	$-S^2$	S^2	S^2	$\sqrt{5}S$	$-\sqrt{5}S$
c'			3	$\sqrt{5}S$	S^2	$-S^2$	$\sqrt{5}S$	$-S^2$	$\sqrt{5}S$	S^2
d'				3	S^2	$-S^2$	S^2	$-\sqrt{5}S$	S^2	$\sqrt{5}S$
e'					3	$\sqrt{5}S$	$\sqrt{5}S$	S^2	$-S^2$	$\sqrt{5}S$
f'						3	S^2	$\sqrt{5}S$	$-\sqrt{5}S$	S^2
g'							3	S^2	S^2	S^2
h'								3	$-S^2$	$-S^2$
i'									3	$-S^2$
j'										3

and $H_{12}^{(2)}$ is the matrix elements of H^2 corresponding to the trigonal minimum with itself.

Then, the matrix elements of H^2 between any two different nearest neighbouring states is ± $H_{12}^{(2)}$

where,

$$H_{12}^{(2)} = \sqrt{5}S(\hbar\omega)^2[A + B_{12}(\gamma V_1')^2 + C_{12}(\gamma V_1')^4] :$$

B_{12} and C_{12} have values:

$$
\begin{aligned}
B_{12} &= \frac{1}{300}[-3375 + 240\sqrt{2}V_2' + 480\sqrt{10}V_3' - 294\sqrt{5}V_2'V_3' + 195(V_2')^2 + 335(V_3')^2]; \\
C_{12} &= \frac{1}{40}[160 + 2\sqrt{2}V_2' - 70\sqrt{10}V_3' - 2\sqrt{5}V_2'V_3' - (V_2')^2 + 75(V_3')^2];
\end{aligned}
$$

or for next-neighbours, the overlap is ± $H_{13}^{(2)}$

where,

$$
H_{13}^{(2)} = S^2(\hbar\omega)^2[A + B_{13}(\gamma V_1')^2 + C_{13}(\gamma V_1')^4] :
$$

similarly, B_{13} and C_{13} have values:

$$
\begin{aligned}
B_{13} &= \frac{1}{60}[-1035 - 120\sqrt{2}V_2' + 180\sqrt{10}V_3' - 60\sqrt{5}V_2'V_3' + 42(V_2')^2 + 34(V_3')^2]; \\
C_{13} &= \frac{1}{20}[155 + 25\sqrt{2}V_2' - 59\sqrt{10}V_3' - 10\sqrt{5}V_2'V_3' + (V_2')^2 + 57(V_3')^2];
\end{aligned}
$$

In fact, the matrix elements of the Hamiltonian squared of the system between the states associated with the wells for D_{3d} minima are in the same form as Table 7.1, but with H_{ij} replaced by $H_{ij}^{(2)}$.
The $E_{T_{1u}}$ energy ground states for T_{1u} vibronic state were found in ref [23] to be;

$$
E_{T_{1u}} = \frac{H_{11} + \sqrt{5}H_{12} + 2H_{13}}{3 + 5S + 2S^2} \tag{7.17}
$$

This definition of the energy differed from that used in earlier work [23], because the notation used is:

$$
\begin{aligned}
H_{11} &= \left\langle a' \left| H \right| a' \right\rangle \\
H_{12} &= \left\langle a' \left| H \right| b' \right\rangle \\
H_{13} &= \left\langle a' \left| H \right| c' \right\rangle
\end{aligned}
$$

whereas, the previous method factorised out the orbital overlap from the definition of H_{ij}.

In the same way, the energies of the T_{2u} are found in ref.[23] to be,

$$E_{T_{2u}} = \frac{H_{11} - \sqrt{5}H_{12} + 2H_{13}}{3 - 5S + 2S^2} \tag{7.18}$$

and the energies for the states G_u have been written in the form;

$$E_{G_u} = \frac{H_{11} - 3H_{13}}{3(1 - S^2)} \tag{7.19}$$

- Energies of pentagonal minima D_{5d}

For pentagonal symmetry, it was found that the matrix elements of H between the states corresponding to the trigonal wells and itself have been written in the form;

$$H_{11} = \sqrt{5}\phi\hbar\omega\left[\frac{5}{2} - \frac{1}{\sqrt{6}}\beta(V_1')^2\right],$$

where β is relevant to the quadratic constant V_2' from the relation;

$$\beta = \frac{\sqrt{6}}{(5 - 4\sqrt{2}V_2')}$$

The matrix elements of H between the two nearest neighbouring states $\pm H_{12}$ takes the form;

$$H_{12} = \phi S\hbar\omega\left[\frac{5}{2} - \frac{F}{120}(\beta V_1')^2\right];$$

where;

$$F = 45 + 12\sqrt{10}V_3' + \frac{35\sqrt{6}}{\beta}$$

Then, the matrix elements of the Hamiltonian squared for any pentagonal wells and itself will take the form;

$$H_{11}^{(2)} = \sqrt{5}\phi(\hbar\omega)^2[A' + B_{11}'(\beta V_1')^2 + C_{11}'(\beta V_1')^4]:$$

where,

$$\begin{aligned}
A' &= [6.25 + 0.500(V_3')^2 + 0.500(V_2')^2] \\
B_{11}' &= [-2.23606V_2'V_3' + 2.5(V_2')^2 + 0.500(V_3')^2 + 1.5811V_3' \\
&+ 1.1785V_2' - 2.9166] \\
C_{11}' &= [0.01388(8V_2' - 7.071)^2]
\end{aligned}$$

and between any two different nearest neighbours is given by;

$$H_{12}^{(2)} \;=\; \phi S(\hbar\omega)^2[A' + B_{12}'(\beta V_1')^2 + C_{12}'(\beta V_1')^4] :$$

where,

$$\begin{aligned}
B_{12}' &= [+2.0124V_2'V_3' - 1.15(V_2')^2 + 0.25(V_3')^2 - 1.00138V_3' \\
&- 6.1282V_2' + 15.166] \\
C_{12}' &= [-1.7515V_2'V_3' - 0.0972(V_2')^2 + 0.025(V_3')^2 + 0.63245V_3' \\
&+ 9.70307V_2' - 14.1527]
\end{aligned}$$

These matrix elements of the Hamiltonian squared will be the main useful variables in order to investigate the width of the transition lines of the $T \otimes h$ JT system.

The $E_{T_{1u}}'$ energy ground states for the T_{1u} vibronic state of pentagonal minima were found to be;

$$E_{T_{1u}}' = \frac{H_{11} + \sqrt{5}H_{12}}{\sqrt{5}\phi(1+S)} \tag{7.20}$$

However, the $E_{T_{2u}}'$ energy ground states for the T_{2u} vibronic state are

$$E_{T_{2u}}' = \frac{H_{11} + \sqrt{5}H_{12}}{\sqrt{5}\phi(1-S)} \tag{7.21}$$

Then,

$$\begin{aligned}
\langle E_{T_{1u}}^2 \rangle &= (\hbar\omega)^2(A + \frac{(3B_{11} + 5SB_{12} + 2S^2B_{13})(\gamma^2 V_1'^2)}{3 + 5S + 2S^2} \\
&+ \frac{(3C_{11} + 5SC_{12} + 2S^2C_{13})(\gamma^4 V_1'^4)}{3 + 5S + 2S^2})
\end{aligned} \tag{7.22}$$

and similarly, the Hamiltonian in earlier work [23] has the form,

$$\langle E_{T_{1u}} \rangle \;=\; (\hbar\omega)\left(a + \frac{(3b_{11} + 5Sb_{12} + 2S^2b_{13})(\gamma^2 V_1'^2)}{3 + 5S + 2S^2}\right) \tag{7.23}$$

where,

$$\begin{aligned} a &= \frac{5}{2} \\ b_{11} &= -\frac{\sqrt{3}0}{10\gamma} \\ b_{12} &= -\frac{V}{10} \\ b_{13} &= -\frac{W}{10} \end{aligned}$$

as defined earlier in matrix elements H_{11}, H_{12}, and H_{13}.

7.5 Uncertainty of energy for D_{3d} and D_{5d} symmetries

As discussed in chapter 2, and from the uncertainty principle relation for the total energies of the T_{1u} state in eq.(7.5) and after going through many calculations, and using eq. (7.22) and eq. (7.23) into eq. (7.5), the $\Delta E_{T_{1u}}$ of the $T \otimes h$ JT system was found as a function of the linear coupling constant V_1' and the quadratic coupling constants V_2' and V_3' in very strong coupling.

Thus, from eq.(7.5)

$$\begin{aligned} \Delta E^2_{T_{1u}} &= (\hbar\omega)^2(A + \frac{(3B_{11} + 5SB_{12} + 2S^2B_{13})(\gamma^2 V_1'^2)}{3 + 5S + 2S^2} \\ &+ \frac{(3C_{11} + 5SC_{12} + 2S^2C_{13})(\gamma^4 V_1'^4)}{3 + 5S + 2S^2}) \\ &- (\hbar\omega)^2 \left(a + \frac{(3b_{11} + 5Sb_{12} + 2S^2b_{13})(\gamma^2 V_1'^2)}{3 + 5S + 2S^2} \right)^2 \end{aligned}$$

The next step is substituting the values of the constants in the matrix elements for Hamiltonian and Hamiltonian squared of T⊗h in C_{60}^- JT system, which have been evaluated in earlier sections, into ΔE^2 above. In this case, when the quadratic coupling constants are zero, the calculations have shown that;

$$(b_{11})^2 = (C_{11}) = \frac{9}{4}$$

This implies that

$$\Delta H \sim V_1'$$

where ΔH increases linearly with the increase in the linear coupling constant.

However, in this system, the relative strengths of the quadratic coupling constants V_2' and V_3' are unknown.

In a similar way, the energies of the other states T_{2u}, G_u will take the forms;

$$\begin{aligned}\Delta E^2_{T_{2u}} &= (\hbar\omega)^2(A+\frac{(3B_{11}-5SB_{12}+2S^2B_{13})(\gamma^2V_1'^2)}{3-5S+2S^2}\\ &+ \frac{(3C_{11}-5SC_{12}+2S^2C_{13})(\gamma^4V_1'^4)}{3-5S+2S^2})\\ &- (\hbar\omega)^2\left(a+\frac{(3b_{11}-5Sb_{12}+2S^2b_{13})(\gamma^2V_1'^2)}{3-5S+2S^2}\right)^2\end{aligned}$$

and;

$$\begin{aligned}\Delta E^2_{G_u} &= (\hbar\omega)^2(A+\frac{(B_{11}-S^2B_{13})(\gamma^2V_1'^2)}{1-S^2}\\ &+ \frac{(C_{11}-S^2C_{13})(\gamma^4V_1'^4)}{1-S^2})\\ &- (\hbar\omega)^2\left(a+\frac{(b_{11}-S^2b_{13})(\gamma^2V_1'^2)}{1-S^2}\right)^2\end{aligned}$$

In fact, it is very useful to use the values of ΔE in order to investigate the width of the transition lines of the $T\otimes h$ JT system.

The calculations provided are helpful in matching the experimental data in ref. [27], through altering the unknown coupling constants in order to interpret the recorded results.

- Pentagonal minima D_{5d}

However, for pentagonal minima, the forms of the energies of T_{1u} state will be;

$$\begin{aligned}\Delta E^2_{T_{1u}} &= (\hbar\omega)^2(A+\frac{(\sqrt{5}\phi B_{11}+\phi\sqrt{5}SB_{12})(\beta^2V_1'^2)}{\sqrt{5}\phi(1+S)}\\ &+ \frac{(\sqrt{5}\phi C_{11}+\phi\sqrt{5}SC_{12})(\beta^4V_1'^4)}{\sqrt{5}\phi(1+S)})\\ &- (\hbar\omega)^2\left(a+\frac{(\sqrt{5}\phi b_{11}+\phi\sqrt{5}Sb_{12})(\beta^2V_1'^2)}{\sqrt{5}\phi(1+S)}\right)^2\end{aligned}$$

And the T_{2u} state will take the form;

$$\begin{aligned}
\Delta E^2_{T_{2u}} &= (\hbar\omega)^2(A + \frac{(\sqrt{5}\phi B_{11} + \phi\sqrt{5}SB_{12})(\beta^2 V_1'^2)}{\sqrt{5}\phi(1-S)} \\
&+ \frac{(\sqrt{5}\phi C_{11} + \phi\sqrt{5}SC_{12})(\beta^4 V_1'^4)}{\sqrt{5}\phi(1-S)}) \\
&- (\hbar\omega)^2 \left(a + \frac{(\sqrt{5}\phi b_{11} + \phi\sqrt{5}Sb_{12})(\beta^2 V_1'^2)}{\sqrt{5}\phi(1-S)} \right)^2
\end{aligned}$$

7.6 Calculations on the width of transition lines

From fig. 7.2, the widths of transition lines W_i between the ground and the excited states are;

$$\begin{aligned}
\Gamma_{T_{1u}} + \Gamma_{T_{1g}} &= W_0 \\
\Gamma_{T_{2u}} + \Gamma_{G_g} &= W_I \\
\Gamma_{G_u} + \Gamma_{G_g} &= W_{II} \\
\Gamma_{G_u} + \Gamma_{T_{2g}} &= W_{III}
\end{aligned} \tag{7.24}$$

Where experimentally, these values of W_0, W_I, W_{II}, and W_{III} have been measured from the first peak given in fig. 7.2. In addition, this figure shows the transition energies between the ground and the excited states calculated to be;

$$\begin{aligned}
E_{T_1g} - E_{T_1u} &= 9294cm^{-1} \\
E_{G_g} - E_{T_{2u}} &= \Delta_1'' + [(E_{T_1g} - E_{T_{1u}}) - (\Delta_1' + \Delta_3')] \\
E_{G_g} - E_{G_u} &= \Delta_1'' + [(E_{T_1g} - E_{T_{1u}}) - \Delta_1'] \\
E_{T_2g} - E_{G_u} &= (\Delta_1'' + \Delta_3'') + [(E_{T_1g} - E_{T_{1u}}) - \Delta_1']
\end{aligned} \tag{7.25}$$

It was found from ref.[27] that, the energy ratio q' is given by;

$$q' = \frac{\Delta_1'}{\Delta_3'} = \frac{(3-2S)(X+2SY)}{(3+2S)(X-2SY)}$$

In this chapter, the notation ($'$) will be used for the ground states and ($''$) for the excited states.

The phonon overlap S between adjacent D_{3d} wells as given in ref. [98] is;

$$S = \exp[-12(\frac{V_1'}{3\sqrt{10} - 8V_3'})^2]$$

Where the numerical factors X and Y are related to the two JT parameters V_2' and V_3' by;

$$\begin{aligned} X &= 10+\sqrt{2}V_2'-\sqrt{10}V_3' \\ Y &= 5+2\sqrt{2}V_2'-\sqrt{10}V_3' \end{aligned} \tag{7.26}$$

This expression in eq. (7.26) implies that the quadratic coupling constants have non-zero effect on the potential energy surface, in case of preferring D_{3d} symmetry. It was also found in ref. [27] that the values of the linear constants for the ground and excited states are likely to be greater than the two quadratic couplings. It was assumed that the values are X=10 and Y=5, and so the ratio q' depends on the phonon overlap only as;

$$S = \exp(-\frac{2V_1'^2}{15})$$

Fitting the data to the possible bands in fig.7.1 indicates that

$$\begin{aligned} \Delta_3' &= E_{W_{II}} - E_{W_0} \\ \Delta_3'' &= E_{W_{III}} - E_{W_{II}} \\ q'' &= \frac{(1+q')E_{W_{II}} - q'E_{W_I}}{E_{W_{III}} - E_{W_{II}}} \end{aligned}$$

where E$_{Wi}$ is the energy of band i, according to the strongest peak, while q' and q'' are the associated energy ratio of the ground and excited states.
Thus,

$$\Delta_1'' = q''\Delta_3'' = 630$$

By using the energies of the bands from fig.7.2, gives

$$\Delta_3' = 350cm^{-1}$$
$$\Delta_3'' = 747cm^{-1}$$

and,

$$q'' = \frac{721+350q'}{747}$$

then,

$$\Delta_1'' = q'\Delta_3'' = 1344$$

By applying an approximation method, it was found that the energy ratio between the ground and the excited states is similar, so q'=q''=1.8 [27]. This implies that

the phonon overlap is S=0.635, and the linear coupling constant associated was found to be V_1'=1.84.
Then, the experimental values of the transition energies between the ground and the excited states are calculated from eq. (7.25) to be;

$$E_{G_g} - E_{T_{2u}} \approx 9658cm^{-1} \tag{7.27}$$

$$E_{G_g} - E_{G_u} \approx 10008cm^{-1} \tag{7.28}$$

$$E_{T_{2g}} - E_{G_u} \approx 10755cm^{-1} \tag{7.29}$$

Also, from ref. [98], the expression for $\hbar\omega'$ has the form;

$$\hbar\omega' = \frac{-(1+S)(3-2S)\Delta_3'}{5S\ln S}$$

The effective mode frequencies used in [27] are $\hbar\omega' = 687\text{cm}^{-1}$ for the ground states, and $\hbar\omega'' = 1466\text{cm}^{-1}$ for the excited states in the C_{60} known frequencies range.

By applying eq. (7.15), the theoretical quantum mechanical width, which contributes to the overall width of transition lines for the transition of trigonal minima D_{3d} can vary between (80 cm^{-1}) and (1650 cm^{-1}). These values are smaller than the experimental values found due to other unknown factors. However, the transition energy will stay about the same.
The subset of values for the linear and coupling constants of the ground and excited states that can make all the transitions possible will be given by V_1'=1.84, V_2'= -0.88, and V_3'= 1.12 for the ground states, and V_1''=1.80172, V_2''= -0.87, and V_3''= 1.06 for the excited states. In fact, the initial approximation from experimental work is that the linear coupling constants ratio for the ground and excited states should be approximately equal to 1. Also, the fit is based on D_{3d} distorted ions, which limited the results to the zone, where $3V_2' \leq \sqrt{5}V_3'$ in ref. [23], is associated with S $\geq$ 0.635. However, the interpretation of the experimental results in ref.[27] assumed that the quadratic coupling constants V_2'=V_3'=0, which means that no effects of higher-order couplings is considered.

7.7 Discussion and Conclusion

An appropriate model applicable to C_{60}^- anions was developed in 1995 by Dunn and Bates [23] using numerical and analytical techniques. This model has been treated by applying a unitary shift transformation method and energy minimisation procedure presented originally by Bates *et al* in 1987 [24]. It has been shown that by including quadratic coupling there are two possible types of minima, one with D_{3d} symmetry, and the other with D_{5d} symmetry. However, some authors, for example, Wang *et al* [99] argue that the minima have only pentagonal symmetry. However, in the limit as $V_2' = V_3' = 0$, D_{3d} in $T_{1u} \otimes$ h_g Jahn-Teller system is lower in energy in References [100], [23],[101] and the near-infrared (NIR) data in ref. [97] fits the D_{3d} trigonal minima. Also the energies and the corresponding eigenstates for the dynamic JT interaction have been found for D_{3d} minimum distortion.

In the present work, the model above has been used. Matrix elements of the Hamiltonian squared for the $T_{1u} \otimes$ h_g Jahn-Teller system of trigonal D_{3d} symmetries have been found in order to investigate the widths of the transition lines Γ. Advantages have been added to the method, as has been used in ref. [23] in order to describe further investigations of this system. The Uncertainty principle has been applied for this reason in order to provide expected values of the energy minima. Spectral line widths of the $T \otimes h$ JT system in C_{60}^- have been observed to approximately follow a Gaussian distribution. This distribution has been used to investigate the width of the transition lines in the JT system.

Due to the unknown ratio between the line widths of the ground and the excited states, and on the other hand, between the coupling constants themselves, it might be difficult to determine accurate values for the coupling constants. Also, other physical factors will cause broadening of the line widths, where the broader lines indicate stronger quadratic coupling.

Further calculations at a later stage may become more useful, if further data becomes available to evaluate some links to experimental data, as given in References [97][27] for the $T_{1u} \otimes h_g$ system.

Chapter 8

Conclusion

The current work has focused on the factors which could have a significant influence on the STM images of C_{60} anions with JT effect present. STM is a good method to display the lowest density of states of the molecule on the surface at high resolution to the level of single atoms. This method has been used in two important scanning modes, i.e. constant height and constant current. The STM images have been produced from LUMO of different ions. The Jahn-Teller (JT) effect has been influenced by the surface and the other complications, which have been considered in this work. As a result, JT effect and surface interaction both reduced the energy of the system and partially removed the degeneracy.

The aim of this work was to investigate the combined effects of the dynamic JT and surface interactions in different JT active systems placed on some surfaces, and the expected images of these ions in STM. These ions can be placed on the substrate, either as individual ions. Hückel molecular orbital theory has been used with the symmetry arguments of group theory techniques to analyse the symmetry reduction due to the combination's influence. Imaging molecules distorted by the JT effect in order to provide some information about the symmetry reduction from the icosahedral symmetry of the neutral C_{60} to D_{5d},D_{3d},D_{2h},C_{2h} and the splittings of the states has been done by using STM method. As a result, a selection of equivalent wells are generated in the lowest adiabatic potential energy surface. In relation to this, the strength of the quadratic JT effects have been considered in both static and dynamic situations.
In this work, the model has been considered to give surface and JT interactions of equal importance. The JT effect has been incorporated into the system through second order quadratic constants that were added. In modelling the JT effect and the other external surface interactions in C_{60} anions, it was assumed that the C_{60} ions are adsorbed onto a surface substrate as an external interaction com-

bined with the internal JT effect of different orientations. The effects of three possible orientations on the surface have been obtained. The method has been treated with different unknown parameters, such as JT coupling constants, term splittings and surface parameters.

The work started by determining the positions of minima in the APES and the associated eigen states. Then, theory that was modified for multi-electron functions was used to investigate the total current for tunnelling in highly charged systems in a simple way. The system electronic states have been demonstrated to form the basis for representing the interaction Hamiltonian as a matrix.
It was found that C_{60}^{2-} anions have been modelled from the product $T_{1u} \otimes T_{1u}$ as two electrons interacting with each other, however, two holes have also been interacting in the case of C_{60}^{4-} anions. This resulted in A_g and H_g antisymmetric states coupled in C_{60}^{2-} and C_{60}^{4-} systems by the JT effect. The JT and the surface interaction Hamiltonians in Ceulemans and Fowler's basis have been combined with each other to investigate these interactions. The surface Hamiltonian has been extended from the single electron $T \otimes h$ JT problem. This extension showed that the surface Hamiltonian depends on the orientation of the molecule only. An alternative direct integration method was introduced in order to represent the current in the simplest form, in terms of single electron states to be a linear combination of T_{1ux},T_{1uy},T_{1uz} states. This method was then applied to show the behaviour of the C_{60}^{2-} and C_{60}^{4-} systems when pentagon-prone and hexagon-prone adsorbed on the surface, in case of positive and negative surface interactions. Further information about the symmetry regions and the boundary of $p^2 \otimes h$ and $p^4 \otimes h$ systems has been found. Some simulations have managed to generate images of both systems. In addition, theoretical comparison between published STM images of C_{60}^{-} with C_{60}^{2-} have been provided.

The triply charged ions have been modelled from the triple product $T_{1u} \otimes T_{1u} \otimes T_{1u}$. T_{1u} has been coupled to the H_g symmetric state, in the case of the C_{60}^{3-} ion, by the JT effect. The wells in this ion preferred either D_{2h} or C_{2h}, which made the situation more complicated. Similarly, the electronic basis of the system was found to form the surface interaction Hamiltonian in different geometries. Then, the treatment of the surface was extended, and a combined Hamiltonian between the JT and the surface interactions was investigated. Results have been obtained for this ion facing the surface with several orientations, such as pentagon, hexagon, and double bond prone for positive and negative surface interactions. Additional unknown parameters in the higher charged states were compared with the single electron state due to the extra dimension of their basis and the distinct orbital energies.

In fact, it was found that the STM images are a superposition of $(\psi_x^2 + \psi_y^2)$ and ψ_z^2 for both pentagon and hexagon prone, and only two of ψ_x^2,ψ_z^2 and ψ_y^2 in case of the double bond prone with no cross terms. Interpretations with observed images have been produced for C_{60}^{3-}, and C_{60}^{4-} ions in a simpler way than using other complicated DFT methods.

Matching with Wachowiak's *et al* STM images in their published paper [18] of the positive sample bias of C_{60}^{4-} empty states along the double-bond orientation has been obtained. It was found mathematically and from the wells distribution in the JT problem that the possible regions of matching are a combination of electronic states $(A_g, H_{g\theta}, H_{g\epsilon})$, which have interacted, with no cross terms involved. This result has reduced the matrix dimension to be more manageable. Then, the direct integration method has been used to numerically find the possible ranges of combinations of the coefficients (a_{2x}, a_{2y}, a_{2z}). In fact, it was found that the STM current should be almost dominated by ψ_y^2.

However, C_{60}^{3-} ions were found to be more complicated due to the repeated irreps and the extra electron. Again, matching with Wachowiak's *et al* STM images in ref. [18] of the filled and empty states of C_{60}^{3-} ion along the hexagon-prone orientation has been achieved. It was found mathematically that the STM current preferred ψ_z^2. This also showed that the JT effect may not be ignored. The theoretical STM images of this ion could be one of the techniques that are useful in describing the superconductivity of this complicated ion, which cannot be described by other groups, such as D_{3d} or D_{5d} as in the previously investigated molecules of C_{60}.

The matching between the STM simulated images and the published experimental ones is generally good. Then, it is clear that the signature of the JT effect is on the STM images during the matching with the experimental images. This implies that in the literature, it could be possible to match the theoretical STM images of particular distortions. These particular distortions could be due to any other perturbations of a system.

In addition, hopping between the equivalent minima of the distortions have been considered with spending neglected time in the intermediate path. On the other hand, the pseudorotation process has been taken into account with the connection paths to the distortions. In fact, it was found that distinguishing between the pseudorotation and the surface effects is not possible.

There is still much work to be done in this field, so as to fully comprehend the complicated interaction and the rate of contribution between the triplet (JT effect, surface interaction and finally, the pseudorotation process). In case of JT interpretation, many factors affected the ideal STM images, and indeed, some of them may be quite significant. On the other hand, the theoretical simulation of scanning images of fullerene molecules on surfaces may specifically consider only the effects of a JT interaction. Then, the collected results can be used to expect what may be observed in nature. The results have shown evidence that the JT effect was not the only one responsible for the behaviour of C_{60} anions, as there were supporting effects from the surface on which the the molecule was placed. Different strengths of the surface have resulted in different positions for the wells. Future work may take into account other interactions, such as neighbouring ions, and may be interested in imaging the overall surfaces. In addition, this work can be a good starting base to relate the fullerene C_{60} anions with the other different icosahedral molecules.

This work has ended by calculations of the quantum mechanical width of transition lines between the ground and the excited states of C_{60}^{-} anion, when second order quadratic coupling constants have been involved. In case of the D_{3d}, trigonal minima has been considered experimentally as the most likely ground state. Matrix elements of the Hamiltonian squared have been derived in order to define the width of transition lines, which was found to be a function of linear and quadratic coupling constants. Approximation values for these unknown linear and quadratic constants have been obtained from comparing the theoretical calculated widths with experimentally observed ones. As a result, the intrinsic quantum mechanical width could be an important factor; however, there are other factors, which cause line width to broaden, and which have not been taken into account. In addition, the limited experimental data available indicates that the fit is under resolved. The line width calculations could be extended to the other allowed distortion symmetries, such as D_{5d} and D_{2h}. However, it will not be able to match the results to experimental data as the observed transitions indicate that the C_{60}^{-} molecule is distorted to D_{3d} symmetry. The same problem persists in higher charge states, such as C_{60}^{2-}, C_{60}^{3-} and C_{60}^{4-}. However, little information relevant to C_{60}^{2-} on the coupling constants exists, as in ref.[102]. More data is needed in the future for further investigations, as working with fullerene ions required more information about JT parameters.

Bibliography

[1] H. A. Jahn and E. Teller, Proc. Roy. Soc. London. A **161**, 220 (1937).

[2] C. P. Moate *et al.*, Phys. Rev. Lett. **77**, 4362 (1996).

[3] P. D. L. Rios, N. Manini, and E. Tosatti, Phys. Rev. B **54**, 7157 (1996).

[4] U. Öpik and M. H. L. Pryce, Proc. Roy. Soc. London. A **238**, 425 (1957).

[5] H. W. Kroto, J. R. Heath, S. C. O'Brien, R. F. Curl, and R. E. Smalley, Nature **318**, 162 (1985).

[6] W. Kratschmer, L. D. Lamb, K. Foristopoulos, and D. R. Huffman, Nature **347**, 354 (1990).

[7] C. M. Varma, J. Zaanen, and K. Raghavachari, Science **254**, 989 (1991).

[8] N. Manini, E. Tosatti, and A. Auerbach, Phys. Rev. B **49**, 13008 (1994).

[9] R. E. Walstedt, D. Murphy, and M. Rosseinsky, Nature **362**, 611 (1993).

[10] S. Sookhun, J. L. Dunn, and C. A. Bates, Phys. Rev. B **68**, 235403 (2003).

[11] M. Fabrizio and E. Tosatti, Phys. Rev **55**, 13465 (1997).

[12] A. Auerbach, N. Manini, and E. Tosatti, Phys. Rev. B **49**, 12998 (1994).

[13] L. F. Yuan *et al.*, Chem. Soc **125**, 169 (2003).

[14] C. C. Chancey and M. C. M. O'Brien, *The Jahn-Teller Effect in* C_{60} *and other Icosahedral Complexes* (Princeton University Press, Princeton, 1997).

[15] A. Auerbach, Phys. Rev. Lett **72**, 2931 (1994).

[16] L. M. Sindi, I. D. Hands, J. L. Dunn, and C. A. Bates, J. Mol. Struct. **838**, 78 (2007).

[17] C. Faber, J. L. Janssen, M. Côté, E. Runge, and X. Blase, Phys. Rev. B **84**, 155104 (2011).

[18] A. Wachowiak *et al.*, Science **310**, 468 (2005).

[19] J. I. Pascual *et al.*, Chem. Phys. Lett. **321**, 78 (2000).

[20] M. Casarin *et al.*, J. Phys. Chem. C **111**, 9365 (2007).

[21] I. D. Hands, J. L. Dunn, C. S. A. Rawlinson, and C. A. Bates, Jahn-Teller effects in molecules on surfaces with specific application to C_{60}, in *The Jahn-Teller Effect*, edited by H. Koeppel, D. R. Yarkony, and H. Barentzen, , Springer Series in Chemical Physics Vol. 97, pp. 517–551, Springer-Verlag, 2009.

[22] J. L. Dunn, A. J. Lakin, and I. D. Hands, New J. Phys. **14**, 083038 (2012).

[23] J. L. Dunn and C. A. Bates, Phys. Rev. B **52**, 5996 (1995).

[24] C. A. Bates, J. L. Dunn, and E. Sigmund, J. Phys. C **20**, 1965 (1987).

[25] I. D. Hands, J. L. Dunn, and C. A. Bates, Phys. Rev. B **81**, 205440 (2010).

[26] I. D. Hands, J. L. Dunn, and C. A. Bates, Phys. Rev. B **82**, 155425 (2010).

[27] I. D. Hands *et al.*, Phys. Rev. B **77**, 115445 (2008).

[28] Y. Deng and C. N. Yang, Phys. Lett. A **170**, 116 (1992).

[29] G. Binnig, H. Roher, C. H. Gerber, and E. Weibel, Appl. Phys. Lett. **40**, 178 (1982).

[30] G. Binnig, H. Roher, C. H. Gerber, and E. Weibel, Phys. Rev. Lett. **49**, 57 (1982).

[31] C. Bai, *Scanning Tunneling Microscopy and Its Application*, 2nd ed. (Springer, 2000).

[32] R. V. Lapshin, Nanotechnlogy. **15**, 1135 (2004).

[33] C. J. Chen, *Introduction to Scanning Tunneling Microscopy*, 2nd ed. (Oxford University Press, New York, 2008).

[34] D. A. Bonnell and B. D. Huey, *Basic Principles of Scanning Probe Microscopy* (New York, 2001).

[35] L. Forro and L. Mihaly, Phys. **64**, 649 (2001).

[36] X. B. Wang, C. F. Ding, and L. S. Wang, J. Chem. Phys. **110**, 8217 (1999).

[37] N. Manini, A. Dal Corso, M. Fabrizio, and E. Tosatti, Philos. Mag. B **81**, 793 (2001).

[38] I. D. Hands, J. L. Dunn, and C. A. Bates, Fullerenes, Nanotubes and Carbon Nanostructures **14**, 551 (2006).

[39] R. S. Berry, J. Chem. Phys. **32**, 933 (1960).

[40] I. B. Bersuker, *The Jahn-Teller Effect* (Cambridge University Press, Cambridge, 2006).

[41] P. W. Fowler and J. Woolrich, Chem. Phys. Lett. **127**, 78 (1986).

[42] M. S. Dresselhaus, G. Dresselhaus, and P. C. Eklund, *Science of Fullerenes and Carbon Nanotubes* ((Academic, SanDiego), 1996).

[43] R. C. Haddon, Acc. Chem. **25**, 127 (1992).

[44] P. W. Fowler, Contemp. Phys. **37**, 235 (1996).

[45] H. W. Kroto, Nature **329**, 529 (1987).

[46] A. R. Kortan *et al.*, Nature. **355**, 529 (1992).

[47] C. Silien, N. A. Pradhan, W. Ho, and P. A. Thiry, Phys. Rev. B **69**, 115434 (2004).

[48] J. G. Hou *et al.*, Phys. Rev. Lett. **83**, 3001 (1999).

[49] X. H. Lu, M. Grobis, K. H. Khoo, S. G. Louie, and M. F. Crommie, Phys. Rev. Lett. **90**, 096802 (2003).

[50] X. Lu, M. Grobis, K. H. Khoo, S. G. Louie, and M. F. Crommie, Phys. Rev. B **70**, 115418 (2004).

[51] M. Calvaresi and F. Zerbetto, Acs. Nano. **4**, 2283 (2010).

[52] G. Saito *et al.*, Met. **64**, 359 (1994).

[53] M. Baenitz *et al.*, Solid State Commun. **96**, 539 (1995).

[54] J. H. Weaver, Acc. Achem. Res. **25**, 143 (1992).

[55] L. Haritha, G. G. Reddy, A. Ramakanth, S. K. Ghatak, and W. Nolting, Phys. B-Con. Mat. **405**, 1701 (2010).

[56] C. X. Chen, J. Y. Zheng, Y. Y. Jiang, J. Li, and R. K. Zheng, Phys. B-Con. Mat. **405**, 2088 (2010).

[57] A. F. Hebard *et al.*, Nature **350**, 600 (1991).

[58] H. Park *et al.*, Nature. **407**, 57 (2000).

[59] M. C. M. O'Brien, Phys. Rev. B **53**, 3775 (1996).

[60] R. L. Carter, *Molecular Symmetry and Group Theory* (John Wiley and Sons, New York, 1998).

[61] Z. C. Wu, D. A. Jelski, and T. F. George, Chem. Phys. Lett **137**, 291 (1987).

[62] J. P. Cullerne and M. C. M. O'Brien, Phys. **6**, 9017 (1994).

[63] L. Boyle and Y. M. Parker, Mol. Phys. **39**, 95 (1980).

[64] N. D. Mermin, Rev. Mod. Phys. **64**, 1 (1992).

[65] I. D. Hands, J. L. Dunn, C. A. Bates, and V. Z. Polinger, Chem. Phys. **278**, 41 (2002).

[66] J. Tersoff and D. R. Hamann, Phys. Rev. B **31**, 805 (1985).

[67] E. Clementi and D. L. Raimondi, J. Chem. Phys. **38**, 2686 (1963).

[68] K. Y. Amsharov, Y. Kramer, and M. Jansen, Angew. Chem. -Int. Edit **50**, 11640 (2011).

[69] Y. Wang *et al.*, Phys. Rev. Lett. **99**, 086402 (2007).

[70] N. Iwahara, T. Sato, K. Tanaka, and L. F. Chibotaru, Phys. Rev. B **82**, 245409 (2010).

[71] N. Manini and P. De Los Rios, Phys. Rev. B **62**, 29 (2000).

[72] P. W. Fowler and A. Ceulemans, Mol. Phys. **54**, 767 (1985).

[73] G. Klupp *et al.*, Phys. Rev. B **74**, 195402 (2006).

[74] J. Bardeen, Phys. Rev. **6**, 57 (1961).

[75] A. J. Lakin, H. S. Alqannas, and J. L. Dunn, J. Phys: Conference Series , In Press (2013).

[76] S. C. Erwin and C. Bruder, Physica B **199-200**, 600 (1994).

[77] A. J. Lakin, H. S. Alqannas, J. A. Farrow, and J. L. Dunn, (2013 to be submitted).

[78] A. V. Nikolaev and B. N. Plakhutin, Russ. Chem. Rev. **79**, 729 (2010).

[79] G. Klupp, K. Kamarás, N. M. Nemes, C. M. Brown, and J. Leão, Phys. Rev. B. **73**, 085415 (2006).

[80] A. Ceulemans and L. G. Vanquickenborne, Structure and Bonding **71**, 125 (1989).

[81] P. Dahlke and M. J. Rosseinsky, Chem. Mater **14**, 1285 (2002).

[82] W. Fulton and B. Amer, Math. Soc **37**, 209 (2000).

[83] I. D. Hands, W. A. Diery, J. L. Dunn, and C. A. Bates, J. Mol. Struct. **838**, 66 (2007).

[84] I. D. Hands, J. L. Dunn, W. A. Diery, and C. A. Bates, Phys. Rev. B **73**, 115435 (2006).

[85] H. S. Alqannas, A. J. Lakin, J. A. Farrow, and J. L. Dunn, Phys. Rev. B **88**, 165430 (2013).

[86] J. L. Dunn and H. Li, Phys. Rev. B **71**, 115411 (2005).

[87] A. Lakin, I. D. Hands, C. A. Bates, and J. L. Dunn, The quadratic $p^3 \otimes h$ jahn-teller system as a model for the c_{60}^{3-} anion, in *Vibronic Interactions and the Jahn-Teller effect: Theory and Applications*, Springer, 2012.

[88] G. Klupp *et al.*, Nat. Commun **3**, 912 (2012).

[89] M. Capone, M. Fabrizio, C. Castellani, and E. Tosatti, Rev. Mod. Phys. **81**, 943 (2009).

[90] A. Ceulemans, Topics in Current Chemistry **171**, 27 (1994).

[91] J. L. Dunn, J. Phys.: Condens. Matter **17**, 5499 (2005).

[92] I. D. Hands, W. A. Diery, J. L. Dunn, and C. A. Bates, Phys. Rev. B **76**, 085426 (2007).

[93] N. Koga and K. Morokuma, Chem. Phys. Lett **196**, 191 (1992).

[94] H. Ramanantoanina, M. Gruden-Pavlovic, M. Zlatar, and C. Daul, Int. J. Quantum Chem. , DOI: 10.1002/qua.24080 (2012).

[95] S. Tomita *et al.*, Phys. Rev. Lett. **94**, 053002 (2005).

[96] O. Gunnarsson *et al.*, Phys. Rev. Lett. **74**, 1875 (1995).

[97] X. B. Wang, H. K. Woo, and L. S. Wang, J. Chem. Phys. **123**, 051106 (2005).

[98] I. D. Hands, J. L. Dunn, and C. A. Bates, Phys. Rev. B **73**, 235425 (2006).

[99] C. L. Wang, Phys. Rev. B **50**, 5676 (1994).

[100] M. Saito, Phys. Rev. B **65**, 220508 (2002).

[101] K. Tanaka, M. Okada, K. Okahara, and T. Yamabe, Chem. Phys. Lett **193**, 101 (1992).

[102] M. J. Hope *et al.*, Chem. Phys. Lett. **474**, 112 (2009).

Chapter 9

Appendix

The following Tables show the minima of different symmetries D_{2h} and C_{2h} of C_{60}^{3-} of different JT parameters V_2' and V_3' in case of no surface interaction.

Table 9.1: Q values of D_{2h} symmetry of C_{60}^{3-} for V_2'= 0 and V_3'= 0.4

a_θ	a_ϵ	a_4	a_5	a_6
0.504955	-0.870808	-1.42357	-0.70946	0.714114
0.504955	-0.870808	1.42357	0.70946	0.714114
0.504955	-0.870808	-1.42357	-0.70946	0.714114
-1.00662	-0.00189999	0.70946	-0.714114	-1.42357
0.501664	0.872708	-0.714114	-1.42357	0.70946
0.501664	0.872708	0.714114	-1.42357	-0.70946
0.504955	-0.870808	-1.42357	0.70946	-0.714114
0.504955	-0.870808	1.42357	-0.70946	-0.714114
-1.00662	-0.00189999	-0.70946	0.714114	-1.42357
-1.00662	-0.00189999	-0.70946	-0.714114	1.42357
0.501664	0.872708	0.714114	1.42357	0.70946
0.501664	0.872708	-0.714114	1.42357	-0.70946
-2.01324	0.00379999	0	0	0
1.00333	-1.74542	0	0	0
1.00991	1.74162	0	0	0

Table 9.2: Q values of C_{2h} symmetry centred around pentagon of C_{60}^{3-} for of V_2'= -0.4 and V_3'= 0

a_θ	a_ϵ	a_4	a_5	a_6
1.55972913435	0.98671282057	2.21556423766	0.20137869540	0.095802276586
1.55972913435	0.98671282057	-2.21556423766	-0.20137869540	0.09580227658
1.5666404966	0.74007529617	-2.31136651425	0.095802276586	-0.105576418816
0.074653801678	-1.84412146366	-0.20137869540	-0.095802276586	2.2155642376
-0.14239624110	-1.7267881	-0.095802276586	0.105576418816	-2.3113665142
-1.63438293603	0.85740864308	0.095802276586	2.21556423766	0.20137869540
-1.42424425550	0.98671282057	0.105576418816	-2.31136651425	-0.095802276586
-1.42424425550	0.98671282057	-0.10557641881	2.31136651425	-0.09580227658
0.07465380167	-1.84412146366	0.20137869540	0.095802276586	2.21556423766
1.56664049660	0.74007529617	2.31136651425	-0.095802276586	-0.105576418816
-0.14239624110	-1.7267881	0.095802276586	-0.105576418816	-2.31136651425
-1.63438293603	0.85740864308	-0.095802276586	-2.21556423766	0.20137869540
-0.14239624110	-1.7267881	-0.095802276586	-0.105576418816	2.31136651425
-0.14239624110	-1.7267881	0.095802276586	0.105576418816	2.31136651425
0.074653801678	-1.84412146366	0.20137869540	-0.095802276586	-2.21556423766
1.56664049660	0.74007529617	-2.31136651425	-0.095802276586	0.105576418816
-1.63438293603	0.85740864308	-0.095802276586	2.21556423766	-0.20137869540
-1.63438293603	0.85740864308	0.095802276586	-2.21556423766	-0.20137869540
0.074653801678	-1.84412146366	-0.20137869540	0.095802276586	-2.21556423766
1.56664049660	0.74007529617	2.31136651425	0.095802276586	0.105576418816
1.64129429828	1.10404616749	-2.10998781885	0	0
-1.77677917714	0.86937947365	0	2.10998781885	0
-1.77677917714	0.86937947365	0	-2.10998781885	0
-1.42424425550	0.98671282057	-0.105576418816	-2.31136651425	0.095802276586
1.55972913435	0.98671282057	2.21556423766	-0.20137869540	-0.095802276586
1.64129429828	1.10404616749	2.10998781885	0	0
-1.42424425550	0.98671282057	0.105576418816	2.31136651425	0.095802276586
1.55972913435	0.98671282057	-2.21556423766	0.20137869540	-0.095802276586
0.135484878855	-1.97342564114	0	0	-2.10998781885
0.135484878855	-1.97342564114	0	0	2.10998781885

Table 9.3: Q values of C_{2h} symmetry around double bond in direction of pentagon of C_{60}^{3-} for V_2'= 0 and V_3'= 0.2

a_θ	a_ϵ	a_4	a_5	a_6
0.49157613955	0.59554966982	0.71922436156	0.73956844599	0.35776886396
0.49157613955	0.59554966982	-0.71922436156	-0.73956844599	0.35776886396
0.50856842325	-0.310232991447	-1.07699322553	0.35776886396	-0.381799582033
0.2699730735	-0.72349225966	-0.73956844599	-0.3577688639	0.71922436156
-0.52295386331	-0.28531667838	-0.35776886396	0.381799582033	-1.07699322553
-0.76154921306	0.12794258983	0.35776886396	0.71922436156	0.73956844599
0.014385440055	0.59554966982	0.381799582033	-1.07699322553	-0.35776886396
0.014385440055	0.59554966982	-0.381799582033	1.07699322553	-0.35776886396
0.2699730735	-0.72349225966	0.73956844599	0.35776886396	0.71922436156
0.50856842325	-0.310232991447	1.07699322553	-0.35776886396	-0.381799582033
-0.52295386331	-0.28531667838	0.35776886396	-0.381799582033	-1.07699322553
-0.76154921306	0.12794258983	-0.35776886396	-0.71922436156	0.73956844599
-0.52295386331	-0.28531667838	-0.35776886396	-0.381799582033	1.07699322553
-0.5229538633	-0.28531667838	0.35776886396	0.381799582033	1.07699322553
0.2699730735	-0.72349225966	0.73956844599	-0.35776886396	-0.71922436156
0.50856842325	-0.310232991447	-1.07699322553	-0.35776886396	0.381799582033
-0.76154921306	0.12794258983	-0.35776886396	0.71922436156	-0.73956844599
-0.76154921306	0.12794258983	0.35776886396	-0.71922436156	-0.73956844599
0.2699730735	-0.72349225966	-0.73956844599	0.35776886396	-0.71922436156
0.50856842325	-0.310232991447	1.07699322553	0.35776886396	0.381799582033
0.77854149676	1.03372525111	-0.337424779534	0	0
-1.28450307637	0.157374088547	0	0.337424779534	0
-1.28450307637	0.157374088547	0	-0.337424779534	0
0.014385440055	0.59554966982	-0.381799582033	-1.07699322553	0.35776886396
0.49157613955	0.59554966982	0.71922436156	-0.73956844599	-0.35776886396
0.77854149676	1.03372525111	0.337424779534	0	0
0.014385440055	0.59554966982	0.381799582033	1.07699322553	0.35776886396
0.49157613955	0.59554966982	-0.71922436156	0.73956844599	-0.35776886396
0.50596157961	-1.19109933965	0	0	-0.337424779534
0.50596157961	-1.19109933965	0	0	0.337424779534

Table 9.4: Q values of C_{2h} symmetry around double bond in direction of hexagon of C_{60}^{3-} for V_2'= 0 and V_3'= 0.5

a_θ	a_ϵ	a_4	a_5	a_6
-1.78576042959	0.092654257875	0.80852363587	-0.58156798158	-1.95776911807
-1.78576042959	0.092654257875	-0.80852363587	0.58156798158	-1.95776911807
0.57171254567	0.80492666068	1.14924548219	-1.95776911807	-1.37620113648
0.97312115588	1.5001867681	0.58156798158	1.95776911807	0.80852363587
0.4112306634	-0.89758091856	1.95776911807	1.37620113648	1.14924548219
0.81263927371	-1.59284102604	-1.95776911807	0.80852363587	-0.58156798158
-0.98294320917	0.092654257875	1.37620113648	1.14924548219	1.95776911807
-0.98294320917	0.092654257875	-1.37620113648	-1.14924548219	1.95776911807
0.97312115588	1.5001867681	-0.58156798158	-1.95776911807	0.80852363587
0.57171254567	0.80492666068	-1.14924548219	1.95776911807	-1.37620113648
0.4112306634	-0.89758091856	-1.95776911807	-1.37620113648	1.14924548219
0.81263927371	-1.59284102604	1.95776911807	-0.80852363587	-0.58156798158
0.4112306634	-0.89758091856	1.95776911807	-1.37620113648	-1.14924548219
0.4112306634	-0.89758091856	-1.95776911807	1.37620113648	-1.14924548219
0.97312115588	1.5001867681	-0.58156798158	1.95776911807	-0.80852363587
0.57171254567	0.80492666068	1.14924548219	1.95776911807	1.37620113648
0.81263927371	-1.59284102604	1.95776911807	0.80852363587	0.58156798158
0.81263927371	-1.59284102604	-1.95776911807	-0.80852363587	0.58156798158
0.97312115588	1.5001867681	0.58156798158	-1.95776911807	-0.80852363587
0.57171254567	0.80492666068	-1.14924548219	-1.95776911807	1.37620113648
1.54483370156	-2.30511342885	0.56767750061	0	0
1.2238699372	2.4904219446	0	-0.56767750061	0
1.2238699372	2.4904219446	0	0.56767750061	0
-0.98294320917	0.092654257875	-1.37620113648	1.14924548219	-1.95776911807
-1.78576042959	0.092654257875	0.80852363587	0.58156798158	1.95776911807
1.54483370156	-2.30511342885	-0.56767750061	0	0
-0.98294320917	0.092654257875	1.37620113648	-1.14924548219	-1.95776911807
-1.78576042959	0.092654257875	-0.80852363587	-0.58156798158	1.95776911807
-2.76870363877	-0.185308515750	0	0	0.56767750061
-2.76870363877	-0.185308515750	0	0	-0.56767750061

Table 9.5: Q values of C_{2h} symmetry around hexagon of C_{60}^{3-} for V_2'= 0.2 and V_3'= 0.6

a_θ	a_ϵ	a_4	a_5	a_6
-3.8880827053	0.477322854040	1.10357588644	0.065621548525	-3.26826681569
-3.8880827053	0.477322854040	-1.10357588644	-0.065621548525	-3.26826681569
0.78034599285	0.396953199030	2.16469092925	-3.26826681569	-3.33388836422
2.35741507005	3.12851696779	-0.065621548525	3.26826681569	1.10357588644
-0.046401441954	-0.87427605307	3.26826681569	3.33388836422	2.16469092925
1.5306676352	-3.60583982183	-3.26826681569	1.10357588644	0.065621548525
-0.73394455090	0.477322854040	3.33388836422	2.16469092925	3.26826681569
-0.73394455090	0.477322854040	-3.33388836422	-2.16469092925	3.26826681569
2.35741507005	3.12851696779	0.065621548525	-3.26826681569	1.10357588644
0.78034599285	0.396953199030	-2.16469092925	3.26826681569	-3.33388836422
-0.046401441954	-0.87427605307	-3.26826681569	-3.33388836422	2.16469092925
1.5306676352	-3.60583982183	3.26826681569	-1.10357588644	0.065621548525
-0.046401441954	-0.87427605307	3.26826681569	-3.33388836422	-2.16469092925
-0.046401441954	-0.87427605307	-3.26826681569	3.33388836422	-2.16469092925
2.35741507005	3.12851696779	0.065621548525	3.26826681569	-1.10357588644
0.78034599285	0.396953199030	2.16469092925	3.26826681569	3.33388836422
1.5306676352	-3.60583982183	3.26826681569	1.10357588644	-0.065621548525
1.5306676352	-3.60583982183	-3.26826681569	-1.10357588644	-0.065621548525
2.35741507005	3.12851696779	-0.065621548525	-3.26826681569	-1.10357588644
0.78034599285	0.396953199030	-2.16469092925	-3.26826681569	3.33388836422
3.1377610629	-3.5254701668	2.23031247777	0	0
1.48426619329	4.4801158749	0	-2.23031247777	0
1.48426619329	4.4801158749	0	2.23031247777	0
-0.73394455090	0.477322854040	-3.33388836422	2.16469092925	-3.26826681569
-3.8880827053	0.477322854040	1.10357588644	-0.065621548525	3.26826681569
3.1377610629	-3.5254701668	-2.23031247777	0	0
-0.73394455090	0.477322854040	3.33388836422	-2.16469092925	-3.26826681569
-3.8880827053	0.477322854040	-1.10357588644	0.065621548525	3.26826681569
-4.6220272562	-0.95464570808	0	0	2.23031247777
-4.6220272562	-0.95464570808	0	0	-2.23031247777